Three-Dimensional Fluid Flow Structures and Heat Transfer Characteristics of a Backward-Facing Step Flow in a Rectangular Duct

Shuai Zou

March, 2021

Three-Dimensional Fluid Flow Structures and Heat Transfer Characteristics of a Backward-Facing Step Flow in a Rectangular Duct

Specialty: Fluid Flow and Heat Transfer

Author: Shuai Zou

Advisor: Prof. Kyoji Inaoka

March, 2021

Table of Contents

CHAPTER 1

General Introduction

1.1 Background

Backward-Facing Step (BFS) flow is one of the common geometric models to study the separation and reattachment flow and heat transfer enhancement. It is a fundamental model and the flow field shows complex characteristics of the separation flow. In the stepped duct, when the fluid flows through such a sudden enlargement cross-section, the flow separation can make the steady flow state turn into an unstable flow state. The enhanced flow instability can destroy the wall boundary layer, which has a positive effect on heat transfer enhancement. It is a common method for heat transfer enhancement under a relatively low Reynolds number range. The most important features of flow separation, vortex generation, and reattachment could be found in BFS flow. The general understanding of the physics in BFS flow has attracted the attention of many scholars in recent years [1-4]. In addition, specifically in engineering applications, the step structure can constitute a sudden change in the cross-sectional area of the flow channel, which causes changes in the velocity boundary layer and temperature boundary layer in the heat exchange equipment. For example, the step structure in a compact heat exchanger can enhance heat transfer. The sudden expansion of the cross-section in the combustion chamber promotes the formation of a recirculation zone, which is beneficial to improve combustion efficiency. In general, studying the effect of the separation and reattachment flow phenomenon contained in the flow around the step on the heat transfer characteristics not only has strong academic value but also has a certain guiding significance in engineering applications [5-10]. Since few studies have taken the comprehensive analysis of such representative flow situations with BFS [1-3] into consideration and no general summary has been conducted yet. This chapter will summarize the study in such flow conditions and generalizations for BFS flow, which is necessary for future research works.

1.2 Basic geometry and features of Backward-facing step (BFS) flow

Although the geometric structure of the flow around the BFS is simple, the flow phenomenon contained in this type of structure is relatively rich. Basic geometry and physical models of the stepped duct flow is shown in Fig. 1-1. BFS flow fully develops from the entrance of a channel, with a channel height of H, a channel width of W_D, a step height of S. The expansion ratio ER and aspect ratio AR could be defined by H/S *and* W_D/S. Then the fluid in the initial boundary layer (I) flows passing through the separation point, generating a separated shear layer (II). Due to the sudden expansion effects, part of the fluid impacts the bottom wall to form a reattachment zone (VI). Under the separated shear layer, a primary recirculation region (IV) could be observed. In some circumstances, corner eddy (III) and second recirculation region could be detected in the stepped corner and near the upper wall. If AR of the channel is greater than 24, according to Iwai et al. [11], the side walls have a negligible effect on the flow along the channel centerline. While considering that the actual flow and thermal fields in heat exchangers are expected to be three-dimensional, it is necessary to understand the details of such flow and thermal structures. Some investigations on flow, heat transfer and control process under this 3D flow condition will be discussed in more detail in later sections. In this study, the basic assumption for fluids is a single-phase Newtonian fluid with constant fluid properties.

1.3 Experimental developments

Various experimental studies were carried out in the past years. Representative studies in a large Reynolds number range from laminar to turbulent flow state are summarized in Table 1-1 [1, 12-54]. In this table, the duct expansion ratio, $ER=H/(H-S)$. the duct aspect ratio, $AR=W_D/S$. Re numbers based on step height (S), the dimensionless reattachment length x_r/S are recorded for major research groups in BFS field. AR Here, the reattachment point is defined as the point at which the streamwise velocity in the experiment aspect or skin friction coefficient in the numerical simulation aspect changes its sign from negative to positive. Brief and necessary comments are also listed in the table for the convenience of comparison.

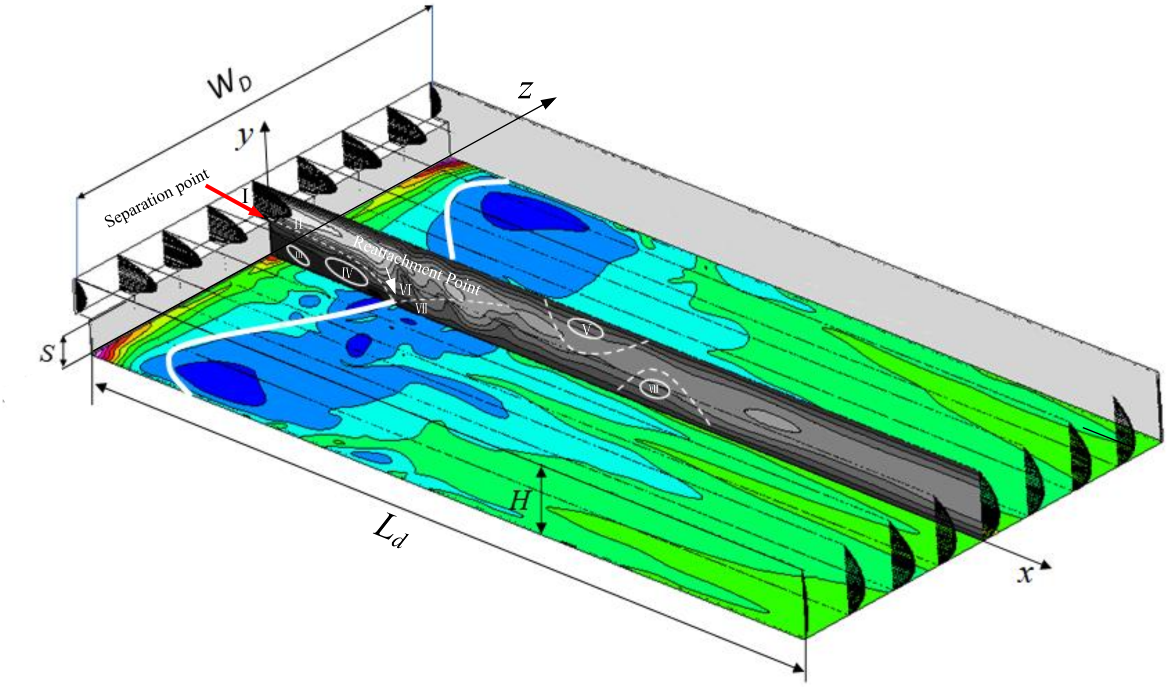

Fig. 1-1. Simplified geometry and formations of BFS. The Flow scheme: Initial boundary layer (I), separated shear layer (II), corner eddy (III), Primary recirculation region (IV), Second recirculation region (V), Reattachment zone (VI), Redeveloping boundary layer (VII), Third recirculation zone (VIII).

According to the systematic investigation of Table 1-1, most of the experimental studies are concentrated on the measurements of reattachment length, the expansion ratio (*ER*) was also recorded in this table. The layout in Table 1-1 follows the order of quite low *Re* to quite high *Re* level. From this table, multiple findings could be summarized. (a) Most research is still related to 2D flow structures. (b) Even in the case of the same geometric configuration, the size of the reattachment points of different research groups still has large differences. (c) In the high *Re* cases (*Re*>10000), the reattachment length is usually within the saturation range of 6.0-8.0. This trend indicates that the 3D effect is intensively limited, and the general structure under high *Re* may dominate after the step.

Among this table, some representative experimental research will be described again here. A representative experimental design for BFS flow measurement is shown in Fig. 1-2 [1]. In the PIV measurement study of Nadge and Govardhan [1], the aspect ratio is maintained to be greater than 16 in all experiments, well above the value of 10 suggested by De Brederode and Bradshaw [55]. With this, the reattachment length reaches a saturated value at high *Re* for all *ER* cases. As the *Re* number is higher than 20000, the flow reattachment length is almost not affected by *Re* number and expansion ratio as long as the spanwise uniformity could be maintained. The mean flow field, or the mean separation bubble, also remains in a similar structure for high *Re* numbers, which belongs to a universal sort of BFS nature under the conditions discussed. Therefore, the saturated reattachment length phenomenon under high *Re* number has been fully confirmed, but there are still differences in the reattachment length corresponding to the low and medium *Re* numbers obtained by different scholars, more detailed and systematical measurements are necessary. The three-dimensional flow structure far away from the central section along the spanwise direction still needs to be systematically studied.

Table 1-1. Characteristics of representative experimental studies on BFS flow [54].

References	*ER*	*Re*	x_r/S	Comments
Armaly et al. (1983) [26]	1.94	70–8000	Wide range	2D; Laser-Doppler measurements
Nie & Armaly (2002, 2004) [27, 28]	2.02	100–8000	3.0-18.0	3D-LDV; inclination
Durst & Tropea (1982) [30]	1.06–3.0	2000–20,000	7.2–8.65	2D-LDV;
Lee & Mateescu (1998) [31]	1.17, 2.0	~3000	6.0	2D; multi-element hot-film sensor
Wengle et al. (2001) [32]	1.09	~3000	6.5	2D; Perturbed flow; LDV
Bouda et al. (2008) [39]	2.0	7600	3.0–5.0	2D (*AR*=35); LDV
Adams & Johnston (1988) [40]	1.25	8000–40000	6.07–6.8	2D; LDV; Separation shear layer effect
Lim et al. (1990) [42]	2.0	10,000	~6.0	3D effects on flow characteristics; Turbulent, incompressible duct flow; very small *AR*=3.3
Eaton & Johnston (1980) [43]	1.67	11,000–39,000	7.0–8.2	2D; Turbulent effect
Nguyen & Souad (2015) [44]	open	11,900	4.0–6.0	3D; Turbulent wall jet; PIV
Ruck & Makiola (1988) [45]	2.0	15,000–64,000	6–8	2D (*AR*=20); Microscale particle flow, LDA
Fessler & Eaton (1999) [46]	1.67	18,400	7.4	2D; Turbulence modification; particle flow
Otugen (1991) [17]	2.15–3.13	26,500–38,000	4.9–6.5	Mixing enhancement; *ER* Effects on the separated shear layer and reattachment
Vogel & Eaton (1985) [48]	1.25	28,000	6.7	2D; Combined heat transfer and fluid dynamic measurements
Kim et al. (1978) [49]	1.32–1.50	30,000–45,000	7.0	3D; Low aspect ratio (*AR*=3.3); Separation/reattachment
Driver & Seegmiller (1985) [52]	1.11	37,500	6.26	2D (*AR*=12); Diverging channel
Westphal et al. (1984) [15] [16]	1.67	42,000	7.0–8.6	2D; Expanding channel; parameters
Kuehn (1980) [14]	1.14–1.33	79,000	6.19–6.80	2D; Effects of adverse pressure gradient on the incompressible reattachment

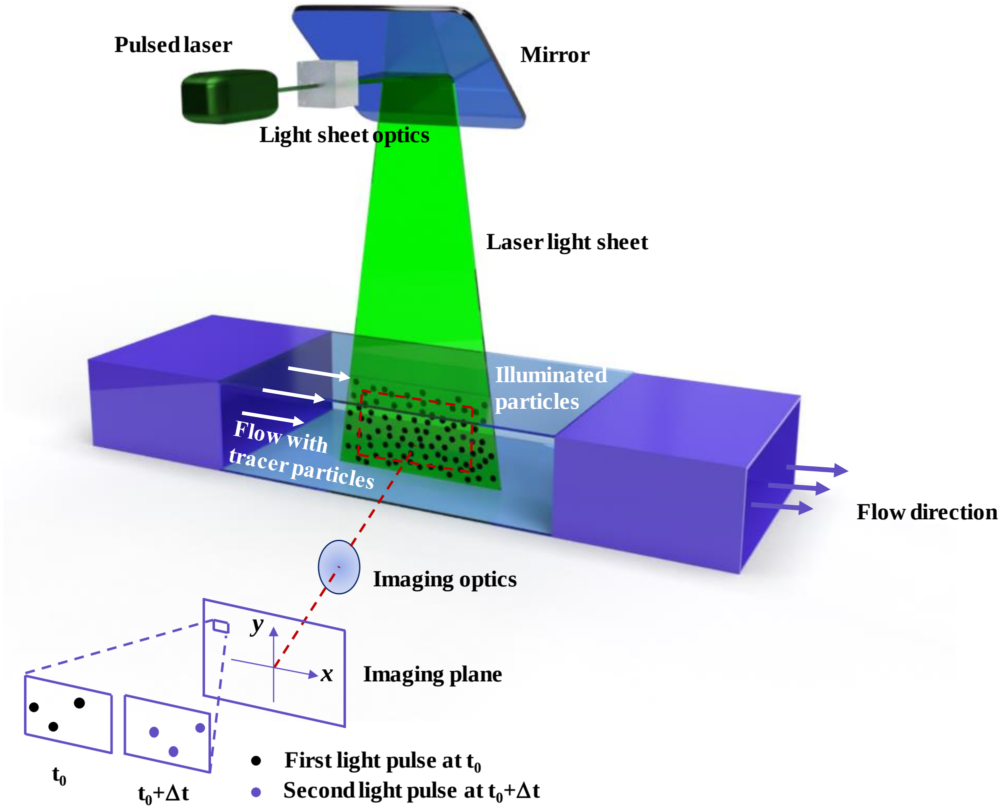

Fig. 1-2. Concept figure of the measurement system in BFS experiments (PIV; FOV field of view) [1].

1.4 Numerical developments

Representative numerical studies with BFS flows are summarized in Table 1-2 [2, 21, 39, 42, 56-99]. In this table, the numerical methods, *ER*, *Re*, and the dimensions reattachment length x_r/S are recorded. Similar to experimental studies, numerical studies are also mainly focused on reattachment length comparisons.

In recent years, with the improvement of computing power, more and more numerical simulation studies have been implemented, a large number of different forms of calculations on backward step flow are under development. Representative numerical cases are shown in Table 1-2. From this table, several major features could be summarized for the numerical aspect of BFS flow. (a) Same as experimental cases, most numerical research is still related to 2D flow structures. 3D effects in detail have not much been considered yet. The reattachment length in the 3D case is generally shorter than that in the 2D case (b) For the reattachment research, the agreement among the numerical studies or comparison with experiments is still not satisfactory. (c) There are mainly three types of calculation methods used, namely CFD (Computational Fluid Dynamics), In-house code. Among In-house code, turbulent models are generally used, the most popular calculation model is the LES (Large Eddy Simulation） model, some DNS (Direct Numerical Simulation) method could also be found. As far as I know, DNS is generally used to study fluid/turbulence theory, such as how turbulence is dissipated, how to merge, etc. The LES is generally used for small and medium-scale simulations of practical/experimental problems (d) There still exists some saturated range when *Re* is high, which is similar to the tendency of the experimental result (e) Although the results of numerical simulation are extremely numerous. However, due to the lack of experiments, systematic verifications are rarely seen in those aspects, especially in the three-dimensional case.

One typical and basic numerical model design with BFS flow is shown in Fig. 1-3 proposed by Iwai et al [11]. The investigations were systematically carried out at a low *Re* number. The expansion ratio of the duct is kept constant at 2.0. The research is mainly conducted by changing the aspect ratio, *Re* number, the buoyancy level, the inclination angles, the types of turbulent models, and the scale of the model (microscale). It was found that there were conditions under which the three-dimensionality could play an important role in terms of heat transfer enhancement. It is also mentioned that it would be worthwhile to perform an accurate and reliable measurement for three-dimensional flow and thermal fields, especially near the side walls adjacent to the step where the flow structure was expected to be very different from the flow in the center of the duct even at a relatively large aspect.

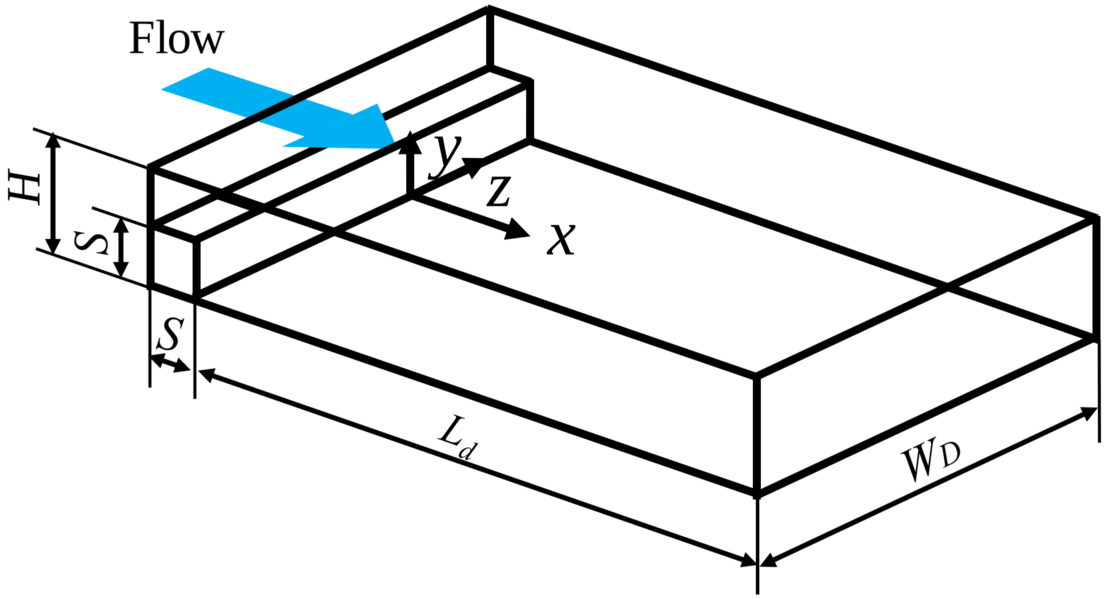

Fig. 1-3. A representative numerical model for BFS flow [64].

Analyzing from the perspective of *Re* number, prediction said that side wall effects will become quite apparent when *Re* is over 500 [100-102], while it will become weak when *Re* is over than 5000 judging from the saturation state of the reattachment points, indicating that the flow structure becomes much complicated under relative low *Re* number conditions. As shown in Fig. 1-4 [64], the results show that two bifurcation regions could be found with the increase of *Re* from laminar to turbulent region. One could be observed around *Re*=300–600, and when it goes across laminar-to-turbulent (*Re*=1600–2000), multiple bifurcations could also be found indicating the three-dimensional and complicated happenings in BFS flows. There are many studies on trends analysis and convective structure analysis. However, the comparison between prediction and experiments does not agree well with each other, due to boundary and three-dimensional effects.

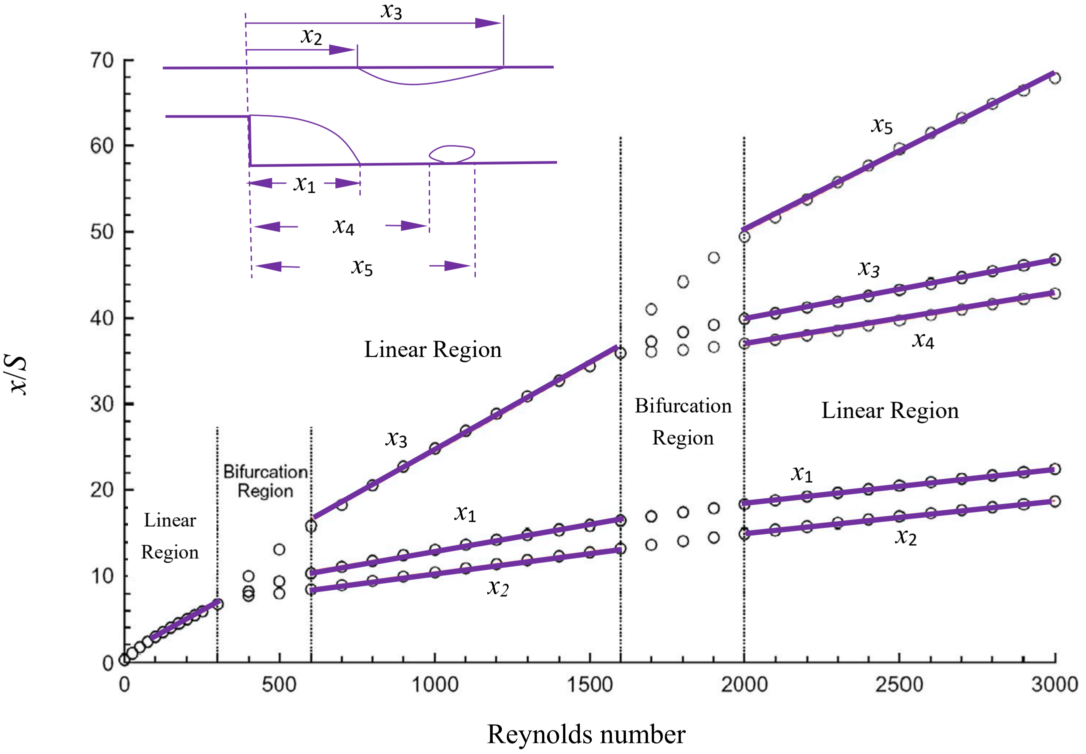

Fig. 1-4. Locations of reattachment points with respect to *Re* numbers [64].

Table 1-2. Characteristics of representative numerical studies on BFS flow [54].

References	Method	*ER*	*Re*	x_r/S	Comment
Togun et al. (2014) [60]	In-house code	2.0	50–200	2–8	2D; Nanofluid; heat transfer
Rouizi et al. (2009) [62]	In-house code	2.0	10^{-4}–800	3–12	2D; incompressible
Erturk (2008) [64]	In-house code	2.0	100–3000	2–23	2D; incompressible
Biswas et al. (2004) [68]	In-house code	2.0, 2.5, 3.0	~800	4–12	3D; Low and moderate Reynolds numbers
Kaltenbach (2004) [71]	In-house code	1.2	3000–5000	4–6.5	3D; turbulent upstream conditions; swept BFS
Dejoan & Leschziner (2004) [72]	In-house code	1.5	3700	~7	2D; LES; periodic perturbed; injection of a slot jet
Kobayashi et al. (1993) [73]	In-house code	1.5	5400	5.4–7.1	2D; LES; Anisotropic mode
Zhu (1995) [74]	In-house code	2.0	25–5000	wide range	2D; Second-order projection method
Koutmos & Mavridis (1997) [79]	In-house code	1.125; 1.2	5000; 37,000	~6	2D; LES; unsteady separated flow
Aider & Danet (2006) [81]	In-house code	1.2	5100	5–6	3D; LES; boundary effect; unsteady beheviour
Louda et al. (2013) [85]	In-house code	2.0	15,000–64,000	6.5–8.5	2D & 3D; RANS; inclination;
Yu & Lee (2009) [89]	In-house code	1.67	18,400	7.41	3D; LES; particle flow
Wang et al. (2006) [90]	In-house code	1.67	18,400	10–15	2D; LES; particle flow
Jin et al. (2011) [91]	In-house code	1.67	18,400	7.6	2D; LES/FDF; particle flow; two phase
Wang et al. (2012) [93]	In-house code	1.25	28,000	6.78	2D; LES; Vreman model
Rhee & Sung (2000) [94]	In-house code	1.5	33,000	5.1–7.7	2D; unsteady numerical simulation; internal oscillator
Prud'homme & Elghobashi (1968) [95]	In-house code	1.85	66,000	6.52	2D; Turbulent heat transfer; flow control
Choi et al. (2016) [78]	OpenFOAM	1.48–3.27	5000–64,000	4–8	2D; LES/RANS
Addad et al. (2003) [86]	Star-CD	1.11	17,000	4.7	2D; LES; forward-backward; acoustic source
Halupovich et al. (1999) [58]	Phoenics	1.12	100,000–7,700,000	2.0–4.0	2D; Supersonic turbulent flow; Ma = 3.5
Wengle et al. (2001) [32]	DNS	1.04; 1.09	1480; 3000	11.3; 6.4	2D; Perturbed flow
Le et al. (1997) [80]	DNS	1.2	5100	6.28	2D & 3D; Quasi-periodic behavior
El-Khoury et al. (2010) [76]	DNS	2.0	5200	~22	3D; Confined channel
Barri et al. (2010) [57]	DNS	2.0	5600	7.1	2D; Fully turbulent

1.5 Heat transfer related BFS flow

Most of the research on BFS flow is focused on pure fluid dynamics, and how the flow causes heat transfer changes is rarely discussed [2]. Representative studies on thermal-related BFS flows are recorded in Table 1-3 [2, 11, 48, 66, 103-125]. There are several major conclusions in the heat transfer related studies. (a) Not many researches are involved in the heat transfer aspect of BFS flow, especially experimental research accounts for a smaller proportion, which may be because the heating region becomes more complicated and difficult to control. (b) Experiments are mainly focused on the high *Re* region, while numerical studies are mainly conducted in the relatively low *Re* region. (c) Experiments are concentrated on heat transfer measurement, while flow control to enhance heat transfer is mostly applied in numerical simulation. (d) Many of the studies are focused on heat transfer enhancement, few studies are focused on the heat transfer mechanism affected by fluid flow.

1.6 BFS flow control

As shown in Table 1-3, various control methods have been proposed for BFS flow based on numerical, theoretical and experimental studies in the past years, passive and active control methods are the two main methods of BFS flow control. Passive methods include vortex generator [126], concave design [127], surface design [128] and so on, which may introduce additional pressure loss or change the flow conditions at the same time. Some researchers investigated the influence of obstacles such as circular cylinders inserted in the backward-facing step on the flow fields and heat transfer. Such investigation may help control the flow pressure loss and the boundary layer thickness. The analysis and study of transitional forced convection flow and heat transfer over a backward-facing step by inserting a cylinder is unexplored. How to find the balance point between heat transfer enhancement and smaller energy loss is particularly important in the passive control.

For active control, small disturbances with electromagnetic flap actuators on the step edge were introduced in laminar flow conditions to achieve heat transfer enhancement by Inaoka et al. [129]. Flap oscillation frequency and amplitude were changed variously under the laminar flow condition. The largest heat transfer enhancement could be achieved within the studied frequency ranges. A large-scale unsteady vortex and a downward high-speed flow are two main causes to enhance the heat transfer in the sub-optimum and the high-frequency condition. The main idea of Inaoka's group is eliminating heat transfer deterioration by destroying the recirculation region structures. Similarly, the jet-flow control method was introduced by Glezer et al. [130], the interaction between the jet-flow and the mainstream flow was also studied. Since the active control needs to consider additional energy input, no much discussion was done in my dissertation. A passive control method was adopted, which will be elaborated in Chapter 5

1.7 Summary

Based on the review of recent developments in theoretical, experimental, and numerical aspects of BFS flow. In this thesis, we focus on fulfilling 4 problems: (I) The proportion of 3D flow structure research compared with 2D research is still relatively small, especially in experimental research. (II) In the thermal field, experiments are mainly focused on the high *Re* region, while numerical studies are mainly conducted in a relatively low *Re* region. Thus, thermal structures in laminar flow cases should be intensively studied and systematically investigated. (III) Since many types of research are devoted to heat transfer enhancement, while little attention was paid to the correlation between 3D BFS flow structures and heat transfer, especially near the side walls of the stepped duct. In addition, the investigation of the heat transfer characteristics near the upper wall was very few and is a particular interest. (IV) Inserting a circular cylinder in the stepped channel, which belongs to the passive control method has rarely been investigated. Therefore, the fundamental research on 3D flow and heat transfer mechanism (near the bottom wall and the upper wall), especially their correlation based on this simple model itself in the laminar flow region should be conducted in-depth.

Table 1-3. Representative studies on BFS flow with heat transfer [54].

References	Method	Target	*ER*	*Re*	Details and Comment
Suzuki et al. (1991) [105]	Experiment	Inserted cylinder effect	Open channel	700–1400	LDV; Cylinder inserted in stepped duct
Yamada & Nakamura (2016) [103]	Experiment	Thermal fluctuations	1.10	2500–7600	PIV; high-speed thermography; Combined system
Mittal et al. (2017) [106]	Experiment	Heat mass transfer	1.07	16,000–23,000	Low step design; TC wire; Local heat transfer
Vogel & Eaton (1985) [48]	Experiment	Heat transfer	1.25	28,000	Heat transfer from below ; Flow structure
Abu-Mulaweh et al. (2001) [107]	Experiment	Mixed convection	1.28		T-diff between flow and wall; LDV
Kanna & Das (2006) [113]	In-house code	Heat transfer	2.0	100–800	Boundary and *Pr* effect
Khanafer et al. (2008) [114]	In-house code	Mixed convection	2.0	100–1000	Oscillation effect; Laminar pulsating
Iwai et al. (2000ab) [11, 115]	In-house code	Effect of *AR* and side wall	2.0	125–375	3D; BFS with rectangular duct ; 2D and 3D effect
Ramsak (2015) [118]	In-house code	Conjugate heat transfer	2.0	800	Revisited benchmark Cases
Valencia (1997) [123]	In-house code	Heat transfer	2.0	52,400	Oscillation effect; 2D; Inlet pulsating
Xie et al. (2017) [117, 131, 132]	In-house code	Geometric effect, vortex structure	2.0	500–1200	Forward step; hot wall; Backward and forward steps
Ravikanth et al. (2002) [121]	In-house code	Heat transfer	1.5	5540	LES; Small scale details
Amiri et al. (2016) [120]	Fluent	BFS heat transfer	2.0	5000–15,000	Turbulent heat transfer; nanofluids; Step in a channel flow
Barrios-Pina et al. (2012) [66]	DNS	Heat transfer	2.0	182–521	2D; heat flux effect；

1.8 Outline of thesis

As discussed in the previous sections, the thermal investigation in the laminar flow over a three-dimensional step is not much, the characteristics of 3D flow motion are not clear. Furthermore, the relationship between the 3D flow structures and the heat transfer is urgent to be clarified under this critical laminar flow state. To solve the problems above and reveal the mechanism of heat transfer enhancement in the BFS flow, an experimental platform was set up. Based on the understanding of flow and heat transfer mechanism of this fundamental BFS flow, a geometric modification was also conducted by numerical simulation to further promote the heat transfer performance.

In Chapter 2, the 3D flow structures of the BFS flow in the low *Re* number region were investigated. The spanwise variations of the time-averaged reattachment points and the periodicity of the instantaneous reattachment points were intensively paid attention to. Because the spatial change of the reattachment point can reflect the three-dimensional characteristics of the flow to a certain extent. Their relationship to heat transfer was also discussed in order to explore the effect of this separation and reattached flow on the heat transfer distribution.

In Chapter 3, spatial distributions of the local heat transfer coefficients on the bottom wall and upper wall downstream of a BFS in a duct flow have been measured by making use of a thermo-sensitive liquid crystal sheet. Three components of the time-averaged velocity measurements by 2D PIV have been done for *Re*=400-900. These two measurements make it possible to investigate the heat transfer characteristics affected by flow-related parameters. Various comparisons of the heat transfer coefficient between the bottom wall and the upper wall were also discussed.

In Chapter 4, the reattachment length data near the side wall and the center of the duct has been collected and analyzed. The flow at *Re*=400 was chosen as the main research object because of its largest reattachment length near the duct center and some other critical properties. Correlation analysis between the velocity-related parameters and Nusselt number on the bottom wall was also done through the Pearson correlation method, the heat transfer enhancement mechanism at *Re*=400 near the side wall was clarified.

In Chapter 5, after clarifying the heat transfer enhancement mechanism in a simple stepped flow, an incompressible numerical model for the BFS flow with inserting a cylinder was established to explore whether it can further enhance heat transfer. The effects of various streamwise and cross-stream positions of the cylinder on the flow fields and heat transfer were discussed.

Chapter 6 is devoted to summarize the major conclusions of this study and offers suggestions for future work.

References

[1] P. M. Nadge and R. Govardhan, "High Reynolds number flow over a backward-facing step: structure of the mean separation bubble," *Experiments in fluids,* vol. 55, no. 1, p. 1657, 2014.

[2] Z.-Y. Guo, D.-Y. Li, and X.-G. Liang, "Thermal effect on the recirculation zone in sudden-expansion gas flows," *International journal of heat and mass transfer,* vol. 39, no. 13, pp. 2619-2624, 1996.

[3] K. O'Malley, A. Fitt, T. Jones, J. Ockendon, and P. Wilmott, "Models for high-Reynolds-number flow down a step," *Journal of fluid mechanics,* vol. 222, pp. 139-155, 1991.

[4] R. Ruisi, H. Zare-Behtash, K. Kontis, and R. Erfani, "Active flow control over a backward-facing step using plasma actuation," *Acta Astronautica,* vol. 126, pp. 354-363, 2016.

[5] L. Chen, X.-R. Zhang, J. Okajima, and S. Maruyama, "Thermal relaxation and critical instability of near-critical fluid microchannel flow," *Physical Review E,* vol. 87, no. 4, p. 043016, 2013.

[6] L. Chen, X.-R. Zhang, J. Okajima, and S. Maruyama, "Numerical investigation of near-critical fluid convective flow mixing in microchannels," *Chemical Engineering Science,* vol. 97, pp. 67-80, 2013.

[7] L. Chen, X.-R. Zhang, J. Okajima, A. Komiya, and S. Maruyama, "Numerical simulation of stability behaviors and heat transfer characteristics for near-critical fluid microchannel flows," *Energy Conversion and Management,* vol. 110, pp. 407-418, 2016.

[8] M. Baigmohammadi, S. Tabejamaat, and Y. Farsiani, "An experimental study of methane–oxygen–carbon dioxide premixed flame dynamics in non-adiabatic cylinderical meso-scale reactors with the backward facing step," *Chemical Engineering and Processing: Process Intensification,* vol. 95, pp. 105-123, 2015.

[9] M. Baigmohammadi, S. Tabejamaat, and Y. Farsiani, "Experimental study of the effects of geometrical parameters, Reynolds number, and equivalence ratio on methane–oxygen premixed flame dynamics in non-adiabatic cylinderical meso-scale reactors with the backward facing step," *Chemical Engineering Science,* vol. 132, pp. 215-233, 2015.

[10] M. Shahi, J. B. Kok, and A. Pozarlik, "On characteristics of a non-reacting and a reacting

turbulent flow over a backward facing step (BFS)," *International Communications in Heat and Mass Transfer,* vol. 61, pp. 16-25, 2015.

[11] H. Iwai, K. Nakabe, and K. Suzuki, "Flow and heat transfer characteristics of backward-facing step laminar flow in a rectangular duct," *International journal of heat and mass transfer,* vol. 43, no. 3, pp. 457-471, 2000.

[12] I. Tani, "Experimental Investigation of Flow Separation Associated with a Step or a Groove," *Report. No. 864,* 1961.

[13] M. B. Narayanan, Y. Khadgi, and P. Viswanath, "Similarities in pressure distribution in separated flow behind backward-facing steps," *The Aeronautical Quarterly,* vol. 25, no. 4, pp. 305-312, 1974.

[14] D. M. Kuehn, "Effects of adverse pressure gradient on the incompressible reattaching flow over a rearward-facing step," *AIAA Journal,* vol. 18, no. 3, pp. 343-344, 1980.

[15] R. V. Westphal, J. Johnston, and J. Eaton, "Experimental study of flow reattachment in a single-sided sudden expansion," *NASA Contractor Report,* 1984.

[16] R. Westphal and J. Johnston, "Effect of initial conditions on turbulent reattachment downstream ofa backward-facing step," *AIAA journal,* vol. 22, no. 12, pp. 1727-1732, 1984.

[17] M. Ötügen, "Expansion ratio effects on the separated shear layer and reattachment downstream of a backward-facing step," *Experiments in fluids,* vol. 10, no. 5, pp. 273-280, 1991.

[18] S. Jovic and D. Driver, "Reynolds number effect on the skin friction in separated flows behind a backward-facing step," *Experiments in Fluids,* vol. 18, no. 6, pp. 464-467, 1995.

[19] P. G. Spazzini, G. Iuso, M. Onorato, N. Zurlo, and G. M. D. Cicca, "Unsteady behavior of back-facing step flow," *Experiments in Fluids,* vol. 30, no. 5, pp. 551-561, 2001.

[20] S. Jovic and D. M. Driver, "Backward-facing step measurements at low Reynolds number, Re (sub h)= 5000," 1994.

[21] E. O. Macagno and T.-K. Hung, "Computational and experimental study of a captive annular eddy," *Journal of fluid Mechanics,* vol. 28, no. 1, pp. 43-64, 1967.

[22] J.-F. Beaudoin, O. Cadot, J.-L. Aider, and J. E. Wesfreid, "Three-dimensional stationary flow over a backward-facing step," *European Journal of Mechanics-B/Fluids,* vol. 23, no. 1, pp. 147-

155, 2004.

[23] J. Kostas, J. Soria, and M. S. Chong, "A study of backward facing step flow at two Reynolds numbers," in *The 14th Australasian Fluid Mechanics Conference*, Adelaide University, Adelaide, Australia, 2001, pp. 609–612.

[24] J. Kostas, J. Soria, and M. Chong, "Particle image velocimetry measurements of a backward-facing step flow," *Experiments in Fluids,* vol. 33, no. 6, pp. 838-853, 2002.

[25] J. Tihon, V. Pěnkavová, J. Havlica, and M. Šimčík, "The transitional backward-facing step flow in a water channel with variable expansion geometry," *Experimental Thermal and Fluid Science,* vol. 40, pp. 112-125, 2012.

[26] B. F. Armaly, F. Durst, J. C. F. Pereira, and B. Schönung "Experimental and theoretical investigation of backward-facing step flow," *Journal of Fluid Mechanics,* vol. 127, no. -1, pp. 473-496, 1983.

[27] J. H. Nie and B. F. Armaly, "Reverse flow regions in three-dimensional backward-facing step flow," *International Journal of Heat and Mass Transfer,* vol. 47, no. 22, pp. 4713-4720, 2004.

[28] J. Nie and B. F. Armaly, "Three-dimensional convective flow adjacent to backward-facing step-effects of step height," *International journal of heat and mass transfer,* vol. 45, no. 12, pp. 2431-2438, 2002.

[29] L. F. Moon and G. Rudinger, "Velocity distribution in an abruptly expanding circular duct," *Journal of Fluids Engineering,* vol. 99, no. 1, pp. 226-230, 1977.

[30] F. Durst and C. Tropea, "Flow over two-dimensional backward facing steps,in: Structure of Complex Turbulent Shear Flow," in *IUTAM-symposium*, Marseille, France, 1982.

[31] T. Lee and D. Mateescu, "Experimental and numerical investigation of 2-D backward -facing step flow," *Journal of Fluids and Structures,* vol. 12, no. 6, pp. 703-716, 1998.

[32] H. Wengle, A. Huppertz, G. Bärwolff , and G. Janke, "The manipulated transitional backward-facing step flow: an experimental and direct numerical simulation investigation," *European Journal of Mechanics B/fluids,* vol. 20, no. 1, pp. 25-46, 2001.

[33] H. R. Y. Wu and H. Tang, "Turbulent flow over a rough backward-facing step," *International Journal of Heat and Fluid Flow,* vol. 44, pp. 155–169, 2013.

[34] P. P. Zemanick and R. S. Dougall, "Local Heat Transfer Downstream of Abrupt Circular Channel Expansion," *Journal of Heat Transfer,* vol. 92, no. 1, pp. 53-60, 1970.

[35] F. Scarano, C. Benocci, and M. L. Riethmuller, "Pattern recognition analysis of the turbulent flow past a backward facing step," *Physics of Fluids,* vol. 11, no. 12, pp. 3808-3818, 1999.

[36] N. Furuichi, T. Hachiga, and M. Kumada, "An experimental investigation of a large-scale structure of a two-dimensional backward-facing step by using advanced multi-point LDV," *Experiments in Fluids,* vol. 36, no. 2, pp. 274-281, 2004.

[37] C. Schram, P. Rambaud, and M. Riethmuller, "Wavelet based eddy structure eduction from a backward facing step flow investigated using particle image velocimetry," *Experiments in Fluids,* vol. 36, no. 2, pp. 233-245, 2004.

[38] N. Kasagi and A. Matsunaga, " Three-dimensional particle-tracking velocimetry measurement of turbulence statistics and energy budget in a backward-facing step flow," *International Journal of Heat and Fluid Flow,* vol. 16, no. 6, pp. 477–485, 1995.

[39] N. N. Bouda, R. Schiestel, M. Amielh, C. Rey, and T. Benabid, "Experimental approach and numerical prediction of a turbulent wall jet over a backward facing step," *International Journal of Heat and Fluid Flow,* vol. 29, no. 4, pp. 927-944, 2008.

[40] E. W. Adams and J. P. Johnston, "Effects of the separating shear layer on the reattachment flow structure. Part II: reattachment length and wall shear stress," *Experiments in Fluids,* vol. 6, pp. 493–499, 1988.

[41] L. M. Hudy, A. Naguib, and W. M. Humphreys, "Stochastic estimation of a separated-flow field using wall-pressure-array measurements," *Physics of Fluids,* vol. 19, no. 2, 2007.

[42] K. S. Lim, S. O. Park, and H. S. Shim, "A low aspect ratio backward-facing step flow," *Experimental Thermal and Fluid Science,* vol. 3, pp. 508–514, 1990.

[43] J. K. Eaton and J. P. Johnston, "Turbulent flow reattachment: an experimental study of the flow and structure behind a backward facing step Rept," in *MD-39*, Dept. of Mech. Eng. Stanford University Stanford, CA, USA, 1980.

[44] T. D. Nguyen and H. Souad, "PIV measurements in a turbulent wall jet over a backward-facing step in a three-dimensional, non-confined channel," *Flow Measurement and Instrumentation,*

vol. 42, pp. 26-39, 2015.

[45] B. Ruck and B. Makiola, "Particle dispersion in a single-sided backward-facing step flow," *International Journal of Multiphase Flow,* vol. 1988, pp. 787–800, 1988.

[46] J. R. Fessler and J. K. Eaton, "Turbulence modification by particles in a backward-facing step flow," *Journal of Fluid Mechanics,* vol. 394, pp. 97-117, 1999.

[47] H. Park, W.-P. Jeon, H. Choi, and J. Y. Yoo, "Mixing enhancement behind a backward-facing step using tabs," *Physics of Fluids,* vol. 19, no. 10, p. 105103, 2007.

[48] J. C. Vogel and J. K. Eaton, "Combined Heat Transfer and Fluid Dynamic Measurements Downstream of a Backward-Facing Step," *Journal of Heat Transfer,* vol. 107, no. 4, pp. 922-929, 1985.

[49] J. J. Kim, "Investigation of separation and reattachment of a turbulent shear layer: flow over a backward-facing step," *PhDT,* 1978.

[50] I. Lee, S. Ahn, and H. J. Sung, "Three-dimensional coherent structure in a separated and reattaching flow over a backward-facing step," *Experiments in Fluids,* vol. 36, no. 3, pp. 373-383, 2004.

[51] K. E. Feng, Y. Z. Liu, W. Z. Wang, and H. P. Chen, "Wall pressure fluctuations of turbulent flow over backward-facing step with and without entrainment: microphone array measurement," *Journal of Hydrodynamics,* vol. 18, no. 4, pp. 393-396, 2006.

[52] D. M. Driver and H. L. Seegmiller, "Features of a reattaching turbulent shear layer in divergent channelflow," *AIAA journal,* vol. 23, no. 2, pp. 163-171, 1985.

[53] O. Badran and H. Bruun, "The effect of inlet conditions on flow over backward facing step," *Journal of Wind Engineering and Industrial Aerodynamics,* vol. 74, pp. 495-509, 1998.

[54] L. Chen, K. Asai, T. Nonomura, G. Xi, and T. Liu, "A review of backward-facing step (BFS) flow mechanisms, heat transfer and control," *Thermal Science and Engineering Progress,* vol. 6, pp. 194-216, 2018.

[55] V. A. S. L. De Brederode, "Three-Dimensional Flow in Nominally Two-Dimensional Separation Bubbles: I. Flow Behind a Rearward-Facing Step," *Imperial College of Science and Technology, England, Department of Aeronautics, Aero Report,* pp. 72-19, 1972.

[56] G.-m. Guo, H. Liu, and B. Zhang, "Numerical study of active flow control over a hypersonic backward-facing step using supersonic jet in near space," *Acta Astronautica,* vol. 132, pp. 256-267, 2017.

[57] M. Barri, G. K. El Khoury, H. I. Andersson, and B. Pettersen, "DNS of backward - facing step flow with fully turbulent inflow," *International journal for numerical methods in fluids,* vol. 64, no. 7, pp. 777-792, 2010.

[58] Y. Halupovich, B. Natan, and J. Rom, "Numerical solution of the turbulent supersonic flow over a backward facing step," *Fluid Dynamics Research,* vol. 24, no. 5, p. 251, 1999.

[59] A. Al-Aswadi, H. Mohammed, N. Shuaib, and A. Campo, "Laminar forced convection flow over a backward facing step using nanofluids," *International Communications in Heat and Mass Transfer,* vol. 37, no. 8, pp. 950-957, 2010.

[60] H. Togun *et al.*, "Numerical simulation of laminar to turbulent nanofluid flow and heat transfer over a backward-facing step," *Applied Mathematics and Computation,* vol. 239, pp. 153-170, 2014.

[61] T. Chiang, T. W. Sheu, and C. Fang, "Numerical investigation of vortical evolution in a backward-facing step expansion flow," *Applied Mathematical Modelling,* vol. 23, no. 12, pp. 915-932, 1999.

[62] Y. Rouizi, Y. Favennec, J. Ventura, and D. Petit, "Numerical model reduction of 2D steady incompressible laminar flows: Application on the flow over a backward-facing step," *Journal of Computational Physics,* vol. 228, no. 6, pp. 2239-2255, 2009.

[63] A. Liakos and N. A. Malamataris, "Topological study of steady state, three dimensional flow over a backward facing step," *Computers and Fluids,* vol. 118, pp. 1-18, 2015.

[64] E. Erturk, "Numerical solutions of 2-D steady incompressible flow over a backward-facing step, Part I: High Reynolds number solutions," *Computers and Fluids,* vol. 37, no. 6, pp. 633-655, 2008.

[65] A. C. Velivelli and K. M. Bryden, "Domain decomposition based coupling between the lattice Boltzmann method and traditional CFD methods–Part II: Numerical solution to the backward facing step flow," *Advances in Engineering Software,* vol. 82, pp. 65-74, 2015.

[66] H. Barrios-Pina, S. Viazzo, and C. Rey, "A numerical study of laminar and transitional mixed convection flow over a backward-facing step," *Computers and fluids,* vol. 56, pp. 77-91, 2012.

[67] J. H. Nie, Y. Chen, and H.-T. Hsieh, "Effects of a baffle on separated convection flow adjacent to backward-facing step," *International Journal of Thermal Sciences,* vol. 48, no. 3, pp. 618-625, 2009.

[68] G. Biswas, M. Breuer, and F. Durst, "Backward-facing step flows for various expansion ratios at low and moderate Reynolds numbers," *Journal of Fluids Engineering,* vol. 126, no. 3, pp. 362-374, 2004.

[69] J. P. Guerrero and R. Cotta, "Benchmark integral transform results for flow over a backward-facing step," *Computers and fluids,* vol. 25, no. 5, pp. 527-540, 1996.

[70] W. Jürgens and H.-J. Kaltenbach, "The effect of sweep on the forced transitional flow over a backward-facing step," *Computers and fluids,* vol. 59, pp. 1-10, 2012.

[71] H.-J. Kaltenbach, "Turbulent flow over a swept backward-facing step," *European Journal of Mechanics-B/Fluids,* vol. 23, no. 3, pp. 501-518, 2004.

[72] A. Dejoan and M. Leschziner, "Large eddy simulation of periodically perturbed separated flow over a backward-facing step," *International Journal of Heat and Fluid Flow,* vol. 25, no. 4, pp. 581-592, 2004.

[73] T. Kobayashi, Y. Morinishi, and S. Togashi, "Estimation of anisotropic k-ε model on the backward-facing step flow by LES data base," in *Computational Wind Engineering 1*: Elsevier, 1993, pp. 77-84.

[74] J. Zhu, "The second-order projection method for the backward-facing step flow," *Journal of computational physics,* vol. 117, no. 2, pp. 318-331, 1995.

[75] W. C. Lasher and D. B. Taulbee, "On the computation of turbulent backstep flow," *International journal of heat and fluid flow,* vol. 13, no. 1, pp. 30-40, 1992.

[76] G. K. El Khoury, H. I. Andersson, M. Barri, and B. Pettersen, "Massive separation of turbulent Couette flow in a one-sided expansion channel," *International journal of heat and fluid flow,* vol. 31, no. 3, pp. 274-283, 2010.

[77] H. Kanchi, K. Sengupta, and F. Mashayek, "Effect of turbulent inflow boundary condition in

LES of flow over a backward-facing step using spectral element method," *International Journal of Heat and Mass Transfer,* vol. 62, pp. 782-793, 2013.

[78] H. H. Choi and J. Nguyen, "Numerical investigation of backward facing step flow over various step angles," *Procedia Engineering,* vol. 154, pp. 420-425, 2016.

[79] P. Koutmos and C. Mavridis, "A computational investigation of unsteady separated flows," *International journal of heat and fluid flow,* vol. 18, no. 3, pp. 297-306, 1997.

[80] H. Le, P. Moin, and J. Kim, "Direct numerical simulation of turbulent flow over a backward-facing step," *Journal of fluid mechanics,* vol. 330, pp. 349-374, 1997.

[81] J.-L. Aider and A. Danet, "Large-eddy simulation study of upstream boundary conditions influence upon a backward-facing step flow," *Comptes Rendus Mécanique,* vol. 334, no. 7, pp. 447-453, 2006.

[82] R. Friedrich and M. Arnal, "Analysing turbulent backward-facing step flow with the lowpass-filtered Navier-Stokes equations," *Journal of Wind Engineering and Industrial Aerodynamics,* vol. 35, pp. 101-128, 1990.

[83] H. Wang, H. Zhao, Z. Guo, Y. He, and C. Zheng, "Lattice Boltzmann method for simulations of gas-particle flows over a backward-facing step," *Journal of Computational Physics,* vol. 239, pp. 57-71, 2013.

[84] C. Scheit, A. Esmaeili, and S. Becker, "Direct numerical simulation of flow over a forward-facing step–Flow structure and aeroacoustic source regions," *International journal of heat and fluid flow,* vol. 43, pp. 184-193, 2013.

[85] P. Louda, J. Příhoda, K. Kozel, and P. Sváček, "Numerical simulation of flows over 2D and 3D backward-facing inclined steps," *International journal of heat and fluid flow,* vol. 43, pp. 268-276, 2013.

[86] Y. Addad, D. Laurence, C. Talotte, and M. Jacob, "Large eddy simulation of a forward-backward facing step for acoustic source identification," in *Engineering Turbulence Modelling and Experiments 5*: Elsevier, 2002, pp. 719-728.

[87] K. Yu, K. Lau, and C. Chan, "Large eddy simulation of particle-laden turbulent flow over a backward-facing step," *Communications in Nonlinear Science and Numerical Simulation,* vol.

9, no. 2, pp. 251-262, 2004.

[88] K. Yu, K. Lau, and C. Chan, "Numerical simulation of gas-particle flow in a single-side backward-facing step flow," *Journal of computational and applied mathematics,* vol. 163, no. 1, pp. 319-331, 2004.

[89] K. F. Yu and E. W. Lee, "Evaluation and modification of gas-particle covariance models by Large Eddy Simulation of a particle-laden turbulent flows over a backward-facing step," *International journal of heat and mass transfer,* vol. 52, no. 23-24, pp. 5652-5656, 2009.

[90] B. Wang, H. Zhang, and X. Wang, "Large eddy simulation of particle response to turbulence along its trajectory in a backward-facing step turbulent flow," *International Journal of Heat and Mass Transfer,* vol. 49, no. 1-2, pp. 415-420, 2006.

[91] H. Jin, Y. Chen, J. Fan, and K. Luo, "LES/FDF simulation of a gas-particle backward-facing step flow," *Chemical engineering science,* vol. 66, no. 16, pp. 3692-3700, 2011.

[92] H. Lan, B. Armaly, and J. Drallmeier, "Three-dimensional simulation of turbulent forced convection in a duct with backward-facing step," *International Journal of Heat and Mass Transfer,* vol. 52, no. 7-8, pp. 1690-1700, 2009.

[93] W. Wang, L. Zhang, and Y. Yan, "Large eddy simulation of turbulent flow downstream of a backward-facing step," *Procedia Engineering,* vol. 31, pp. 16-22, 2012.

[94] G. H. Rhee and H. J. Sung, "Numerical prediction of locally forced turbulent separated and reattaching flow," *Fluid Dynamics Research,* vol. 26, no. 6, p. 421, 2000.

[95] M. Prud'Homme and S. Elghobashi, "Turbulent heat transfer near the reattachment of flow downstream of a sudden pipe expansion," *Numerical Heat Transfer, Part A: Applications,* vol. 10, no. 4, pp. 349-368, 1986.

[96] S. Kiwan, "Using localized wall discharge to control the fluid flow and heat transfer for the flow over a backward facing step," *International Journal of Numerical Methods for Heat & Fluid Flow,* 2008.

[97] S. Thangam and N. Hur, "A highly-resolved numerical study of turbulent separated flow past a backward-facing step," *International journal of engineering science,* vol. 29, no. 5, pp. 607-615, 1991.

[98] K. Sarker, M. Ali, and Q. Islam, "A numerical study on the physics of flow over a flat plate with backward facing step," *Procedia Engineering,* vol. 90, pp. 351-357, 2014.

[99] K. Sarker, M. Ali, and Q. Islam, "Numerical investigation of effect of mach number over a flat plate with backward facing step," *Procedia Engineering,* vol. 105, pp. 302-308, 2015.

[100] L. Kaiktsis, G. E. Karniadakis, and S. A. Orszag, "Onset of three-dimensionality, equilibria, and early transition in flow over a backward-facing step," *Journal of Fluid Mechanics,* vol. 231, pp. 501-528, 1991.

[101] P. T. Williams and A. J. Baker, "Numerical simulations of laminar flow over a 3D backward‐facing step," *International Journal for Numerical Methods in Fluids,* vol. 24, no. 11, pp. 1159-1183, 1997.

[102] D. Barkley, M. G. M. Gomes, and R. D. Henderson, "Three-dimensional instability in flow over a backward-facing step," *Journal of Fluid Mechanics,* vol. 473, pp. 167-190, 2002.

[103] S. Yamada and H. Nakamura, "Construction of 2D-3C PIV and high-speed infrared thermography combined system for simultaneous measurement of flow and thermal fluctuations over a backward facing step," *International Journal of Heat and Fluid Flow,* vol. 61, pp. 174-182, 2016.

[104] G. L. Juste and E. M. Benavides, "Moiré-Fourier deflectometry for local heat transfer measurement over a backward-facing step," *International journal of thermal sciences,* vol. 77, pp. 244-251, 2014.

[105] H. Suzuki, S. Kida, T. Nakamae, and K. Suzuki, "Flow and heat transfer over a backward-facing step with a cylinder mounted near its top corner," *International journal of heat and fluid flow,* vol. 12, no. 4, pp. 353-359, 1991.

[106] R. Mittal, U. Madanan, and R. Goldstein, "The heat/mass transfer analogy for a backward facing step," *International Journal of Heat and Mass Transfer,* vol. 113, pp. 411-422, 2017.

[107] H. Abu-Mulaweh, B. Armaly, and T. Chen, "Turbulent mixed convection flow over a backward-facing step," *International journal of heat and mass transfer,* vol. 44, no. 14, pp. 2661-2669, 2001.

[108] F. Selimefendigil and H. F. Öztop, "Numerical analysis of laminar pulsating flow at a backward

facing step with an upper wall mounted adiabatic thin fin," *Computers and Fluids,* vol. 88, pp. 93-107, 2013.

[109] F. Selimefendigil and H. F. Öztop, "Numerical investigation and reduced order model of mixed convection at a backward facing step with a rotating cylinder subjected to nanofluid," *Computers and Fluids,* vol. 109, pp. 27-37, 2015.

[110] F. Selimefendigil and H. F. Öztop, "Forced convection and thermal predictions of pulsating nanofluid flow over a backward facing step with a corrugated bottom wall," *International Journal of Heat and Mass Transfer,* vol. 110, pp. 231-247, 2017.

[111] I. Barton, "Laminar flow over a backward-facing step with a stream of hot particles," *International journal of heat and fluid flow,* vol. 18, no. 4, pp. 400-410, 1997.

[112] A. Heshmati, H. A. Mohammed, and A. Darus, "Mixed convection heat transfer of nanofluids over backward facing step having a slotted baffle," *Applied mathematics and computation,* vol. 240, pp. 368-386, 2014.

[113] P. R. Kanna and M. K. Das, "Conjugate heat transfer study of backward-facing step flow–a benchmark problem," *International journal of heat and mass transfer,* vol. 49, no. 21-22, pp. 3929-3941, 2006.

[114] K. Khanafer, B. Al-Azmi, A. Al-Shammari, and I. Pop, "Mixed convection analysis of laminar pulsating flow and heat transfer over a backward-facing step," *International journal of heat and mass transfer,* vol. 51, no. 25-26, pp. 5785-5793, 2008.

[115] H. Iwai, K. Nakabe, K. Suzuki, and K. Matsubara, "The effects of duct inclination angle on laminar mixed convective flows over a backward-facing step," *International journal of heat and mass transfer,* vol. 43, no. 3, pp. 473-485, 2000.

[116] H. Abbassi and S. B. Nassrallah, "MHD flow and heat transfer in a backward-facing step," *International communications in heat and mass transfer,* vol. 34, no. 2, pp. 231-237, 2007.

[117] W. Xie, G. Xi, and M. Zhong, "Effect of the vortical structure on heat transfer in the transitional flow over a backward-facing step," *International Journal of Refrigeration,* vol. 74, pp. 465-474, 2017.

[118] M. Ramšak, "Conjugate heat transfer of backward-facing step flow: A benchmark problem

revisited," *International Journal of Heat and Mass Transfer,* vol. 84, pp. 791-799, 2015.

[119] J. Xu, S. Zou, K. Inaoka, and G. Xi, "Effect of Reynolds number on flow and heat transfer in incompressible forced convection over a 3D backward-facing step," *International Journal of Refrigeration,* vol. 79, pp. 164-175, 2017.

[120] A. Amiri, H. K. Arzani, S. Kazi, B. Chew, and A. Badarudin, "Backward-facing step heat transfer of the turbulent regime for functionalized graphene nanoplatelets based water–ethylene glycol nanofluids," *International Journal of Heat and Mass Transfer,* vol. 97, pp. 538-546, 2016.

[121] R. V. Avancha and R. H. Pletcher, "Large eddy simulation of the turbulent flow past a backward-facing step with heat transfer and property variations," *International Journal of Heat and Fluid Flow,* vol. 23, no. 5, pp. 601-614, 2002.

[122] H. F. Oztop, K. S. Mushatet, and İ. Yılmaz, "Analysis of turbulent flow and heat transfer over a double forward facing step with obstacles," *International Communications in Heat and Mass Transfer,* vol. 39, no. 9, pp. 1395-1403, 2012.

[123] A. Valencia, "Effect of pulsating inlet on the turbulent flow and heat transfer past a backward-facing step," *International communications in heat and mass transfer,* vol. 24, no. 7, pp. 1009-1018, 1997.

[124] J.-T. Lin, B. Armalyy, and T. Chen, "Mixed convection heat transfer in inclined backward-facing step flows," *International journal of heat and mass transfer,* vol. 34, no. 6, pp. 1568-1571, 1991.

[125] J.-T. Lin, B. F. Armaly, and T. Chen, "Mixed convection in buoyancy-assisting, vertical backward-facing step flows," *International Journal of Heat and Mass Transfer,* vol. 33, no. 10, pp. 2121-2132, 1990.

[126] J. C. Lin, "Review of research on low-profile vortex generators to control boundary-layer separation," *Progress in Aerospace ences,* vol. 38, no. 4-5, pp. 389-420, 2002.

[127] S. Eiamsa-ard and P. Promvonge, "Numerical study on heat transfer of turbulent channel flow over periodic grooves," *International Communications in Heat and Mass Transfer,* vol. 35, no. 7, pp. 844-852, 2008.

[128] V. Uruba, P. Jonáš, and O. Mazur, "Control of a channel-flow behind a backward-facing step by

suction/blowing," *International Journal of Heat and Fluid Flow,* vol. 28, no. 4, pp. 665-672, 2007.

[129] K. Inaoka, K. Nakamura, and M. Senda, "Heat transfer control of a backward-facing step flow in a duct by means of miniature electromagnetic actuators," *International journal of heat and fluid flow,* vol. 25, no. 5, pp. 711-720, 2004.

[130] A. Glezer and M. Amitay, "Synthetic jets," *Annual review of fluid mechanics,* vol. 34, no. 1, pp. 503-529, 2002.

[131] W. Xie and G. Xi, "Geometry effect on flow fluctuation and heat transfer in unsteady forced convection over backward and forward facing steps," *Energy,* vol. 132, pp. 49-56, 2017.

[132] W. Xie and G. Xi, "Fluid flow and heat transfer characteristics of separation and reattachment flow over a backward-facing step," *International Journal of Refrigeration,* vol. 74, pp. 177-189, 2017.

CHAPTER 2

Three-Dimensional Fluid Flow Structures and Reattachment Characteristics of a BFS Flow in a Rectangular Duct

2.1 Introduction

Flow separation and reattachment of BFS caused by an abrupt expansion are well applied into many heat exchanging devices, such as energy system equipment, electronic cooling, cooling of turbine blades, dump combustors, and many other heat transfer-exchanging devices. For the sake of improving the performance of these applications, investigating the mechanism of flow and heat transfer enhancement is very crucial. The benchmark problem of laminar and turbulent flow has been extensively studied by experimental (Armaly et al., 1983 [1]; Lee et al., 1998 [2]; Terhaar et al., 2010 [3]; Kapiris et al., 2014 [4]) and numerical (Vogel and Eaton, 1985 [5]; Iwai et al., 2000 [6]; Kozel et al., 2005 [7]; Lan et al., 2009 [8]; Barrios et al., 2012 [9]) methods. In the early years, the laminar ($Re_D < 1200$), the transitional ($1200 < Re_D < 6600$), and the turbulent ($Re_D > 6600$) regimes of the flow in a two-dimensional channel are identified by the primary reattachment length based on the experimental research with Laser-Doppler measurements [10]. The experimental and numerical research carried out by Iwai et al., 2000 [6] and Armaly et al., 1983 [1] on the three-dimensional BFS flow has arisen much more attention. Since then, a lot of three-dimensional laminar flow investigations (Armaly et al., 2002 [11]; Nie and Armaly, 2004 [12]; Chen et al., 2006 [13]; Nie et al., 2009 [14]) have been published.

The effects of side walls caused much attention in the fluid dynamics community for many numerical and laboratory experiments. Williams and Baker [15] was attributed to the three-dimensionality with the effects of side walls and found that the complex jet-like flow was located at the stepped wall near the side walls. The complex flow structure near the side walls was also reported by Chiang and Sheu [16] by numerical simulation. In their work, the limiting streamlines near the roof, floor, and end walls at Re = 800 were investigated to illustrate the spanwise width ($2h \leqslant B \leqslant 100h$) effects on the flow field. Iwai et al. [6] investigated the effects of the duct aspect ratio with a fixed step height and revealed the 2D region can be obtained with an aspect ratio of at least 16 and showed the Nu and C_f distribution in laminar steady flow regime ($125 \leqslant Re \leqslant 375$). Tylli et al. [17]

investigated the effects on the primary and secondary recirculation zones, and explained the differences between experimental and 2D simulations in the transitional and turbulent regimes. Effects of step height on the distribution of Nu, C_f and flow structures were studied by Nie and Armaly [18]. The fact that the three-dimensional behavior and side wall effects increase with increasing step height was also found by them. Biswas et al. [19] reported the spatial evolution and three-dimensionality of jet-like flows with different expansion ratios (ER=1.9423, 2.5, 3.0).

In the low Reynolds number regime, Chiang et al. [16] numerically investigated the vortical evolution in a 2D BFS. They clarified how the recirculating bubble containing flow reversals is turned into smaller eddies and discussed the eddy distortion and the merging of eddies in his study. Flow structures in a 3D BFS channel were carefully studied by Rani et al. [20] to indicate that the flow becomes unsteady along with the effects of the Kelvin-Helmholtz instability and Taylor-Görtler-Like vortices at Re_D=1000 and 2000. Kitoh et al. [21] studied the time-averaged reattachment length and the distribution of Nu and C_f on the floor wall at an unsteady flow state with the effects of expansion ratios by the methodology of DNS. In his work, the flow structure in the separated and reattachment regions was clearly shown at $300 \leqslant Re \leqslant 1000$. Tihon et al. (2012) experimentally and numerically studied the unsteady flow (water) with different expansion ratios and inlet flow conditions at middle Reynolds numbers. The results suggested that the inlet pulsatile flow plays significant roles in flow structures, reattachment length and upper wall recirculation zones.

It is worth noting that there is a lot of steady laminar flow and turbulent flow investigations on the flow structures and reattachment in BFS flow by numerical simulation and experiments but little attention has been paid to an unsteady laminar BFS flow and the study on the three-dimensionality of this flow is still in its infancy. In particular, very few studies have examined the flow structure of the entire flow field, and the relationship between the flow structure and heat transfer characteristics has not yet been clarified, considering the duct with side walls. Accurate and reliable measurement for three-dimensional flow and thermal fields, especially near the side wall where the flow structure was imagined to be different from the flow in the center of the duct. This chapter aims to study the reattachment characteristics of 3D BFS in a low Reynolds flow regime. The flow structure of the BFS flow was investigated by the PIV method, which enables simultaneous measurement of multiple points, and the relationship with heat transfer was also investigated. Referring to Armaly et al. (AR=36) [11] and Iwai et al. [6], the Reynolds number was changed from 200 to 1000 in increments.

2.2 Experimental apparatus and procedures

2.2.1 Experimental apparatus overview

Experiments were done in a closed water channel consisted with an upper tank, honeycombs, wire meshes, a rectifying section, a contraction section, a developing channel, a test section and a lower tank as shown in Fig. 2-1. Water was driven by the head difference between the upper tank and the lower tank and flowed into the test section as a fully developed laminar flow. The test section, illustrated in Fig. 2-2, was W_D=240 mm wide, 30 mm high, 470 mm long and was made of the transparent acrylic plate. Since the step was S=15 mm height, the expansion ratio and aspect ratio of the duct upstream the step were 2 and 16, respectively. The origin of the coordinate system was located at the center of the bottom line of the backward-facing wall. x-, y- and z-coordinates were set for the streamwise, wall-normal and spanwise directions, respectively. Nylon particles (50μm) and a high-illuminance green laser whose average thickness was 0.8 mm were used for PIV measurements. The particle images were acquired by a high-speed camera (1024 pixels^2, KANOMAX, HSS-3). To grasp the flow structures downstream the step, especially to examine the flow reattachment characteristics on the bottom wall, instantaneous velocity vectors mainly in the x-z plane near the bottom wall, and those in the x-y and y-z planes as necessary were also measured. Velocity vectors were calculated using the cross-correlation method combined with postmedian filtering for removing spurious vectors. Here, the flow reattachment point is defined as a position where the obtained streamwise velocity becomes zero from negative to positive.

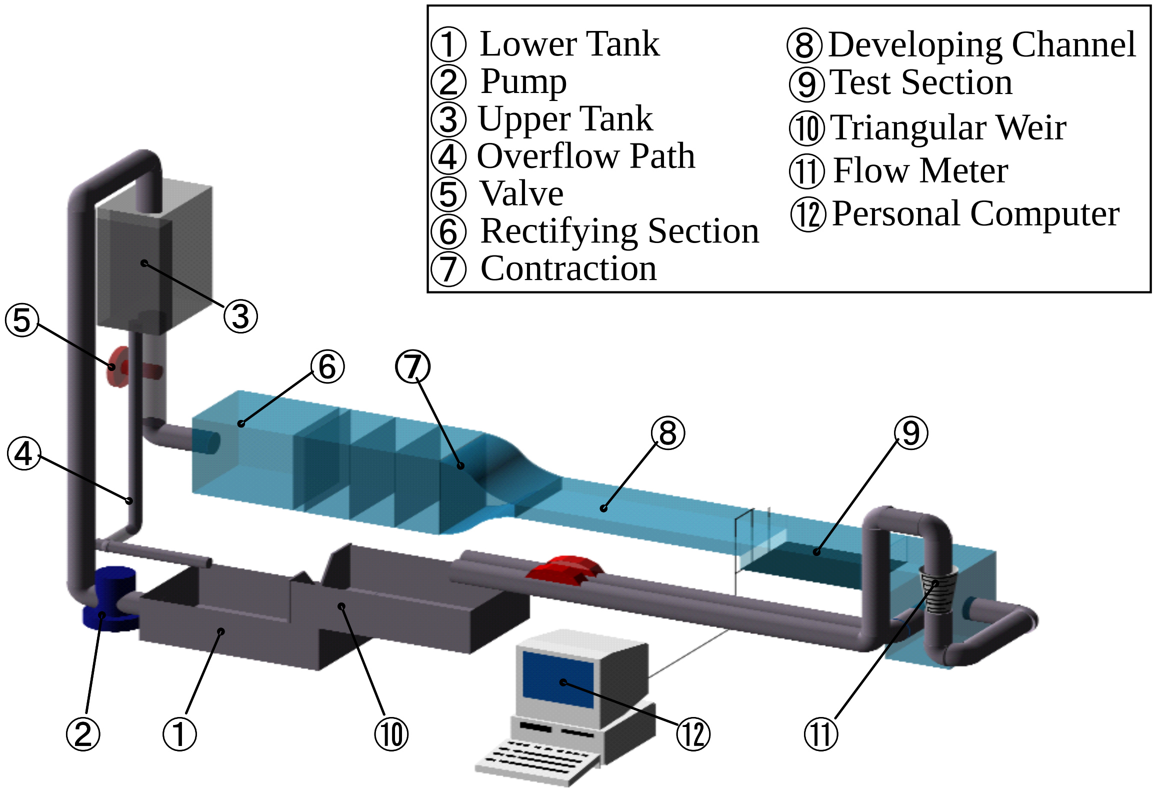

Fig. 2-1. Schematic view of an experimental apparatus.

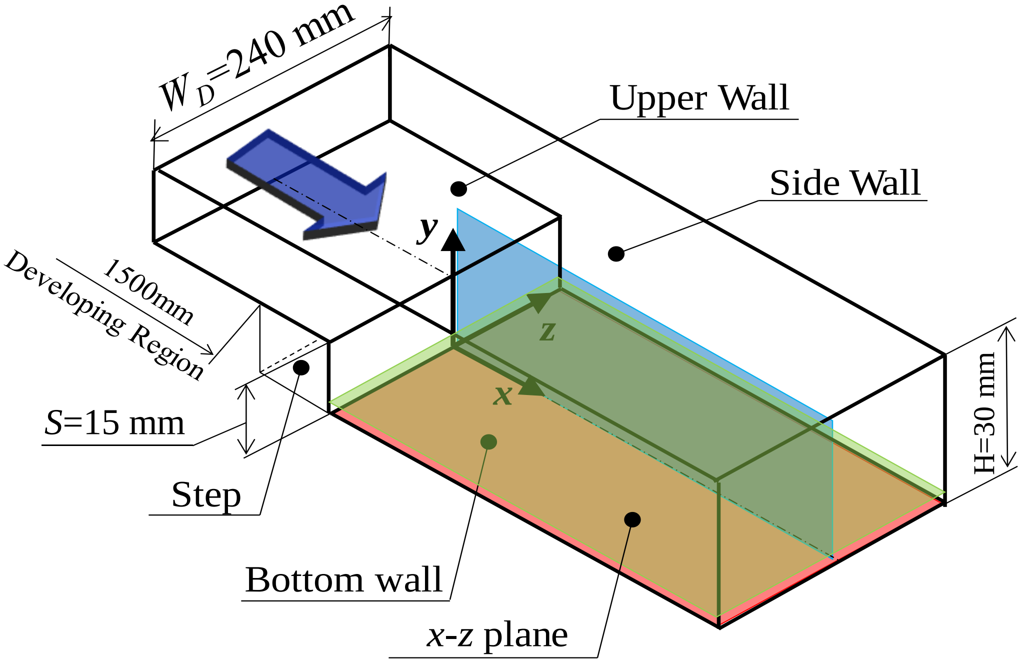

Fig. 2-2. Test section of a BFS flow in a duct.

2.2.2 Velocity measurement

The velocity distribution was measured as follows. Nylon particles of average particle diameter 50 μm were mixed in the working fluid, and a sheet-shaped high-intensity green laser (LASER QUANTUM, opus, output 1.0 W) was irradiated on the *x-y* and *x-z* cross-sections to visualize them, and the scattered light of the particles was photographed with a high-speed camera (KANOMAX, HSS-3). The velocity distribution was obtained from the captured images by the cross-correlation PIV method (LaVision, Davis 10.0). The imaging areas were 120 mm and 30 mm in the *x* and *y* directions in the *x-y* cross-section, and 240 mm and 240 mm in *x* and *z* directions in the *x-z* cross-section, respectively. The acquired images were 1024 pixels and 255 pixels in the *x* and *y* directions, 1024 pixels and 128 pixels in the *y* and *z* directions in the *y-z* cross-section, and 1024 pixels and 1024 pixels in the *x-z* cross-section. Therefore, 1 pixel in the *x-y* cross-section corresponds to 0.12 mm, and 1 pixel in the *y-z* cross-section corresponds to 0.23 mm. In general, the particle image size should be over 2 pixels, the number of particles in the inspection area is about 5, and the moving distance of the particles is within 5 pixels according to PIV Handbook [22]. Therefore, the sampling frequency of the high-speed camera was adjusted appropriately according to the Reynolds number. In this study, the sampling frequency was set at 20～125 fps, and the shooting time was 100s. The speed was calculated concerning the PIV Principle [22]. The inspection area was 16 × 16 pixels and the exploration area was 32 × 32 pixels. The definition of the Reynolds number is given by Eq. 2-1:

$$Re = \frac{U_{m0}S}{\nu} \tag{2-1}$$

where U_{m0} is the streamwise mean velocity upstream the step, ν is the kinematic viscosity of water. The reattachment position is determined as the position where the velocity in the flow direction changes from negative to positive at height y=0.5 mm (y/S=0.03) in the vicinity of the bottom wall surface and y=29.5 mm (y/S=1.97) near the upper wall, respectively. In addition, the time-averaged reattachment position is obtained from the time-averaged velocity vector at each spanwise direction position.

To verify the stability of the experimental apparatus and the accuracy of the PIV method operation, the verification experiment under Reynolds number of 400, 600, 800, 1000 on the inlet flow velocity profile just upstream the step was carried out. As a fully developed laminar flow, the velocity field shows a parabolic shape at the center of duct presented in Fig. 2-3, which is close to the theoretical velocity distribution in streamwise direction (the solid line in the figure) that was given by the approximation [22] which represents a fully developed laminar flow in a rectangular duct. The transverse distribution of mean streamwise velocity component at x/S=-1 and y/S=1.5 shown in Fig. 2-4 also agrees well with each other under different Reynolds numbers, indicating that the experimental apparatus and PIV method operation is reliable. The relative error between the PIV results and the theoretical value was 1.3%.

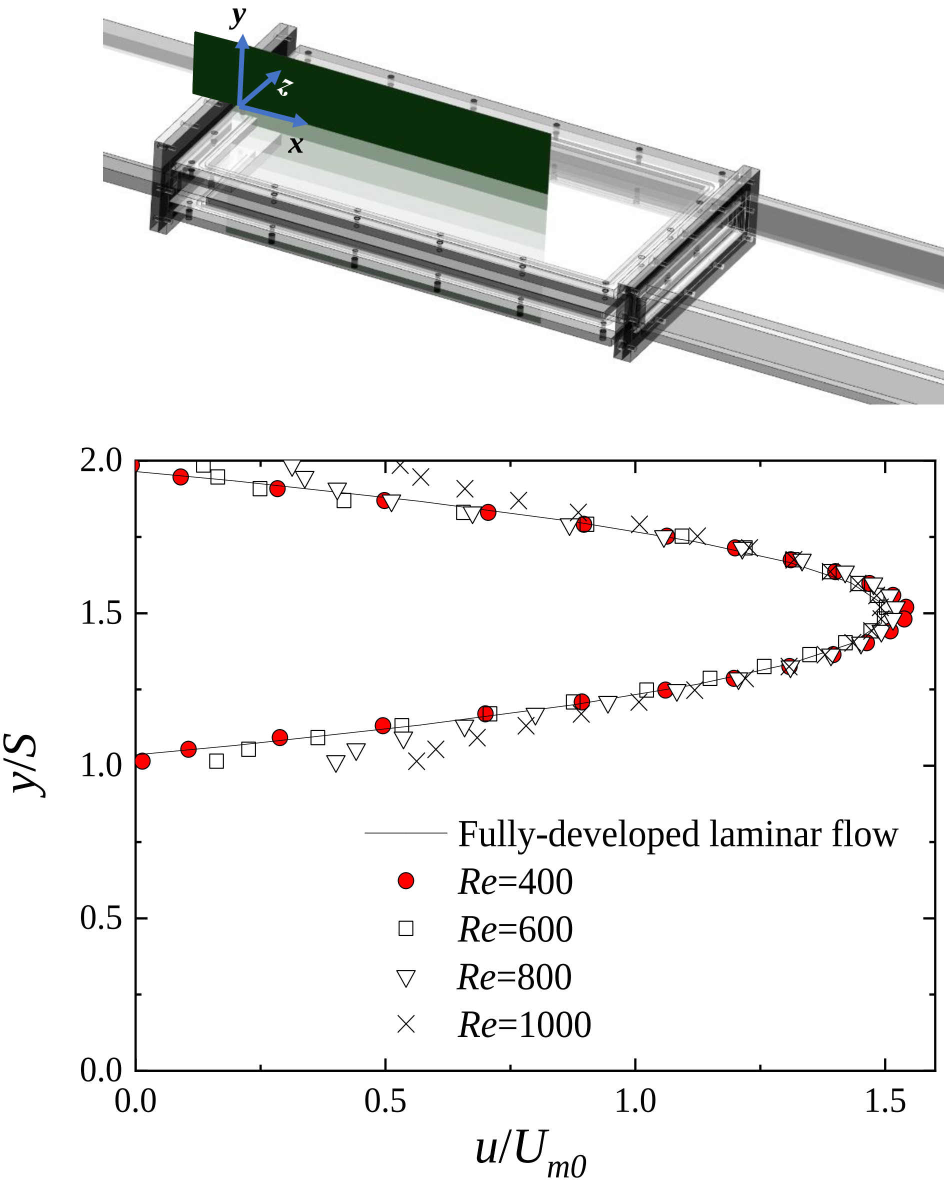

Fig. 2-3. Wall-normal distribution of the streamwise velocity at the center of the duct just upstream the step.

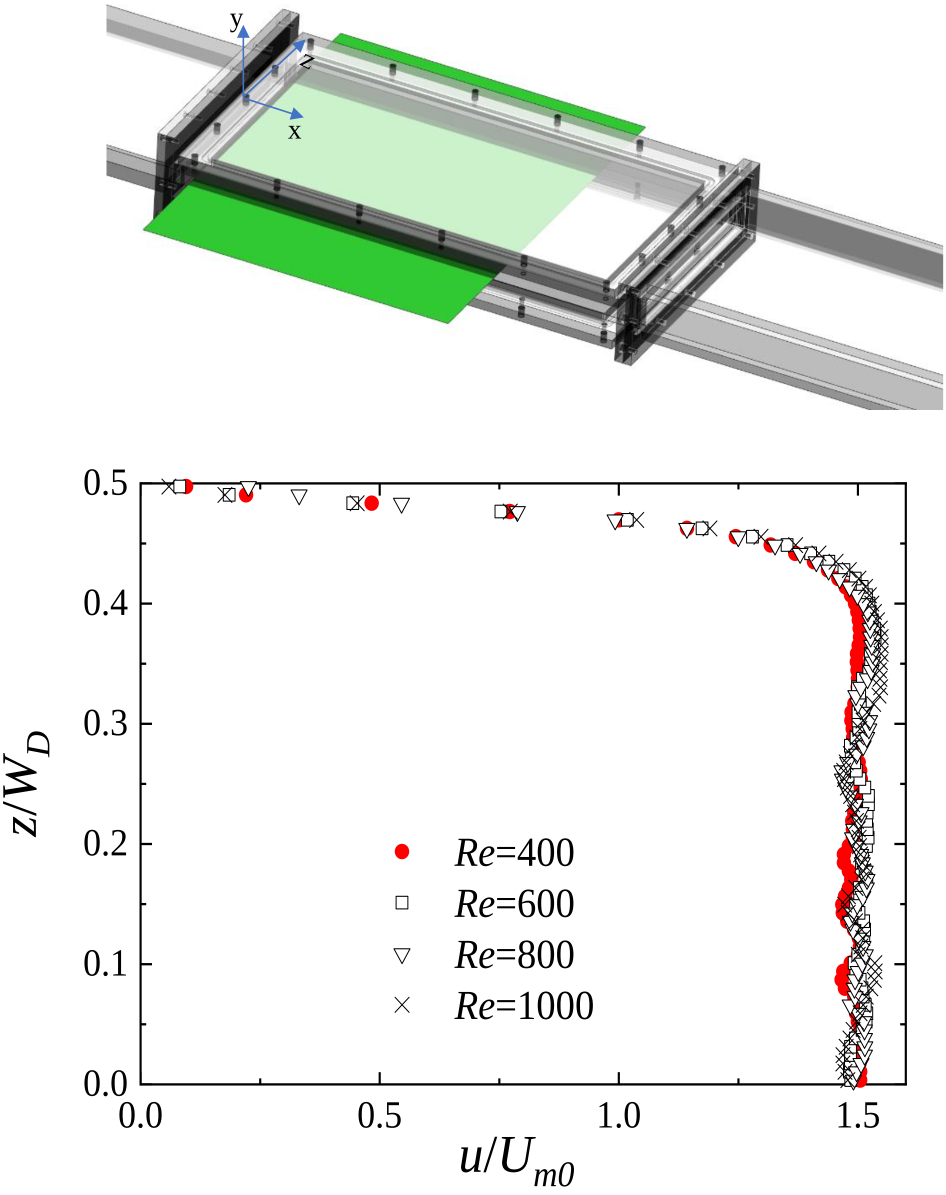

Fig. 2-4. Spanwise distribution of the streamwise velocity at the center of the duct just upstream the step.

2.3 Results and discussions

2.3.1 Heat transfer and flow structures at Re=1000

To elicit the three-dimensional characteristics of the stepped flow, a specific Reynolds number of 1000 was first selected as a prior research object. The time-averaged Nusselt number distribution superimposed with the time-averaged velocity vector and reattachment points at Re=1000 is shown in Fig. 2-5. Here, the local Nusselt number defined based on the step height S as Eq. (2-2) will be used.

$$Nu = \frac{q_w S}{\lambda(T_w - T_{in})} \tag{2-2}$$

where λ is the thermal conductivity of the fluid, T_w is the local wall temperature, and T_{in} is the inlet fluid temperature. q_w is the constant wall heat flux calculated from the electric power input through the stainless foil strips.

The indexed colorful scale drawn in this figure corresponds to the obtained local Nusselt number. The red part represents the high Nusselt number area while the blue part represents that of the low Nusselt number. z/W_D = 0.0 corresponds to the center of the duct while z/W_D =0.5 corresponds to the side wall. Due to the symmetric feature of the duct flow and heat transfer distribution, some of the following figures will be shown just half of the duct.

Even though the aspect ratio is 16 which is relatively large, heat transfer distribution shows unique variations, especially in the spanwise direction. A relatively large high Nusselt number area observed around $8<x/S<12$ represents the heat transfer enhancement caused by the flow reattachment. Upstream that and just behind the step, there generates a large area of heat transfer deterioration which has been generally mentioned concerning the flow re-circulation region for the conventional 2D stepped flow regime. Another unique point worth to mention is that the maximum heat transfer appears in the region near the side wall around $0.4<z/W_D<0.5$ and $6<x/S<12$. The corresponding time-averaged velocity vectors in the x-z plane near the bottom wall obtained by PIV was also superimposed in Fig. 2-5, each of the white circular plots drawn in this figure is the time-averaged reattachment points calculated from these time-averaged velocity vectors. The flow field downstream the step is no longer 2D but intensive 3D. Near the side wall, strong reverse flow toward the channel center is observed, which corresponds well to the high heat transfer exchange near the bottom wall. Owing to that flow, the flow re-circulation region is distorted in the spanwise direction and the unique shape of the low-speed reverse flow area is produced. This slow reverse flow corresponds quite well to the heat transfer deterioration just behind the step. On the other hand, it is naturally confirmed that the reattachment points seem to divide the downstream flow and the reverse flow. The reattachment point changes a lot along the spanwise direction, the apparent positive or negative values of the spanwise velocity components are observed just along the reattachment positions, the flow reattachment of this flow regime is no longer 2D.

Figure 2-8 shows the velocity vectors in the *y*-*z* plane obtained at various streamwise positions. As seen at x/S=6.7, intensive secondary flow from the side wall to the center of the duct can be observed at z/W_D=0.45-0.25. This downwash flow from the step observed from x/S=6.7 to 8.0 corresponds well to the intensive reverse flow near the side wall region seen in Fig. 2-7. This flow enhances the heat transfer there. At the positions x/S=8.0 and 9.3, with the generation of the downwash flow at around z/W_D=0.45, some kind of counter vortices were obtained.

As is mentioned above, heat transfer distribution on the bottom wall is found to be remarkably related to the 3D flow structures downstream the step, especially, the flow behaviors near the bottom wall and the reattachment structures. Such relation was also reported by Iwai et al. [6], however, the flow field seems to be different depending on the Reynolds number. Thus, in the following sections, the flow reattachment characteristics and 3D flow structures depending on the Reynolds number will be discussed.

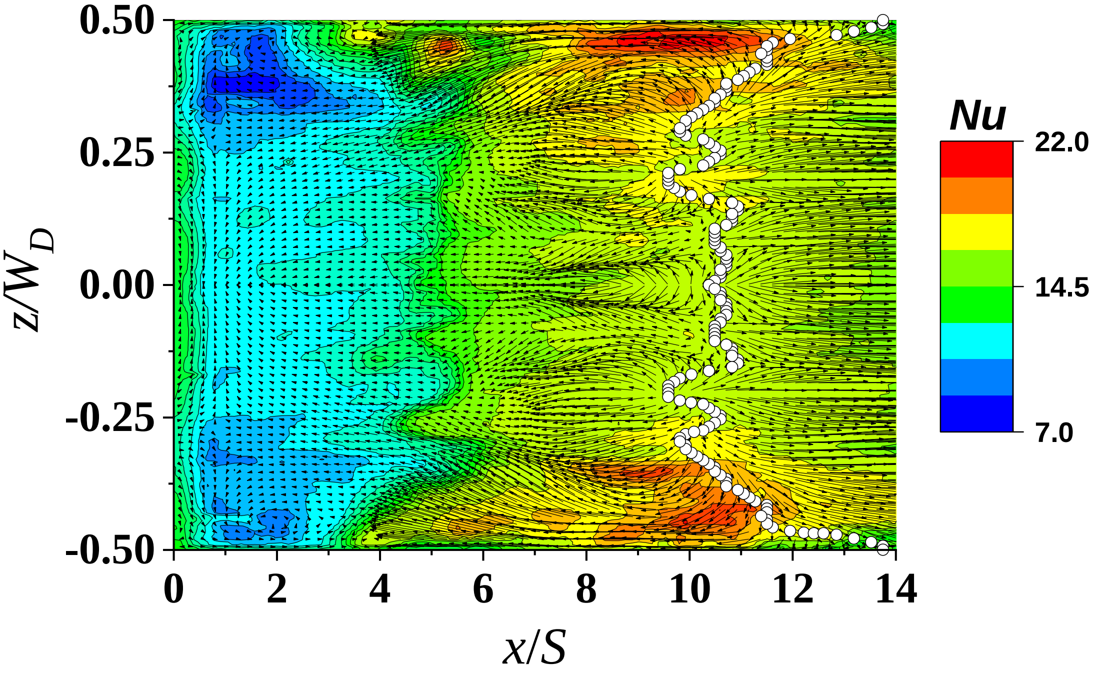

Fig. 2-5. Local Nusselt number (*Re*=1000).

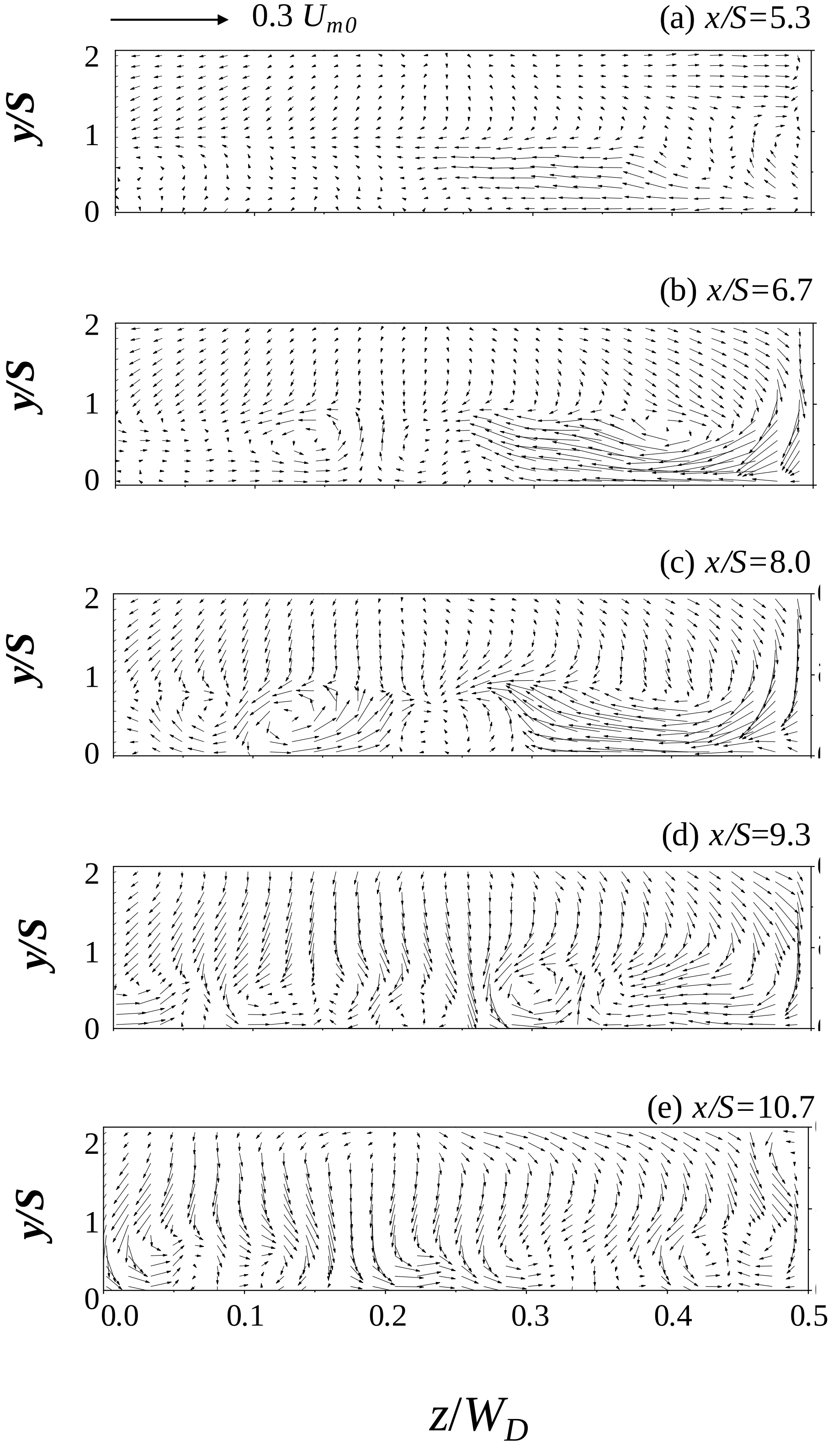

Fig. 2-6. Velocity vectors in the *y*-*z* plane (*Re*=1000).

2.3.2 Time-averaged reattachment points

The distributions of the time-averaged reattachment points for all the representative Reynolds number cases from 200-1000 in the x-z plane were investigated. The time-averaged reattachment point changes its position spanwisely for all the Reynolds number cases, revealing that the flow structure is affected by the 3D stepped flow, though its magnitude and changing pattern were varied for each Reynolds number.

All the patterns can be classified into four parts as shown in Fig. 2-7 (a)-(d). For the first case (Re=200-350), the reattachment points move downstream at each spanwise position as Reynolds number is increased, especially at the center of the duct. A tongue-shaped reattachment flow occurs along the center of the channel. This growing tendency agrees quantitatively well with that reported by Iwai et al. [2]. At the Reynolds number of 200, the reattachment length is the shortest at each spanwise position compared with other cases, showing the steady laminar flow pattern. In Fig. 2-7 (b), an intensive variation of the reattachment point occurs, especially at the central part of the channel around $0<z/W_D<0.2$. As the Reynolds number continues to be increased, the reattachment length also increases near the side wall while the reattachment points intertwine with each other near the center of the duct. In Fig. 2-7 (c), the variation range of the reattachment positions becomes narrow, and the reattachment points move upstream near the center line, it is worth to mention that an abrupt change of the reattachment point is generated near the side wall region around $z/W_D=0.4$ for Re=600-750. A disconnection of reattachment points occurs between the side wall and the center of the duct. For the cases of $Re\geq800$, as observed in Fig. 2-7 (d), the reattachment points near the side wall move more downstream position than the center of the duct and are squeezed in a small range around $x/S=11$.

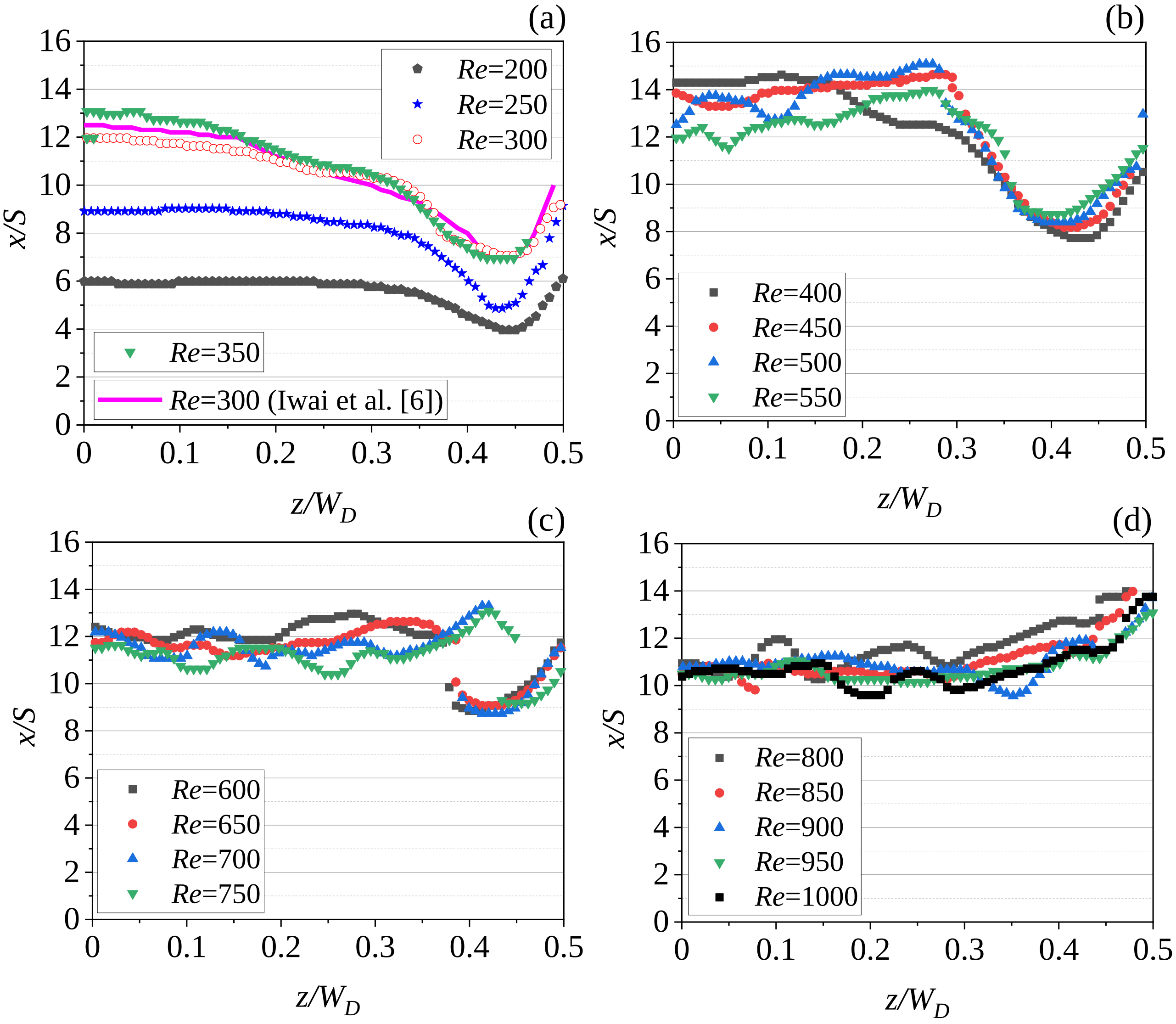

Fig. 2-7. Spatial distribution of time-averaged reattachment positions for each Reynolds number case.

Above mentioned feature of the flow reattachment can also be confirmed in Fig. 2-8 which illustrates the time-averaged velocity vectors corresponding to each representative case in Fig. 2-7 (a)-(d). Here, the reattachment points are superimposed on each figure. In Fig. 2-8 (a), at the low Reynolds number of 200, flow near the bottom wall seems to be almost stable. A flow downstream from the side wall toward the central part of the channel is apparent and seems to dominate the flow near the bottom wall. Large flow recirculation could be observed, though the flow inside there is three dimensional. As the Reynolds number is increased, the flow near the central part of the duct begins to contain another type of reattachment flow. Owing to the large interaction between the flow from the side wall and that from the central part, a relatively large and unstable flow structure is generated near the central part of the duct and this produces the large variation of the reattachment position as shown in Fig. 2-8 (b). Flow structure inside the flow recirculation region turns to be complicated. As the Reynolds number is further increased in Fig. 2-8 (c), the unstable flow invades toward the side wall and seems to temporarily block the flow toward the downstream side. This is thought to be one of the causes of the discontinuous reattachment point there. In Fig. 2-8 (d), smaller unstable flow structures occupy largely over the entire channel width through the flow from the side wall is still observed.

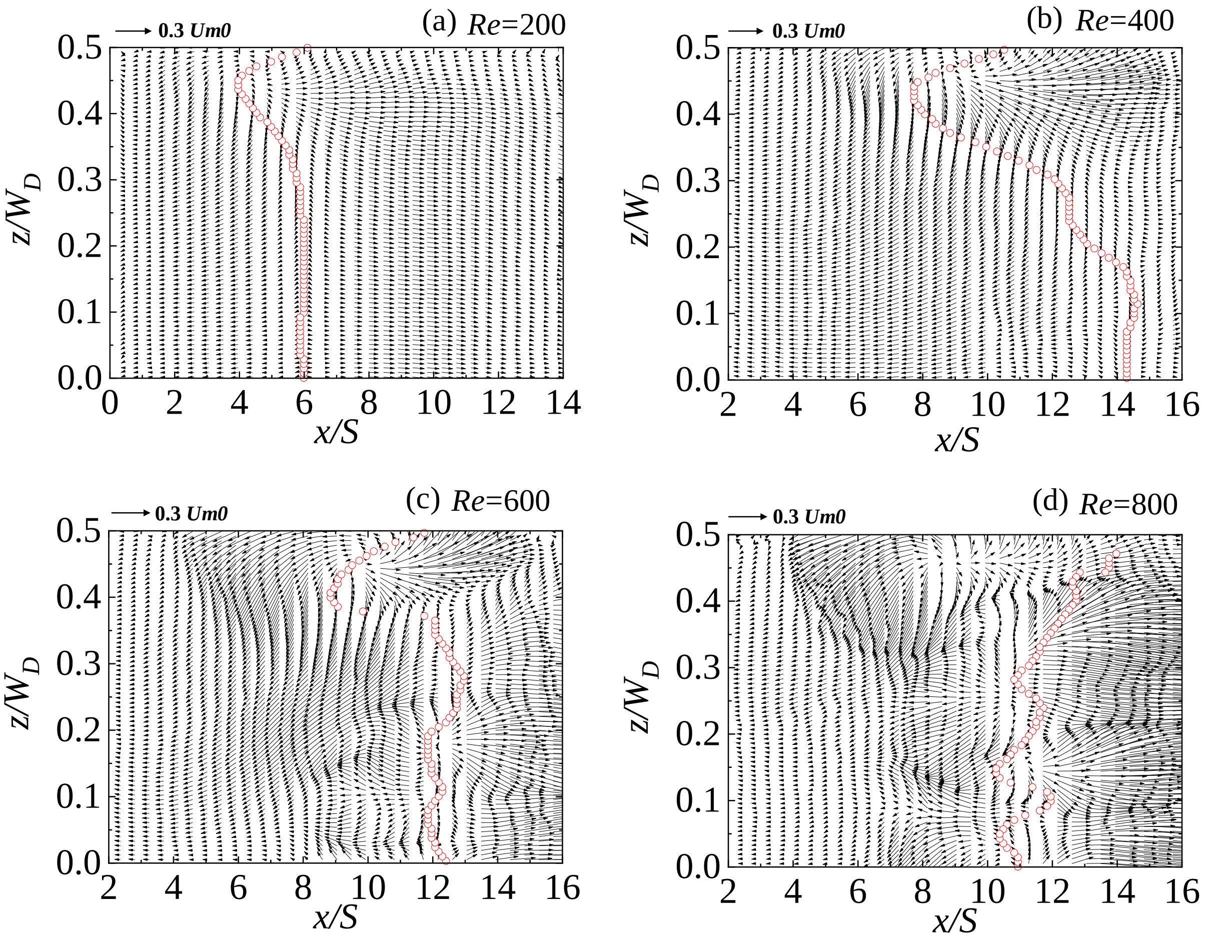

Fig. 2-8 Time-averaged velocity vectors in the *x*-*z* plane near the bottom wall.

2.3.3 *Spatial distributions of the existence probability of the reattachment points*

To further investigate and more clearly clarify the spatial variations of the reattachment phenomena on the bottom wall as time advances, Fig. 2-9 shows the distributions of their existence probability for the representative cases (*Re*=200, 400, 600, 800). The locations where the streamwise velocity took zero were detected spatially at each time frame. The time-averaged reattachment plot marked with a small transparent circular symbol ○ is also superimposed on each figure. From Fig. 2-9 (a).

At a low Reynolds number of 200, it is found that a high probability value was observed almost around the time-averaged reattachment position. The variation of the instantaneous reattachment points is not large, which implies that the flow is quite stable. As the Reynolds number is increased shown in Fig. 2-9 (b), the value becomes a little bit smaller and the existence area of the flow reattachment becomes wider. Especially, near the center of the duct, a relatively wide value area exists showing the time-dependent fluctuations with short and long flow reattachments. Near the side wall, the possibility turns to be the largest in the most upstream position, indicating that here seems to be a stagnant point. The reattachment points swing back and forth in the streamwise direction around this point. Then in Fig. 2-9 (c), near the central part of the duct, although the high value remains in a narrow area along with the time-averaged plots, the low-value area spreads much wider appearing closer toward the step and toward the side wall. This means that the time variation of the flow reattachment becomes weak but more frequently occurs near the backward-facing step. Here, it is worth to mention that near the side wall around z/W_D=0.35, high probability values are distributed discontinuously and much closer to the side wall. Since the high-value area along the time-averaged reattachment plots is as narrow as that seen in Fig. 2-9 (a), the flow near the side wall may still be stable there. On the other hand, at the region $0.3<z/W_D<0.4$, since relatively high value distributes wider around the time-averaged plots, more unstable reattachment affected from the central part of the duct occurs. Thus, a disconnection appearing here seems to show the boundary between the flow dominated by the side wall effect and the flow reattaching with time fluctuation near the central part of the duct. As the Reynolds number is increased, the unstable reattachment flow seen at the central part of the duct becomes more dominated over the whole area of the channel. The disconnection near the side wall cannot be distinguished any more under the control of this unsteady flow.

Figure 2-10 also shows the instantaneous reattachment point fluctuation range as the increase of Reynolds number in the *x*-*z* plane. The shapes of the reattachment point fluctuation range near the side wall and the center of the duct are different. Near the center of the duct, the general trend is that the fluctuation range increases and then decreases as the increase of Reynolds number, and the variation range is larger than that near the side wall. The maximum reattachment variation appears at *Re*=600, which is consistent with the existence distribution at *Re*=600.

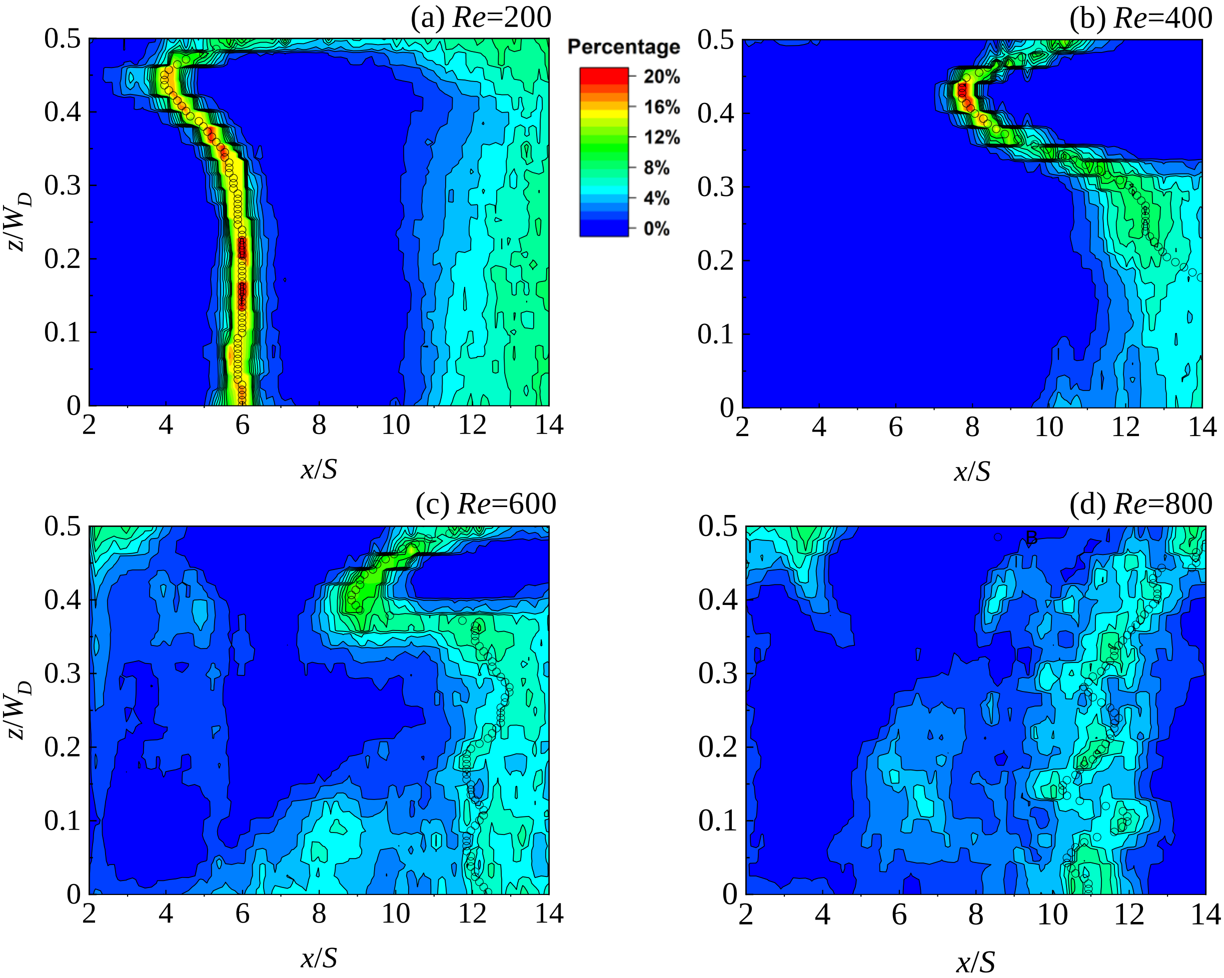

Fig. 2-9. Existence probability of the reattachment position near the bottom wall.

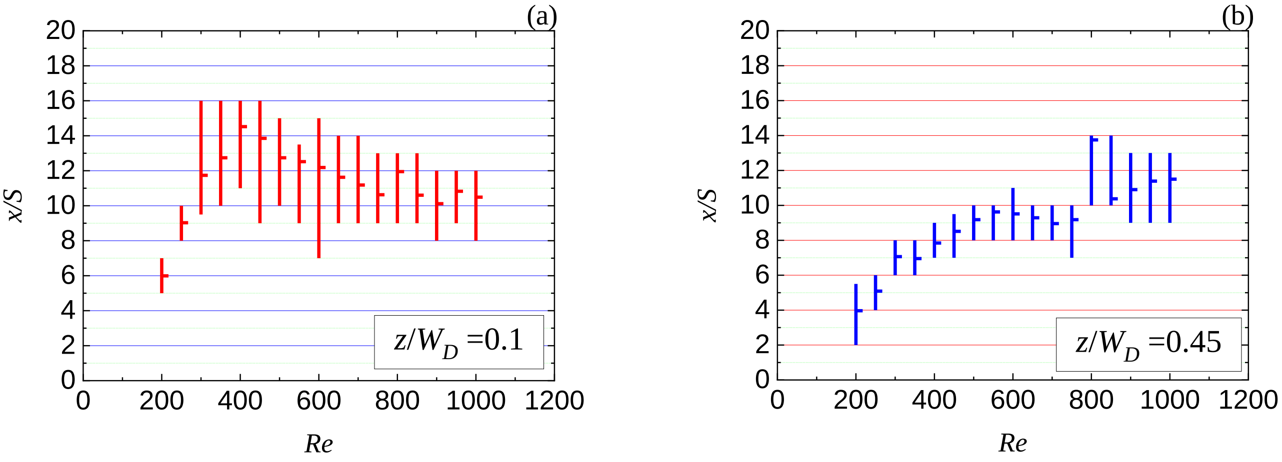

Fig. 2-10. Reattachment point fluctuation range in the *x*-*z* plane on the bottom wall.

2.3.4 Relationship between local Nusselt number distribution and time-averaged reattachment points on the bottom wall.

To explain the effects of the non-uniform spanwise distributions of the reattachment points and 3D fluid flow on the heat transfer distribution on the bottom wall, Fig. 2-11 (a)-(f) show the local Nusselt number distribution of Re=400-900 superimposed with time-averaged reattachment points. The horizontal axis of the figure is the non-dimensional flow direction length x/S. z/W_D=0.0 represents the center of the channel, z/W_D=0.5 represents the side wall. The white plot in the figure represents the time-averaged reattachment point. It is not only shown the overall results that the Nusselt number is higher near the side wall for all cases and is increased as the increase of Reynolds number, but also it increases around the time-averaged reattachment position. In the following discussion, the region around the side wall where heat transfer is enhanced, and the flow around the reattachment point while changing the Reynolds number will be studied, Reynolds number 400, 700, 900 was chosen as the representative research object.

2.3.5 Time-averaged velocity vector

2.3.5.1 Time-averaged velocity vector in the x-y plane

Figure 2-12 (a) to (f) show the distribution of the time-averaged velocity vector $\bar{u}-\bar{v}$ at Re=400, 700, and 900 in the spanwise direction position z/W_D=0.0 and 0.4, respectively. Here, ▲ in each figure indicates the time-averaged reattachment position in the x-y plane near the bottom wall, ▼ and ▼ indicates the time-averaged separation position and the time-averaged reattachment position in the x-y plane near the upper wall. To make sure that all the time-averaged reattachment points, separation points near the bottom wall and upper wall are included in one cross-section, the coordinate settings for each case are not the same. For the Re=400 case, at z/W_D=0.4, the x/S range was chosen from 4 to14, which is different from that at z/W_D=0.0 and other Reynolds number cases.

From Fig. 2-12, a backflow region (hereinafter referred to as a circulation region) could be confirmed near the bottom wall surface downstream of the step at each spanwise direction position. The time-averaged reattachment position in the vicinity of the bottom wall exists downstream of this region. The circulation region changes in each spanwise direction position and becomes smaller as it approaches the side wall from the center of the duct. As a result, the time-averaged reattachment position has moved upstream.

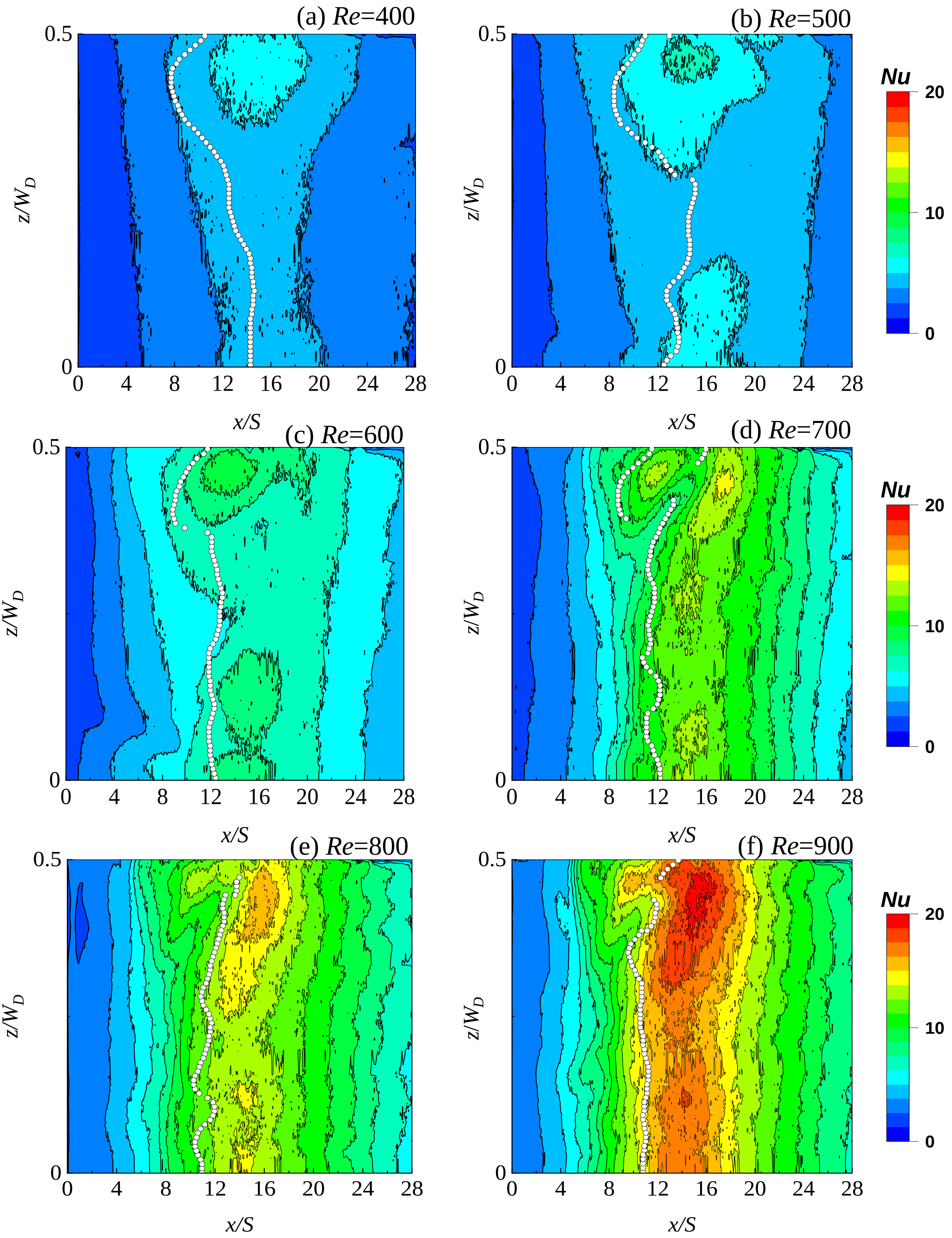

Fig. 2-11. Local *Nu* number distribution on the bottom wall (half width of the duct). White plots represent reattachment points.

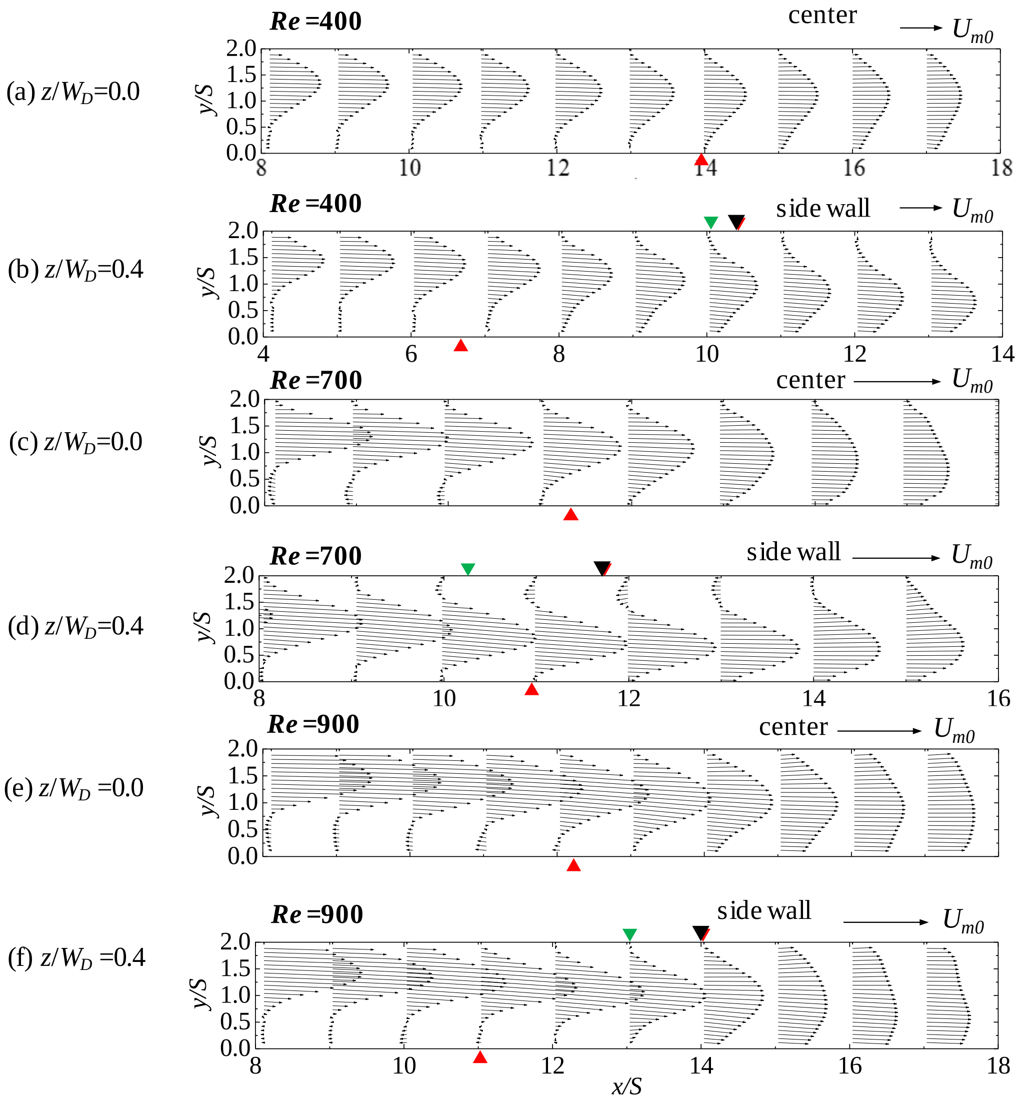

Fig. 2-12. Mean velocity vectors in the *x*-*y* plane for *Re*=400, 700, 900 at z/W_D=0.0 and 0.4.

2.3.5.2 Time-averaged velocity vector in the y-z plane

Figures 2-13, 2-14, and 2-15 (a), (b), (c), and (d) show the time-averaged velocity vectors at the flow direction positions *x*/*S* = 10, 12, 14, and 16 at *Re*=400, 700, and 900. The distributions of $\bar{v} - \bar{w}$ are shown respectively.

From Fig. 2-13, it is possible to confirm the downwash flow at *x*/*S*=10 and z/W_D = 0.4 to 0.5. Downwash flow means the flow of fluid from the upper wall near the side wall to the center of duct and then toward the bottom wall. As it goes further downstream (*x*/*S* = 12 to 14), the downwash flow changes its direction, flows toward the side wall and turns to be a flow toward the upper wall at

x/S=14, z/W_D=0.4-0.5. A longitudinal vortex like flow rotating counterclockwise could be observed around z/W_D=0.47 at x/S=14.

Next, from Fig. 2-14, downwash flow could be seen near the side wall at x/S = 10. In addition, at x/S=12, some small vortex structure could be confirmed at z/W_D=0.05, 0.12, 0.2, and 0.4. Furthermore, at downstream x/S=14, the number of vortex structures decreases and appears only at z/W_D = 0.12, 0.4. The vortex structure cannot be confirmed downstream thereafter. Compared with the existence possibility distribution map of the reattachment position of the bottom wall, there is a region where there is no reattachment position at z/W_D = 0.4 to 0.5, around x/S = 14. This is thought to be caused by the flow rising and falling above this area near the side wall, which could be determined in the y-z plane at x/S=14.

In Fig. 2-15, the downwash flow could also be confirmed near the side wall at x/S=10. When x/S=10, z/W_D=0.08, 0.12, 0.22, 0.27, the vortex structure whose rotation direction is paired can be confirmed. Furthermore, at x/S=12, similar vortices were confirmed at z/W_D=0.05, 0.1, 0.15, 0.2, 0.3, and 0.4. This vortex structure is like that from Inaoka's report [23] (Inaoka, 2013), in which it was found that for a wide variety of the flow Reynolds number ranging from laminar (1000) to turbulent (10000) flow regions, these vortex structures could not be seen after Re=3000. Therefore, this vortex structure is considered to occur between Re=700, where the unsteadiness of the mainstream becomes stronger, and Re=3000, where turbulence occurs.

The position near the side wall where the local Nusselt number is highest coincides with the position where the longitudinal vortex flow. From this, it is considered that a reason why the heat transfer near the side wall is improved is this kind of longitudinal vortex flow. Also, for Re = 700 and 900, the position where the local Nusselt number is high and the position where the vortex structure is seen are in the vicinity of the duct center (z/W_D = 0.0 to 0.2) and the side wall (z/W_D = 0.3). These vortex structures are thought to affect heat transfer distribution.

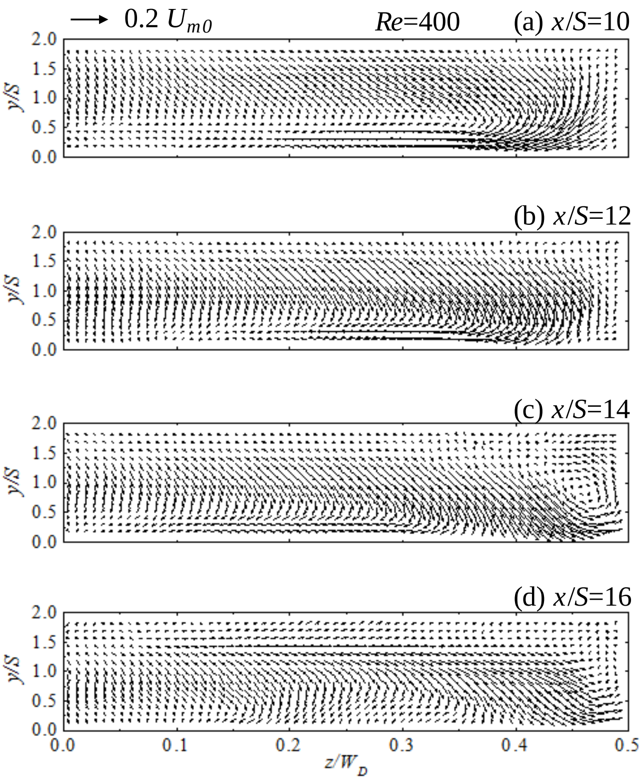

Fig. 2-13. Mean velocity vectors in the *y*-*z* plane of *Re*=400 for *x/S*=10, 12, 14 and 16.

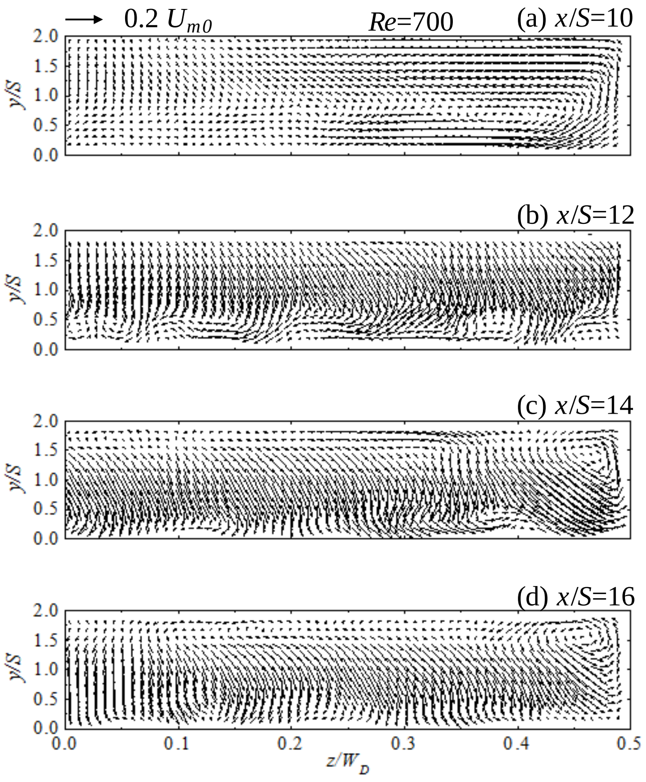

Fig. 2-14. Mean velocity vectors in the *y*-*z* plane of *Re*=700 for *x/S*=10, 12, 14 and 16.

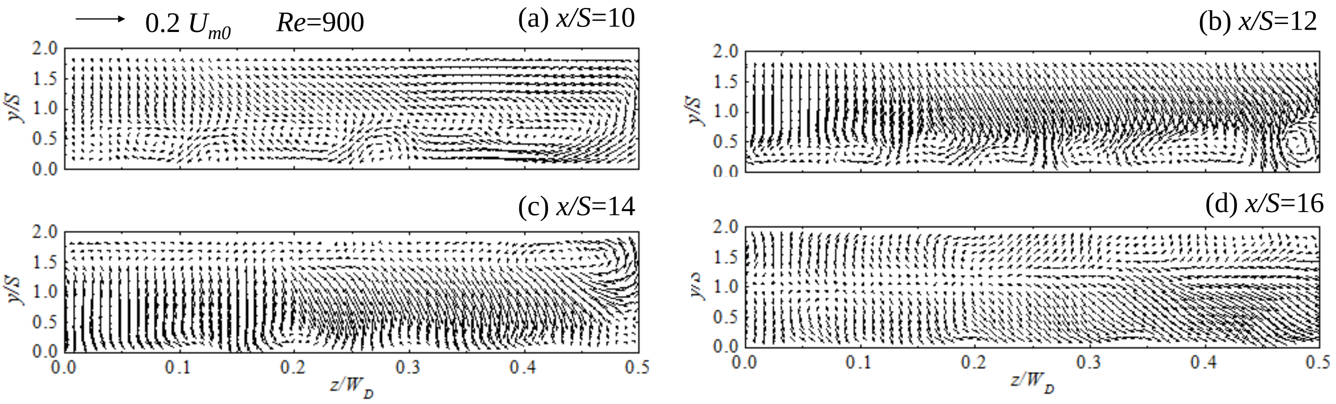

Fig. 2-15. Mean velocity vectors in the *y*-*z* plane of *Re*=900 for *x/S*=10, 12, 14 and 16.

2.3.6 Temporal change of the instantaneous flow structure

The temporal change of the instantaneous flow structure is examined in this section. Figures 2-16, 2-17, 2-18 show the dimensionless instantaneous velocity component in the streamwise direction and the instantaneous velocity vector at z/W_D=0.0, 0.4 for *Re*= 400, 700, 900. $t^*=t*Um0/S$ *was used to normalize t.* Fig. 2-16 shows four figures at 4.2$\boldsymbol{\Delta} t^*$ interval, Fig. 2-17. and 2.20 show four figures at 2.0$\boldsymbol{\Delta} t^*$ interval.

The upper side of Figs. 2-16, 2-17, 2-18 show the flow structures at the center of the duct (z/W_D=0.0), it is found that the mainstream meanders downstream at z/W_D = 0.0. Further downstream, the mainstream diffuses and the flow becomes slow. In addition, a blue region with a negative velocity component is observed near the bottom and upper walls, indicating that there are circulation regions near the bottom and upper walls. Therefore, looking at the instantaneous velocity vector, one or two clockwise transverse vortices are generated on the mainstream bottom wall side. At the same time, one to three counterclockwise transverse vortices are generated on the mainstream upper wall side.

From the lower side of Figs. 2-16, 2-17 and 2-18, the meandering magnitude of the mainstream near the side wall was smaller than that near the center duct. The circulation region near the bottom wall becomes smaller and that near the upper wall becomes larger compared with the center case, and the movement of the circulation region is small but it does move with time. In addition, multiple counterclockwise transverse vortices are generated near the upper wall surface in Fig. 2-16, and one or two are generated in Figs. 2-17 and 2-18. It was, as described in Fig. 2-12, a small time-averaged circulation region appears near the upper wall of the time-averaged velocity vector diagram in the *x*-*y* plane near the side wall (z/W_D=0.4). From this, it is considered that the cause is the small movement of the counterclockwise transverse vortex. As the duct approaches the side wall, the movement of the clockwise vortex near the bottom wall and the counterclockwise vortex near the upper wall become smaller.

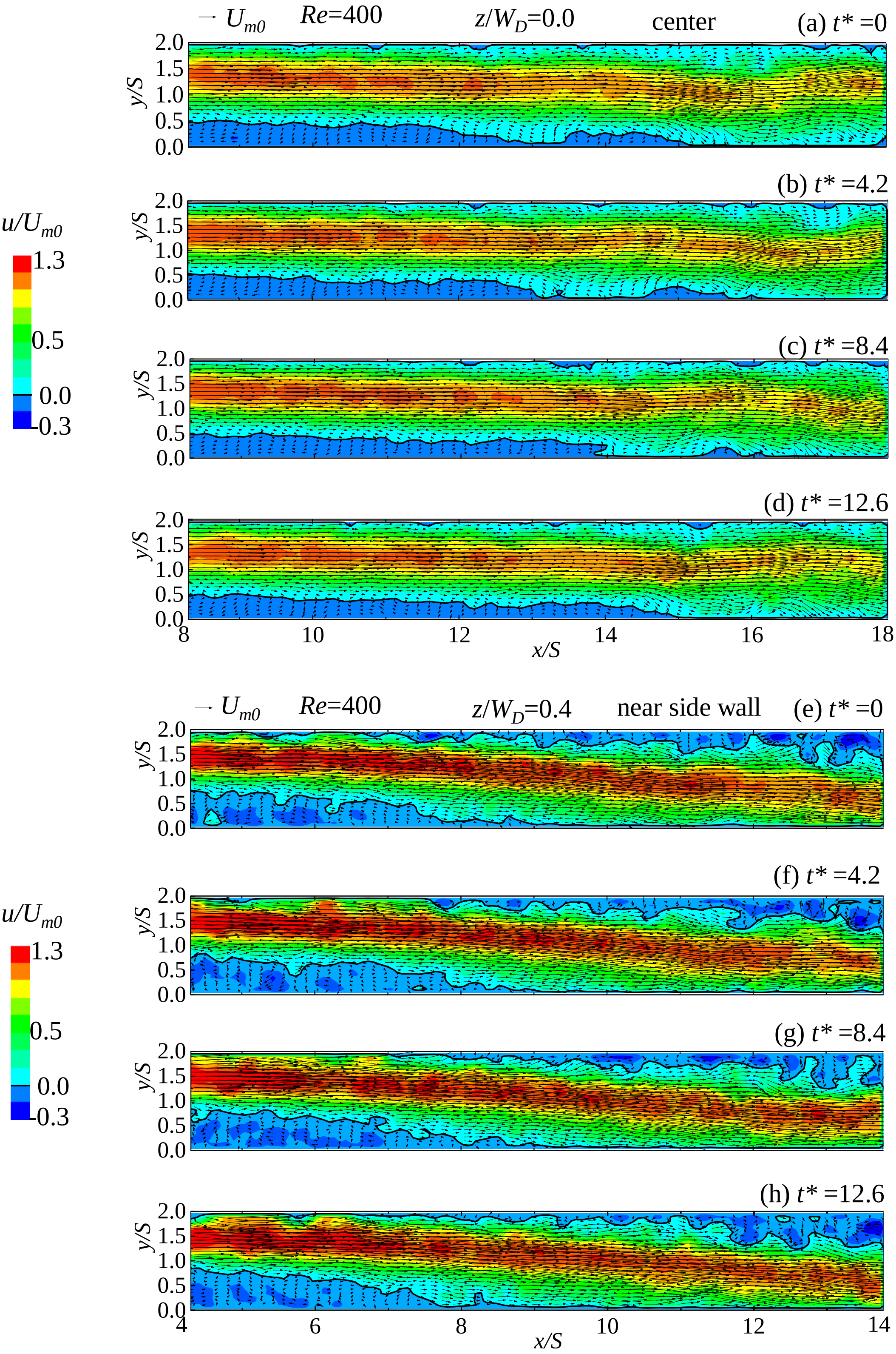

Fig. 2-16. Instantaneous velocity vectors and instantaneous velocity component in the x-y plane at z/W_D=0.0 (the upper figure) and z/W_D=0.4 (the lower figure) for Re=400.

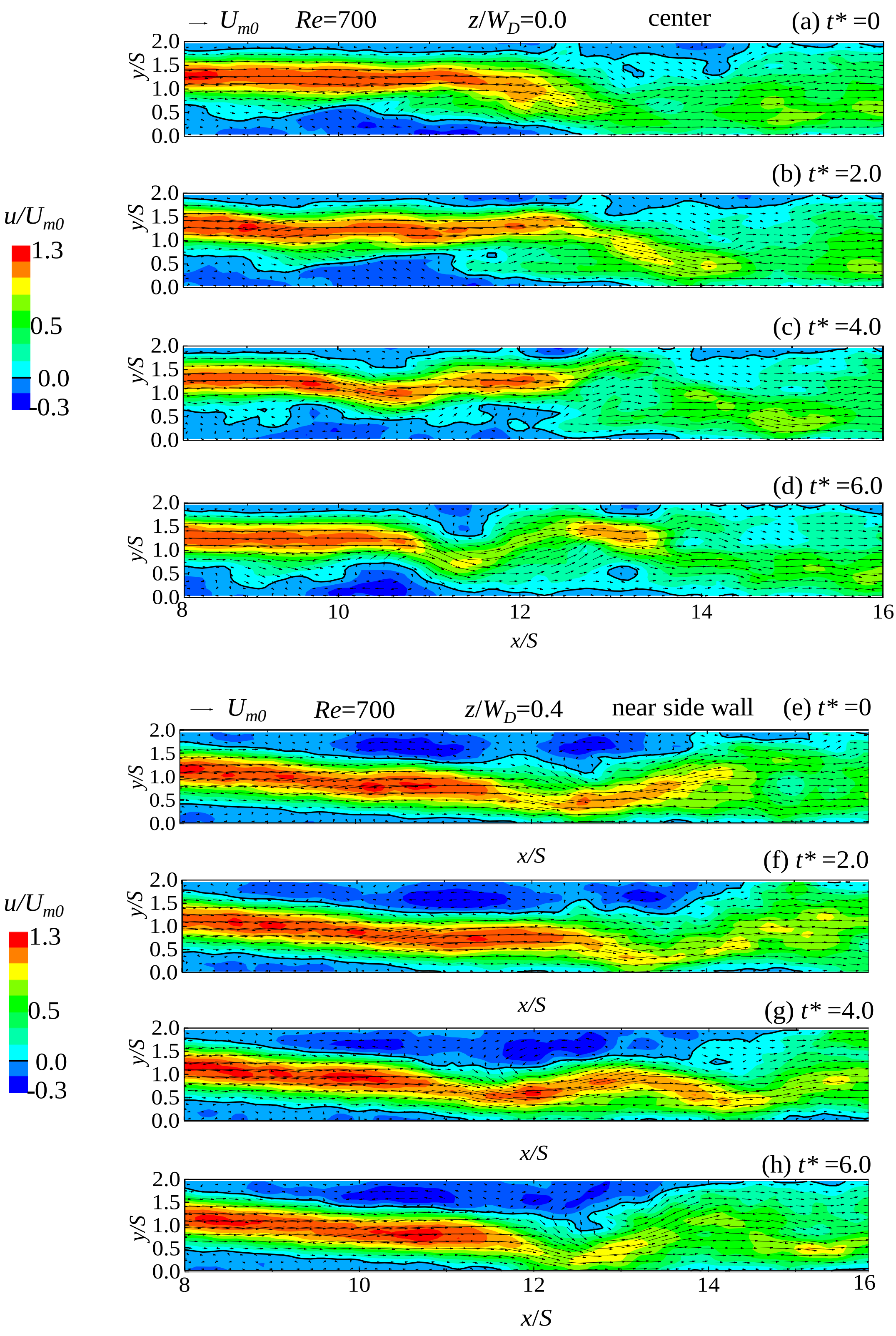

Fig. 2-17. Instantaneous velocity vectors and instantaneous velocity component in the *x*-*y* plane at z/W_D=0.0 (the upper figure) and z/W_D=0.4 (the lower figure) for *Re*=700.

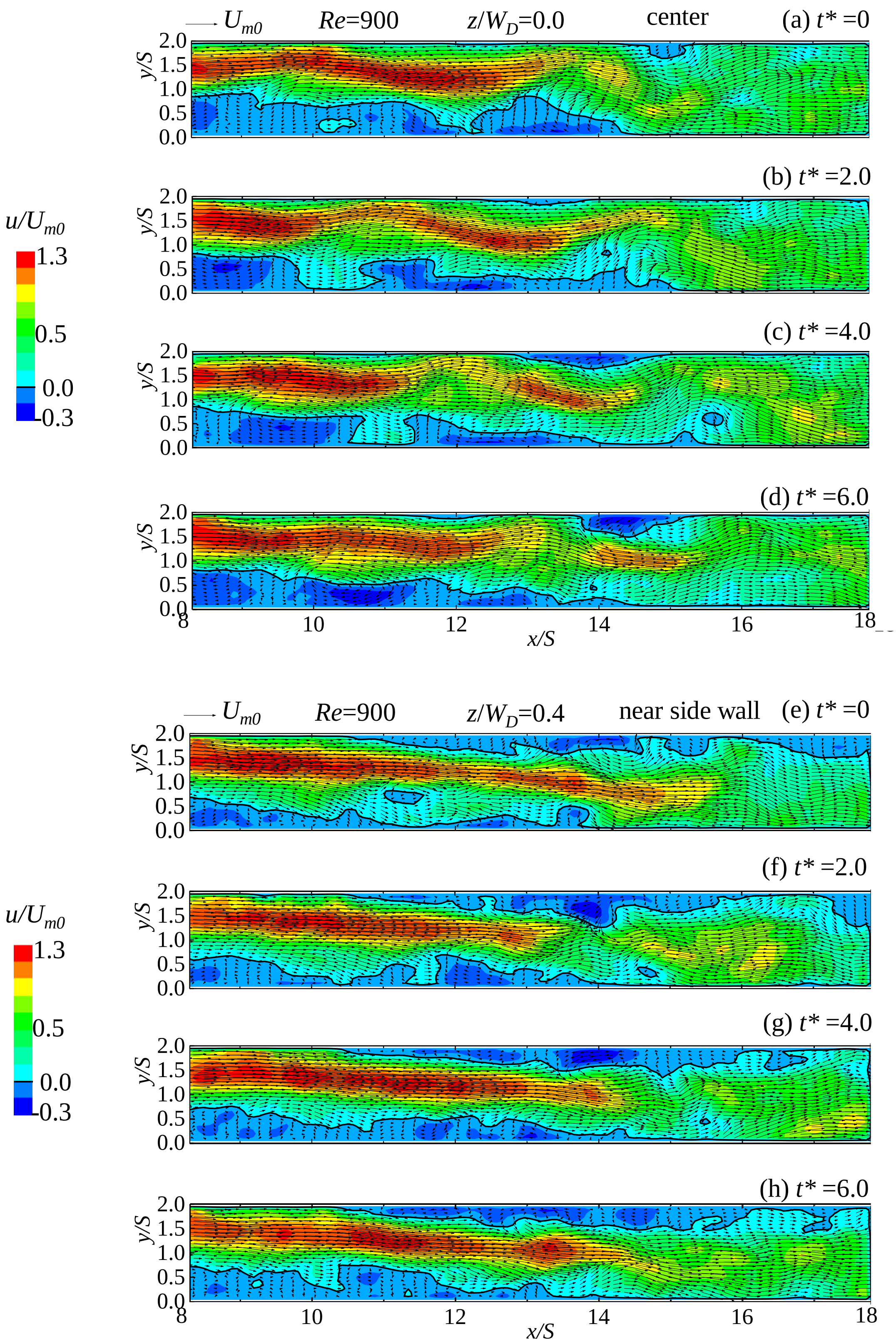

Fig. 2-18. Instantaneous velocity vectors and instantaneous velocity component in the *x*-*y* plane at z/W_D=0.0 (the upper figure) and z/W_D=0.4 (the lower figure) for *Re*=900.

2.3.7 Time trace of the instantaneous reattachment position

2.3.7.1 Temporal change of instantaneous reattachment position near the bottom wall

Figure 2-19 (a)-(f) shows the time-series changes of the instantaneous reattachment position near the bottom wall surface at z/W_D= 0.0 and 0.4. The horizontal axis is the dimensionless time defined by the step height S and the time-averaged cross-sectional velocity U_{m0}. The red solid line indicates the time-averaged position of the reattachment point, and the reattachment position at each time is indicated by a small circle ○.

From Fig. 2-19, the temporal change in the instantaneous reattachment position varies with the spanwise direction at each position. First, at z/W_D=0.0 near the center of the duct in Fig. 2-19 (a), the instantaneous reattachment position occurs at x/S=11 and moves to x/S=15 as time passes. After that, a new instantaneous reattachment position appears on the upstream side, and the repeated periodicity is observed. This result is like that of direct numerical analysis by Le et al. [2, 24]. Next, at z/W_D=0.4 in Fig. 2-19 (b), the temporal change of the instantaneous reattachment position does not show a periodic change compared to that near the duct center. This is because the z-direction velocity W_m became dominant due to the influence of the downwash flow as in Fig. 2-13, it is thought that the time-dependent change in the instantaneous reattachment position became different because the x-direction velocity u turned to be zero. The law of these periodic changes and location variation of instantaneous points could also be identified in Fig. 2-9, that is, near the center of duct, instantaneous reattachment points vary along the streamwise direction with a wide range and high periodicity, while near the side wall, the distribution of non-periodic instantaneous reattachment points is more concentrated in a narrow variation region.

In Fig. 2-19 (c), the periodic change was less obvious than that in Fig. 2-19. (a). In Fig. 2-19 (d), near the side wall shows the behavior of the instantaneous reattachment point like Fig. 2-19 (b), but it tends to move downstream. It worth mentioning that the instantaneous reattachment points move back and forth around two time-averaged reattachment positions (x/S=11 and x/S=13), which is greatly consistent to the disconnection phenomenon in Fig. 2-7 (c). The instantaneous reattachment points around x/S=13 are not always appearing as time advances.

In Fig. 2-19 (e) and (f), the increase of the Reynolds number brought a small change of instantaneous flow reattachment, the behavior of the instantaneous reattachment point shows no obvious periodicity neither near the center of the duct nor near the side wall.

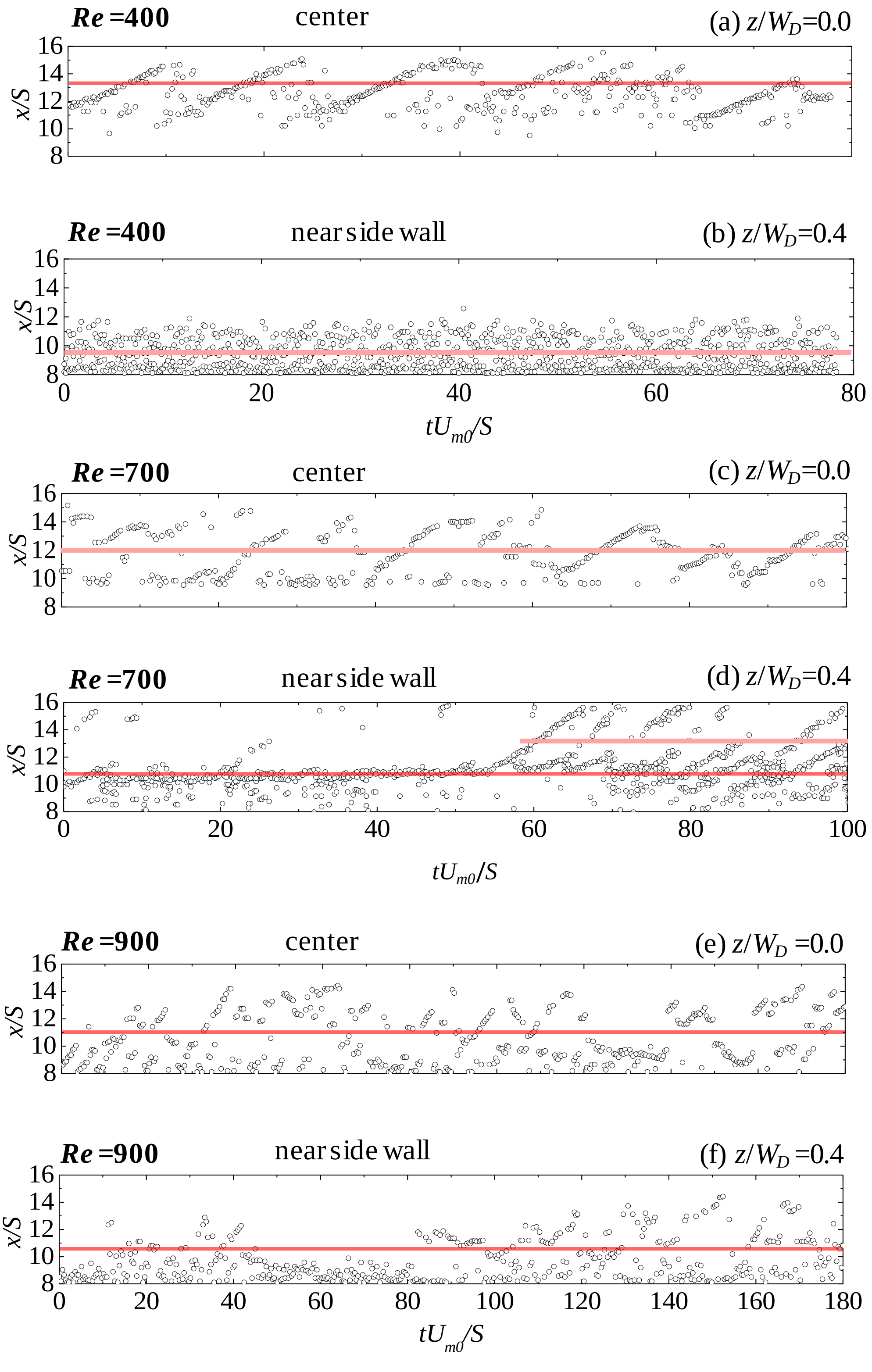

Fig. 2-19. Time trace of the instantaneous reattachment position near the bottom wall of *Re*=400, 700, and 900 for z/W_D=0.0 and 0.4. The red line represents the time-averaged reattachment point while the small circle indicates the instantaneous reattachment point at each flame.

2.3.7.2 Temporal change of instantaneous separation position near the upper wall

Figure 2-20 (a)-(f) show time-series changes in the instantaneous separation position near the upper wall. The horizontal axis is the dimensionless time defined by the step height S and the time-averaged cross-sectional velocity U_{m0}. The solid green line in the figure shows the time-averaged separation position, and the instantaneous separation position at each time is indicated by a small circle ○.

From Fig. 2-20 (a), when z/W_D=0.0 for Re=400, instantaneous separation points appearing at regular intervals could be observed, similar to the results of Le et al. [25] (Le, et al., 1997). The periodicity of the reattachment points on the upper wall is much shorter than that near the bottom wall. From Fig. 2-20 (b), no periodic change could be confirmed at z/W_D=0.4 near the side wall. At Re=700, the moving speed of the instantaneous separation position is constant downstream of the time-averaged separation position. This is thought to be due to the occurrence of an instantaneous separation position upstream of the region where mainstream diffusion occurs, as in Fig. 2-16. Next, in the vicinity of the side wall z/W_D=0.4 for Re=700, the temporal change of the instantaneous separation position has a complex distribution, and no clear periodicity can be seen. The instantaneous separation points are separated by the time-averaged separation line. As for Re=900, the periodic instantaneous separation position with a narrow variation range could be observed both near the side wall and the duct center. No matter near the center of the duct or the side wall, the periodicity becomes more and more obvious and the range of separation variation is becoming more and more concentrated as the increase of Reynolds number.

2.3.7.3 Temporal change of instantaneous reattachment position near the upper wall

Figures 2-21 (a)-(f) show time-series changes in the instantaneous reattachment position near the upper wall. The solid red line and the small plot are also shown in these figures. As the reattachment point and separation point are located upstream and downstream of the secondary recirculation zone (the first recirculation zone is located immediately downstream of the step), it could be observed that the periodicity of the instantaneous reattachment position and the instantaneous separation position are highly consistent for each Reynolds number case. This consistent periodicity can represent the periodicity of the secondary recirculation zone.

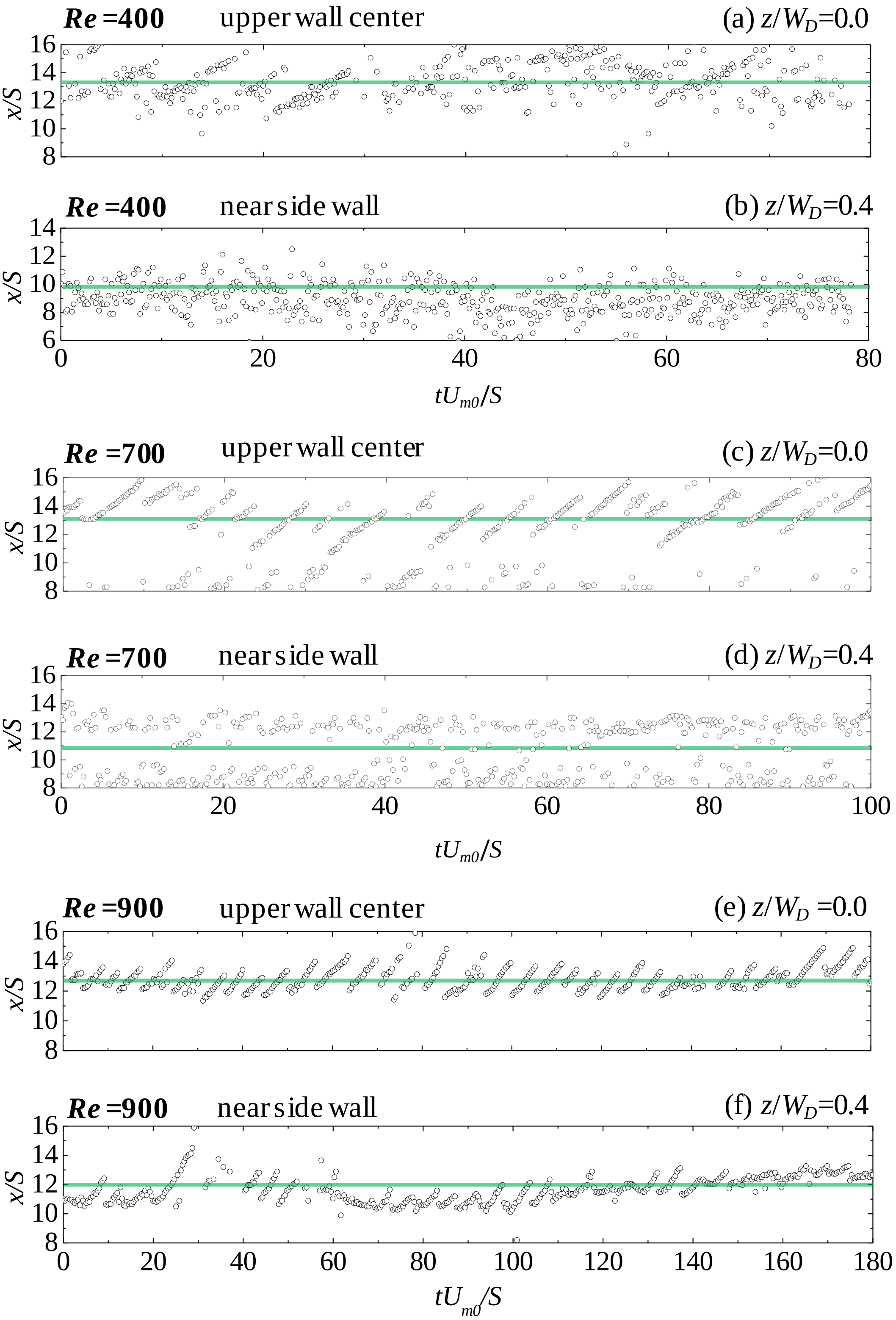

Fig. 2-20. Time trace of the instantaneous separation position near the upper wall of *Re*=400, 700, and 900 for z/W_D=0.0 and 0.4. The green line represents the time-averaged reattachment point while the small circle indicates the instantaneous reattachment point at each flame.

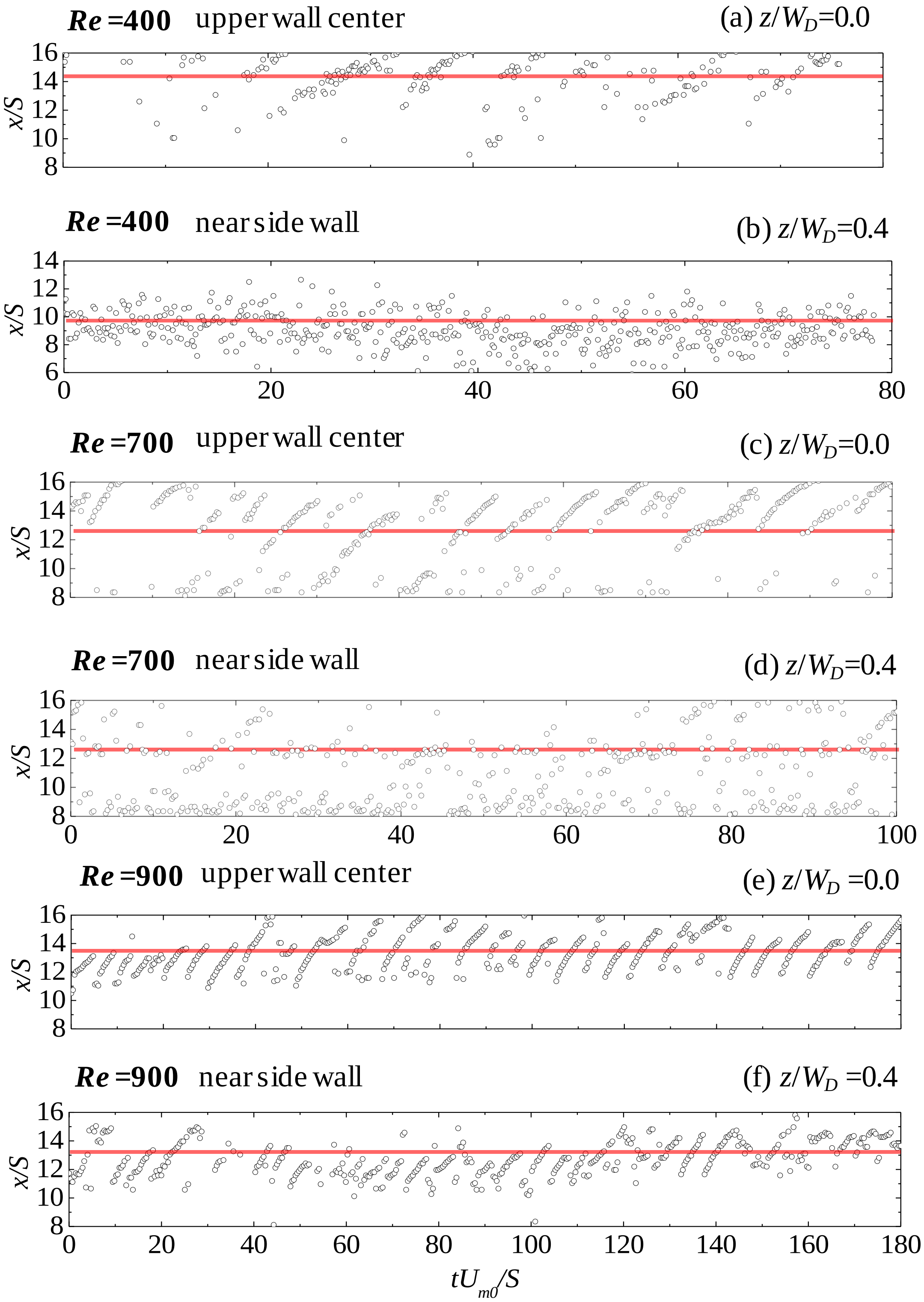

Fig. 2-21. Time trace of the instantaneous reattachment position near the upper wall of *Re*=400 for z/W_D=0.0 and 0.4. The red line represents the time-averaged reattachment point while the small circle indicates the instantaneous reattachment point at each flame.

Table 2-1. Periodicity investigation of reattachment and separation position.

Center or side	*Re*=400	*Re*=700	*Re*=900
Reattachment position near the bottom center (Rea_{bc})	14.05		
Reattachment position near the bottom side wall (Rea_{bs})			
Separation position near the upper center (Sep_{uc})	7.01	5.10	6.14
Separation position near the upper side wall (Sep_{us})			4.58
Reattachment position near the upper center (Rea_{uc})	7.54	5.41	6.57
Reattachment position near the upper side wall (Rea_{us})			5.06

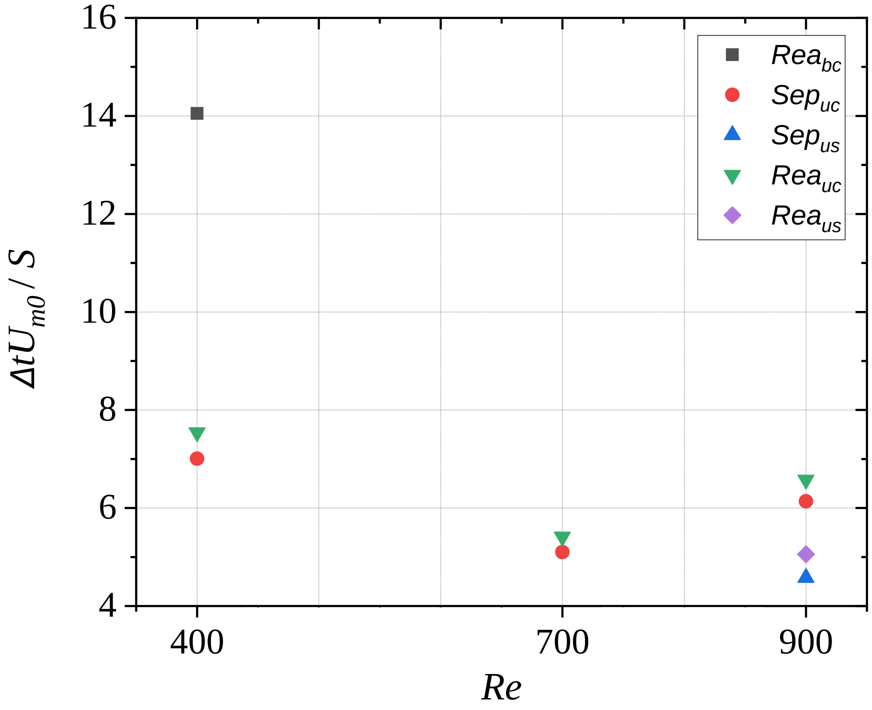

Fig. 2-22. Periodicity investigation of reattachment and separation position.

According to Fig. 2-19, 2-20, 2-21, the periodicity was qualitatively analyzed. Table 2-1 shows the dimensionless periodicity-related parameter $\Delta tU_{m0}/S$ value based on Renolds number, the corresponding figure was shown in Fig. 2-22, the period of the reattachment point on the bottom wall is much larger than that on the upper wall, and decreases with the increase of Reynolds number. A similar tendency and value occur between the reattachment position and separation position near the upper wall, no matter near the duct center or the side wall. The period of the secondary recirculation zone which is connecting the separation and reattachment position near the upper wall could be estimated by that of reattachment position or separation position.

2.3.8 Velocity fluctuation intensity distribution

2.3.8.1 Velocity fluctuation intensity distribution in the flow direction

Figures 2-23 (a)-(f) show the distribution of the value u_{rms}/U_{m0} obtained by the fluctuation intensity u_{rms} of flow direction velocity component u and the cross-sectional average velocity U_{m0}. The position of the time-averaged reattachment point on the bottom wall is indicated by ▲, the time-averaged reattachment position on the upper wall is indicated by ▼, and the time-averaged separation position is indicated by ▼. The maximum Nusselt number position of the bottom wall surface in each spanwise direction is indicated by ↑ h_{max}. In order to make sure that all the time-averaged reattachment points, separation points, h_{max} points are included in one cross-section, the coordinate settings for each case are not the same. For the Re=400 case, at z/W_D=0.4, the x/S range was chosen from 4 to14, which is different from that at z/W_D=0.0 and other Reynolds number cases.

From Fig. 2-23 (a), in the center view of the duct (z/W_D=0.0), the fluctuation intensity is high in the region downstream from the reattachment point position ($x/S > 14$). Therefore, when compared with the instantaneous velocity vector described in Fig. 2-16, this region coincides with the position where the clockwise transverse vortex movement is observed. And the velocity fluctuation on the side wall (z/W_D=0.4) which is presented in Fig. 2-23 (b) is smaller in the entire flow path than that in the vicinity of the center duct. The relatively large fluctuation appears after the secondary recirculation zone near the upper wall ($12 < x/S < 14$), which makes the mainstream strongly meander and diffuse thereafter.

In Fig. 2-23 (c), the fluctuation becomes much stronger, and the fluctuation intensity increases near the upper side of the time-averaged reattachment position (y/S=1.5). Therefore, it is located at a position where the mainstream meanders comparing to the instantaneous velocity vector diagram of Fig. 2-17. On the other hand, the value of the fluctuation intensity is also large near the side wall in Fig. 2-23 (d).

In Fig. 2-23 (e) and (f), fluctuation appears prominently, and the high fluctuation intensity values exist near the upper and bottom walls in the vicinity of the side wall and the center of the duct. Pay attention to the side wall for all Reynolds number cases, the maximum fluctuation intensity moves closer to the bottom side and also closer to the secondary recirculation zone ($14 < x/S < 16$) near the upper wall as the increase of Reynolds number.

The regions with high fluctuation intensity values for the maximum Nusselt number position on the bottom wall of each figure were compared. First, in Fig. 2-23. (a), the maximum Nusselt number position is located slightly downstream of the time-averaged reattachment position near the duct center. Looking at the value of the fluctuation intensity, it becomes higher at the upper wall on the downstream side (after x/S=15.6) of the time-averaged reattachment position and does not agree with the maximum Nusselt number position. The high fluctuation near the upper wall has small effects on the heat transfer near the bottom wall there. The distance between the maximum Nusselt number and the time-average reattachment position is much larger than that near the center duct. Next, in Fig. 2-23 (c), the position of the maximum Nusselt number is located on the bottom wall where the fluctuation intensity value is relatively high. From this, it is considered that one factor that improves the heat transfer in the middle of the channel and the vicinity of the side wall is the fluctuation of the flow. Near the side wall, the high fluctuation intensity position is also located right above the maximum Nusselt number position. The same tendency could be observed in Fig. 2-23 (e) and (f), the maximum Nusselt number is shown at the position where the fluctuation intensity value is high.

2.3.8.2 Velocity fluctuation intensity distribution in the step height direction

Figures 2-24 (a)-(f) show the distribution of the value v_{rms}/U_{m0} obtained by the fluctuation intensity v_{rms} of wall-normal velocity component v and the cross-sectional average velocity U_{m0}. The coordinate axes and plots in the figure are the same as in Fig. 2-23.

From Fig. 2-24 (a), although the fluctuation intensity value is smaller than that in the flow direction, the tendency of the fluctuation intensity value to be higher on the downstream side of the time-averaged reattachment position is the same. It is thought that the factor that increases the fluctuation intensity is the movement of the transverse vortex that exists on the bottom wall from Fig. 2-16. Near the side wall in Fig. 2-24 (b), the flow is thought to be steady because the value of the fluctuation intensity in both streamwise and spanwise directions is small.

From Fig. 2-24 (c), the value of the fluctuation intensity is high near x/S=12, y/S=1.0. This tendency is the same as Fig. 2-23 (c), which shows the fluctuation intensity in the flow direction. The cause of the increase in fluctuation intensity is the mainstream meandering. In Fig. 2-24. (e) and (f) as well, although the fluctuation intensity value in the entire channel is smaller than that in the flow direction. The maximum Nusselt number position could not be found a large relationship with the velocity fluctuation in the height direction.

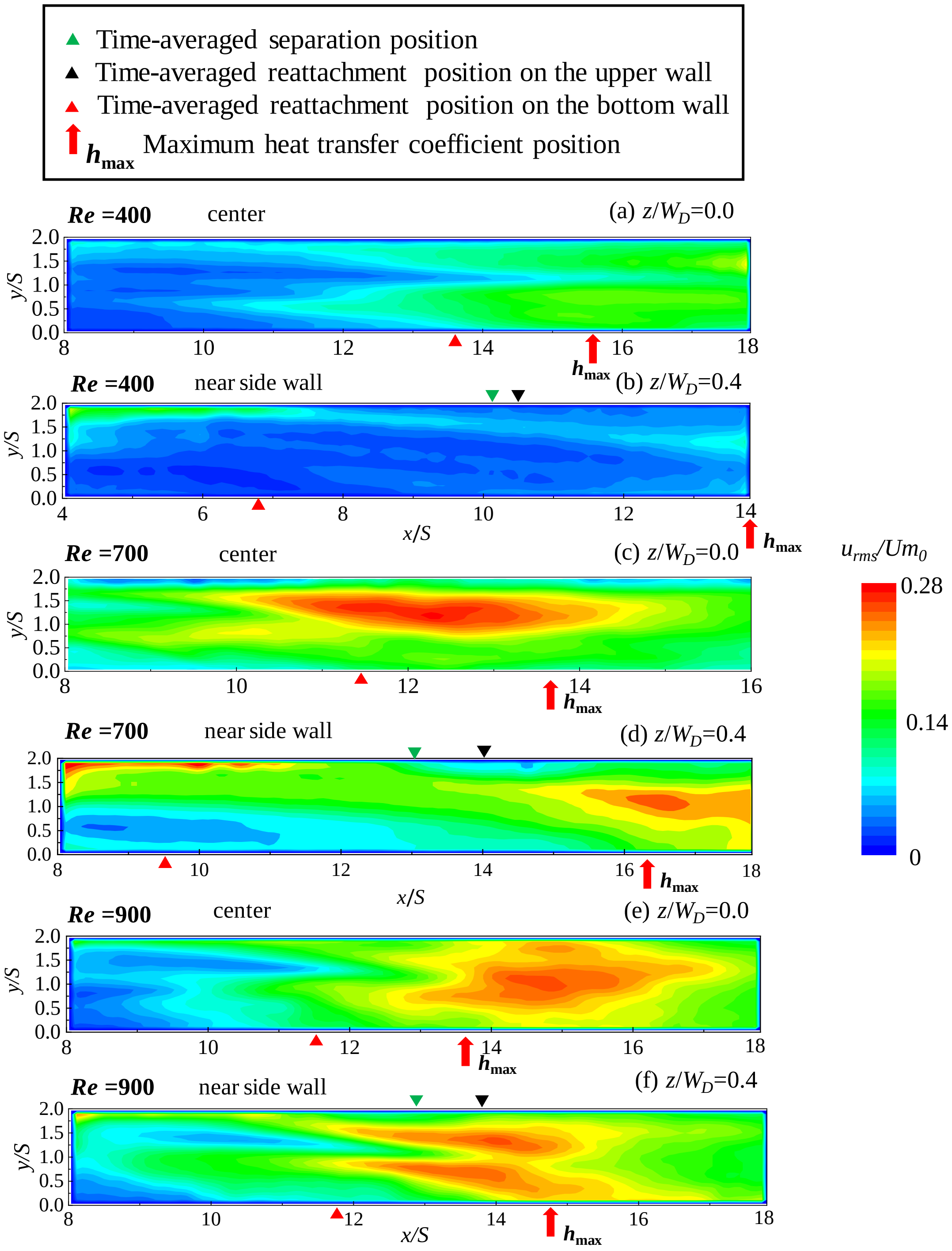

Fig. 2-23. Velocity fluctuation intensity distribution of flow direction of Re=400, 700, and 900 for z/W_D=0.0 and 0.4. Red triangular plots ▲ denote the time-averaged reattachment point on the bottom wall. Black triangular plots ▼ denote the time-averaged reattachment point on the upper wall. Green triangular plots ▼ denote the time-averaged separation point on the upper wall. ↑ h_{max} denotes the maximum Nusselt number points on the bottom wall.

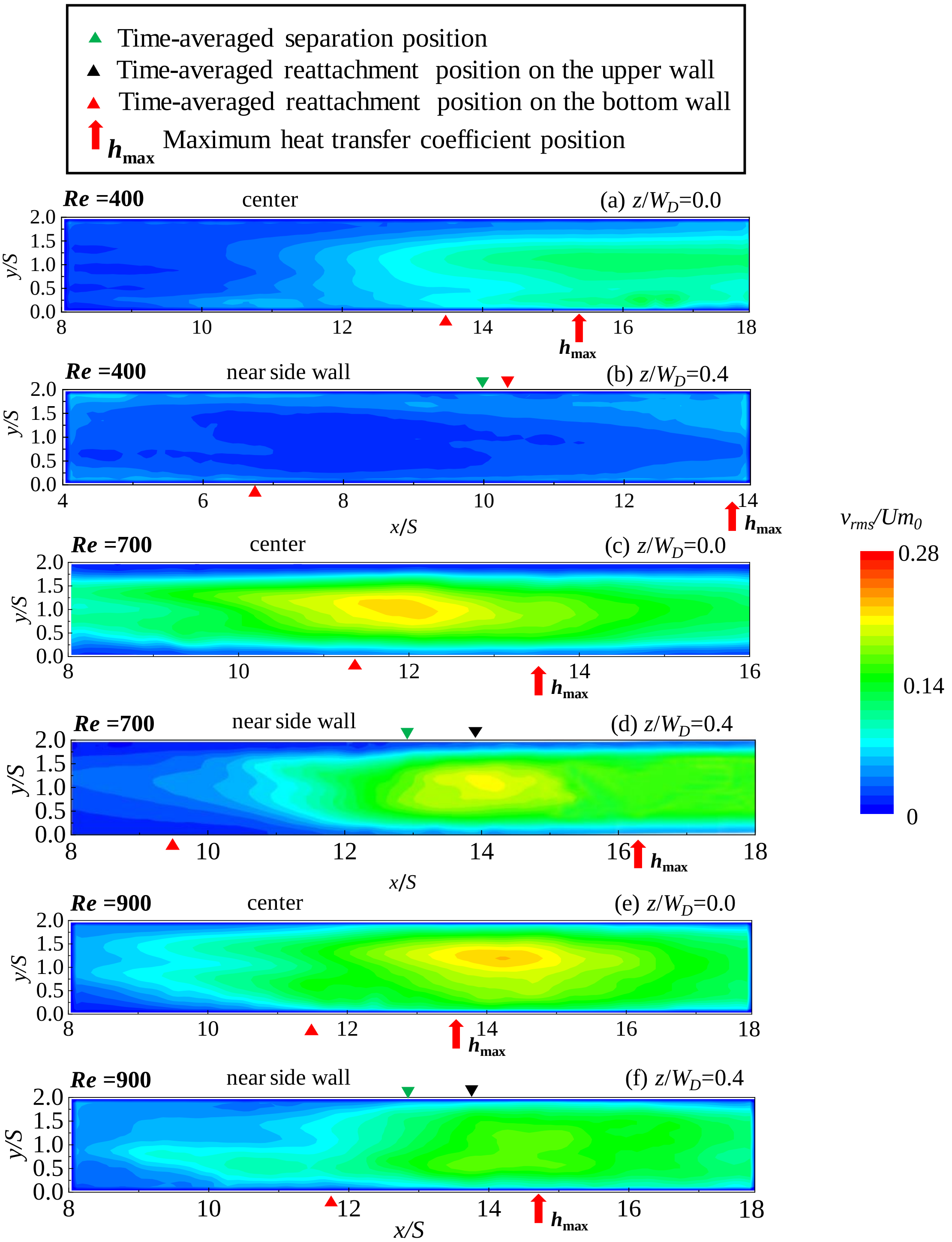

Fig. 2-24. Velocity fluctuation intensity distribution of wall normal direction of *Re*=400, 700, and 900 for z/W_D=0.0 and 0.4. Red triangular plots ▲ denote the time-averaged reattachment point on the bottom wall. Black triangular plots ▼ denote the time-averaged reattachment point on the upper wall. Green triangular plots ▼ denote the time-averaged separation point on the upper wall. ↑ h_{max} denotes the maximum Nusselt number points on the bottom wall.

2.3.8.3 Velocity fluctuation intensity distribution for different height and streamwise directions

Figure 2-25 (a) and (b) show the distribution of the value u_{rms}/U_{m0} obtained by the fluctuation intensity u_{rms} of each spanwise flow direction velocity component u and the cross-sectional average velocity U_{m0}.

From Fig. 2-25 (a), the maximum value is obtained at $x/S = 16$ and $y/S = 0.8$ at the center of duct z/W_D=0.0. In addition, the convex shape of the maximum value becomes gentler as it goes downstream. This is thought to be because the transverse vortex shown in Fig. 2.16 decreases and disappears as it moves downstream. The position of the maximum value changes to the upper wall side as it goes to the side wall. In addition, the value of the fluctuation intensity on the bottom wall tends to be smaller, the behavior of the transverse vortex on the bottom wall surface turns to be smaller.

From Fig. 2-26, the same tendency as in Fig. 2-25. On the other hand, the maximum value is taken on the upper wall, and the value becomes higher as it goes downstream, it seems to be higher due to the meandering mainstream. Furthermore, the region with higher velocity fluctuation intensity values can be divided into two parts as the flow approaches the side wall.

From Fig. 2-27, regions with high values of fluctuation intensity are generally larger than the other Reynolds number cases. The variation of fluctuation intensity near the duct center changes more moderate along the height direction.

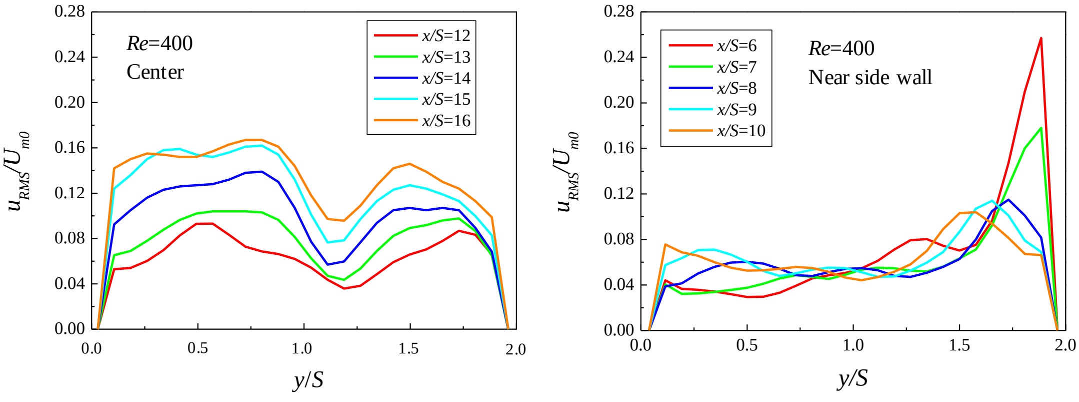

(a) z/W_D=0.0 (b) z/W_D=0.4

Fig. 2-25. Velocity fluctuation intensity of flow direction of *Re*=400 for z/W_D=0.0 and 0.4.

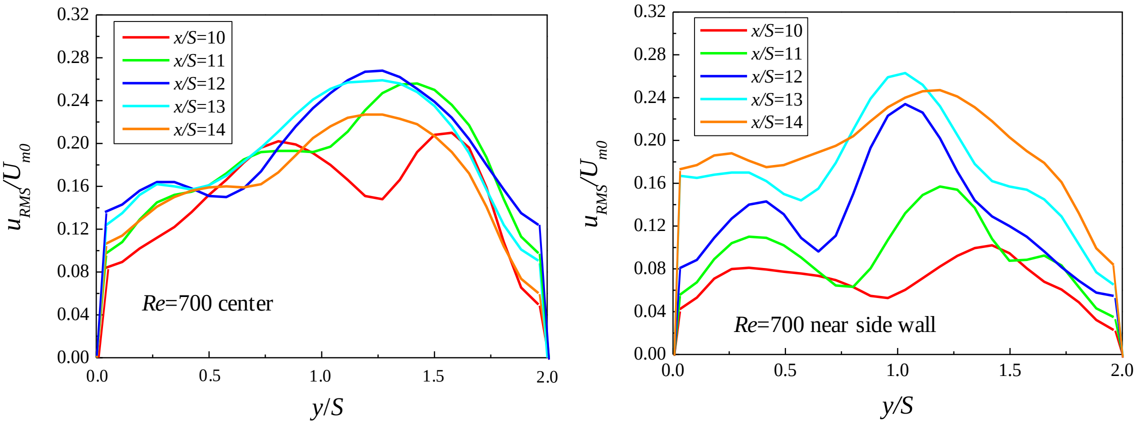

(a) z/W_D =0.0 (b) z/W_D =0.4

Fig. 2-26. Velocity fluctuation intensity of flow direction of *Re*=700 for z/W_D =0.0 and 0.4.

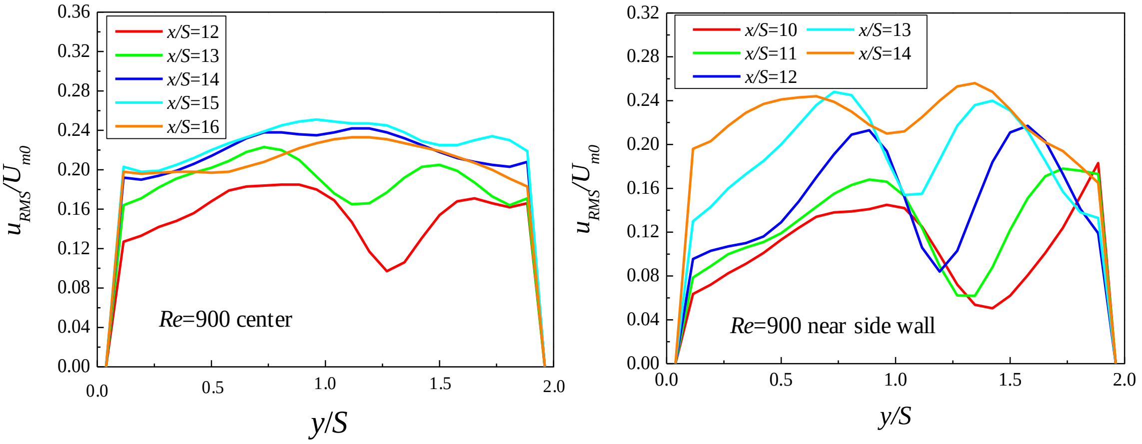

(a) z/W_D =0.0 (b) z/W_D =0.4

Fig. 2-27. Velocity fluctuation intensity of flow direction of *Re*=900 for z/W_D =0.0 and 0.4.

2.4 Conclusion and discussions

In this study, in order to make clear the structure of BFS flow in a rectangular duct experimentally, Velocity measurements by PIV have been done at the low Reynolds number range in the BFS geometry configured by 240 mm wide, 30 mm high, and 15 mm step high, and mounted in a rectangular duct having an aspect ratio of 16 and an expansion ratio of 2. Attention was paid to grasp the spanwise variations of both the time-averaged and the instantaneous reattachment points and their relationships to the flow structures. The main results obtained in this study are summarized as follows:

(1) The time-averaged reattachment position is changed in the spanwise direction in every case. The reattachment distributions can be classified into four patterns within the Reynolds number range ($200 \leqq Re \leqq 1000$). In the range of $Re<400$, the flow near the bottom wall is stable and reattaches more downstream at the center of the duct while it reattaches closer behind the step near the side wall. In the range of $400 \leqq Re<550$, flow reattachment begins to vary largely near the center of the duct owing to the unstable flow reattachment. This variation of the flow reattachment extends to the near wall region as the Reynolds number is increased ($600 \leqq Re<750$). The dominant flow is changed from side wall flow to center flow, which leads to the disconnection between these two flow areas. As the Reynolds number is further increased ($800 \leqq Re$), the unstable flow reattachment appears over the whole width of the duct. Owing to this, relatively short flow reattachment is realized in this relatively large Reynolds number range.

(2) The periodicity of the instantaneous reattachment points on the bottom wall is more obvious in the lower Reynolds number (Re=400) near the duct center. It could not be observed any more near the side wall for all investigated Reynolds numbers. However, the instantaneous separation and reattachment points show more obvious periodicity near the upper wall as the increase of Reynolds number from Re=400 to Re=900. It can be inferred from the corresponding highly consistent periodic characteristics of the reattachment point and the separation point on the upper wall: A secondary recirculation area with an obvious periodicity appears near the upper wall.

(3) Velocity fluctuation intensity distribution in the streamwise direction contributes more than that in the height direction to heat transfer enhancement near the bottom wall.

References

[1] B. F. Armaly, F. Durst, J. C. F. Pereira, and B. Schönung "Experimental and theoretical investigation of backward-facing step flow," *Journal of Fluid Mechanics,* vol. 127, no. -1, pp. 473-496, 1983.

[2] T. Lee and D. Mateescu, "Experimental and numerical investigation of 2-D backward -facing step flow," *Journal of Fluids and Structures,* vol. 12, no. 6, pp. 703-716, 1998.

[3] S. Terhaar, A. Velazquez, J. Arias, and M. Sanchez-Sanz, "Experimental study on the unsteady laminar heat transfer downstream of a backward facing step," *International Communications in Heat and Mass Transfer,* vol. 37, no. 5, pp. 457-462, 2010.

[4] P. Kapiris and D. Mathioulakis, "Experimental study of vortical structures in a periodically perturbed flow over a backward-facing step," *International Journal of Heat and Fluid Flow,* vol. 47, pp. 101-112, 2014.

[5] J. Vogel and J. Eaton, "Combined heat transfer and fluid dynamic measurements downstream of a backward-facing step," vol. 107, no. 4, pp. 922-929, 1985.

[6] H. Iwai, K. Nakabe, and K. Suzuki, "Flow and heat transfer characteristics of backward-facing step laminar flow in a rectangular duct," *International Journal of Heat and Mass Transfer,* vol. 43, no. 3, pp. 457-471, 2000.

[7] P. Louda, J. Příhoda, K. Kozel, and P. Sváček, "Numerical simulation of flows over 2D and 3D backward-facing inclined steps," *International Journal of Heat and Fluid Flow,* vol. 43, pp. 268-276, 2013.

[8] H. Lan, B. Armaly, and J. Drallmeier, "Three-dimensional simulation of turbulent forced convection in a duct with backward-facing step," *International Journal of Heat and Mass Transfer,* vol. 52, no. 7-8, pp. 1690-1700, 2009.

[9] H. Barrios-Pina, S. Viazzo, and C. Rey, "A numerical study of laminar and transitional mixed convection flow over a backward-facing step," *Computers and Fluids,* vol. 56, pp. 77-91, 2012.

[10] B. F. Armaly, F. Durst, J. Pereira, and B. Schönung, "Experimental and theoretical investigation of backward-facing step flow," *Journal of Fluid Mechanics,* vol. 127, pp. 473-496, 1983.

[11] B. Armaly, A. Li, and J. Nie, "Three-dimensional forced convection flow adjacent to backward-

facing step," *Journal of thermophysics and heat transfer,* vol. 16, no. 2, pp. 222-227, 2002.

[12] J. H. Nie and B. F. Armaly, "Reverse flow regions in three-dimensional backward-facing step flow," *International Journal of Heat and Mass Transfer,* vol. 47, no. 22, pp. 4713-4720, 2004.

[13] Y. Chen, J. Nie, H.-T. Hsieh, and L. Sun, "Three-dimensional convection flow adjacent to inclined backward-facing step," *International Journal of Heat and Mass Transfer,* vol. 49, no. 25-26, pp. 4795-4803, 2006.

[14] J. H. Nie, Y. Chen, and H.-T. Hsieh, "Effects of a baffle on separated convection flow adjacent to backward-facing step," *International Journal of Thermal Sciences,* vol. 48, no. 3, pp. 618-625, 2009.

[15] P. Williams and A. Baker, "Numerical simulations of laminar flow over a 3D backward‐facing step," *International Journal for Numerical Methods in Fluids,* vol. 24, no. 11, pp. 1159-1183, 1997.

[16] T. Chiang, T. W. Sheu, and C. Fang, "Numerical investigation of vortical evolution in a backward-facing step expansion flow," *Applied Mathematical Modelling,* vol. 23, no. 12, pp. 915-932, 1999.

[17] N. Tylli, L. Kaiktsis, and B. Ineichen, "Sidewall effects in flow over a backward-facing step: Experiments and numerical simulations," *Physics of Fluids,* vol. 14, no. 11, pp. 3835-3845, 2002.

[18] J. Nie and B. F. Armaly, "Three-dimensional convective flow adjacent to backward-facing step-effects of step height," *International Journal of Heat and Mass Transfer,* vol. 45, no. 12, pp. 2431-2438, 2002.

[19] G. Biswas, M. Breuer, and F. Durst, "Backward-facing step flows for various expansion ratios at low and moderate Reynolds numbers," *Journal of Fluids Engineering,* vol. 126, no. 3, pp. 362-374, 2004.

[20] H. Rani, T. W. Sheu, and E. S. Tsai, "Eddy structures in a transitional backward-facing step flow," *Journal of Fluid Mechanics,* vol. 588, p. 43, 2007.

[21] A. Kitoh, K. Sugawara, H. Yoshikawa, and T. Ota, "Expansion ratio effects on three-dimensional separated flow and heat transfer around backward-facing steps," 2007.

[22] B. Raheli, M. T. Aalami, A. El-Shafie, M. A. Ghorbani, and R. C. Deo, "Uncertainty assessment of the multilayer perceptron (MLP) neural network model with implementation of the novel hybrid MLP-FFA method for prediction of biochemical oxygen demand and dissolved oxygen: a case study of Langat River," *Environmental Earth Sciences,* vol. 76, no. 14, p. 503, 2017.

[23] K. Inaoka and M. Senda, "Heat transfer and fluid flow characteristics of a backward-facing step flow in a duct," *Transactions of the Japan Society of Mechanical Engineers, Series B,* vol. 79, no. 804, pp. 1651-1663, 2013.

[24] I. Lee, S. Ahn, and H. J. Sung, "Three-dimensional coherent structure in a separated and reattaching flow over a backward-facing step," *Experiments in Fluids,* vol. 36, no. 3, pp. 373-383, 2004.

[25] T. Lee and D. Mateescu, "Experimental and numerical investigation of 2-D backward-facing step flow," *Journal of Fluids and Structures,* vol. 12, no. 6, pp. 703-716, 1998.

CHAPTER 3

Three-dimensional Fluid Flow and Heat Transfer Characteristics of a BFS Flow in a Rectangular Duct

3.1 Introduction

Backward-facing step (BFS) flow which was applied to many heat exchanging devices was introduced as a basic model that involves the most important features of a separated and reattachment flow [1]. As is summarized in the review study of Chen et al. [2], early basic studies [3] mainly focused on theoretical models and experiments for reattachment length, friction, pressure variations. The aspect ratio of the stepped duct in most studies was set large and the spanwise direction of the flow path was set sufficiently, especially in the basic research works. However, in practical applications, the flow channel is thought to be a duct having side walls and upper walls, which cannot be ignored.

Since the three-dimensional feature of the flow has been observed [4], new investigations focusing on the three-dimensional flow structures have been started and some useful results have been obtained. From this point of view, Iwai et al. [5, 6] have carried out the three-dimensional numerical computation changing the channel aspect ratios from 4 to 24 for the laminar flow regime. It was revealed that the existence of a side wall intensively affects the flow and thermal fields downstream the step and showed unique heat transfer distribution on the bottom wall. Intensive efforts have also been done by Nie and Armaly [7-9] using numerical and experimental methods. The aspect ratio was set to be 8 and reported that near the side wall, the jet-like flow impinges on the bottom wall from the step and causes the maximum local heat transfer there [8]. The fact that the flow reattachment region of the 3D duct case is quite different from that of the 2D case was published by Inaoka et al. [10, 11]. Some numerical predictions reported that 3D flow effects will become important when $Re > 500$ [12, 13], under low Re number conditions, and the 3D flow effects will become largely limited while the universal structure under high Re may dominant the flow after the step. However, the comparison between prediction and experiments does not agree well with each other in the low Reynolds number range, due to boundary and three-dimensional effects [14]. According to the review report of Chen et al. [2], the thermal effects on the BFS flow separation, evolution of coherent structures, and reattachment process, which are very important for real applications, have rarely been discussed, there are not many experimental studies on heat transfer aspect, as the heating region (global or local) becomes more complicated. Experiments are mainly conducted in the high *Re* region, while numerical studies are mainly focused on the relatively low *Re* region.

To sum up, three-dimensional heat transfer characteristics of backward-facing step flow in a duct at a low Reynolds number should be clarified. Therefore, in this study, referring to the report by Inaoka et al.[10, 11, 15], the heat transfer experiments of BFS flow in the duct with an aspect ratio of 16 and an expansion ratio of 2 in the low Reynolds number range (400-900) were conducted. The local heat transfer coefficient of the bottom wall surface behind the step was measured from the center of the flow path to the side wall, and its heat transfer mechanism was investigated. In the heat transfer experiment, a thermo-sensitive liquid crystal method that shows different colors depending on the temperature was adopted to obtain the local heat transfer coefficient over the entire spanwise direction of the duct flow path. In addition, under typical flow conditions, velocity was measured by PIV (particle image velocimetry) to understand the characteristics of the flow velocity distribution and to consider the flow structure and its relationship with heat transfer. To realize this purpose, in detail, the time-averaged *Nu* and the maximum *Nu*, the ratio of maximum *Nu* over the entire wall to that in the duct centerline should be investigated both on the bottom wall and upper wall for a wide variety of the flow Reynolds number in the low Reynolds number range (*Re*=400-900).

3.2 Experimental apparatus and procedures

3.2.1 Experimental apparatus overview

In this experiment, a closed channel using water as the working fluid which is mentioned in Chapter 2 was adopted. Fig. 3-1 shows a schematic diagram of the experimental apparatus. Fig. 3-2 shows a schematic diagram of the test section which is a rectangular duct with a width W_D=240 mm and a height H=30 mm, and a step with a height S=15 mm was installed inside. In this experiment, the Reynolds number defined by the step height S as the representative length was changed from 400 to 900. The coordinate axis setting is the same as Chapter 2. In terms of the definition of velocity, *u, v, w* represent the velocity in the flow direction, wall-normal direction and spanwise direction, respectively.

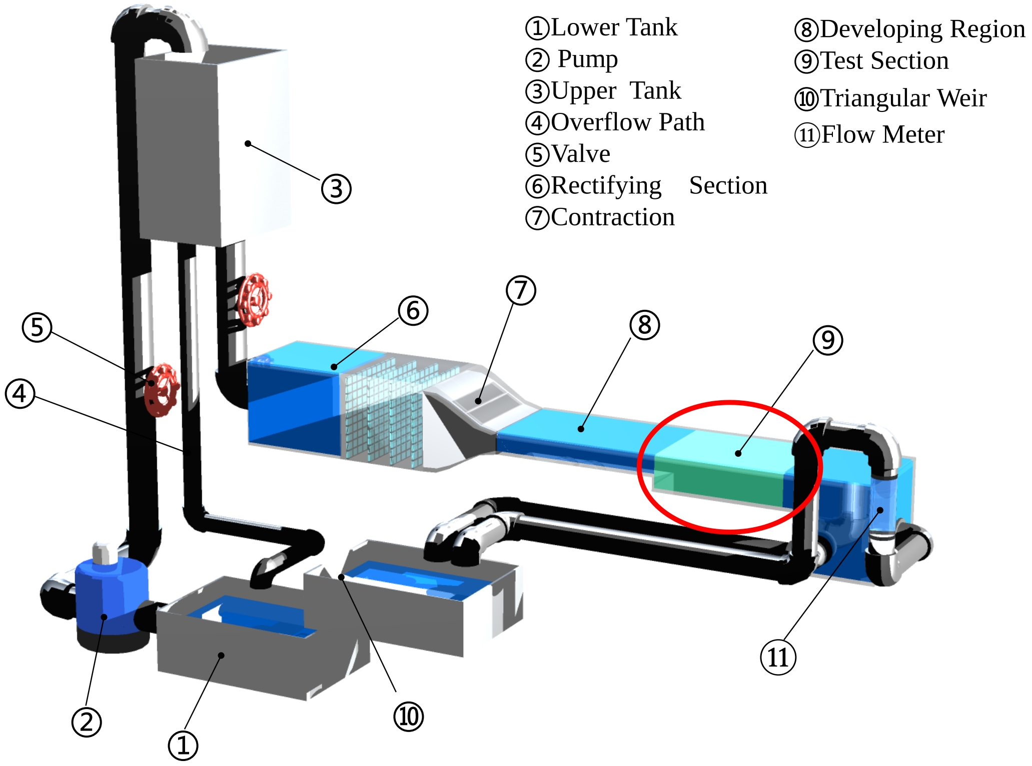

Fig. 3-1. Closed water channel used in the present study flow in a duct.

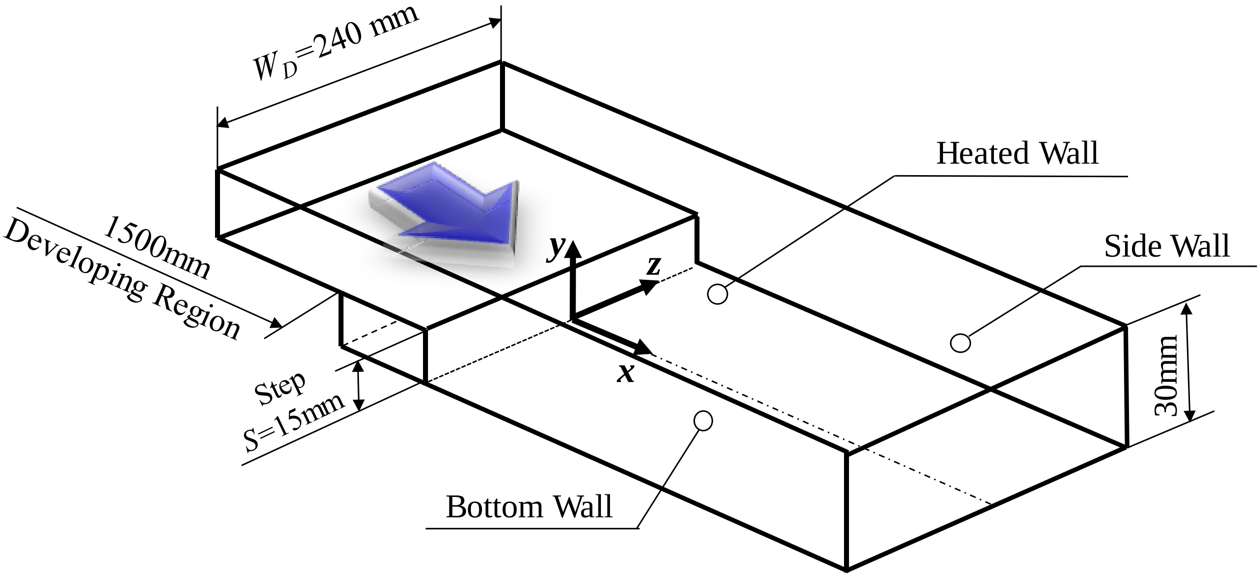

Fig. 3-2. Test section of a backward-facing step flow.

3.2.2 Heat transfer experiment procedure

3.2.2.1 Heat transfer test section

Thermal measurements were conducted each on the bottom wall and the upper wall of the BFS model, respectively. A thermo-sensitive liquid crystal sheet was adopted to measure the distributions of the local heat transfer coefficient on the bottom wall or upper wall downstream of the step. Since the heat transfer measurement method of the upper wall is the same as that of the bottom wall surface, here, the bottom wall representing the upper wall is utilized to describe the heat transfer experiment procedure.

As shown in Fig. 3-3 (a), stainless steel foil was applied to the entire bottom wall for $31S$ length in the streamwise direction, the inner surface of the bottom plate was covered with thin stainless-steel foil strips of 47.2 mm wide, 470 mm long, and 20 μm thick, having 1 mm spanwise spacing with each other. These foil strips were connected electrically in series and were heated by passing an alternating current through them, a constant heat flux heating condition was established at the wall. Heat conduction loss toward the outside of the duct was neglected since its value was less than 0.3% of the total heat flux. The liquid crystal sheet of 75 μm thick was glued between the heater strips and the transparent bottom wall to monitor the local distributions of the bottom wall temperature [11]. The color distribution of a thermo-sensitive liquid crystal sheet (*RW*20-25 manufactured by Nippon Capsule Products Co., Ltd.) attached to the bottom wall surface of the stainless-steel foil was photographed by a CMOS camera (Nikon D7000) through a transparent acrylic bottom wall. As shown in Fig. 3-4, the relative luminance values of *R, G, B* colors were obtained from the acquired images, and the local wall temperature was obtained using SVR (Support Vector Regression) and MLP (Multilayer Perceptron) method [16] which will be illustrated in detail in the later section.

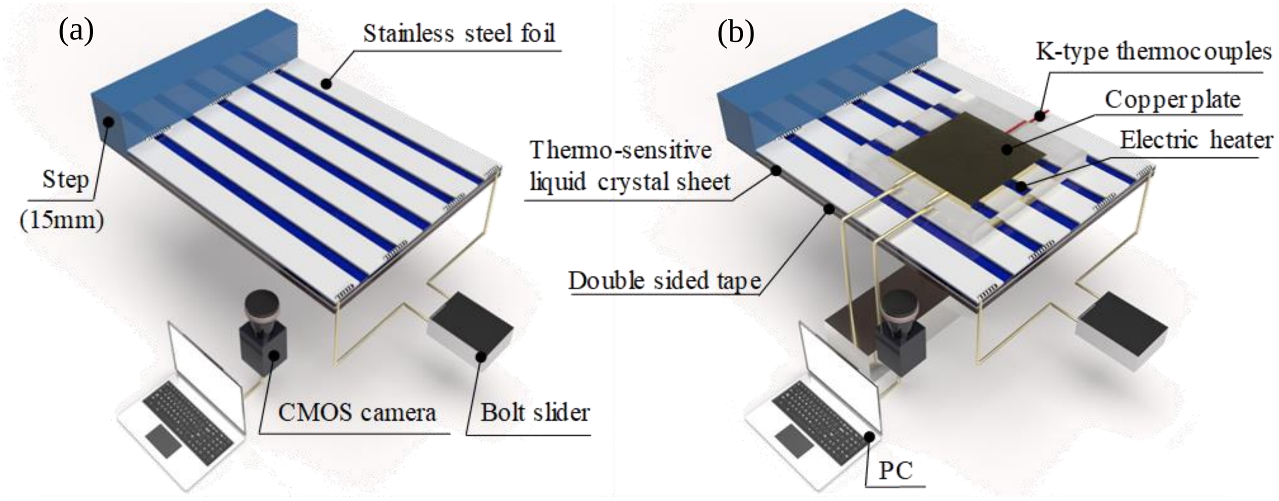

Fig. 3-3. Illustration of the heat transfer experiment (a) and calibration experiment (b).

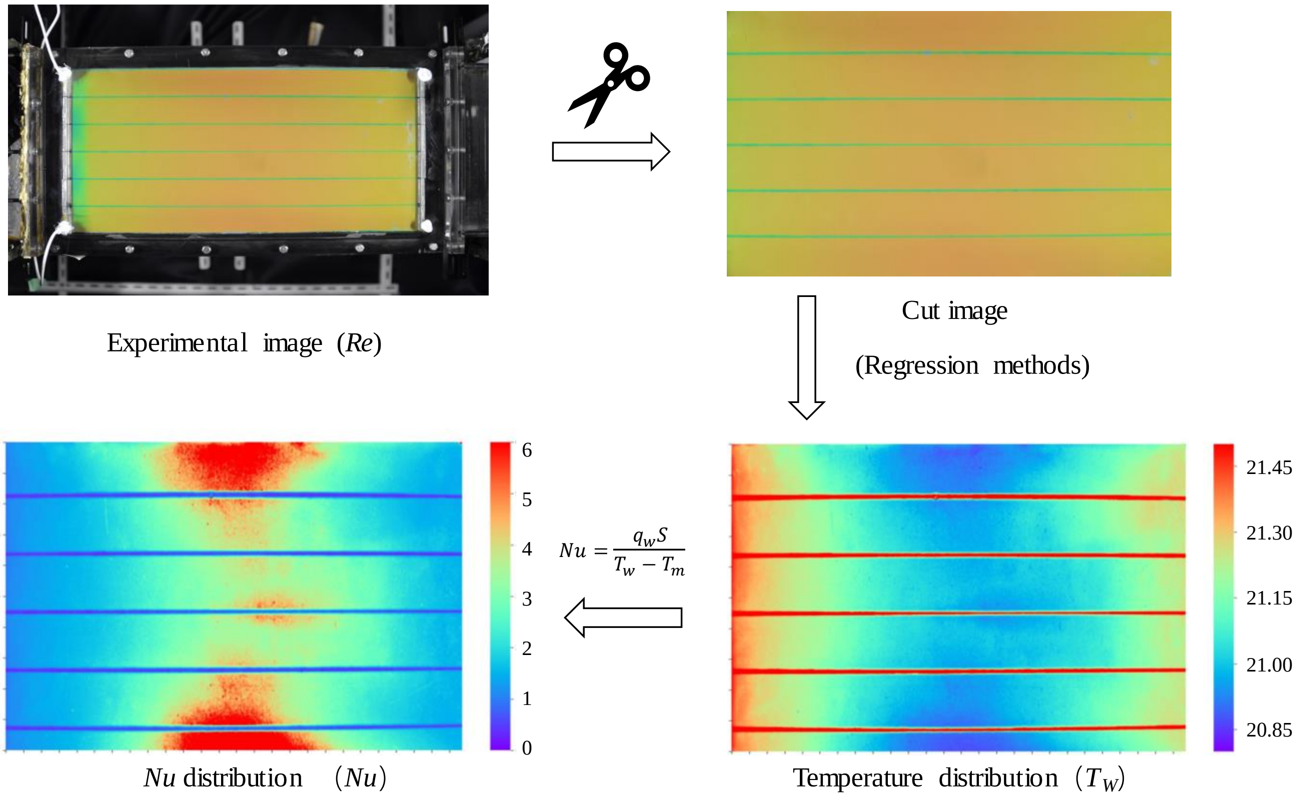

Fig. 3-4. Measurement of the heat transfer coefficient.

3.2.2.2 Calibration experiment

Calibration experiments were done before and after each heat transfer experiment to accurately associate the color information of the thermo-sensitive liquid crystal with the temperature. A calibration plate as shown in Fig. 3-3 (b) was used for calibration. The calibration plate is a copper plate ③ with a thickness of 100 mm × 100 mm and a thickness of 10 mm, and a rubber heater ④ is installed on the backside. In addition, to prevent external heat loss, a heat insulating material ⑥ is attached around the copper plate. In the experimental method, the copper plate is brought into close contact with the test surface, and the rubber heater is energized to heat the copper plate to an isothermal temperature. The image of the liquid crystal sheet was taken with the CMOS camera ② The temperature measured by one K-type sheath thermocouple ⑦ embedded in the copper plate was defined as the temperature of the temperature-sensitive liquid crystal. In the calibration experiment, the temperature of the calibration plate was changed from 20 °C to 25 °C at 0.2 °C intervals to obtain an 8-bit luminance value on the liquid crystal surface (See Fig. 3-5). Since the *RGB* luminance value obtained in this experiment includes color light information, even slight non-uniformity such as lighting is reflected in the output data, Eq. (3-1) was used as the *r, g, b* standard value for each temperature from which only the color components were extracted.

$$r=R/X \quad g=G/X \quad b=B/X \qquad X=R+G+B \tag{3-1}$$

The *r, g, b* luminance values for each temperature obtained in this experiment are shown in Figure 3-6.

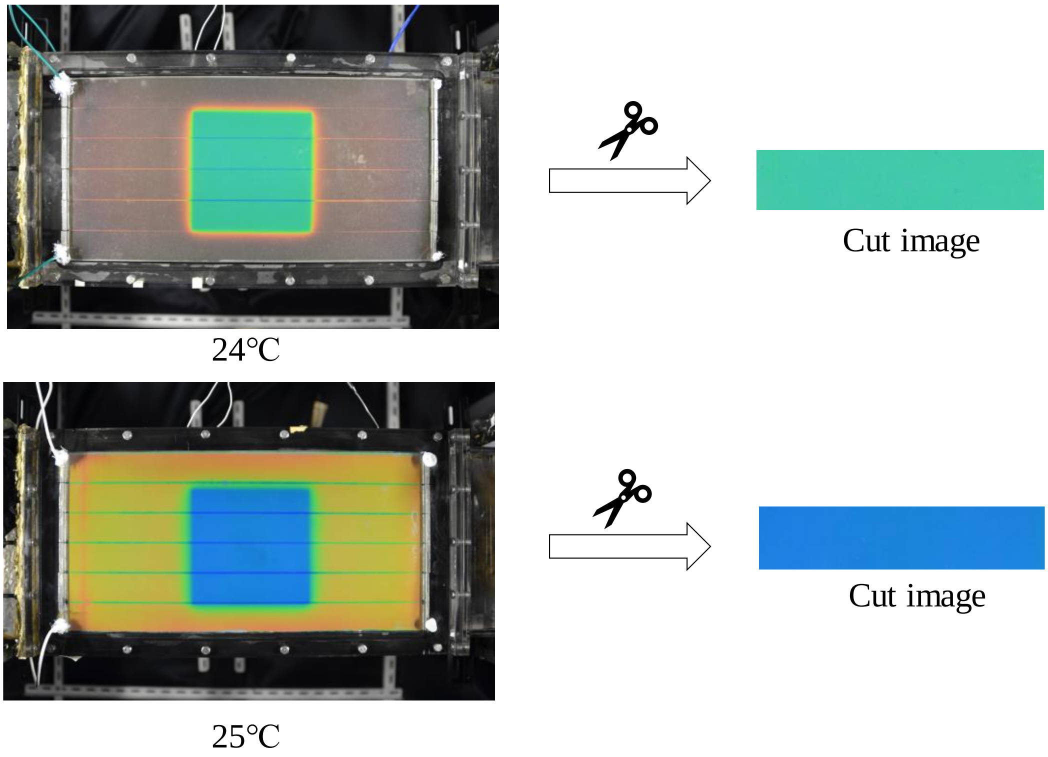

Fig. 3-5. Illustration of a calibration experiment.

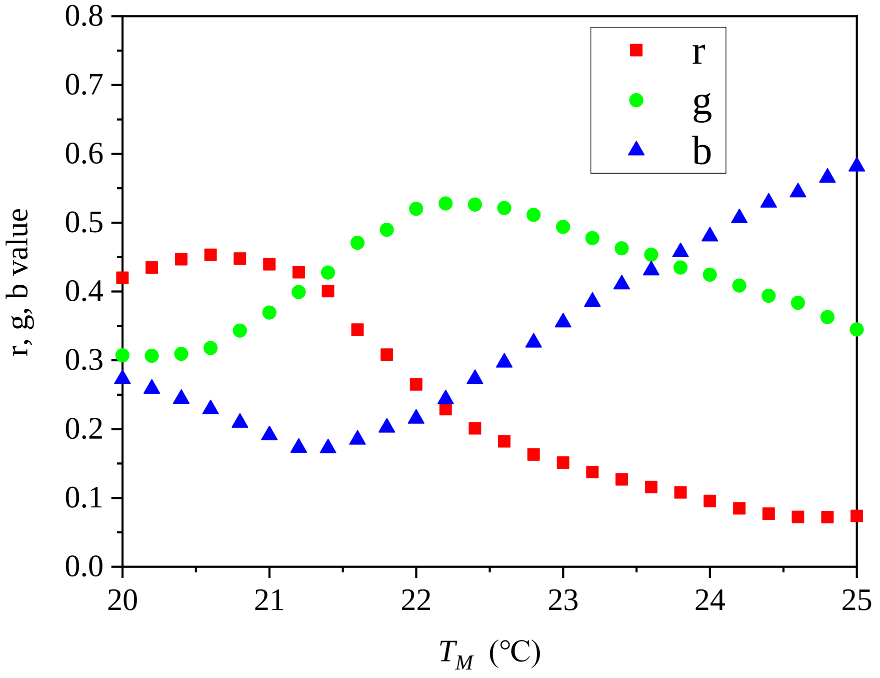

Fig. 3-6. Relationship between *r*, *g*, *b* value and temperature T_M.

3.2.2.3 Investigations of different regression methods for this experimental model

Various regression methods such as Multilayer Perceptron (MLP), Light Gradient Boosting Machine (Light GBM), Convolutional Neural Network (CNN), and Support Vector Regression (SVR) were tentatively tried to build the relationship between the color information of the thermo-sensitive liquid crystal sheet and temperature value.

Among the methods mentioned above, two methods called SVR and MLP will be briefly introduced per the comprehensive consideration for the number of samples, calculation accuracy, calculation cost, the difficulty of code construction. The main idea of SVR (Support Vector Regression) [17-21] is to minimize error, individualizing the hyperplane which maximizes the margin, and part of the error is tolerated [22]. SVR methods can be divided into linear SVR and non-linear SVR corresponding to Fig. 3-7 and Fig. 3-8. ξ and ξ^* are the slack variables in SVR, N means the number of samples, C is the regularization constant. w is the normal vector to the hyperplane. This is much like Hesse normal form, except that w is not necessarily a unit vector. For non-linear SVR, as illustrated in Fig. 3-8, the kernel functions transform the data into a higher dimensional feature space to make it possible to perform the linear separation [22]. In the calibration experimental case, *RGB* values are independent variables and corresponding temperatures are dependent variables. *RGB* (red, green, and blue) refers to a system for representing the colors to be used on a computer display. Red, green, and blue can be combined in various proportions to obtain any color in the visible spectrum. Levels of *R*, *G*, and *B* can each range from 0 to 100 percent of full intensity. Each level is represented by the range of decimal numbers from 0 to 255 (256 levels for each color). The total number of available colors is 256*256*256, or 16,777,216 possible colors.

For building the relationship between these two kinds of variables, various tuned parameters such as kernel function including 'linear', 'rbf', 'poly', 'sigmoid' methods, 'gamma' which implicitly determines the distribution of data after mapping to the new feature space, penalty parameter 'c' which is the tolerance of error and so on were adopted. The grid search provided by GridSearchCV (Python 3.6.8) exhaustively generates candidates from a grid of parameter values mentioned above. All the possible combinations of parameter values are evaluated and the best combination is retained. The maximum and average temperature differences between the measured temperature by a thermocouple and the predictive value by the SVR method were 0.053 °C and 0.0014°C which are much smaller than the measurement accuracy of the thermocouple.

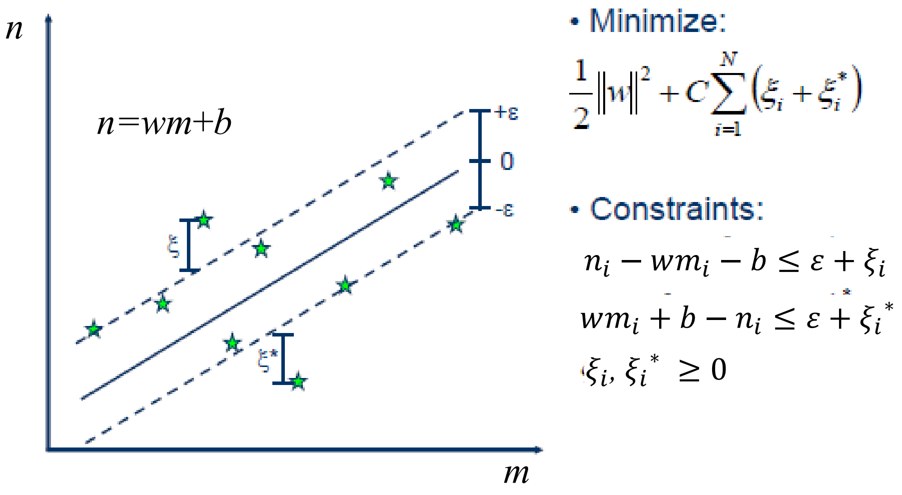

Fig. 3-7. Illustration of linear SVR method.

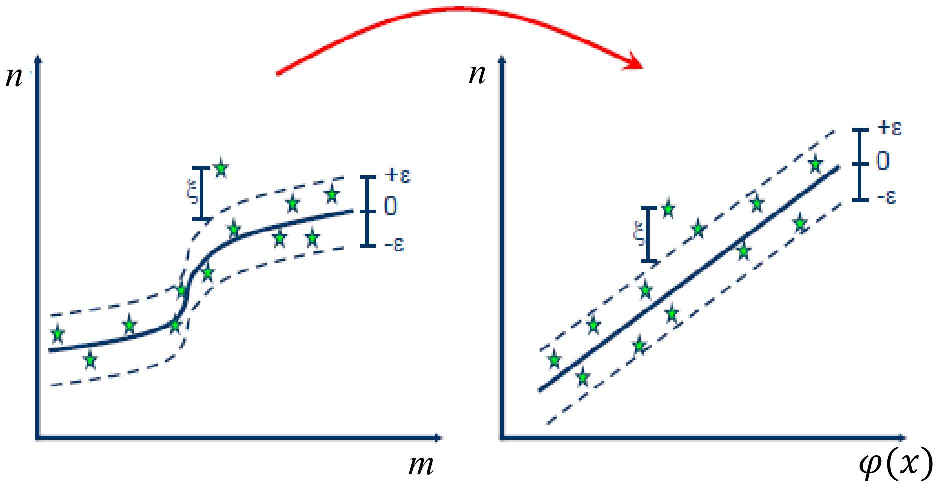

Fig. 3-8. Schematic diagram of transformation from non-linear SVR to linear SVR using a Kernel function.

An MLP [23, 24] (or Artificial Neural Network-ANN [25-27]) with double hidden layers was adopted and can be represented graphically as follows:

Formally, a one-hidden-layer MLP is a function $f: R^D \rightarrow R^L$, where D is the size of input vector m and L is the size of the output vector $f(m)$, such that, in matrix notation:

$$f(m)=G(b^{(2)}+W^{(2)}(s(b^{(1)}+W^{(1)}m))) \tag{3-2}$$

with bias vectors $b^{(1)}$, $b^{(2)}$; weight matrices $W^{(1)}$, $W^{(2)}$ and activation functions G and S.

The vector $h(m) = \Phi(m) = s((b^{(1)} + W^{(1)}(m))$ constitutes the hidden layer. $W^{(1)} \in R^{D \times D_h}$ is the weight matrix connecting the input vector to the hidden layer. Each column $W_i^{(1)}$ represents the weights from the input units to the i-th hidden unit. Typical Kernal functions for s include tanh, with $\tanh(a) = (e^a - e^{-a})/(e^a + e^{-a})$, or the logistic sigmoid function, with $\mathrm{sigmoid}(a) = 1/(1 + e^{-a})$. In the case of *RGB*-temperature case, kernel function "tanh" was adopted because of its high precision for this case. The output vector is then obtained as $o(m) = G(b^{(2)} + W^{(2)}h(m))$.

Figure 3-9 shows the structure of the neural network (MLP) used to calculate the temperature *Tw* from the *r, g, b* standard value which is obtained by the above equation as an input layer and outputs it via a hidden layer. Here, the white circles in the hidden layer and the output layer are neurons, and the red circles, green circles, and blue circles in the input layer indicate the *rgb* standard value data of the input layer, respectively.

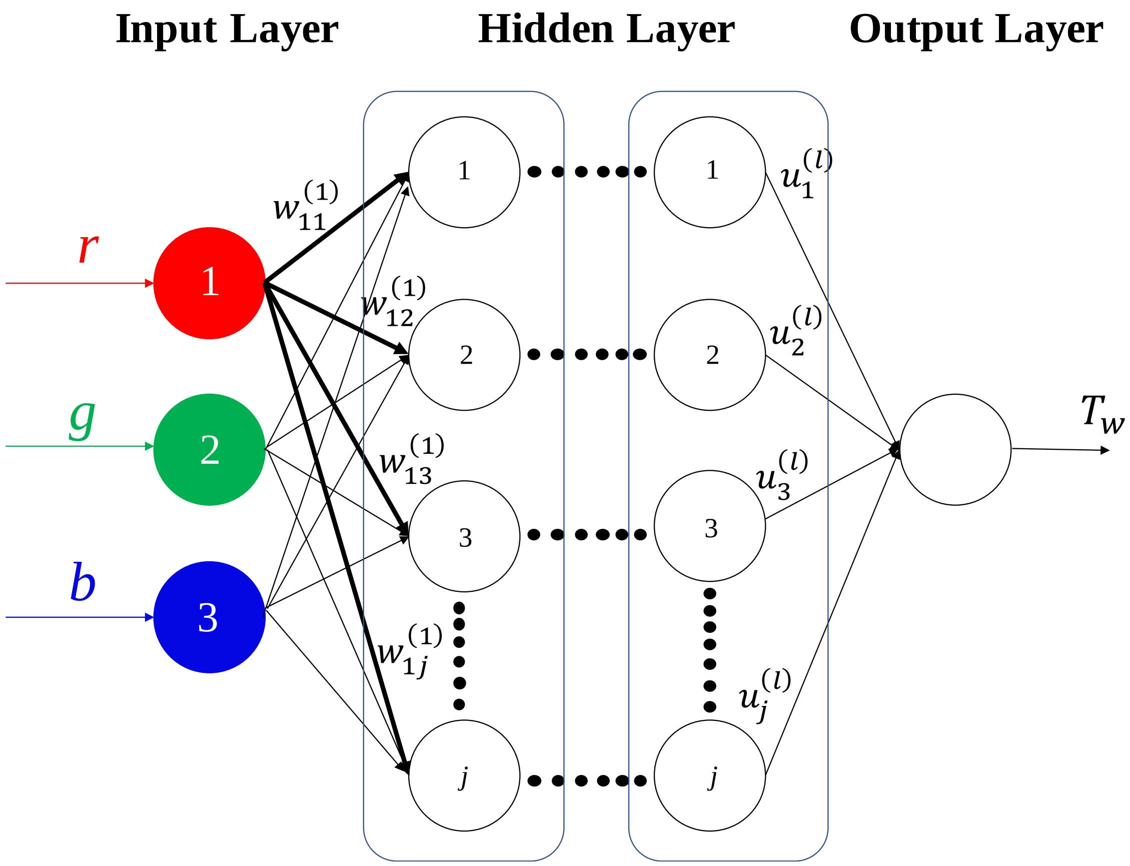

Fig. 3-9. Illustration of the MLP structure.

In the multilayer perceptron, the weights are updated using the stochastic gradient descent method.

$$w_{ji,t+1}^{(l+1)} = w_{ji,t}^{(l)} - \epsilon \frac{\partial E_n}{\partial w_{ji,t}^{(l)}} \tag{3-3}$$

where $w_{ji,t+1}^{(l+1)}$ is the weight from the i_{th} unit in the (l-1) layer to the j_{th} unit in the l_{th} layer, $w_{ji,t}^{(l)}$ is the weight from the i_{th} unit of the l_{th} layer to the j_{th} unit of the $(l + 1)_{th}$ layer, the learning rate is ϵ, and when En called the square error is higher than the set threshold, backpropagation will be carried out, $\frac{\partial E_n}{\partial w_{ji,t}^{(l)}}$ will be calculated [27].

The activation function sigmoid function [28] is $g(x) = \frac{1}{1+\exp(-x)}$ Partial differentiation of the squared error E_n with respect to the output layer weights $w_{ji,t}^{(l)}$ can be expressed as:

$$\frac{\partial E_n}{\partial w_{ji,t}^{(l)}} = \frac{\partial}{\partial w_{ji}^{(l)}} \frac{1}{2} (t_j - g(u_j^{(l)}))^2 \tag{3-4}$$

$$\frac{\partial E_n}{\partial w_{ji,t}^{(l)}} = \left(g\left(u_j^{(l)}\right) - t_j\right) g\left(u_j^{(l)}\right) \left(1 - g\left(u_j^{(l)}\right)\right) g\left(u_i^{(l-1)}\right) \tag{3-5}$$

In addition, the weight of the hidden layer is obtained by partially differentiating the square error En with the weight $w_{ji}^{(l)}$ of the hidden layer.

$$\frac{\partial E_n}{\partial w_{ji}^{(l)}} = \frac{\partial E_n}{\partial u_j^{(l)}} \frac{\partial u_j^{(l)}}{\partial w_{ji}^{(l)}} = \delta_j^{(l)} \frac{\partial u_j^{(l)}}{\partial w_{ji}^{(l)}} \tag{3-6}$$

Therefore,

$$\frac{\partial E_n}{\partial w_{ji}^{(l)}} = \left(\sum_k \delta_k^{(l+1)} w_{kj}^{(l+1)}\right) g\left(u_j^{(l)}\right) \left(1 - g\left(u_j^{(l)}\right)\right) g\left(u_i^{(l-1)}\right) \tag{3-7}$$

When updating the weight of the hidden layer l, $\delta_k^{(l+1)}$ of the next layer (l+1) is required, and δ in the output layer is obtained from the difference between the output value and the teacher data. This was propagated from the output layer to the input layer, and the weight of the intermediate layer was changed so that the square error was reduced. Here, n is the number of data sets of *rgb* value and temperature T_M was shown above. In this study, learning was performed in the range of 20 °C to 25 °C, and the stochastic gradient descent method was used for learning.

The most suitable combination of the number of hidden layers and the number of neurons was explored in the previous research by control variates method, that is, firstly the number of hidden layers was controlled to be the empirical value of 3, the number of neurons was changed from 0 to 1000 in each layer. The RMS (Root Mean Square) value between the predictive temperature T_p and calibration temperature T_c was the smallest (0.031) when the number of neurons is 15 (See Fig. 3-10 (a)), here, the RMS is defined as eq. (3-8).

$$\mathrm{RMS} = \sqrt{\sum(T_p - T_c)^2} \tag{3-8}$$

then the number of neurons in each layer was fixed and the number of hidden layers was changed, the minimum value of RMS (0.0037) appears when the number of layers is 5 (see Fig. 3-10 (b)). Finally, the neural network structure represented graphically in Fig. 3-11 was confirmed.

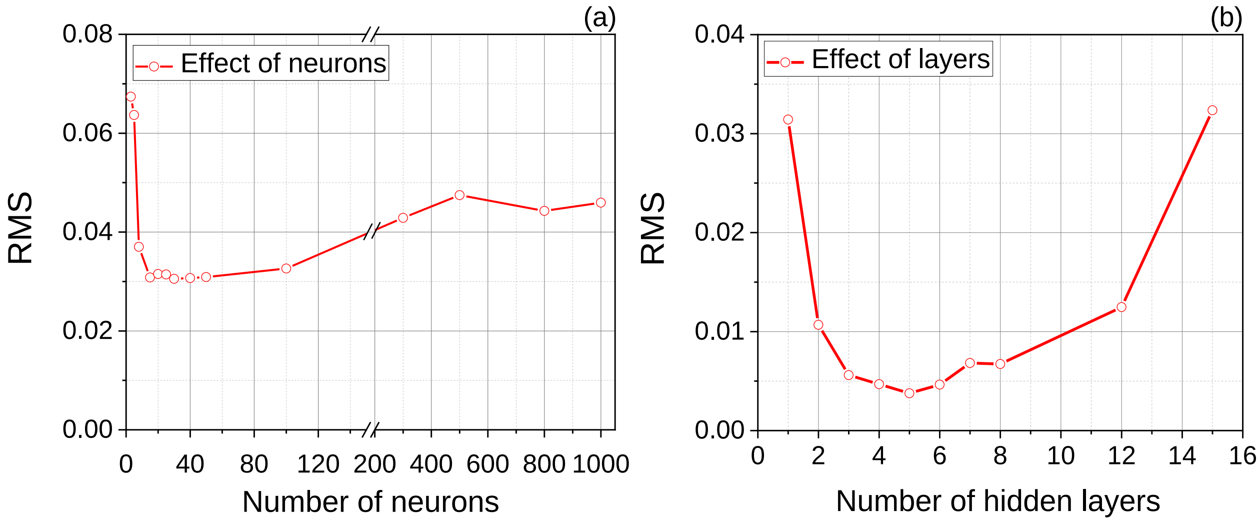

Fig. 3-10. Investigation of the most suitable number of neurons and layers.

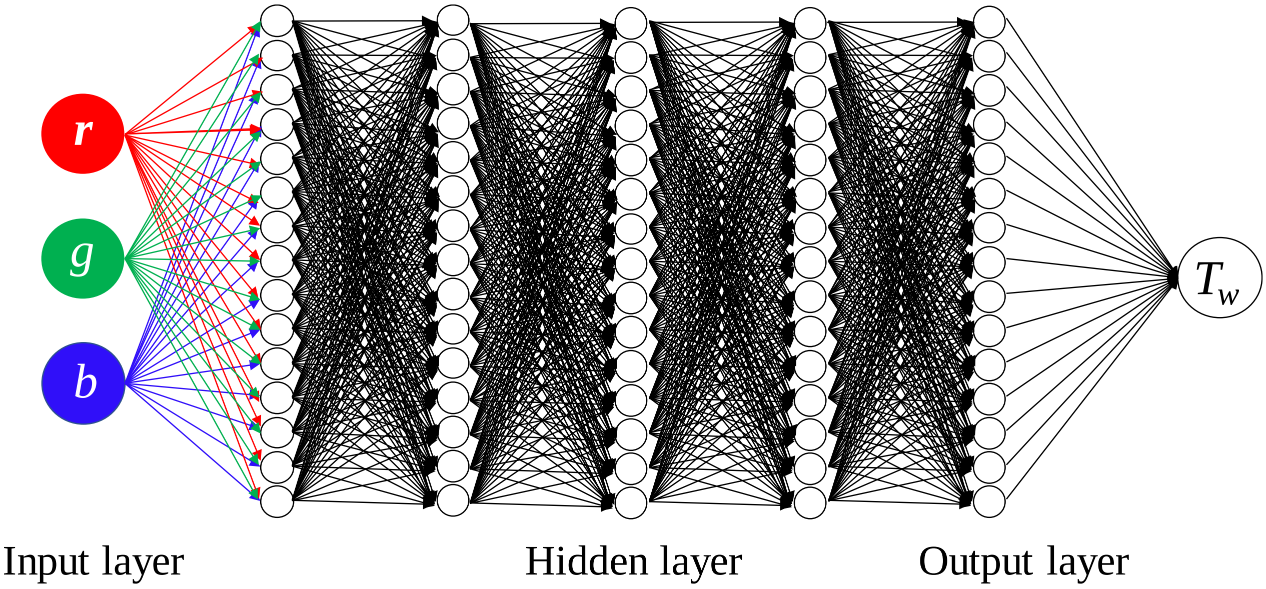

Fig. 3-11. MLP structure.

In general, the size of the training and testing set was arranged into 10% testing and 90% training. The training set includes the *r, g, b* value under the corresponding temperature from 20.0 to 25.0 °C with 0.2 °C interval except for 20.0, 22.0, 24.0°C which were put into the testing set as shown in Fig. 3-12 (a) and Fig. 3-12 (b). Comparing the average relative error of ten calculation results of SVR (0.14%) and MLP (0.031%), MLP was finally chosen as the regression model. The result of the relationship between calibration value and predictive value is shown in Fig. 3-12 (c), which indicates the reliability of the MLP method for this *rgb*-temperature conversion model.

In addition, the theoretical value and empirical formula [29] of the local heat transfer coefficient of the bottom wall surface near the center of the flow path in the parallel plate flow were obtained. When the laminar flow in the circular tube is heated by constant heat flux heating and the flow is fully developed at the starting point, the empirical heat transfer coefficient in the flow direction was calculated in Eq. (3-9) [29].

$$Nu_t(l) = 5.364\left\{1 + (220l^+/\pi)^{-10/9}\right\}^{3/10} - 1.0 \tag{3-9}$$

$$l^+ = \frac{l/d}{Re \cdot Pr} \tag{3-10}$$

where *l* is the distance from the heating start point, *d* is the equivalent diameter, *Pr* is the Prandtl number.

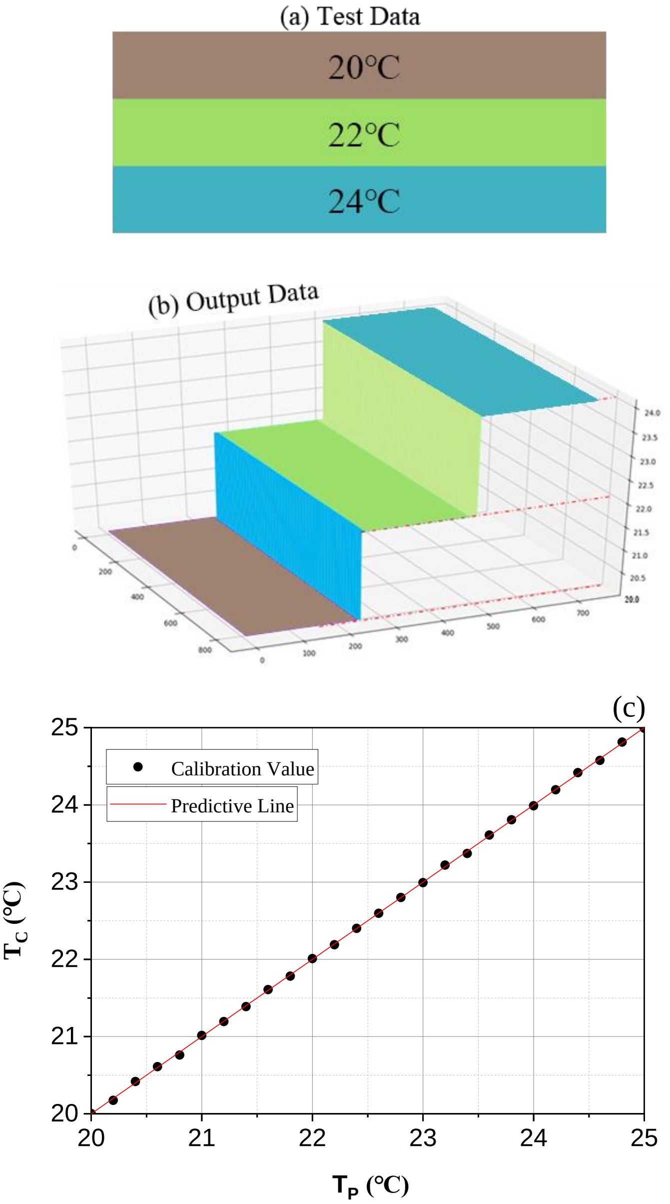

Fig. 3-12. Result of calibration test of thermo-sensitive liquid crystal method.

Since the flow path in this experiment is a rectangular flow path, the equivalent diameter *d* that can be obtained by using the flow path cross-sectional area *B* (240·15 mm^2) and the wetted perimeter *L* (2·(240+15) mm) through the following equation:

$$d=\frac{4\cdot B}{L} \tag{3-11}$$

Regarding the parameters of this experiment, the local heat transfer coefficient $h(l)$ at the position *l* in the flow direction from the duct inlet could be expressed as:

$$h(l) = q_w/[T_w(l) - T_m(l)] \tag{3-12}$$

where Tw (*l*) is the temperature on the bottom wall, T_m (*l*) is the bulk temperature, q_w is the constant heat flux on the bottom wall. Eq. (3-13) is the definition of T_m (*l*):

$$T_m(l) = T_0 + \dot{Q}/(c_p\dot{m}) \tag{3-13}$$

Where T_0 is the fluid temperature at the inlet, $\dot{Q}$ is the heat transfer rate on the bottom wall, c_p is the specific heat at constant pressure and $\dot{m}$ is the mass flow rate.

Therefore, to unify the unit and compare with the theoretical value in this section, the experimental value of the local Nusselt number is defined by Eqs. (3-14) as follows:

$$Nu_e(l) = \frac{h(l)\cdot d}{\lambda} \tag{3-14}$$

The buoyancy could be ignored under Ri=0.03 within the experimental Reynolds number range, the modified Richardson number $Ri*$ was used to investigate the effect of buoyancy (Eq. (3-15)).

$$Ri*=\frac{\mathrm{Gr}^*}{Re^2} \tag{3-15}$$

where the modified Grashof number Gr^* is defined as Eq. (3-16):

$$Gr*=\frac{g\beta qS^4}{\mu^2\lambda} \tag{3-16}$$

where g is gravitational acceleration, β is the volume expansion coefficient.

To verify the precision of the MLP method and reliability of the liquid crystal method, validation experiments were done in advance in the normal parallel flow shown in Fig. 3-13 (a), and the *Nu* distribution along the center line on the bottom wall was compared with the theoretical value, the relative error was 4.8%. Then the heat transfer experiments were done on the bottom wall and upper wall respectively (See Fig. 3-13(b), and Fig. 3-13(c)).

The validity of the heat transfer coefficient distribution measurement of the BFS flow should be evaluated. For this, the local heat transfer coefficient of the wall surface of the parallel plate flow was calculated, and the obtained experimental value was compared with the theoretical value [30]. The measurement accuracy of the local heat transfer coefficient was examined. As shown in Fig. 3-14, by comparison, it could be seen that the discrepancies between the experimental value and theoretical value are large on the upstream side. It is considered that the temperature difference between the mainstream temperature and the wall surface temperature was large on the upstream side where heat transfer is actively performed, and the error in calculating the local wall surface temperature is greatly affected. However, except for these regions, for the downstream after $x/S = 3.3$, the experimental Nusselt number value along the bottom center line of the parallel flow has great correspondence with the theoretical value. The relative error after $x/S=3.3$ was 2.7%, which indicates the correctness of the MLP method and reliability of the experimental condition.

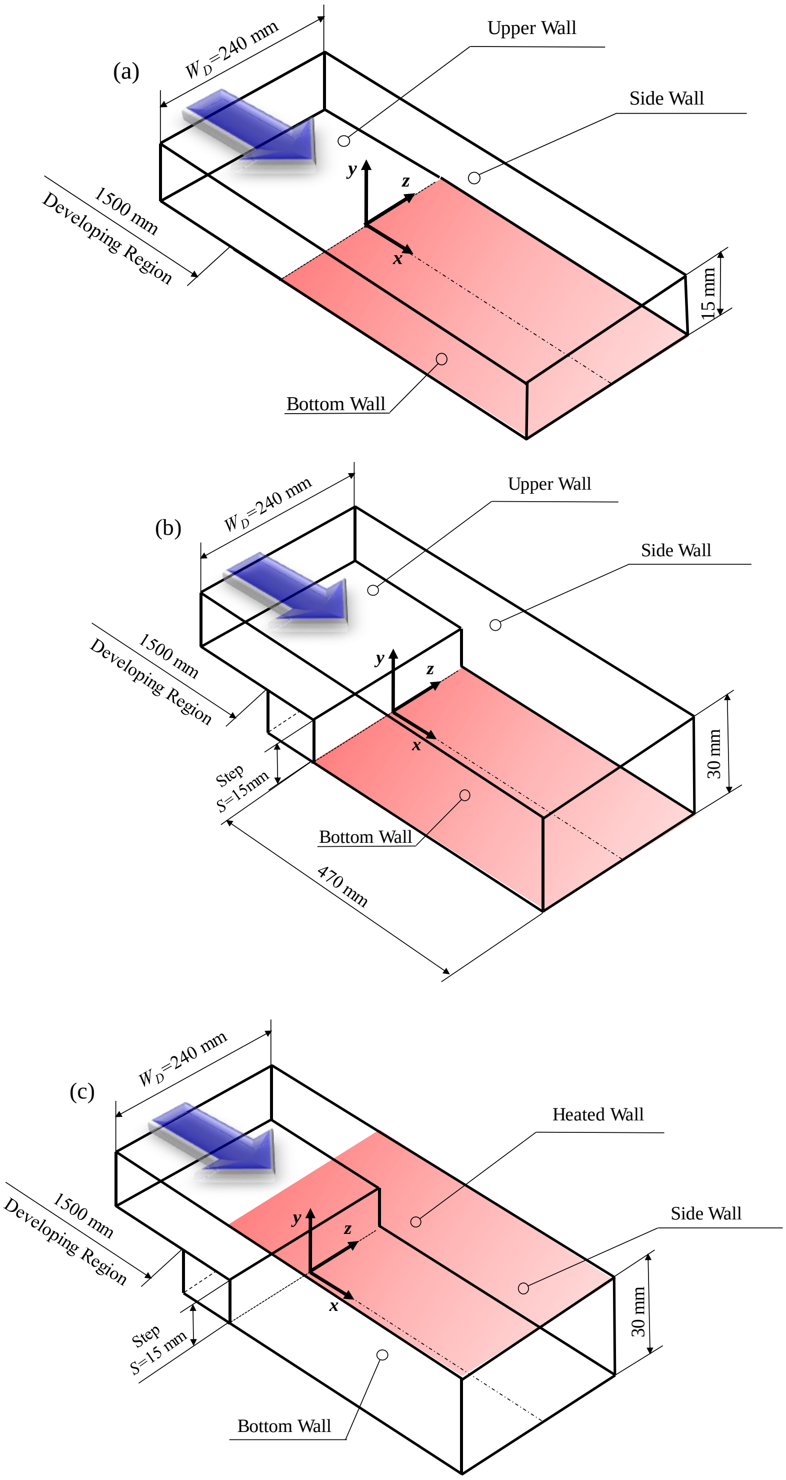

Fig. 3-13. Heat transfer measurement setup. (a) Bottom wall heated for parallel plated flow case; (b) Bottom wall heated for stepped flow case; (c) Upper wall heated for stepped flow case.

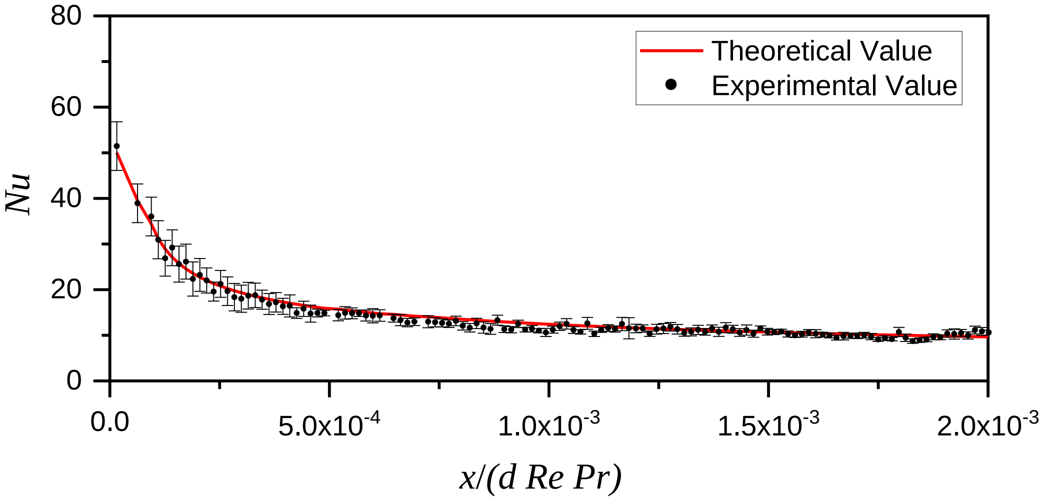

Fig. 3-14. Streamwise distribution of *Nu* along the center line of the parallel-plate channel.

3.3 Results and discussions

3.3.1 Distributions of heat transfer coefficient on the bottom wall

Figures 3-15 (a)–(f) show the distribution of the local *Nu* on the bottom wall for the representative Reynolds numbers (400, 500, 600, 700, 800, 900), *x*-coordinate represents the flow direction and *z*-coordinate represents the spanwise direction. z/W_D=0 represents the duct center and z/W_D=±0.5 represents the side wall. As is mentioned in the previous section, the stainless-steel foil strips have 1mm spanwise spacing with each other, in order to make the Nusselt number in the spanwise direction look more continuous, at the same time, make sure the focused region and the corresponding tendency are not destroyed. The interpolation method was applied to remove these spacings. According to the data on both sides of the spacing, the spacing was filled with the data after interpolation.

For all cases, a large heat transfer deterioration area is generated just behind the step, and increases along the streamwise direction then decreases after the peak value. The most noticeable point is that, the maximum *Nu* value appears near the side wall. In the low Reynolds number range, the heat transfer distribution is similar to that in the research of Iwai et al. [5], and Nie et al. [31]. The contour is integrated with reattachment points extracted by PIV experiments. As mentioned in Chapter 2, the reattachment point is a collection of a series of points along the spanwise direction where the streamwise velocity changes from negative to positive [15], which is used to delineate the recirculation zone along the spanwise direction. For all cases, a large heat transfer deterioration area is generated just behind the step and before the reattachment position, and increases along the streamwise direction then decreases after the peak value. As shown in Fig. 3-15, two horizontal lines include H_1 line at z/W_D=0.0 and H_2 line passing through the Nu_{max} position near the side wall, one vertical line called V line were superimposed in the contour to extract the Nu along these lines for investigating the variation of Nu along with some certain positions.

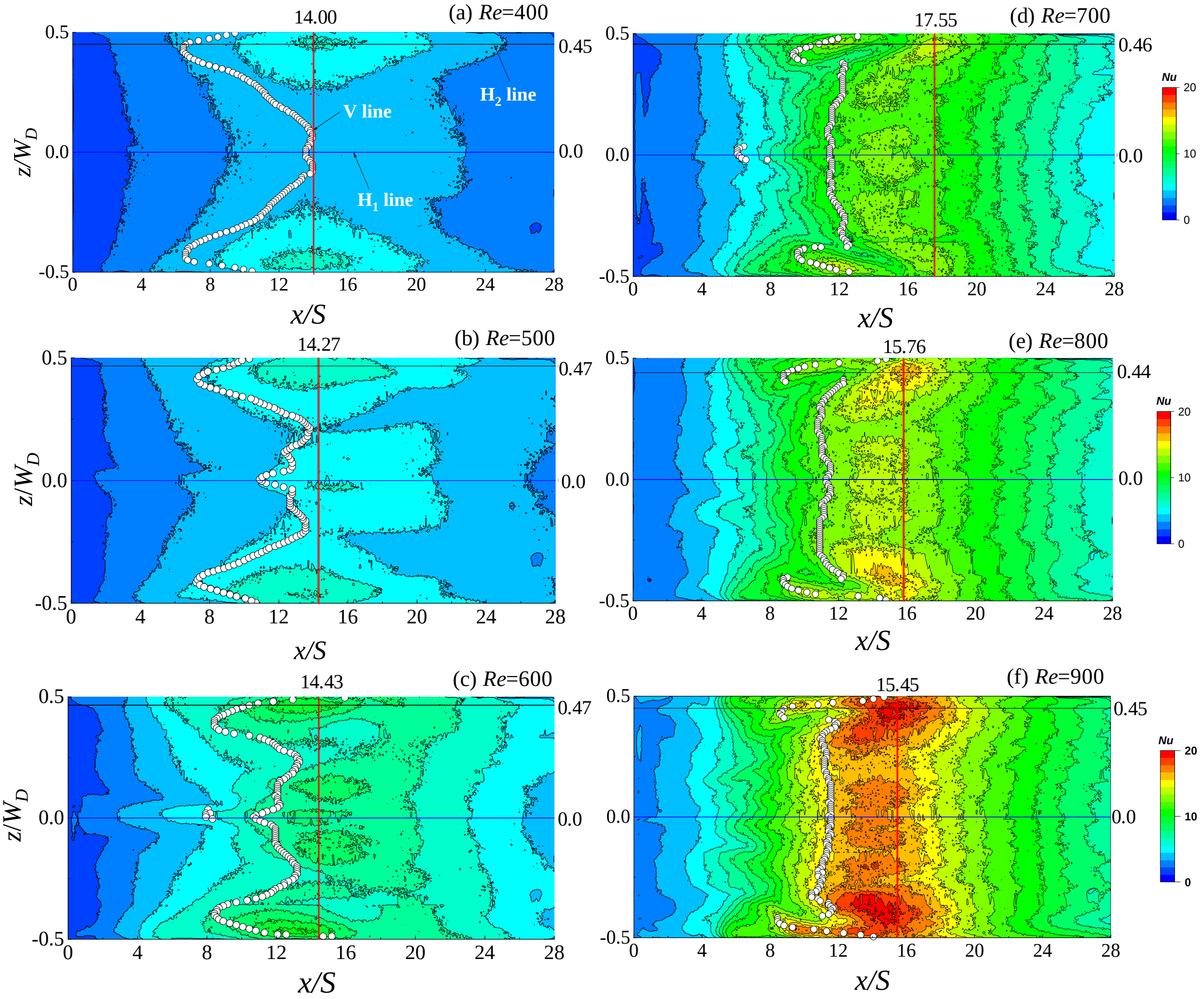

Fig. 3-15. Nusselt number distribution on the bottom wall for various Reynolds number range.

In the spanwise direction, the *Nu* distribution along the V line for the same Reynolds number cases as Fig. 3-15 were superimposed in Fig. 3-16, the *Nu* increases with the increase of Reynolds number. In any *Re* cases, Nusselt number peaks show near the side wall, and the ratio to the center value in *Re*=400 is about 1.46 and it is about 1.16 in *Re*=400. The Nusselt number variation range in the spanwise direction for all cases is obvious. Judging only by the value at the center of the flow path based on the assumption of 2D flow, it can be seen that there is a risk of underestimating the Nusselt number. The corresponding spanwise position of the Nusselt number peak near the side wall moves toward the duct center as the increase of Reynolds number.

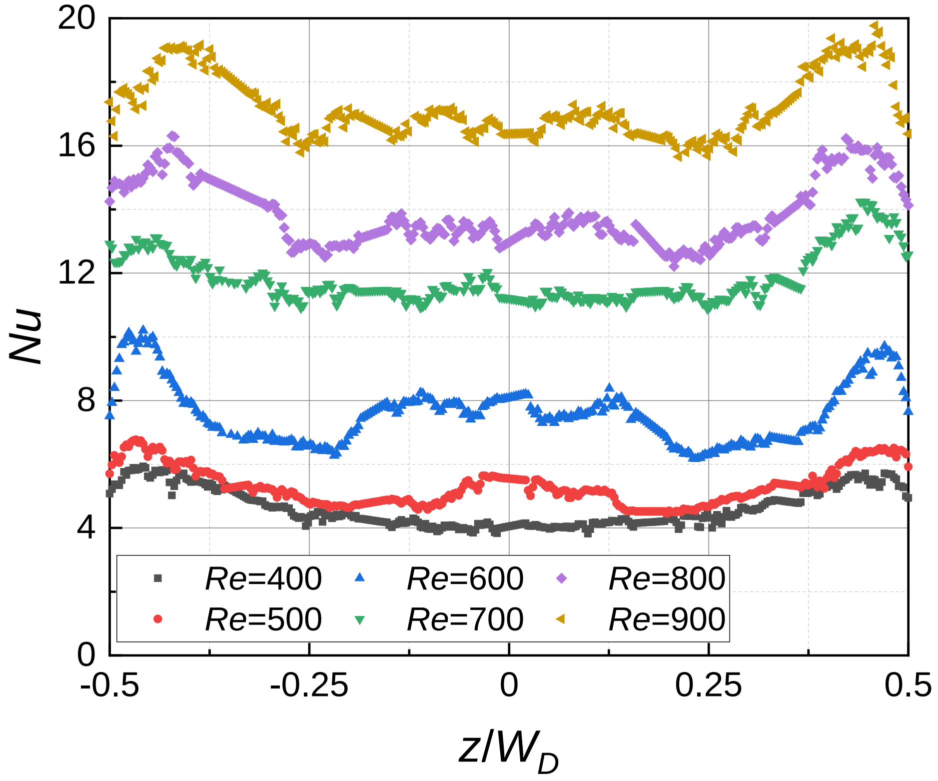

Fig. 3-16. *Nu* distribution along the V line passing through the $Nu_{\max}$ position near the side wall.

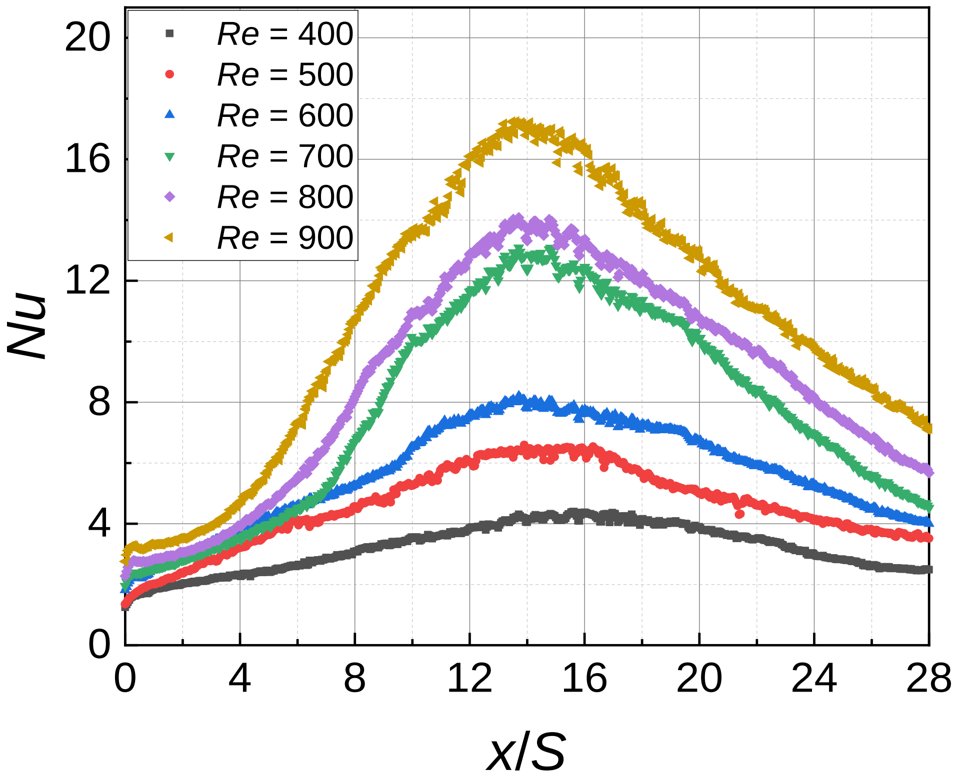

Fig. 3-17. Streamwise distribution of *Nu* along the H_1 line.

The streamwise distribution of *Nu* along the center line (H_1 line) was extracted and shown in Fig. 3-17, the minimum *Nu* value appears immediately after the step, the *Nu* peak values are all located in the range x/S=12 to x/S=16. While a sharp increase of *Nu* could be seen from *Re*=600 to *Re*=700, similarly, the reattachment point distribution near the center line for *Re*=600 and *Re*=700 also shows a special status, that is, near the center line, lots of breakaway points appear upstream far away from the gathering area of reattachment points. The sudden change of the flow state may affect the heat transfer distribution in the central flow channel.

Near the side wall, shown in Fig. 3-18, the distribution of Nusselt number along the H_2 line becomes complicated, although the overall trend is still rising firstly and then failing. Two obvious peaks could be found from *Re*=700 to *Re*=900, the first peak is smaller than the second one along the streamwise direction. Correspondingly, in Fig. 3-15, the reattachment distribution also has a disconnection feature near the side wall from *Re*=700 to *Re*=900, which was mentioned in Chapter 2. The reasons why the disconnection phenomenon appears near the side wall, why two Nusselt number peaks appear near the side wall for *Re*=700-900, and why the heat transfer peak near the center of the duct is located slightly away from the right center line will be explained in the following section.

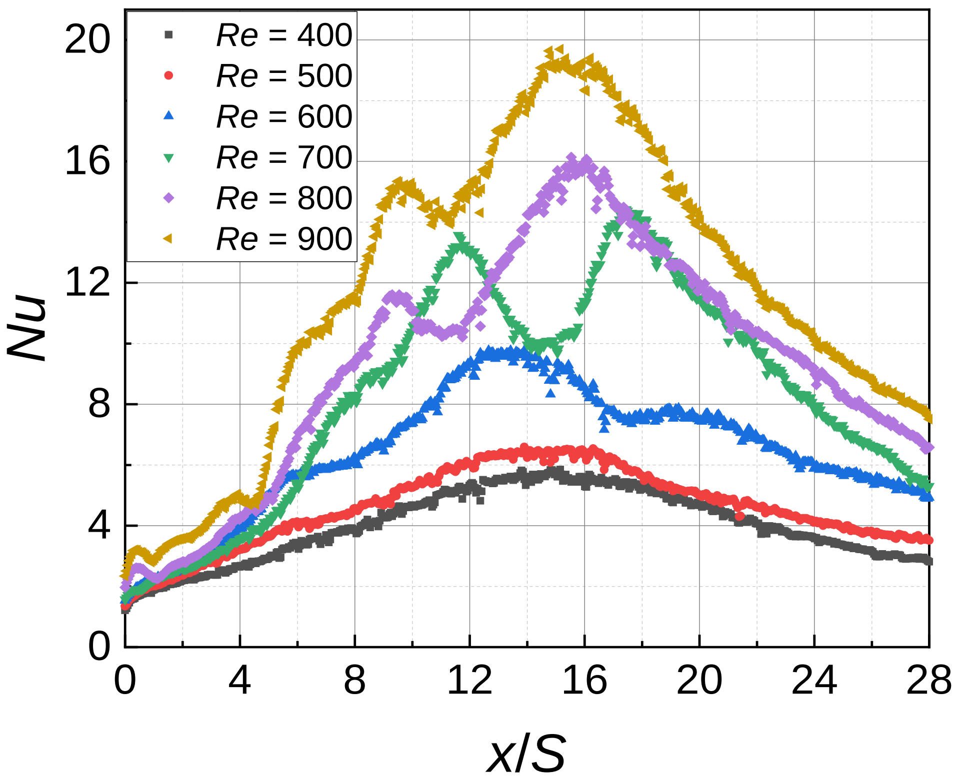

Fig. 3-18. *Nu* distribution along the H_2 line passing through the $Nu_{\max}$ position near the side wall.

Figure 3-19 shows the relationship between the spanwise direction position of the maximum Nusselt number and the Reynolds number. The vertical axis shows the spanwise direction and the horizontal axis shows the Reynolds number. From Fig. 3-19, it could be seen that all shown positions of the maximum Nusselt number are near the side wall. From Reynolds number 400 to 700, the $Nu_{\max}$ positions are located inside the region between the side wall and $z/W_D = 0.45$. However, since the Reynolds number increases over 700, it is located inside the region between $z/W_D = 0.3$ and $z/W_D = 0.4$, tending to shift slightly to the center side of the flow path. But overall, in any case, since the value of the maximum Nusselt number appears near the side wall, it is considered that the influence of the flow affected by the side wall appears.

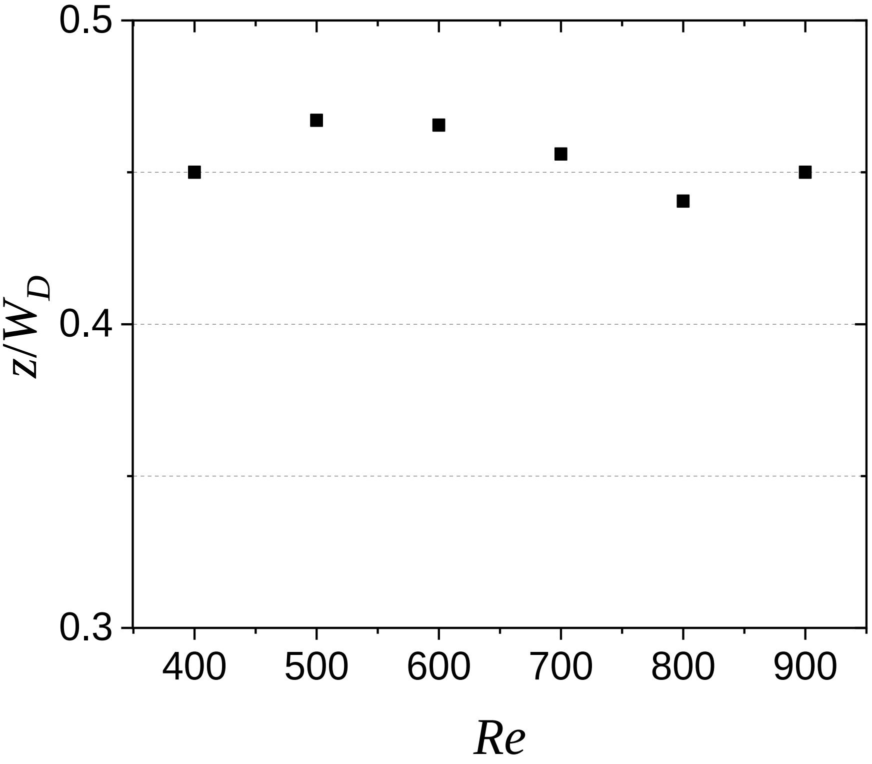

Fig. 3-19. Spanwise location of $Nu_{\max}$ for various Reynolds numbers.

In the streamwise direction, Fig. 3-20 shows the most upstream time-averaged reattachment position near the bottom wall surface ($y/S = 0.03$) adjacent to the side wall obtained from the velocity experiment, and the peak Nusselt number position near the side wall. The coordinate axes are the flow direction position on the vertical axis and the Reynolds number on the horizontal axis. An overview of the figure shows that the peak Nusselt number is located downstream of the reattachment position at any Reynolds numbers, which is consistent with the numerical analysis of Iwai et al [5] stating that for aspect ratios smaller than 24, the peak Nusselt number position is located downstream of reattachment. Furthermore, the tendency of $Nu_{\max}$ position corresponds greatly well with that of the most upstream reattachment position. Thus, this kind of reattached flow has some effects on the heat transfer enhancement. Similar numerical results could be found in the report of Nie et al. [32]. It was concluded that the "jet-like" flow is responsible for the minimum and for the maximum that develops near the side wall in the spanwise distributions of the primary reattachment length and of the Nusselt number, respectively. Whether the jet-like flow is the main reason for the heat transfer enhancement near the side wall needs to be further explored through experimental means, which will be explained in detail in Chapter 4.

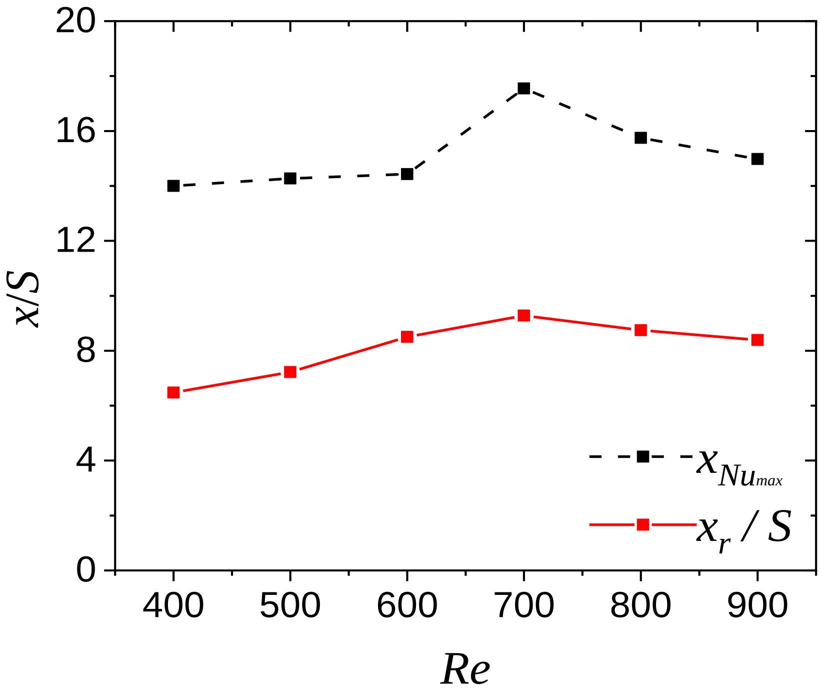

Fig. 3-20. Relationship of most upstream reattachment position near the side wall and streamwise $Nu_{\max}$ position. The red plot represents the most upstream reattachment position near the side wall; the black plot represents the streamwise $Nu_{\max}$ position.

3.3.2 Time-averaged velocity vectors and reattachment points near the bottom wall

In order to analyze heat transfer from the perspective of flow structure, the fluid flow pattern near the bottom wall (y/S=0.03) was confirmed, Fig. 3-21 illustrates the time-averaged velocity vectors corresponding to each representative case in Fig. 3-15 (a)-(f). Here, the reattachment point is superimposed on each figure. In Fig. 3-21 (a), at the low Reynolds number of 400, flow near the bottom wall seems to be almost stable. A flow downstream from the side wall toward the central part of the channel is apparent and seems to dominate the flow near the bottom wall (y/S=0.03). This fluid motion is produced by the downwash flow reported by Iwai et al. [5]. Large slow flow recirculation is observed, though the flow inside there is three dimensional. As the Reynolds number is increased, the flow near the central part of the duct begins to contain another type of reattachment flows. Owing to the large interaction between the flows from the side wall and the central part, a relatively large and unstable flow structure is generated near the central part of the duct and this produces the large variation of the reattachment position as shown in Fig. 3-21 (b)-(c). The flow structure inside the flow recirculation turns to be complicated. As the Reynolds number is further increased in Fig. 3-21 (d)-

(e), the unstable flow invades toward the side wall and seems to temporarily block the flow toward the downstream of the downwash flow.

The vectors around the disconnection area is like a hairpin illustrated in Fig. 3-22, the reverse fluid flowing toward the side wall and the fluid flowing toward the center of the flow channel meet and interact inside the region (x/S=7-11, z/W_D=0.25-0.4). The vectors here lift up and intertwined on a certain line, this is thought to be one of the causes of the discontinued reattachment point there. Due to the limited range (x/S=0-16) of the velocity measurement along the streamwise direction on the x-z plane, to understand the causes of the region with the largest Nusselt number, it is necessary to choose the representative Reynolds number in which the largest Nusselt number position is located inside the limited area (x/S=0-16) as the research object to conduct flow and heat transfer research. Thus, the eligible Re=900 was selected.

3.3.3 Relationship between local Nusselt number distribution and flow structure in the y-z plane for Re=900

Figure 3-23 shows the local Nusselt number with the time-averaged velocity vectors in the x-z plane near the bottom wall obtained by PIV. Each of the white plots drawn in this figure is the time-averaged reattachment point and obtained from this time-averaged velocity vector. And the blue plots will be described in detail later. At a glance, as can be imagined from Fig. 3-23, the flow field downstream the step should no longer be 2D but intensive 3D. Near the side wall, strong reverse flow toward the channel center is observed, which corresponds well to the relatively high heat transfer showing green contour color upstream the reattachment points. However, the heat transfer enhancement caused by this kind of strong reverse flow was not as high as that near the downstream side of the reattachment point near the side wall. Owing to this flow, the flow re-circulation region is distorted in the spanwise direction and the unique shape of the low-speed reverse flow area is produced in the region adjacent to the step. This slow reverse flow corresponds quite well to the heat transfer deterioration just behind the step. On the other hand, it is naturally confirmed that the reattachment points seem to divide the downstream flow and the reverse flow in the region where x/S=8-12, z/W_D=0-0.5. The reattachment point appears almost the same streamwise position along the spanwise direction from z/W_D=0 to z/W_D=0.375, but near the side wall, obvious three-dimensional characteristics appear. The apparent positive or negative values of the spanwise velocity components are observed just along the reattachment positions.

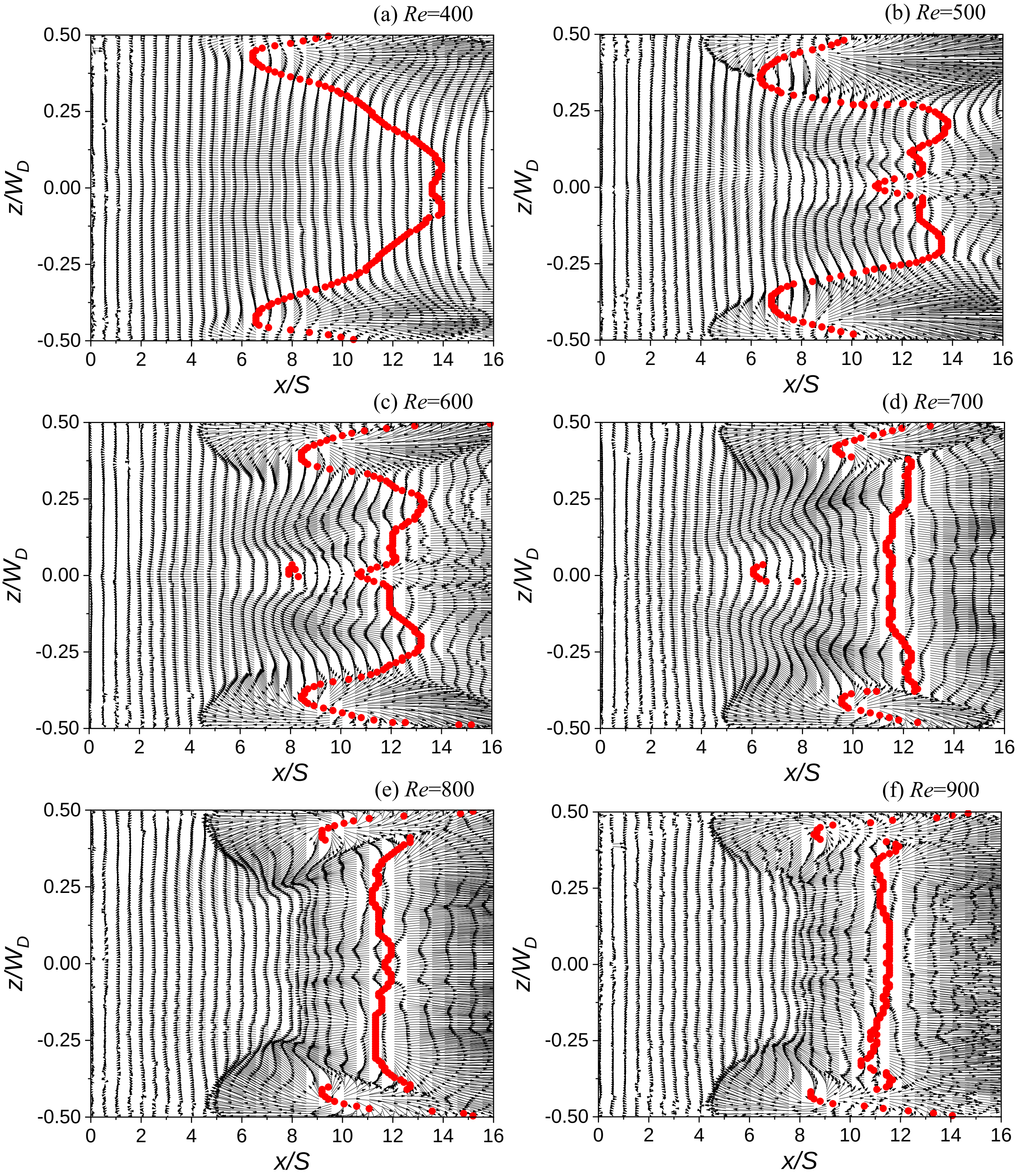

Fig. 3-21. Time-averaged velocity vector near the bottom wall superimposed with reattachment points.

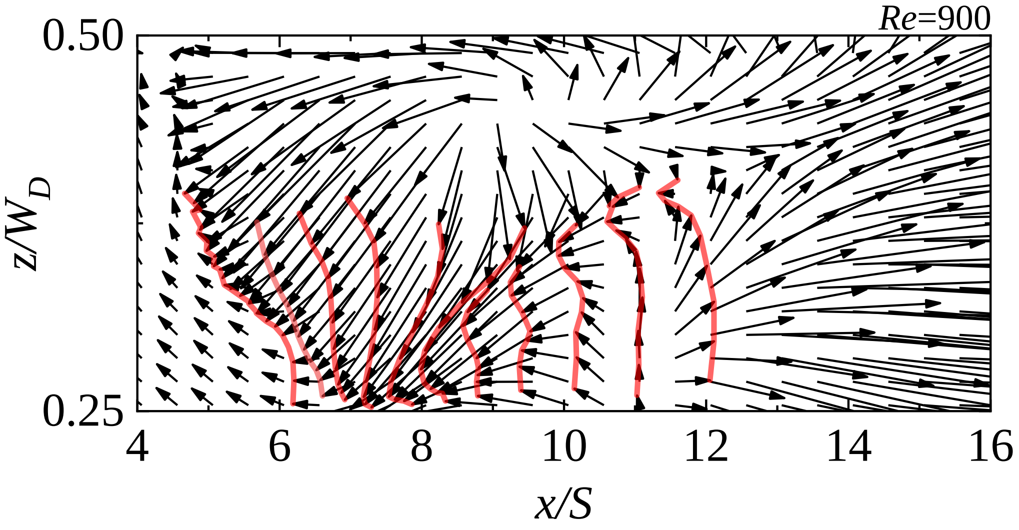

Fig. 3-22. Magnified view of the time-averaged velocity vector near the side wall for *Re*=900. The red curve is the connection curve of the head of the arrow near the side wall.

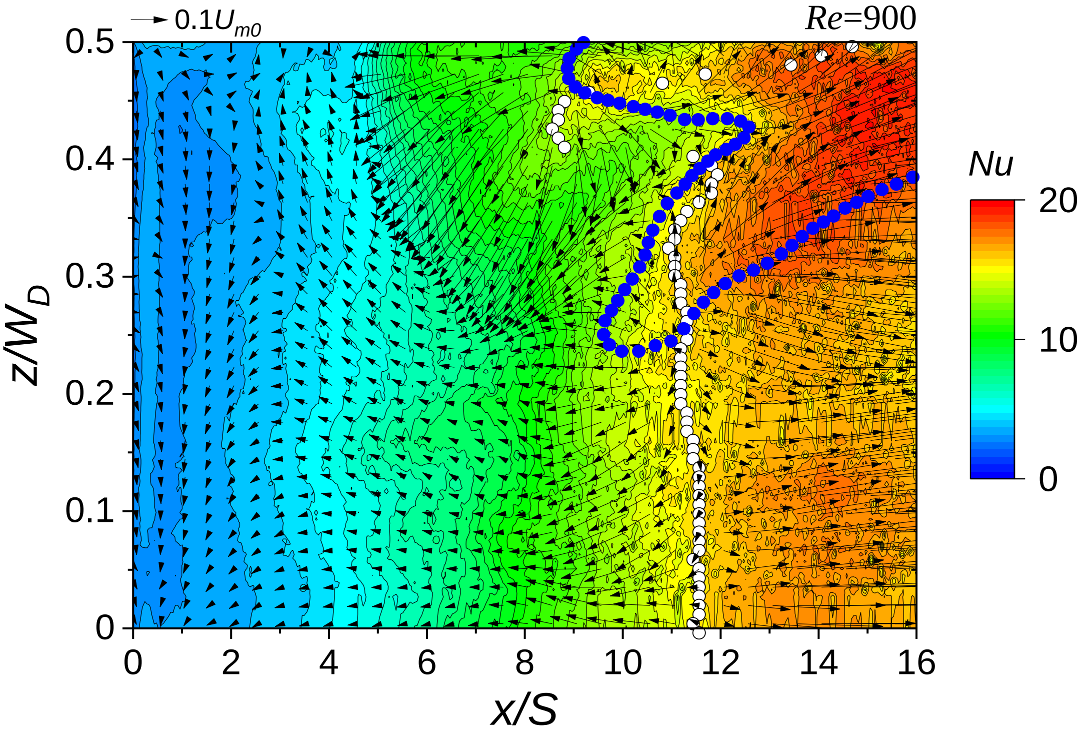

Fig. 3-23. Local *Nu* distribution superimposed with time-averaged vector and reattachment points at *Re*=900. White plots represent the reattachment points and blue plots represent the points whose gradient of the spanwise velocity component *w* equaling 0.

Figure 3-24 shows the velocity vectors in the *y-z* plane obtained at various streamwise positions. As seen at x/S=8.0, intensive secondary flow from the side wall to the center of the duct can be observed, it flows from z/W_D=0.36-0.48 at y/S=1.25 near the upper wall to z/W_D=0.47-0.35, shown in Fig. 3-24 (a). This strong reverse flow observed from x/S=8.0 corresponds well to the intensive reverse flow near the side wall region presented in Fig. 3-23. This high-speed flow enhances the heat transfer around the region where x/S=5.0-9.0 and z/W_D=0.25-0.5. As x/S=13.0, a kind of fluid flowing from duct center toward the side wall could be seen, when x/S=15.0, the corner flow becomes stronger toward the angle between the side wall and the bottom wall, it is worth noting that in this position (x/S=15.0) near the side wall, the heat transfer is greatly improved, as is shown in Fig. 3-23. Near the side wall, compare the scalar size of the reverse flow velocity at the position x/S=8.0 and that near the downstream side (x/S=15.0), there are no large differences between them, but the reason why the Nusselt number distribution around x/S=15.0 is much larger than that around the region immediately upstream the reattachment point should be further investigated.

The stream trace lines were drawn in the *y-z* plane to trace the signs of fluid movement. The spanwise velocity component was also superimposed in Fig. 3-25. It could be found that an obvious dividing line that separates the flow velocity in the wall-normal direction appears near the upper wall at x/S=8.0. A corner fliud flows from side wall to the center of the duct and then lifts up, forming a small vortex like flow at around $|z/W_D|$=0.375. Some vortices could also be observed near the duct center. At x/S=15.0, such kind of vortices disappear, the flow from duct center to side wall breaks the bottom wall boundary layer directly, which may enhance the heat transfer nearby. The region above the dividing line mentioned above turns to be larger than that in the *y-z* cross-section at x/S=8.0.

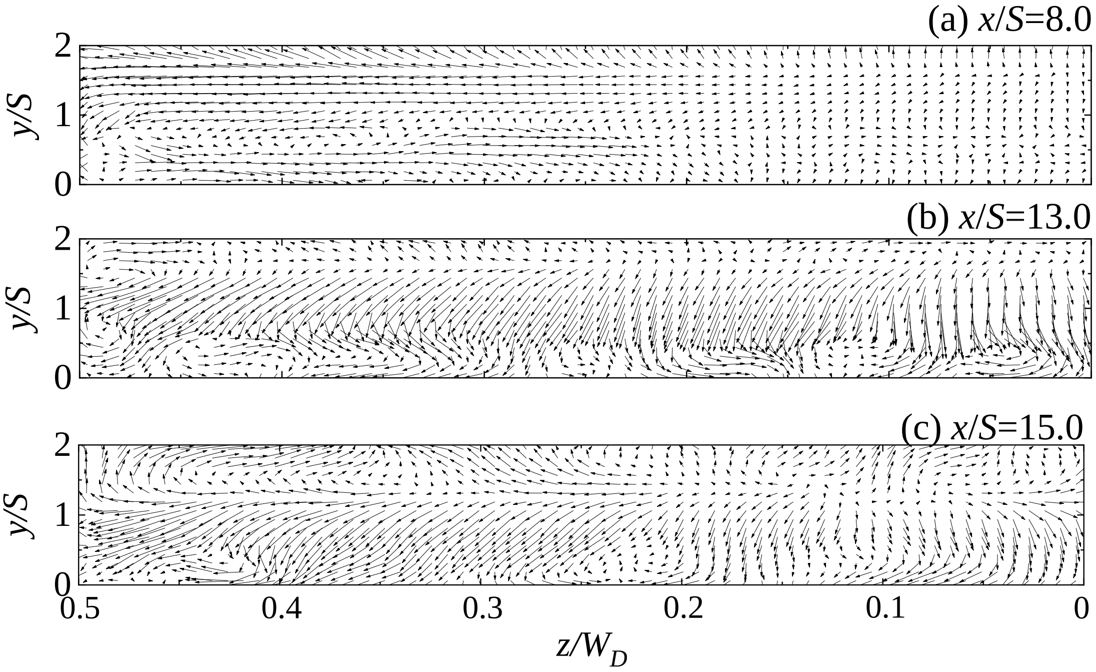

Fig. 3-24. Velocity vectors in the *y*-*z* plane at *Re*=900.

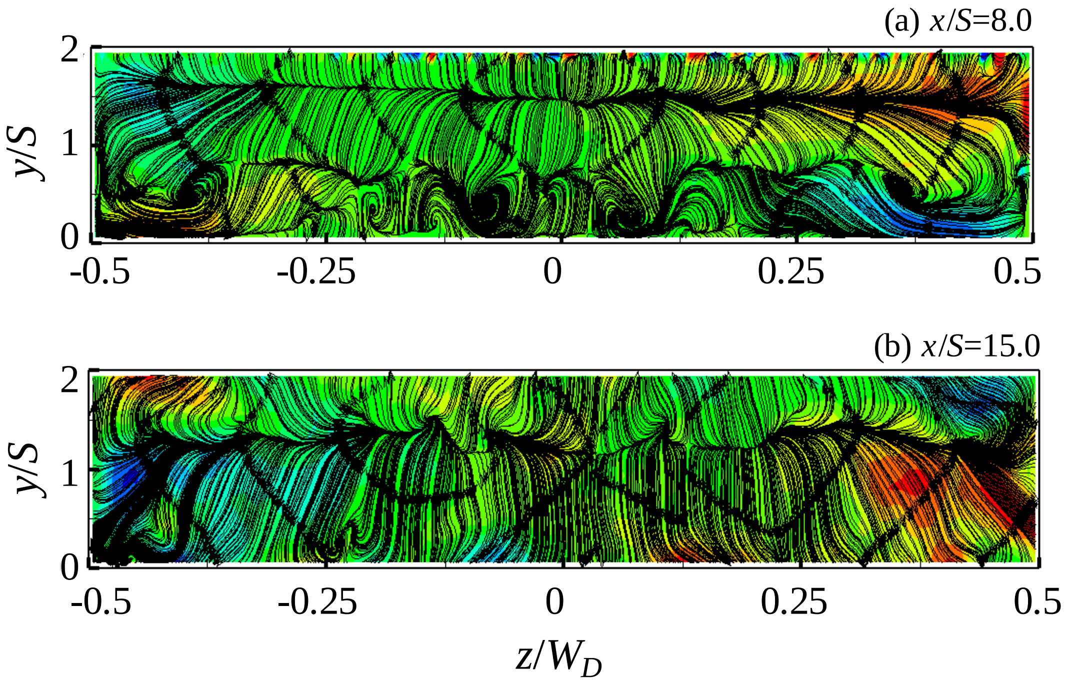

Fig. 3-25. Stream trace line in the *y*-*z* plane at *x*/*S*=8.0 and 15.0 at *Re*=900.

3.3.4 *Relationship between local Nusselt number distribution and flow-related parameters near the bottom wall*

As mentioned above, heat transfer distribution is found to be remarkably related to the 3D flow structures downstream the step, especially, the flow behaviors near the bottom wall and the reattachment structures. Such a relation was also reported by Iwai et al. [9]. However, the flow field near the bottom wall seems to be quite complicated and the main reason for the heat transfer enhancement has not been clarified yet. So possible velocity-related quantities on the bottom wall were taken into account for in-depth exploration.

Figures 3-26 to 3-31 show the same scale with Fig. 3-23 both in the streamwise and spanwise directions to investigate the effects of the velocity-related parameters on the bottom wall on heat transfer distribution. Fig. 3-26 and Fig. 3-27 show the dimensionless velocity component along the streamwise and spanwise directions in x-z plane located at y/S=0.03 from the bottom wall. Fig 3-28 shows the dimensionless velocity magnitude of the velocity V/U_{m0}, where $V = \sqrt{u^2 + w^2}$. In these figures, u/U_{m0}, w/U_{m0} and V/U_{m0} show relatively large values in x/S range from 5 to 8 while z/W_D range from 0.4 to 0.45 (this area named "region A" hereafter) upstream the reattachment position and near the side wall. And u/U_{m0}, w/U_{m0} and V/U_{m0} share the same value in region downstream side of the reattachment point ("region B", the area located in x/S=14-16, z/W_D=0.4-0.5) with "region A". However, the Nusselt number in these two regions shown in Fig. 3-23 are not the same. "Region B" shows a much higher Nusselt number value than "Region A". Thus, it implies that the heat transfer enhancement could be partially affected by the time-averaged velocity magnitude near the side wall, the other parameters may exist.

In Fig. 3-27, not only the reattachment points were extracted, but also the points whose gradient of the spanwise velocity component w equaling 0 were also extracted. Blue plots represent this kind of position. Within the area surrounded by these plots, the magnitude of the w component shows a high value, and pay attention to the corresponding area in Fig. 3-23, the relatively high Nu region almost around there. The flow structure inside this area has close dominant effects on the heat transfer enhancement. Dimensionless fluctuation intensity of each flow component was also adopted as a parameter to study the possibility of flow fluctuating effects on heat transfer.

Fig. 3-29 and 3-28 are presented the fluctuation intensity of the streamwise element and spanwise element respectively. Fig. 3-31 shows $Vrms/U_{m0}$ near the bottom wall. From these figures, pay attention to the fluctuation intensity in "region A", the fluctuation intensity here is quite small. However, the fluctuation intensity is much larger in "Region B". By comparing the Nusselt number, velocity magnitude and fluctuation intensity in "Region A" and "Region B", it could be concluded that the flow magnitude and fluctuation intensity both play a role to affect heat transfer distribution on the bottom wall, but the influence of fluctuation intensity seems to be more dominant than the velocity magnitude in the case of *Re*=900.

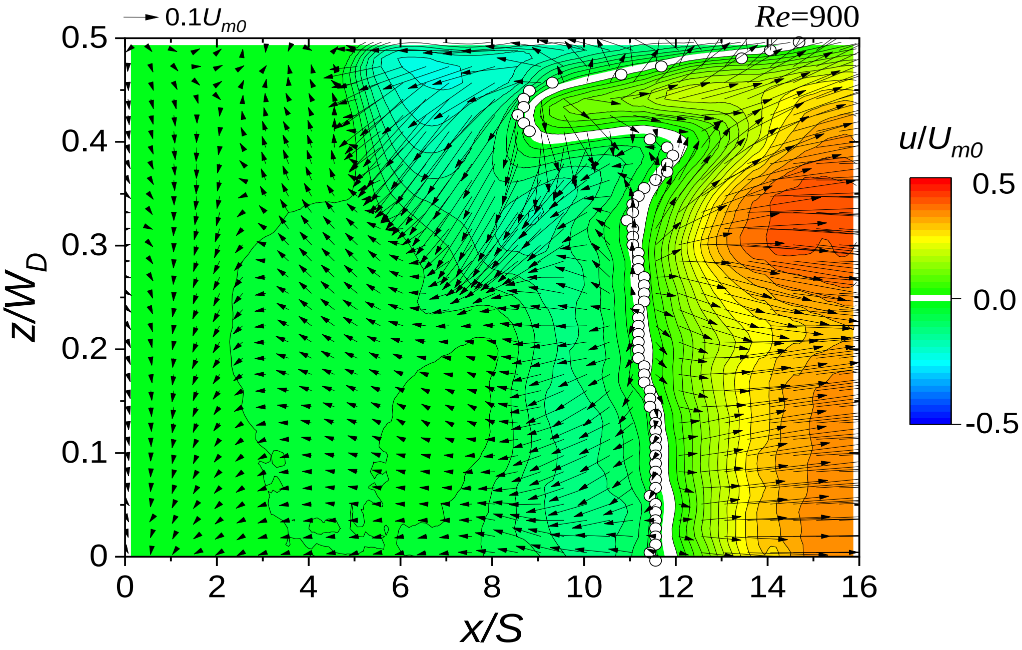

Fig. 3-26. The *u* component magnitude superimposed with time-averaged velocity vector and reattachment points.

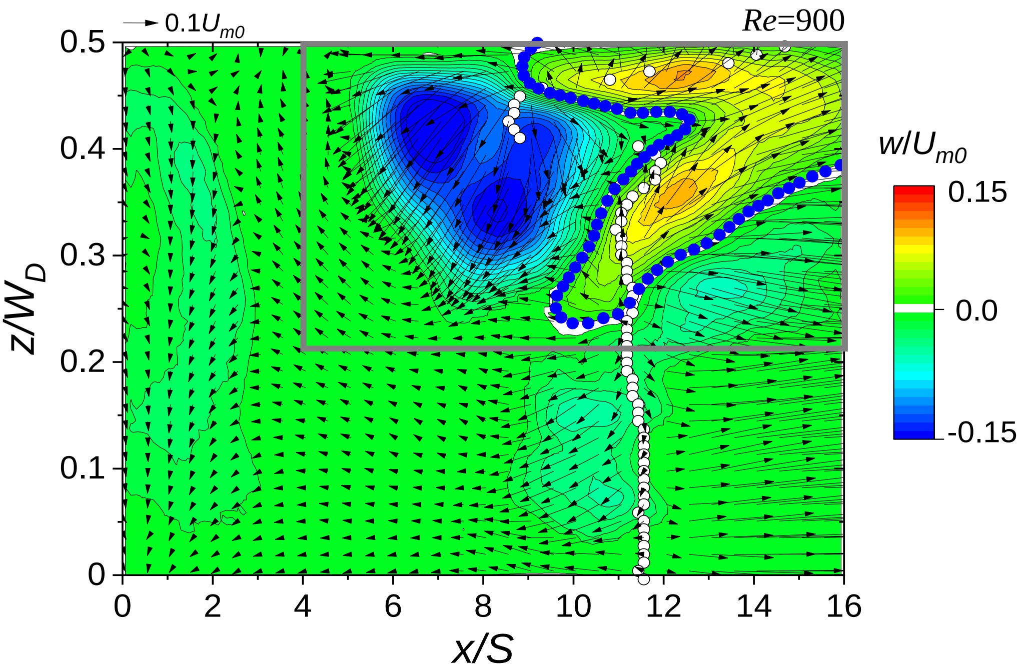

Fig. 3-27. The *w* component magnitude superimposed with time-averaged velocity vector and reattachment points.

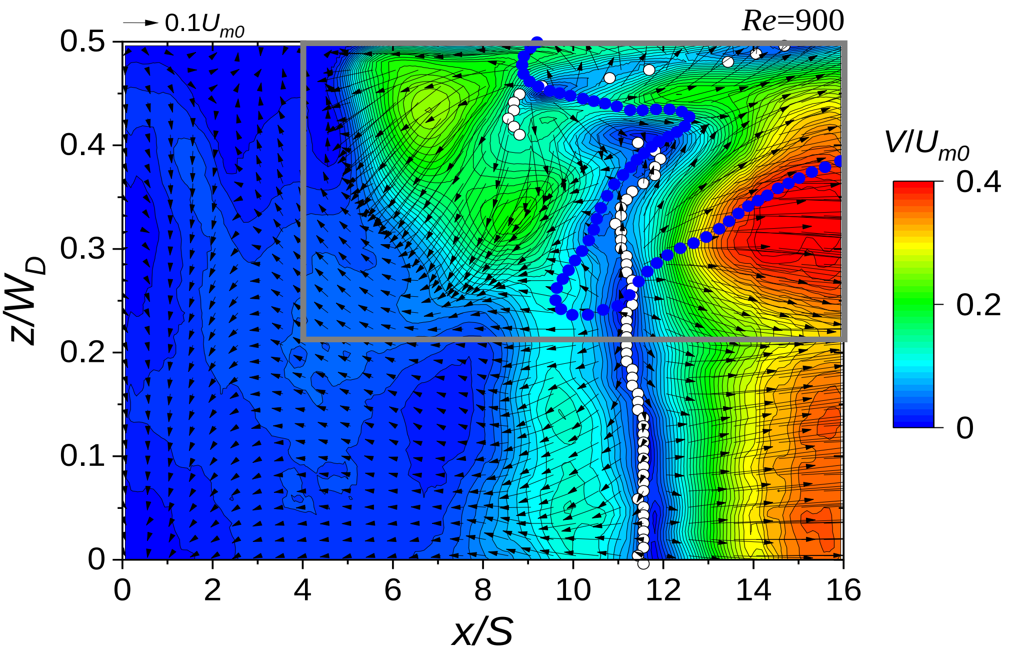

Fig. 3-28. Velocity magnitude superimposed with time-averaged velocity vector and reattachment points.

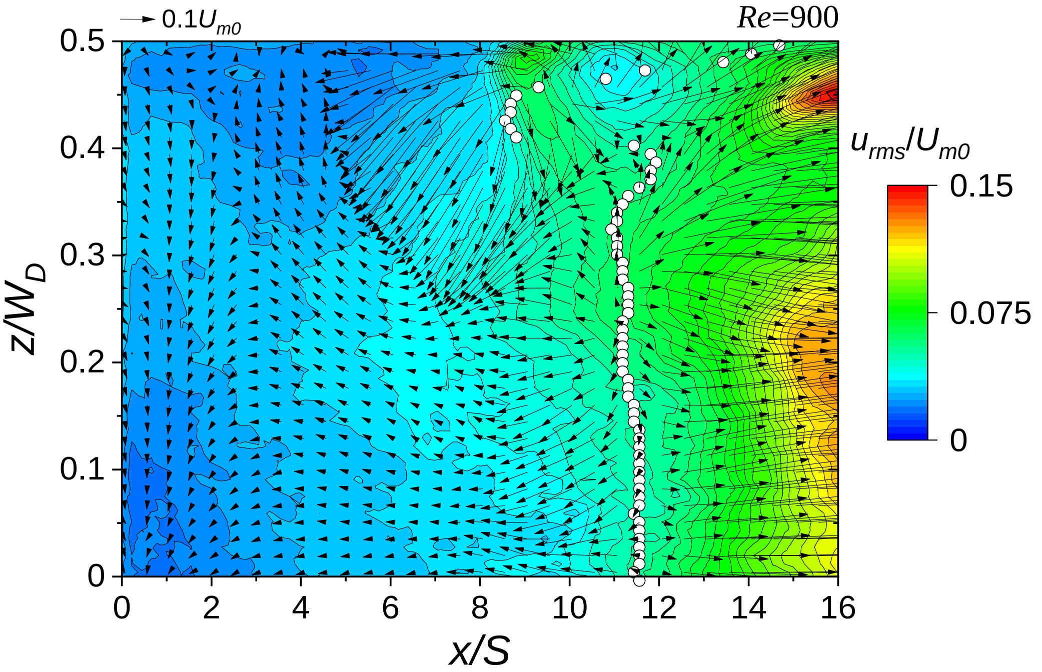

Fig. 3-29. The fluctuation intensity distribution of *u* component superimposed with time-averaged velocity vector and reattachment points.

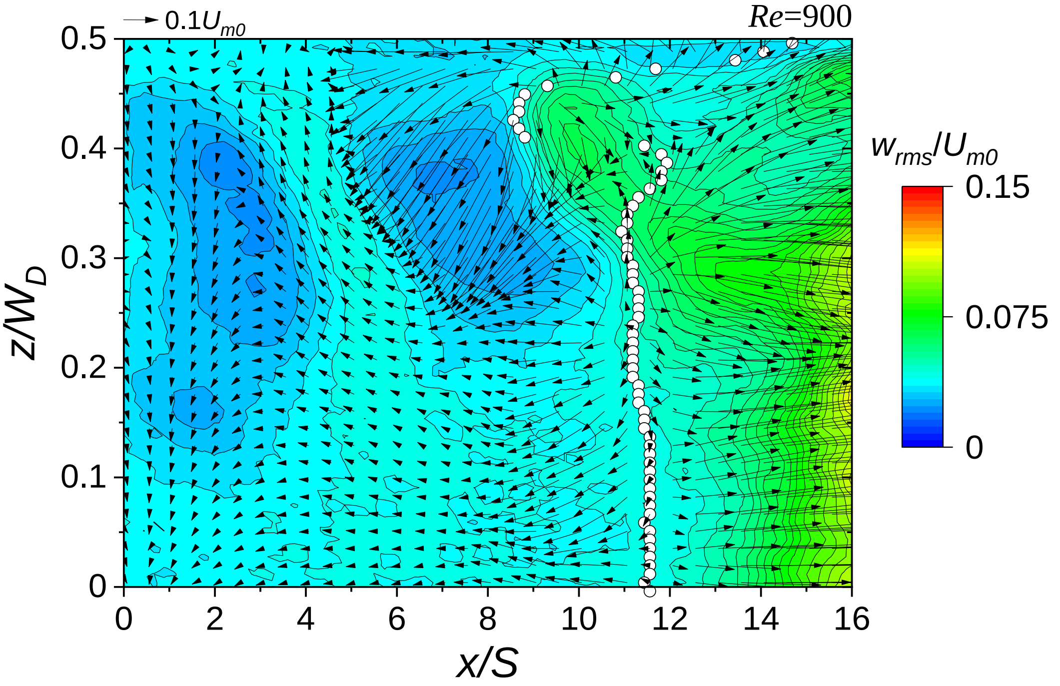

Fig. 3-30. The fluctuation intensity distribution of *w* component superimposed with time-averaged velocity vector and reattachment points.

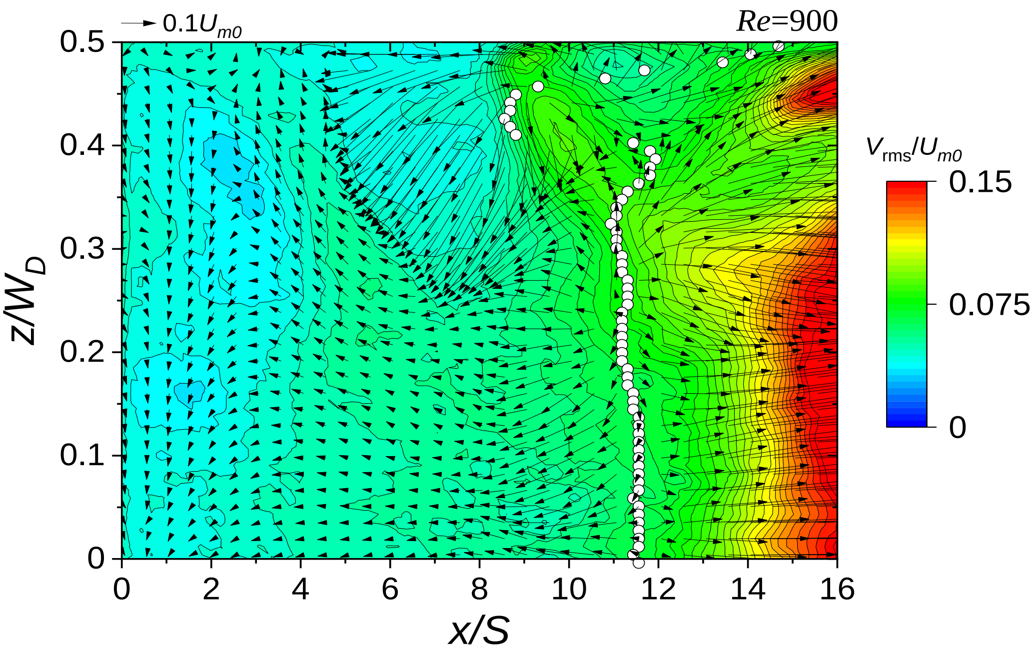

Fig. 3-31. The fluctuation intensity distribution of velocity magnitude superimposed with time-averaged velocity vector and reattachment points.

3.3.5 Distributions of heat transfer coefficient on the upper wall

Same as the coordinate set of the bottom wall, Fig. 3-32 shows the Nu distribution on the upper wall for the representative Reynolds number cases (Re=400-900). Since the heat transfer coefficient investigation of the upper wall is concentrated on the side wall and the center of the flow channel, the spacings between each slice were not removed by interpolation. The changing trend of the Nu distribution along the flow path on the upper wall surface is not consistent with that on the bottom wall surface. The area where the heat transfer deteriorates is no longer adjacent to the step but in a specific narrow area downstream. While the high heat transfer area still keeps near the side wall for all Reynolds number cases.

The same extraction operation of Nu was carried out on the upper wall near the center line (z/W_D=0.0) and side wall (z/W_D=0.4) of the duct. In Fig. 3-33 and Fig. 3-34, for all cases, the Nusselt number value in the same streamwise position is increased with the increase of Reynolds number. The overall trend is to firstly decline and then rise in the streamwise direction. The variation magnitude near the side wall and for higher Reynolds number cases is more obvious.

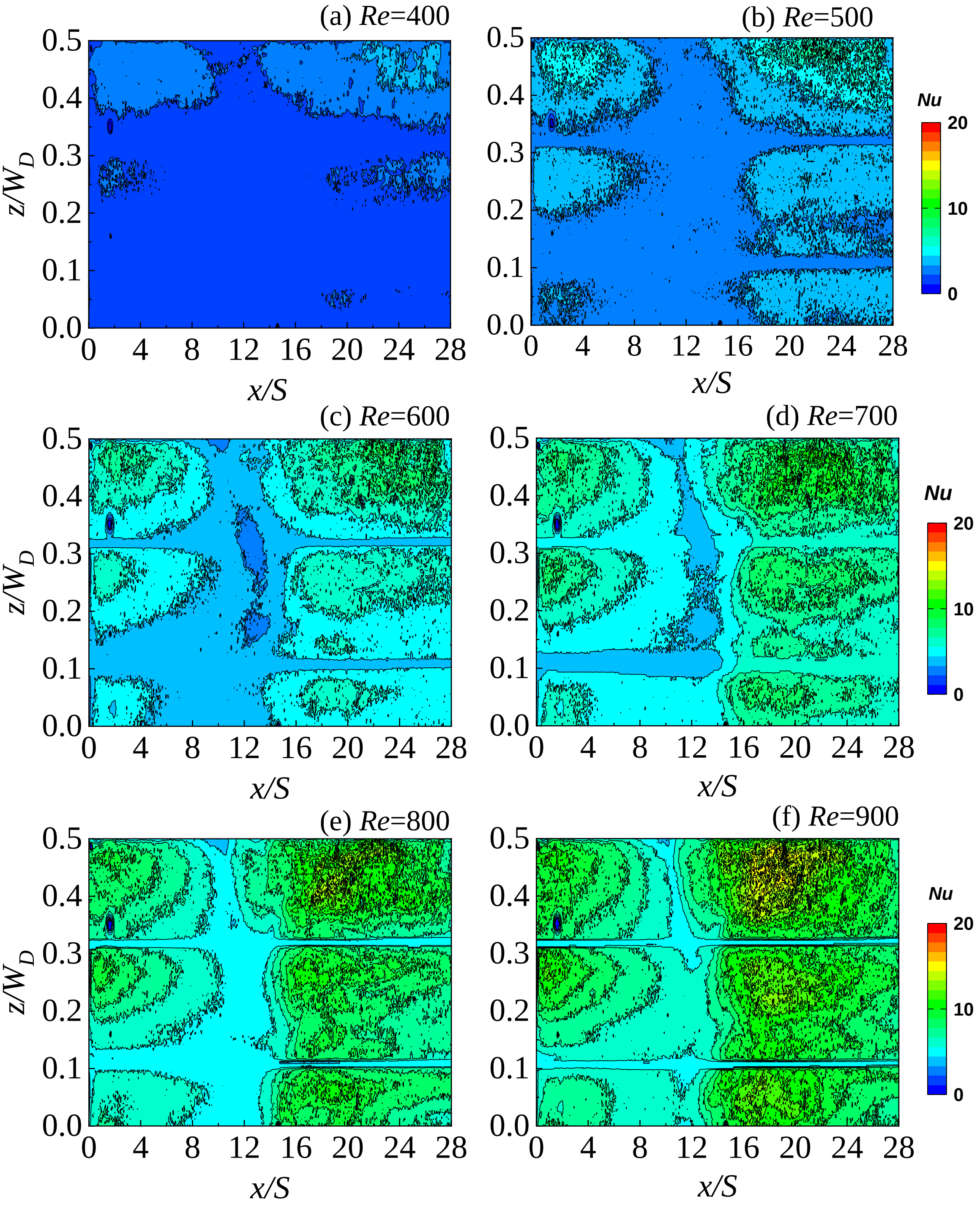

Fig. 3-32. Distribution of the local Nusselt number on the upper wall for the representative Reynolds number cases

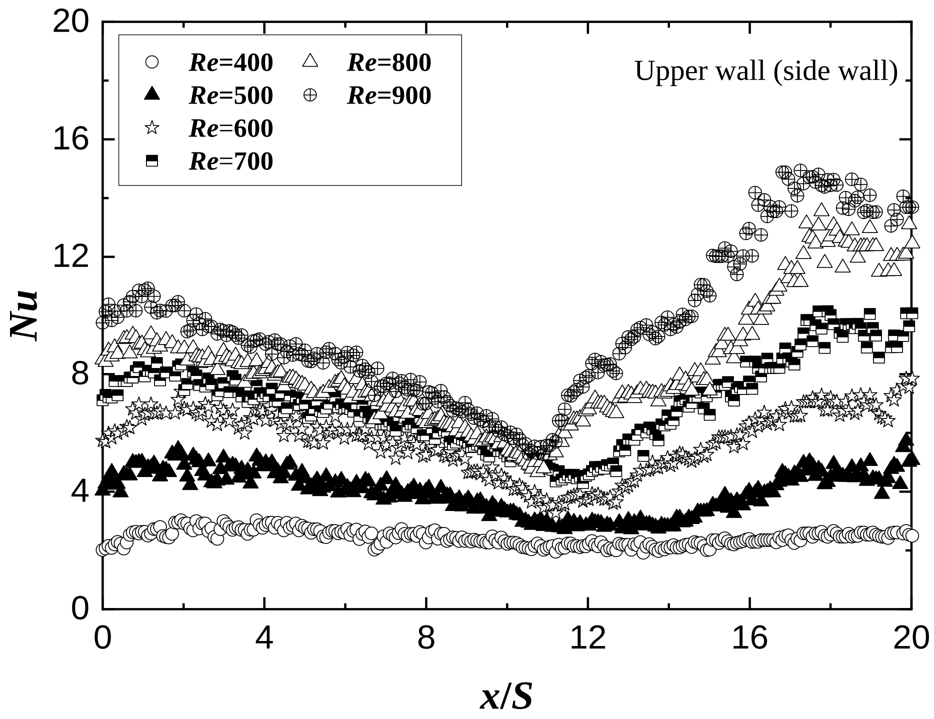

Fig. 3-33. Streamwise distribution of Nu along the center line (z/W_D=0.0) of the duct on the upper wall.

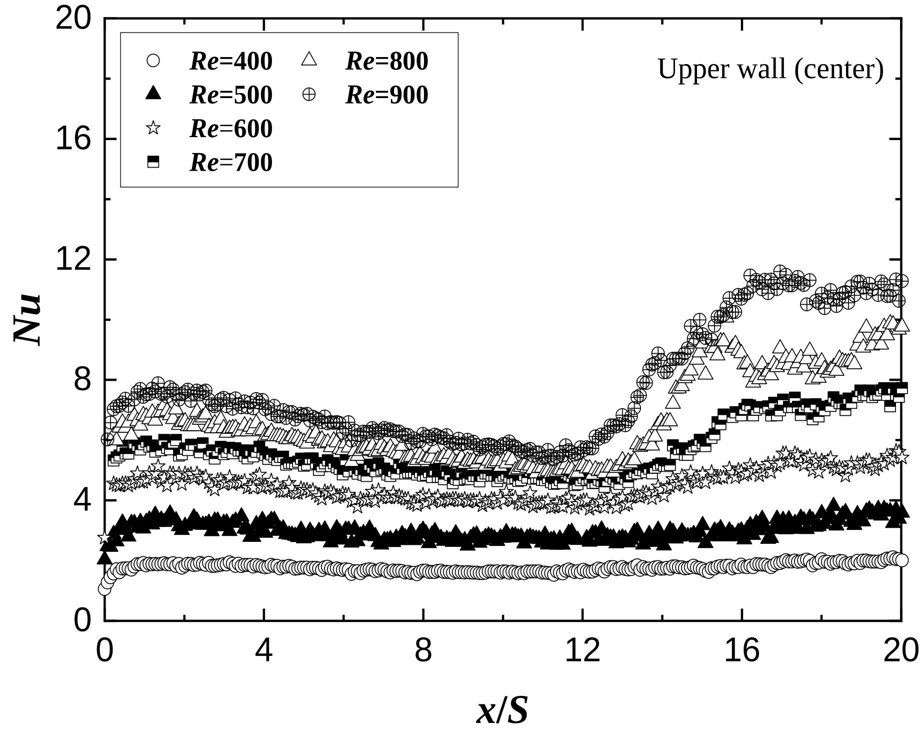

Fig. 3-34. Streamwise distribution of *Nu* near the side wall (z/W_D=0.4) of the duct on the upper wall.

3.3.6 Relationship between local Nusselt number distribution and flow structures

Fig. 3-35 and 3-36 show the time-averaged velocity vector and velocity contour in the streamwise direction. The tendency agreement between the *Nu* distribution and the velocity contour could be observed. It worth noting that in an area where $u<0$ is located near the side wall, the *Nu* in the corresponding position shows minimum value there. The low-speed fluid flowing from the duct center to the side wall inside this region plays an important role in the heat transfer deterioration.

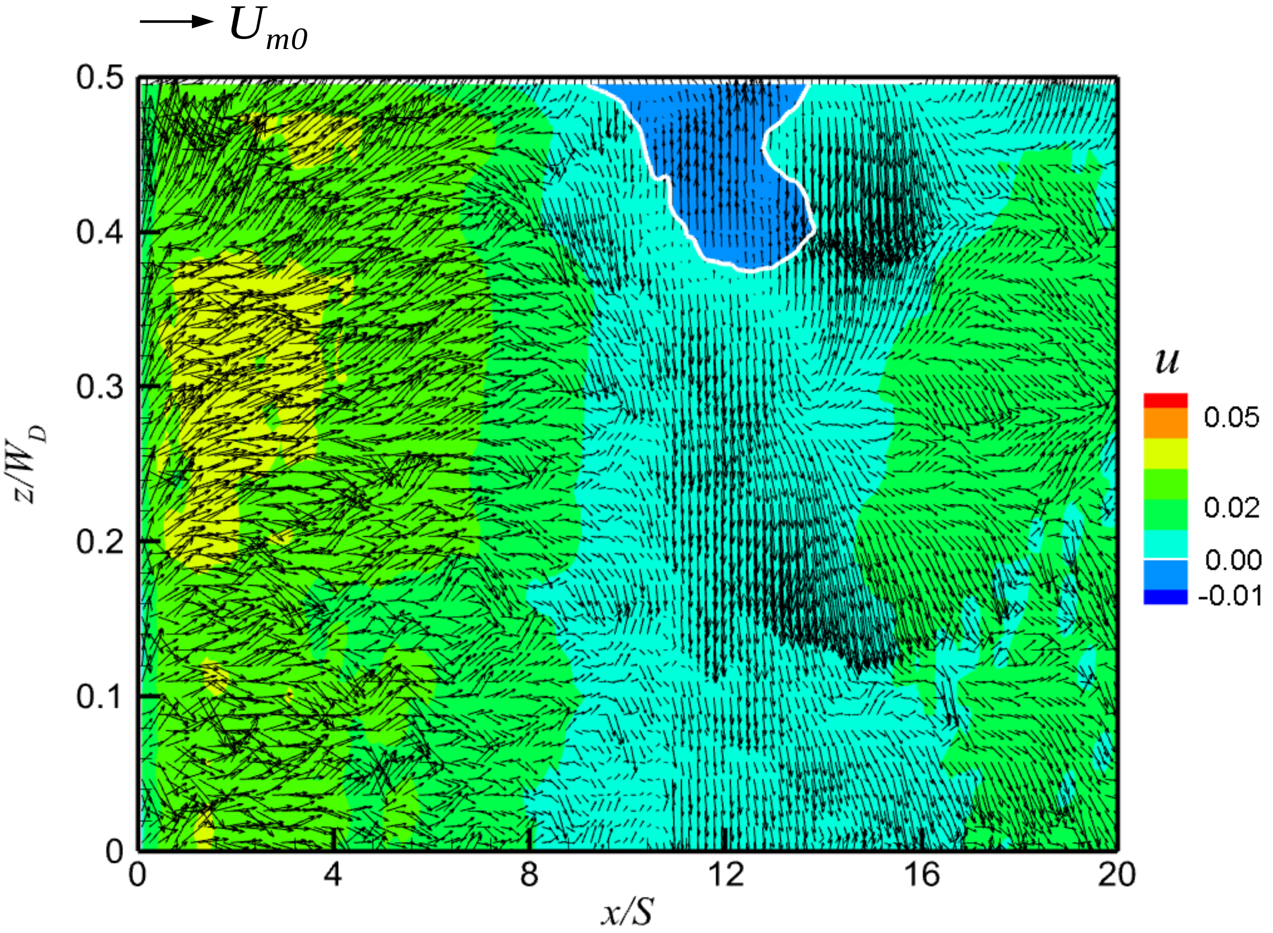

Fig. 3-35. Velocity vector superimposed with velocity contour in streamwise direction for *Re*=700.

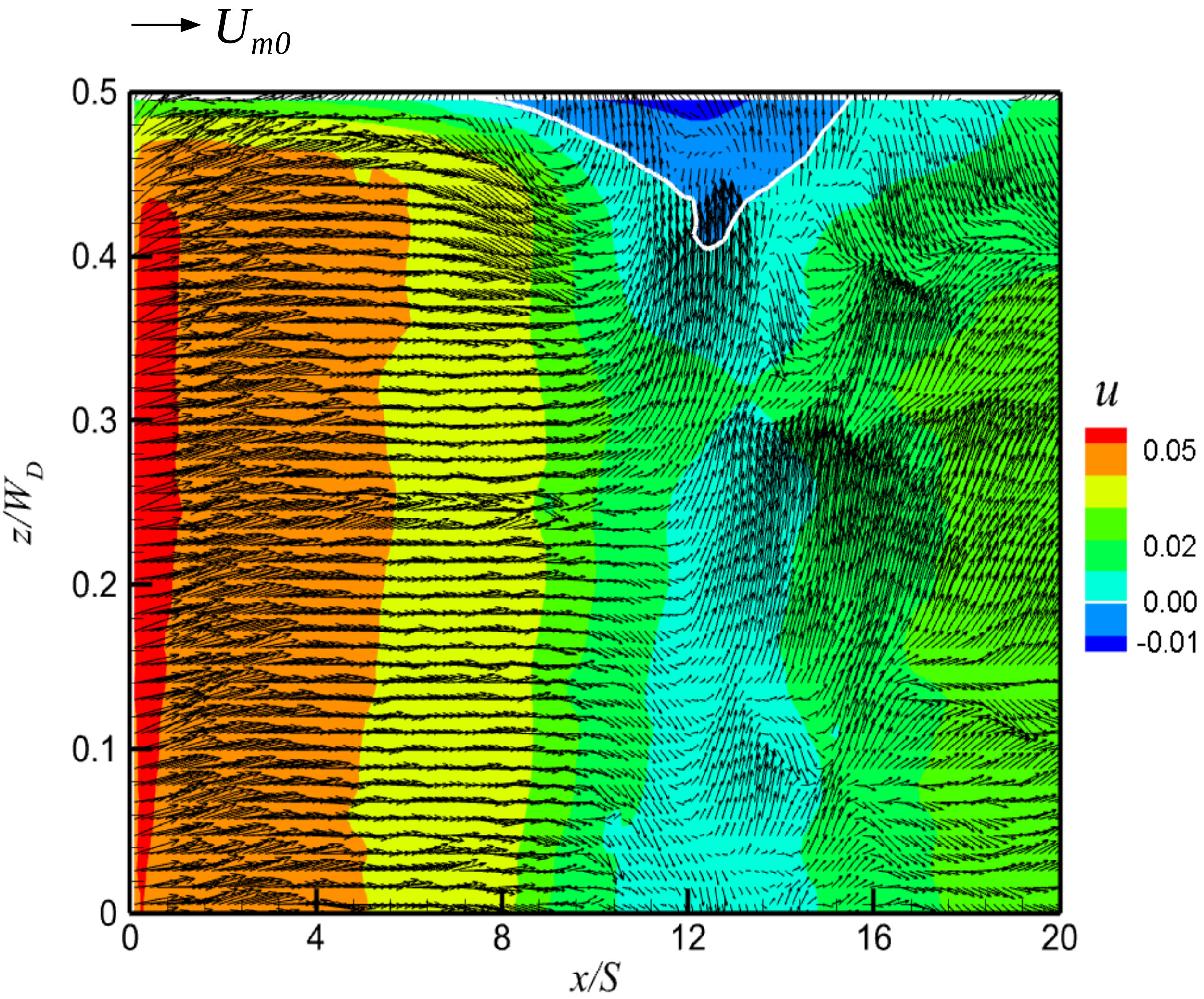

Fig. 3-36. Velocity vector superimposed with velocity contour in streamwise direction for *Re*=900.

3.3.7 Comparison of heat transfer coefficient on the bottom wall and upper wall

In Fig. 3-37, Nu_{bave} represents the average *Nu* over the entire bottom wall, Nu_{upave} represents the average *Nu* over the entire upper wall, Nu_{bcave} represents the average *Nu* at the centerline of the bottom wall, and Nu_{upcave} represents the average *Nu* at the centerline of the upper wall at different Reynolds numbers. Here, the channel length for doing average was 31*S*. The black and blue plots show the experimental results obtained at Reynolds number less than 1000, and the red plot shows the results of previous experimental research of Inaoka et al. [10]. From this figure, it can be seen that both Nu_{bcave} and Nu_{bave} are smoothly linked to the previous results and that the average heat transfer increases significantly up to *Re*=1000 with the increase of Reynolds number, and then increases relatively slowly thereafter. On the upper wall, the increasing tendency even values are almost the same as that on the bottom wall. For all cases, the values of Nu_{ave} and Nu_{cave} are almost the same in all regions of the Reynolds numbers. From this, it can be said that when considering the range of 31*S'* downstream of the flow channel, the average *Nu* of the entire bottom wall and the upper wall can be estimated by the average *Nu* at the center of the flow channel.

Figure 3-38 shows the maximum *Nu* over the entire bottom wall Nu_{bmax} and upper wall Nu_{upmax}, and the maximum *Nu* at the centerline of the bottom wall Nu_{bcmax} and upper wall Nu_{upcmax} at different Reynolds numbers. Fig. 3-39 shows the ratio between the two in Fig. 3-38. The black and blue plots in each figure show the results of the present experiment, and the red plots show the results of Inaoka et al. [10]. From Fig. 3-38, both values increase with the increase of Reynolds number. As for the present experimental results, Nu_{cmax} has linear change not only on the bottom wall but also on the upper wall. It is worth noting that the discrepancies between Nu_{upmax} and Nu_{upcmax} are larger than those between Nu_{bmax} and Nu_{bcmax}. From Fig. 3-39, on the bottom wall, after Re=1000, the ratio value is around 1.3 and does not change much even if the Reynolds number increases. On the other hand, in the region below $Re = 1000$, the ratio value increases as the Reynolds number decreases. The fact that all the ratios are over 1 indicates non-uniform heat transfer distribution in the spanwise direction exists on the bottom wall, when Re=400, the non-uniform intensity is strongest. On the upper wall, the ratio is much higher than that of the bottom wall, indicating the higher effect by the flow three-dimensionality occurs there, especially around the relatively low Reynolds number range (400, 500, 600).

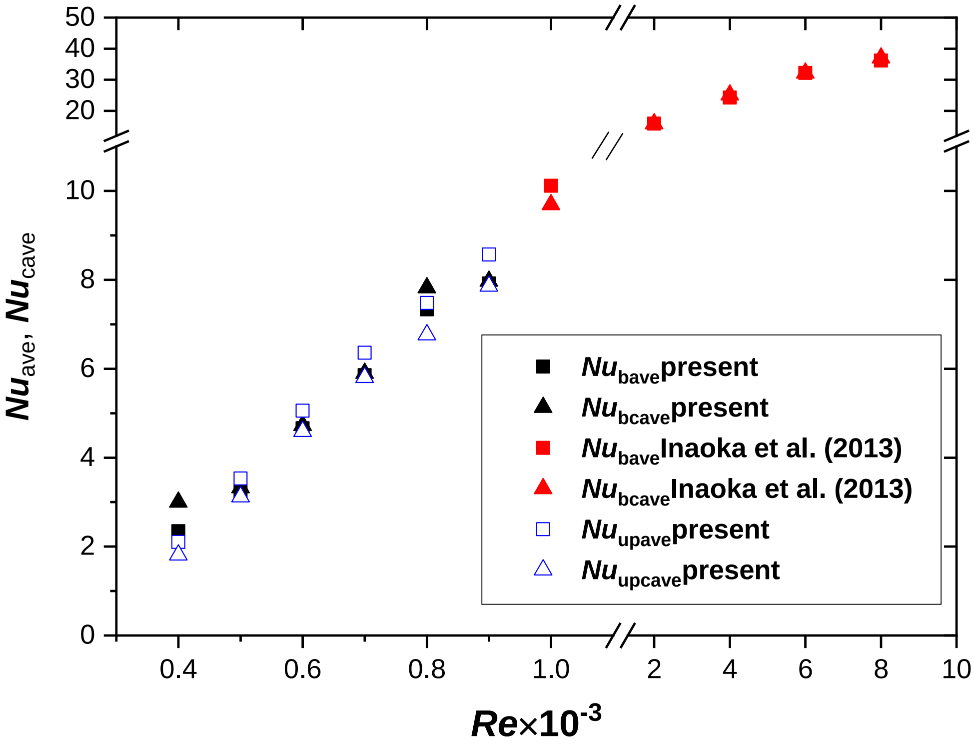

Fig. 3-37. Nu_{ave} and Nu_{cave} in different Re.

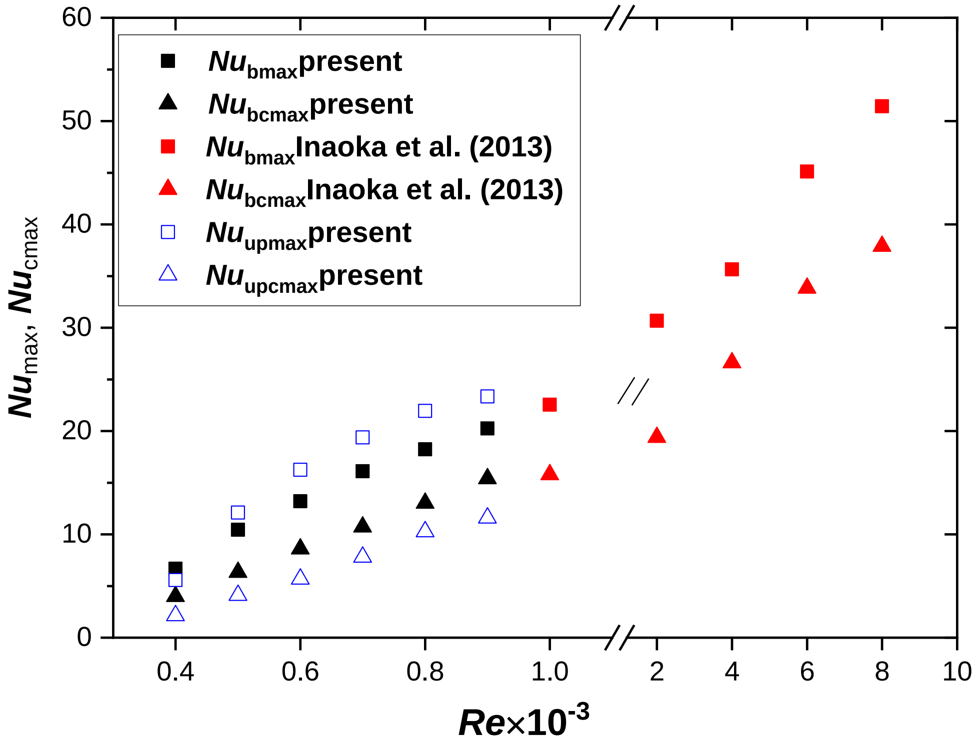

Fig. 3-38. Nu_{max} and Nu_{cmax} in different Re.

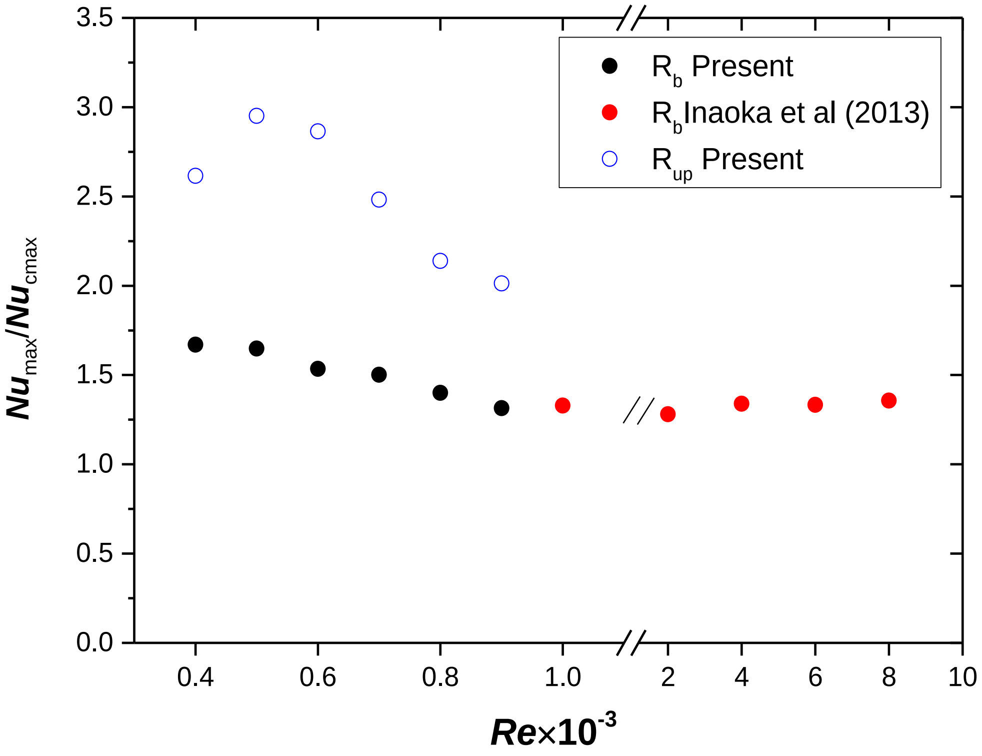

Fig. 3-39. Variation of the ratio of Nu_{max} to Nu_{cmax} for *Re*.

3.4 Conclusion and discussions

In chapter 3, heat transfer measurements were done on the bottom and upper wall of the BFS flow in a duct in a relatively low Reynolds number range (Re=400-900). From the perspective of heat transfer distribution, it is summarized that this flow model has three-dimensional characteristics and intensively affects the heat transfer distribution on the walls. The specific conclusions are as follows:

(1) When considering the range of $31S$ downstream of the flow channel, the average Nu value over the entire bottom wall or upper wall can be estimated by averaging that at its center line in the Reynolds number range from 400 to 900.

(2) On the bottom wall, the area where heat transfer is enhanced and deteriorated is mainly distributed downstream of the step near the side wall and before the reattachment positions, respectively. Flow disturbances play a leading role in heat transfer, especially in the relatively high Nusselt number region downstream of the reattachment near the side wall. The velocity magnitude also has a contribution to heat transfer distribution. The ratio of Nu_{max} to Nu_{cmax} in different Re on the bottom wall proves the existence of a three-dimensional feature of this fluid flow model. The three-dimensional flow effect is most apparent at approximately Re=400.

(3) On the upper wall, the low-speed fluid flowing from the duct center to the side wall inside the region where u<0 plays an important role in the heat transfer deterioration. The ratio of Nu_{max} to Nu_{cmax} which is much larger than 1.0 in different Re also indicates that the three-dimensional flow affects heat transfer characteristics of the upper wall. Furthermore, the three-dimensional characteristics there is stronger than that of the bottom wall in various Reynolds number conditions.

References

[1] J. Xu, S. Zou, K. Inaoka, and G. Xi, "Effect of Reynolds number on flow and heat transfer in incompressible forced convection over a 3D backward-facing step," *International Journal of Refrigeration,* vol. 79, pp. 164-175, 2017.

[2] L. Chen, K. Asai, T. Nonomura, G. Xi, and T. Liu, "A review of backward-facing step (BFS) flow mechanisms, heat transfer and control," *Thermal Science and Engineering Progress,* vol. 6, pp. 194-216, 2018.

[3] E. Adams and J. Eaton, "An LDA study of the backward-facing step flow, including the effects of velocity bias," 1988.

[4] G. Papadopoulos and M. O¨ tu¨ gen, "Separating and reattaching flow structure in a suddenly expanding rectangular duct," *Journal of Fluids Engineering,* vol. 117, no. 1, pp. 17-23, 1995.

[5] H. Iwai, K. Nakabe, and K. Suzuki, "Flow and heat transfer characteristics of backward-facing step laminar flow in a rectangular duct," *International Journal of Heat and Mass Transfer,* vol. 43, no. 3, pp. 457-471, 2000.

[6] H. Iwai, K. Nakabe, K. Suzuki, and K. Matsubara, "The effects of duct inclination angle on laminar mixed convective flows over a backward-facing step," *International Journal of Heat and Mass Transfer,* vol. 43, no. 3, pp. 473-485, 2000.

[7] J. Nie and B. Armaly, "Reverse flow regions in three-dimensional backward-facing step flow," *International Journal of Heat and Mass Transfer,* vol. 47, no. 22, pp. 4713-4720, 2004.

[8] J. Nie and B. F. Armaly, "Three-dimensional convective flow adjacent to backward-facing step-effects of step height," *International Journal of Heat and Mass Transfer,* vol. 45, no. 12, pp. 2431-2438, 2002.

[9] J. Nie and B. F. Armaly, "Reattachment of three-dimensional flow adjacent to backward-facing step," *Journal of Heat Transfer,* vol. 125, no. 3, pp. 422-428, 2003.

[10] K. Inaoka and M. Senda, "Heat Transfer and Fluid Flow Characteristics of a Backward-Facing Step Flow in a Duct," *Transactions of the Japan Society of Mechanical Engineers, Series B,* vol. 79, no. 804, pp. 1651-1663, 2013, doi: 10.1299/kikaib.79.1651.

[11] K. Inaoka, K. Nakamura, and M. Senda, "Heat transfer control of a backward-facing step flow

in a duct by means of miniature electromagnetic actuators," *International Journal of Heat and Fluid Flow,* vol. 25, no. 5, pp. 711-720, 2004.

[12] L. Kaiktsis, G. E. Karniadakis, and S. A. Orszag, "Onset of three-dimensionality, equilibria, and early transition in flow over a backward-facing step," *Journal of Fluid Mechanics,* vol. 231, pp. 501-528, 1991.

[13] E. Steinthorsson, M.-S. Liou, L. A. Povinelli, and A. Arnone, "Numerical simulations of three-dimensional laminar flow over a backward facing step; flow near side walls," presented at the ASME, Washington, DC, July 1, 1993, 1993.

[14] J. C. Lin, "Review of research on low-profile vortex generators to control boundary-layer separation," *Progress in Aerospace Sciences,* vol. 38, no. 4-5, pp. 389-420, 2002.

[15] N. Suyama, K. Inaoka, and M. Senda, "Flow Characteristics Over a Backward-Facing Step in a Duct in Low Reynolds Number Range," in *ASME/JSME 2011 8th Thermal Engineering Joint Conference*, 2011, vol. ASME/JSME 2011 8th Thermal Engineering Joint Conference, T10084, doi: 10.1115/ajtec2011-44246. [Online]. Available: https://doi.org/10.1115/AJTEC2011-44246

[16] M. Hemmat Esfe, M. Afrand, S. Wongwises, A. Naderi, A. Asadi, S. Rostami, and M. Akbari, "Applications of feedforward multilayer perceptron artificial neural networks and empirical correlation for prediction of thermal conductivity of Mg(OH) 2 –EG using experimental data," *International Communications in Heat and Mass Transfer,* vol. 67, pp. 46-50, 2015, doi: 10.1016/j.icheatmasstransfer.2015.06.015.

[17] S. R. Gunn, "Support vector machines for classification and regression," *ISIS Technical Report,* vol. 14, no. 1, pp. 5-16, 1998.

[18] H. Drucker, C. J. Burges, L. Kaufman, A. J. Smola, and V. Vapnik, "Support vector regression machines," in *Advances in Neural Information Processing Systems*, 1997, pp. 155-161.

[19] A. J. Smola and B. Schölkopf, "A tutorial on support vector regression," *Statistics and Computing,* vol. 14, no. 3, pp. 199-222, 2004.

[20] J. Ma, J. Theiler, and S. Perkins, "Accurate on-line support vector regression," *Neural Computation,* vol. 15, no. 11, pp. 2683-2703, 2003.

[21] B. Gu, V. S. Sheng, Z. Wang, D. Ho, S. Osman, and S. Li, "Incremental learning for ν-support

vector regression," *Neural Networks,* vol. 67, pp. 140-150, 2015.

[22] S. Sayad. "Support Vector Machine - Regression (SVR)." http://www.saedsayad.com/support_vector_machine_reg.html (accessed 2020).

[23] C. Zanchettin, T. B. Ludermir, and L. M. Almeida, "Hybrid training method for MLP: optimization of architecture and training," *IEEE Transactions on Systems, Man, and Cybernetics, Part B (Cybernetics),* vol. 41, no. 4, pp. 1097-1109, 2011.

[24] J. Tang, C. Deng, and G.-B. Huang, "Extreme learning machine for multilayer perceptron," *IEEE Transactions on Neural Networks and Learning Systems,* vol. 27, no. 4, pp. 809-821, 2015.

[25] G. Xie, B. Sunden, Q. Wang, and L. Tang, "Performance predictions of laminar and turbulent heat transfer and fluid flow of heat exchangers having large tube-diameter and large tube-row by artificial neural networks," *International Journal of Heat and Mass Transfer,* vol. 52, no. 11-12, pp. 2484-2497, 2009.

[26] T. Hill, L. Marquez, M. O'Connor, and W. Remus, "Artificial neural network models for forecasting and decision making," *International Journal of Forecasting,* vol. 10, no. 1, pp. 5-15, 1994.

[27] G. J. Gibson, S. Siu, and C. Cowen, "Multilayer perceptron structures applied to adaptive equalisers for data communications," in *International Conference on Acoustics, Speech, and Signal Processing*, 1989: IEEE, pp. 1183-1186.

[28] K. Basterretxea, J. M. Tarela, and I. Del Campo, "Approximation of sigmoid function and the derivative for hardware implementation of artificial neurons," *IEE Proceedings-Circuits, Devices and Systems,* vol. 151, no. 1, pp. 18-24, 2004.

[29] A. Bejan and A. D. Kraus, *Heat Transfer Handbook*. John Wiley & Sons, 2003.

[30] S. Mori, A. Tanimoto, T. Shinke, and M. Sakakibara, "Steady heat transfer to laminar flow between parallel plates with conduction in wall," *KKR,* vol. 1, pp. 235-240, 1976.

[31] J. H. Nie and B. F. Armaly, "Reverse flow regions in three-dimensional backward-facing step flow," *International Journal of Heat and Mass Transfer,* vol. 47, no. 22, pp. 4713-4720, 2004.

[32] J. H. N. F. Armaly, "Three-dimensional convective flow adjacent to backward-facing step - effects of step height," *International Journal of Heat and Mass Transfer,* 2002.

CHAPTER 4

Experimental Study on Heat Transfer Mechanism of Periodic Vortex for Unsteady Laminar Flow in a Stepped Duct

4.1 Introduction

The BFS flow phenomenon is common and is often used as one of the most fundamental models to generate flow separation and reattachment caused by an abrupt expansion. The flow field shows the complex characteristics of the separation flow when the fluid flows through the sudden enlargement cross-section, the flow separation can make the steady flow state turn into an unstable flow state earlier. It is one of the common methods for heat transfer enhancement. It has intentionally been used for many thermo-fluidic devices as one of the heat exchange elements due to its high heat transfer performance around the flow reattachment region. As is summarized in the previous chapter, a lot of experimental, theoretical analysis were conducted, which mainly focus on the 3D flow structure in BFS flow [1-8]. Among these researches, the 3D flow structures in a steady laminar flow region could be numerically simulated accurately by using laminar flow model. Experiments are mainly conducted in the high *Re* region for the research of turbulent flow. However, the flow and thermal measurements in the unsteady laminar flow region are very few, due to the more complicated flow and heating region in this flow state. There are not many systematic and solid experimental data in this field, making it still difficult for comparison and validation. Many discrepancies were found among the results of different groups [9].

As is reported by Erturk et al. [10], the bifurcation Reynolds number region around Re=400 could be seen . The secondary recirculation zone near the upper wall starts to be observed at Re=400. For three-dimensional predictions under different Reynolds numbers, Biswas et al. [11] reported that at relatively low Reynolds numbers ($Re<400$), the symmetry plane in the channel with an expansion ratio 1.94 could be accurately predicted by numerical simulations. Beyond a Reynolds number of 400, the side wall influences the structure of the laminar flow behind the step. The measured reattachment lengths at the symmetry plane and the predictions do not match. The unsteady and complicated flow region has been attracted a lot of attention, the flow and heat transfer mechanism in this unsteady laminar flow region is meaningful to conduct.

As for the flow instability study, Yamada et al. [12] carried out flow experiments in the low Reynolds number range using a micro flow sensor and a high-speed camera and found that there are certain periodic characteristics of the flow near the bottom and upper wall. The characteristics of flow changes caused by flow instability were mainly investigated. According to the study of Biswas et al. [11] on various expansion ratios of low and moderate *Re* numbers ($<$800), the constant size of corner vortex near the side wall is identified while the wall effect is concluded to be obvious when *Re* is higher than 400, which agrees with the experiments of Armaly et al.[13]. Most flow instability studies are based on the flow itself. There is almost no literature mentioning the effect of this periodicity or flow fluctuation on heat transfer.

In summary, careful and detailed experimental research to investigate the 3D flow instability effects on heat transfer distribution is insufficient. Heat transfer enhancement mechanism that how the unsteady convection flow enhances heat transfer in the unsteady laminar flow case is urgently needed to be clarified.

4.2 Experimental apparatus and procedures

Experimental apparatus and procedures could be referred to the description of Chapter 2. The schematic view of the experimental apparatus and test section are sketched in Fig. 4-1and Fig. 4-2, respectively. The origin of the coordinate system was located at the center of the bottom line of the stepped wall. *x*-, *y*- and *z*- coordinates represent the streamwise, wall-normal and spanwise directions, respectively [7]. *u, v, w* represent the flow velocity along the *x-, y-, z-* coordinates, respectively. Thermal measurements were conducted on the bottom wall of the BFS model by using a thermo-sensitive liquid crystal method which was also described very concretely in Chapter 3. In this study, representative Reynolds number cases were chosen from 200 to 2000. Heat Transfer Mechanism affected by the fluid flow in the unsteady laminar flow state in a stepped duct was mainly investigated.

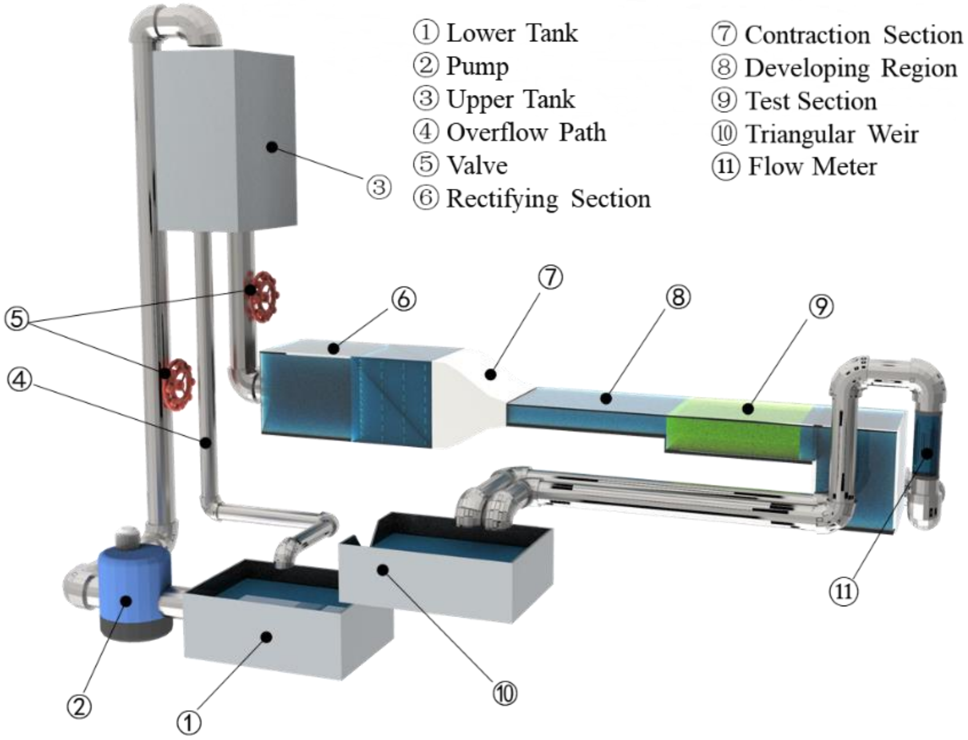

Fig. 4-1. Schematic view of an experimental apparatus.

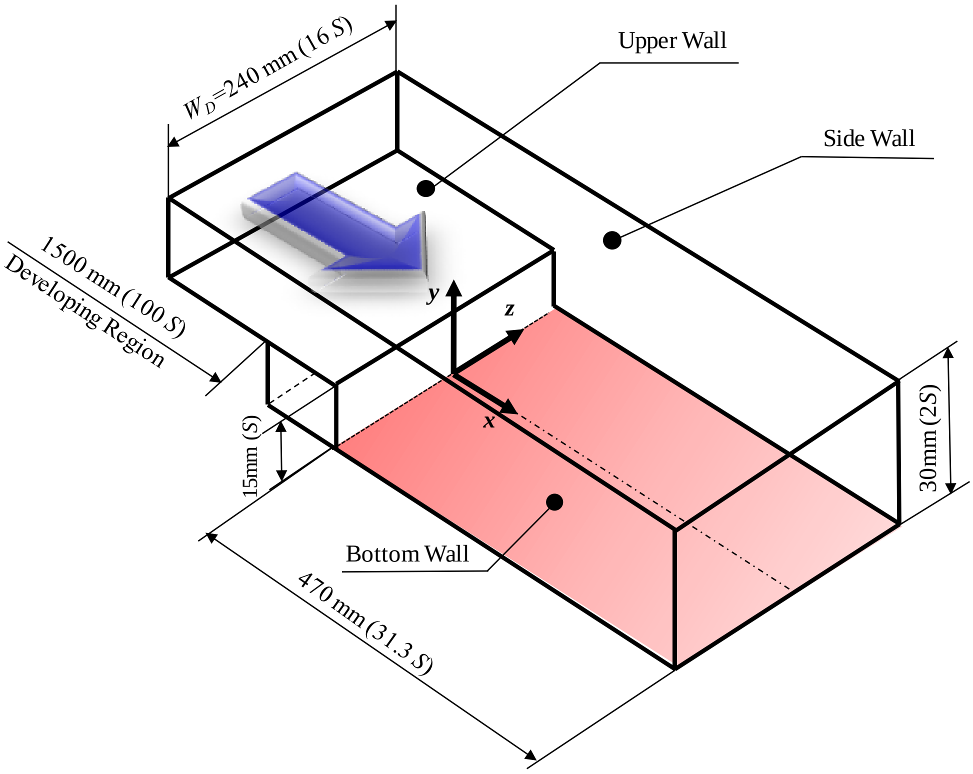

Fig. 4-2. Schematic view of a test section.

4.3 Experimental results and analysis

4.3.1 Time-averaged reattachment points in the spanwise direction of the x-z plane

Reattachment points were extracted by detecting the vectors changing from negative to positive in the streamwise direction near the bottom wall (y/S=0.03) which was mentioned in Chapter 2. Comparative verification (see Fig. 4-3) was done under Re=200 and Re=300, these results of the reattachment position are in perfect agreement with the experimental result of Suyama et al. [14], and the numerical result of Iwai et al. [1]. The distributions of the time-averaged reattachment points for all the representative Reynolds number cases from 200 to 2000 in the x-z plane were investigated. To distinguish the distribution law more clearly under different Reynolds numbers, the flow patterns were divided into three parts in Fig. 4-4 (a)-(c).

As Re=200–400, the reattachment length increases as the Reynolds number increases no matter near the center of the duct or near the side wall. The variation magnitude near the center of the duct is larger than that near the side wall. This growing tendency agrees quantitatively well to that reported by Iwai et al. [1]. The shortest reattachment length is always appearing around z/W_D from 0.4-0.5 near the side wall. As Re=500, 600, the flow pattern has undergone a subtle change, near the side wall, the reattachment points keep at the most upstream position while at z/W_D=0.3–0.1, reattachment length no longer increases monotonically as it approaches the center of the flow channel. The most downstream reattachment point appears at approximately z/W_D = 0.2 and 0.3 where is not the centerline. Near the center of the duct, the reattachment length in Re=600 is smaller than that in Re=500. It could be said that at Re=200, 250, the flow state is quite stable in the whole flow field, and as Re=500, 600, the flow around the side wall still keeps stable while it turns into an unstable state near the center of the duct, Re=400 is a transitional Reynolds number from fully-steady flow to unsteady flow under laminar flow region, due to its comprehensive characteristics of these two flow patterns. At this Reynolds number, the reattachment length near the center of the duct is at the most downstream side and the variation range of the reattachment position is the largest among the Reynolds number interval mentioned above.

As the Reynolds number continues to be increased, as presented in Fig. 4-4 (b), the reattachment length also increases near the side wall but decreases near the center of the duct from Re=600 to Re=700, but as the Reynolds number is over 700, the reattachment length near the side wall starts to gradually move upstream and the same tendency occurs near the center of the duct. So the overall trend of the reattachment position is that moving downstream and turns back, both near the side wall and the center of the duct. However, the critical Reynolds number in which the reattaching movement direction was changed is different near the side wall and duct center. For the reattachment position near the center of the duct, the critical Reynolds number is *Re*=400, for the reattachment position near the side wall, the critical Reynolds number is *Re*=700. Due to careful experimental measurement, another small phenomenon was discovered. That is, part of the reattachment points away from the reattachment concentration area was detected near the center of the duct in *Re*=600 and 700, respectively. It is also worthy to mention that, at z/W_D is about 0.40, breakpoints of reattachment position appear under Reynolds range from 700-1000, which implies that the flow stability of this side wall area was broken. As *Re*=1000-2000, shown in Fig. 4-4 (c), for better comparison, the reattachment position in *Re*=1000 was also superimposed again in this figure, the reattachment position continues to move upstream as Reynolds number increases. The reattachment disconnection phenomenon gradually disappears and could not be found any more at *Re*=1200, the reattachment position near the side wall rebound to the downstream area and the reattachment length becomes shorter and shorter as the Reynolds number increases. The moderate variation magnitude along the spanwise direction indicates that the three-dimensional characteristics are gradually weakening.

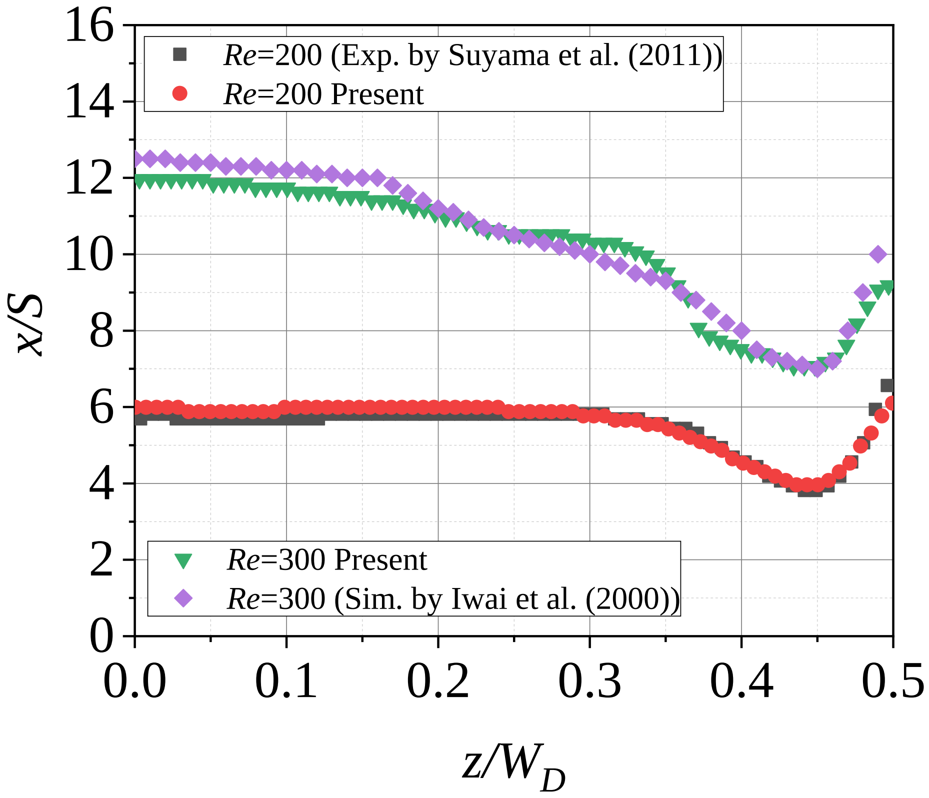

Fig. 4-3. Comparative verification of reattachment position under representative Reynolds number.

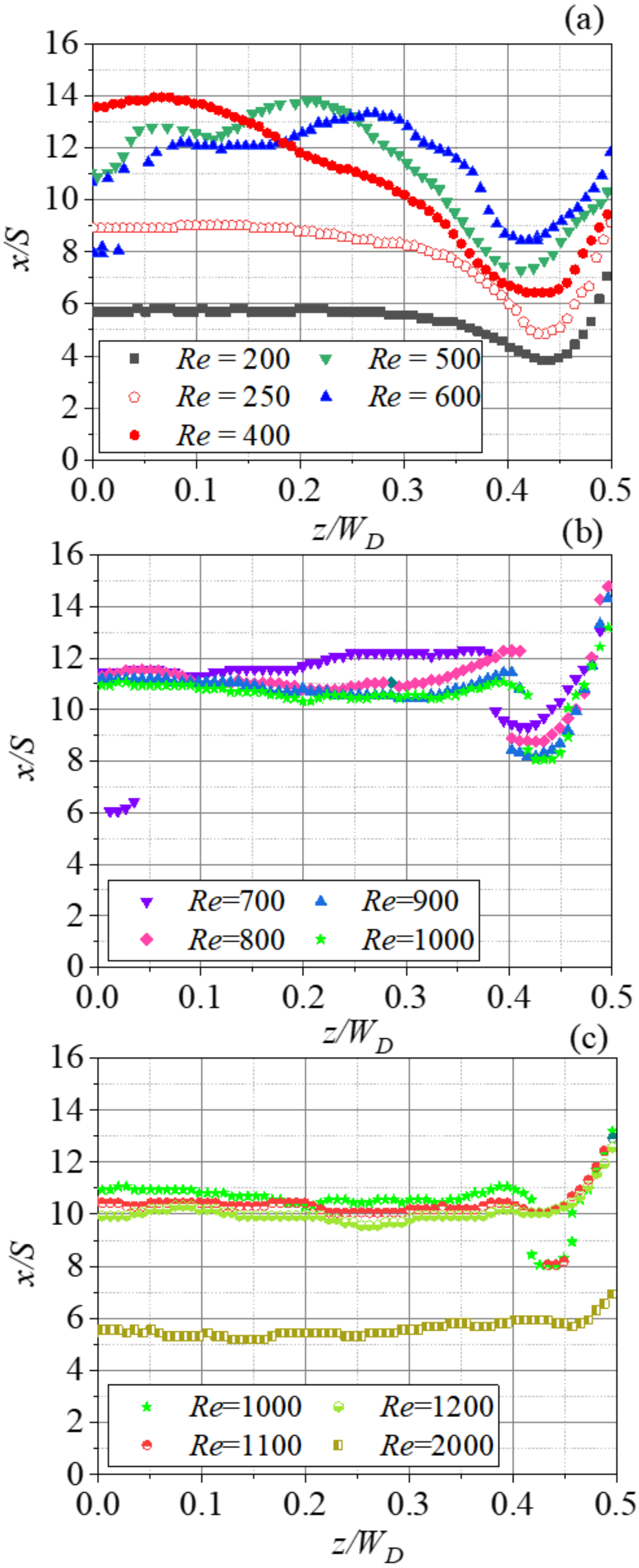

Fig. 4-4. Spatial distribution of time-averaged reattachment positions for each Reynolds number case.

4.3.2 Representative values of the reattachment length

The reattachment length corresponding to Fig. 4-4 is shown in Fig. 4-5 as a function of the Reynolds number. The experimental results of Armaly et al. [15], and Tihon et al., Suyama et al. [4], were superimposed in this figure. A subtle difference could be observed between the present data and that of Suyama et al. [4]. The tendency that the reattachment length near the centerline obtained from the *x-z* plane is sharply increased until *Re* is approximately 400 and experienced a sharp drop until Reynolds number 600 and then gradually decreased corresponds well with the 2D experimental result of Armaly et al.[11,12]. However, the Reynolds number turning point and the reattachment length have large discrepancies between them, the difference between 2D wind tunnel flow and 3D water flow was revealed. The present turning point occurs at a lower Reynolds number, which corresponds well with J. Tihon et al. [13] (*AR*=16.7, *ER*=2). As for the shortest reattachment length location generating near the side wall ($0.4<z/W_D<0.5$), the Reynolds number turning point is at *Re*=700. It is worthy to notice that there are some "breakaway points" near the center of the duct at *Re*=600 and *Re*=700, and near the side wall at *Re*=1100. The flow status has changed under these Reynolds numbers.

Since the turning point of the reattachment length from increase to decrease occurs around *Re*=400 in the center of the duct and the largest reattachment length difference between the center of the duct and near the side wall is also found at *Re*=400, and as mentioned in the introduction, *Re*=400 is a critical Reynolds number. The flow field affecting the heat transfer characteristics in this special unsteady flow state has not been elucidated yet. The following detailed discussions are all based on this critical and representative low Reynolds number aimed to grasp the flow structure, the transient characteristics of instantaneous reattachment positions, and their effects on the heat transfer distribution on the bottom wall adjacent to the step.

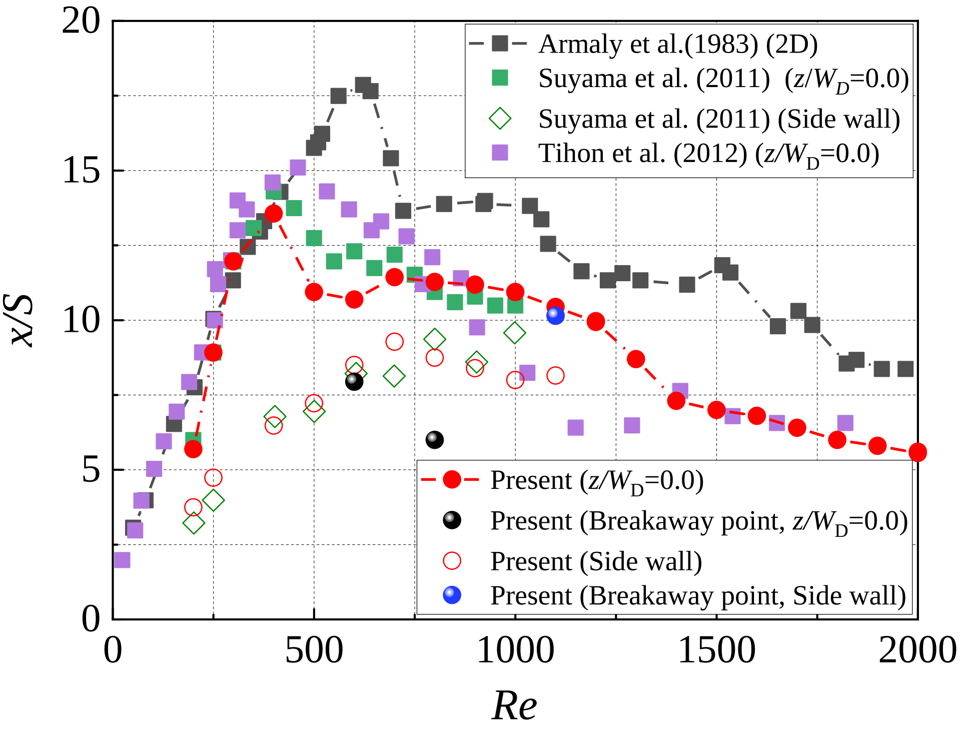

Fig. 4-5. Reattachment points at the center and near the side wall.

4.3.3 Local Nusselt number distribution on the bottom wall

Figures. 4-6 (a)–(f) show the distribution of the local Nusselt number on the bottom wall for the representative Reynolds numbers (*Re*=400-900) which was mentioned in Chapter 3. High heat transfer coefficient distribution in the vicinity of the side wall protrudes to the upstream side compared with the center of the flow path. The reattachment points also protrude like a tongue. It is considered that this sudden upward protrusion of heat transfer distribution near the side wall is due to the rapid migration of reattachment to the upstream side, and it is necessary to grasp further characteristics of flow here. Near the center of the duct, there also exists a relatively high Nusselt number field, the corresponding position of the reattachment point has a sign of turning upstream, leading the similar Nusselt number distribution contour line downstream it. The most downstream reattachment point exists not in the centerline of the duct slightly away from it. It could be concluded that no matter near the side wall or the center of the duct, the Nusselt number will increase on the backside of the area where the reattachment point bulges upstream. As is mentioned in Chapter 3, the impingement of the “jet-like” flow on the stepped wall may cause a minimum to develop in the spanwise distribution of the reattachment region. J. H. Nie et al. [16] reported that “jet-like” flow and its impingement on the stepped wall are mainly responsible for developing a maximum Nusselt number.

Since Reynolds number 400 was used as a key research object for analysis, Fig. 4-7 shows the Nusselt number distribution diagram and the Nusselt number curve along the streamwise and spanwise direction through the center of the maximum Nusselt number position for *Re*=400. The maximum Nusselt number is about 6 at *x*/*S*=14. From the perspective of spanwise direction, high Nusselt number areas are distributed near the side wall at $z/W_D = \pm 0.45$, and low Nusselt number areas are distributed in the duct center. The ratio of the high Nusselt number to the low Nusselt number is about 1.5, so the heat transfer distribution in the spanwise direction needs to be taken into account. Fig. 4-8 shows the magnified view of the local Nusselt number and corresponding time-averaged velocity vectors, time-averaged reattachment points near the bottom wall (*y*/*S*=0.03) obtained by PIV for *Re*=400 case. The low Nusselt number area and high Nusselt number area correspond well to the low-speed reverse flow area behind the step and high-speed flow area near the side wall, respectively. Thus, such a speed magnitude is a cause of heat transfer deterioration or enhancement.

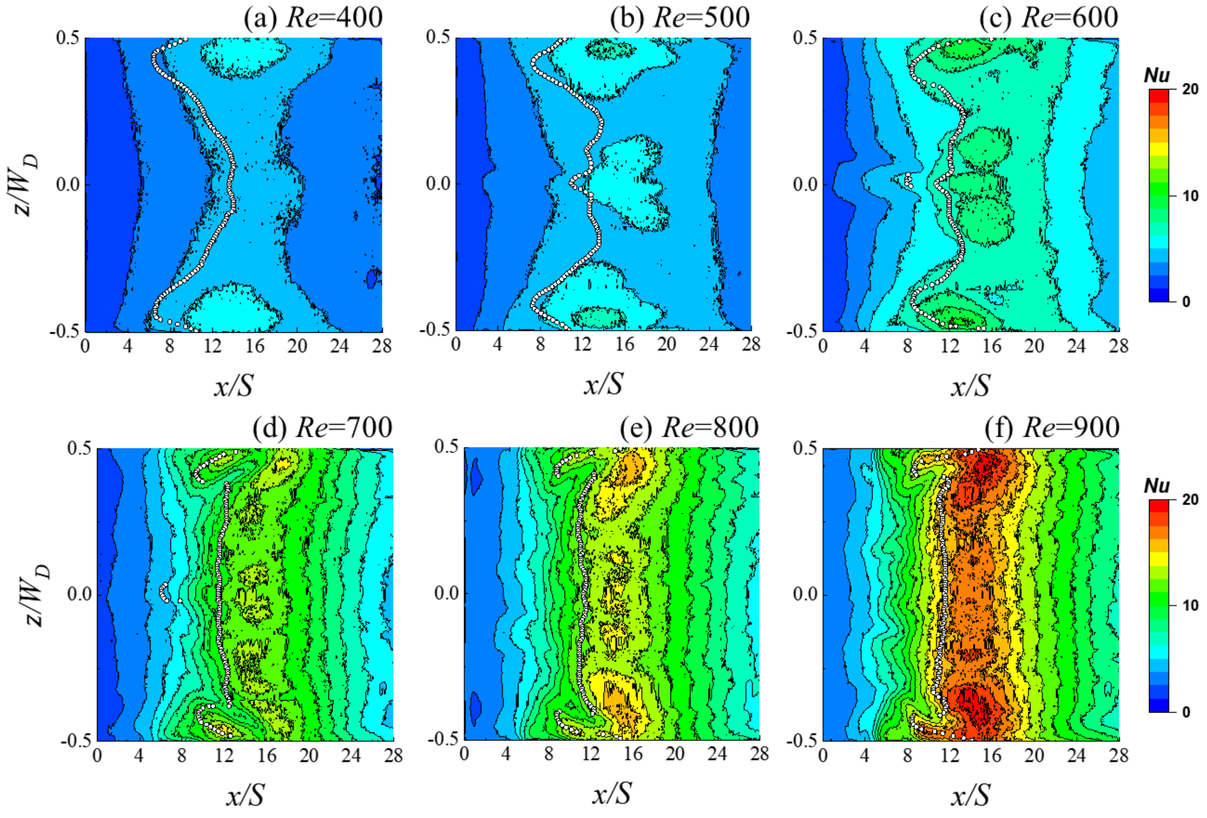

Fig. 4-6. Distribution of the local Nusselt number on the bottom wall for the representative Reynolds number cases.

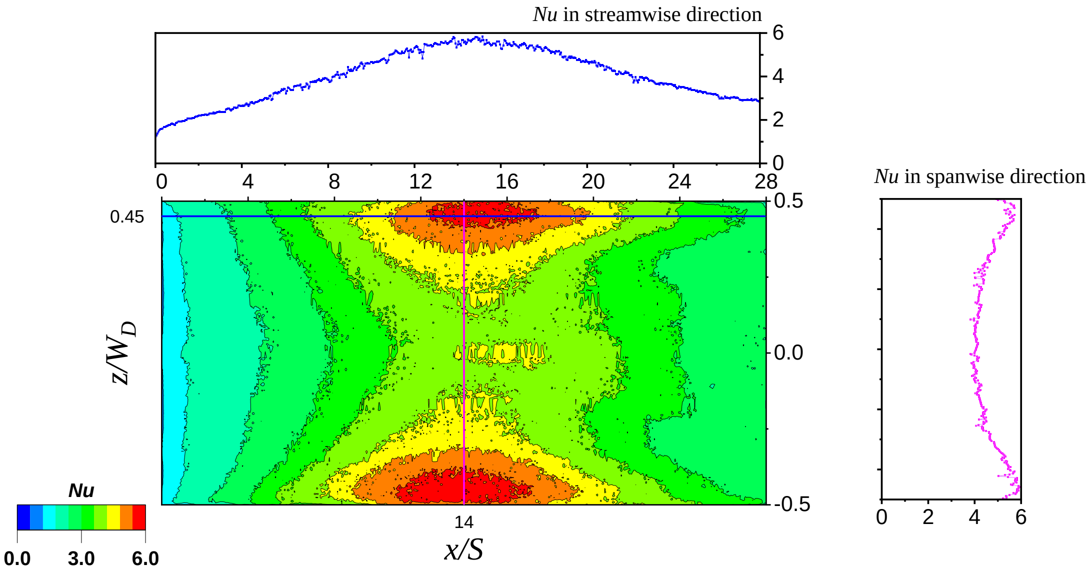

Fig. 4-7. Nusselt number distribution diagram and the Nusselt number value along the streamwise and spanwise direction through the center of the maximum Nusselt number position for *Re*=400.

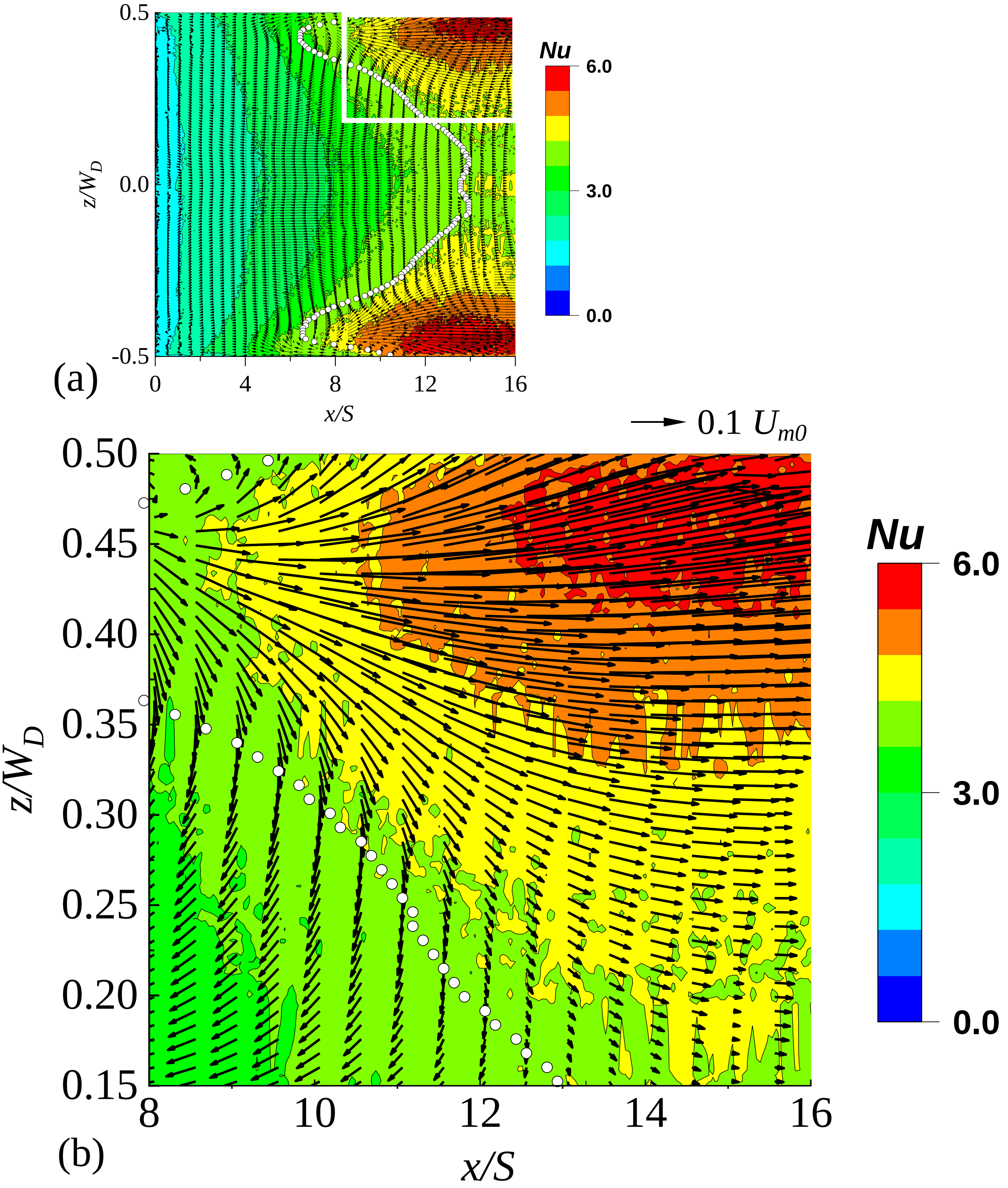

Fig. 4-8. Magnified view of the local Nusselt number and time-averaged velocity vectors near the bottom wall for *Re*=400.

4.3.4 Flow parameters in the x-z plane related to the heat transfer distribution

To explore the similarity between the fluid flow parameters and the Nusselt number, dimensionless velocity component along the streamwise direction u/U_{m0}, spanwise direction w/U_{m0}, the dimensionless fluctuation intensity along the streamwise direction u_{rms}/U_{m0} and spanwise direction w_{rms}/U_{m0} were investigated as presented in Fig. 4-9.

From the superimposed contour figures with the time-averaged velocity vector and reattachment points, the distribution of dimensionless velocity component u/U_{m0} shows high consistency with the Nusselt number distribution contour figure, indicating that u component plays a leading role in heat transfer enhancement. On the other hand, w/U_{m0} component is intensively high near the most upstream reattachment area near the side wall, showing that the flow around here is from the side wall to the center of the duct. As is mentioned in the previous section, the white circle mark represents a time-averaged reattachment position, which characterizes the reattachment length of the main circulation region. While the white triangle mark representing that z-direction wall shear stress is zero, the line connecting these triangle marks is called whirlpool scrubbing line, which is extracted in the region x/S=8-16, z/W_D=0.3-0.5, indicates that there exists a region between the side wall and the triangle mark, which is like the recirculation region in the streamwise direction. Singular points, namely saddle points, nodes and foci which were proposed by Biswas et al. [11] could be also observed here, indicated by gray circular point in Fig. 4-9 (b). The velocity at this point (x/S=8.24, z/W_D=0.48) was zero, which has great consistency with that reported by Biswas et al. using numerical prediction. A flow from the center of the duct to the side wall washes down the bottom wall. Compare this figure with Fig. 4-8, the high Nusselt number region is located downstream of the reattachment point, while side wall whirlpool scrubbing line passes through this region. Thus, the largest Nusselt number area is partially formed by the side wall flow motion washing the bottom adjacent to the side wall.

Fig. 4-9 (c) shows that the high fluctuation intensity of u component is higher near the side wall, the profile of the relative high fluctuation intensity area is greatly similar to that of the relatively high Nusselt number area. Not only the velocity magnitude is large, but also the velocity fluctuates greatly in the streamwise direction. From Fig. 4-9 (d), the velocity in the spanwise direction strongly fluctuates near the most upstream reattachment position, while near the side wall, the fluctuation is a rather low level.

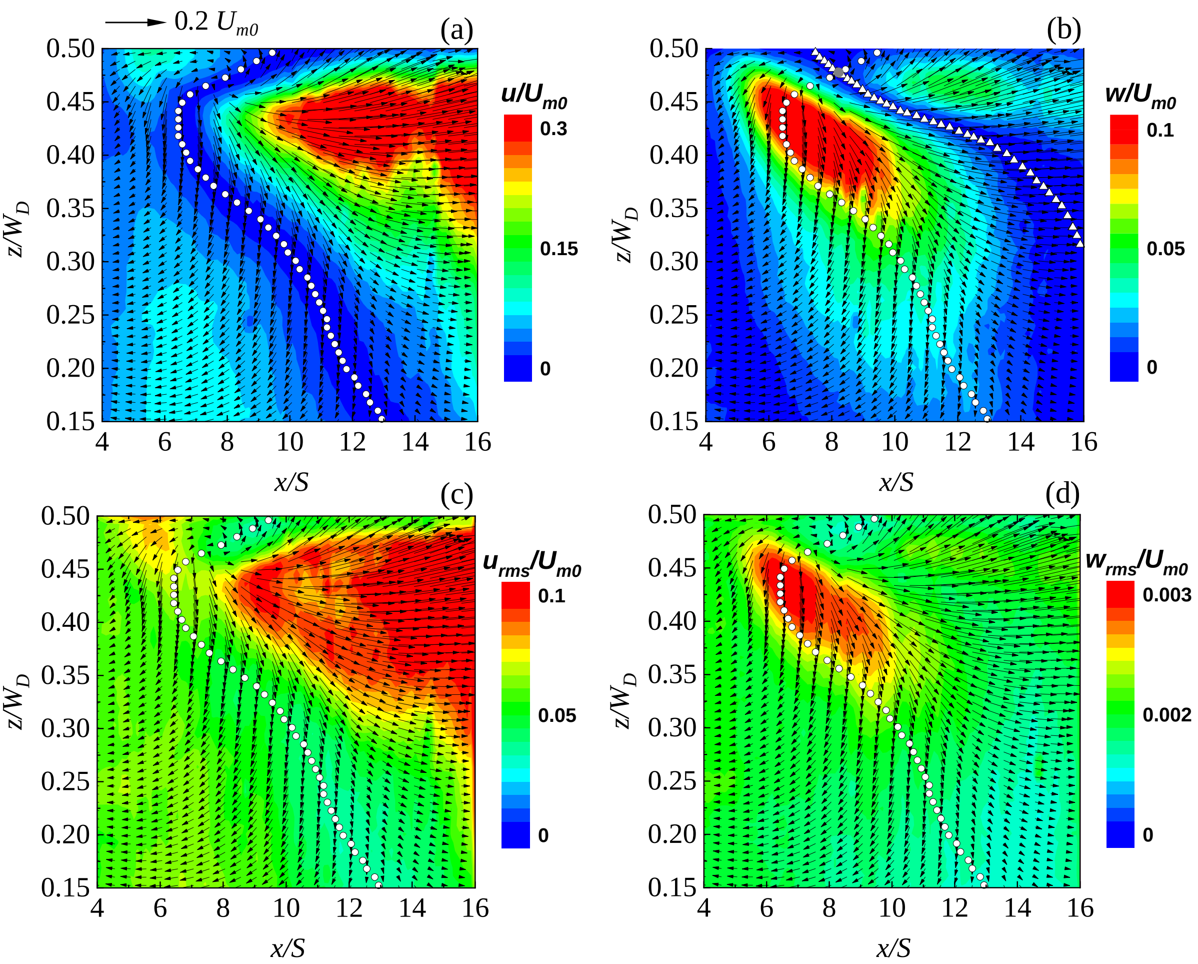

Fig. 4-9. Investigation for factors that may affect the heat transfer coefficient on the bottom wall.

4.3.5 Derivation of the similarity from the Pearson's correlation coefficient

The correlation between heat transfer coefficient and four flow-related parameters could be assessed qualitatively by visually comparing the magnitude of the value in the corresponding position. Furthermore, quantitative analysis is more helpful to our understanding of the nature of flow and heat transfer. Pearson's correlation coefficient [17] (PCC, ρ) described here is a method of quantitatively performing a better assessment. It would be a high positive value if the dimensionless Nusselt number value and flow parameter's value are alike. PCC is based on a linear regression analysis of pairs values taken from different data sources. The formula for the PCC is shown below (Eq. (4-1)):

$$\rho = \frac{\sum_i (x_i - X)(y_i - Y)}{\sqrt{\sum_i (x_i - X)^2}\sqrt{\sum_i (x_i - X)^2}} \tag{4-1}$$

where x_i, y_i are the element in the matrix of heat transfer coefficient and each flow-related parameter, and X, Y are the corresponding mean values. The slope of the linear regression line determines the sign of the coefficient, while the quality of the data's fit to the regression line determines its magnitude [17]. Totally 16384 data elements in the corresponding position of the data matrix were extracted, PCC was calculated and is shown in Table 4-1. The Pearson's correlation coefficient is 0.610 and 0.599 respectively when comparing Nusselt number with u/U_{m0} and u_{rms}/U_{m0}, showing a strong correlation between them. In summary, through the qualitative and quantitative analysis of flow and heat transfer in the *x-z* plane, the high-speed streamwise velocity with high fluctuation intensity and the flow rolled toward the side wall make great contributions to the heat transfer enhancement.

Table 4-1. Pearson Correlation between Nusselt number and several velocity related parameters in the *x-z* plane.

		u_{rms}/U_{m0}	w_{rms}/U_{m0}	u/U_{m0}	w/U_{m0}
Nu	Pearson Correlation	0.599**	0.130	0.610**	0.328
	N	16384	16384	16384	16384

** Correlation is significant at the 0.01 level (2-tailed)

4.3.6 Existence probability of the flow reattachment position

Fig. 4-10 shows the existence probability of the flow reattachment which was briefly mentioned in Chapter 2, to further investigate and more clearly clarify the spatial variations of the reattachment phenomena on the bottom wall as time advances and its effects on heat transfer. The locations where the streamwise velocity took zero were detected spatially at each time frame, then stored at each location over the measuring time and finally divided the stored number by the total frame numbers [14]. The time-averaged translucent reattachment curve replaces the reattachment plots shown in the previous figure, to see the contour distribution on the backside more clearly.

On the contrary to the distribution of u/U_{m0} and u_{rms}/U_{m0}, the existence probability value in the corresponding region where the Nusselt number is relatively high is quite low. No reattachment points exist there. The fluctuation of the reattachment position has no direct influence on heat transfer enhancement. However, the variation of existence probability near the side wall has a high value remaining in a narrow area along the time-averaged position, implying that the reattached flow here is quite stable. The highest value is located at the most upstream reattachment position. All instantaneous reattachment points are fan-shaped swinging around this position in which fluid meets without much movement. The low-value area swings much wider around the time-averaged reattachment points near the center of the duct, suggesting that the fluctuation of this stepped flow may begin at the center of the duct. As mentioned above, immediately downstream of this location, the Nusselt number is very large. Due to fan-shaped swinging, the water flow accumulates downstream of this fixed point, forming relatively strong fluctuations, thereby accelerating the heat exchange at this location and improving the heat transfer efficiency here. Next, the 3D unsteady flow structure around here needs to be further studied.

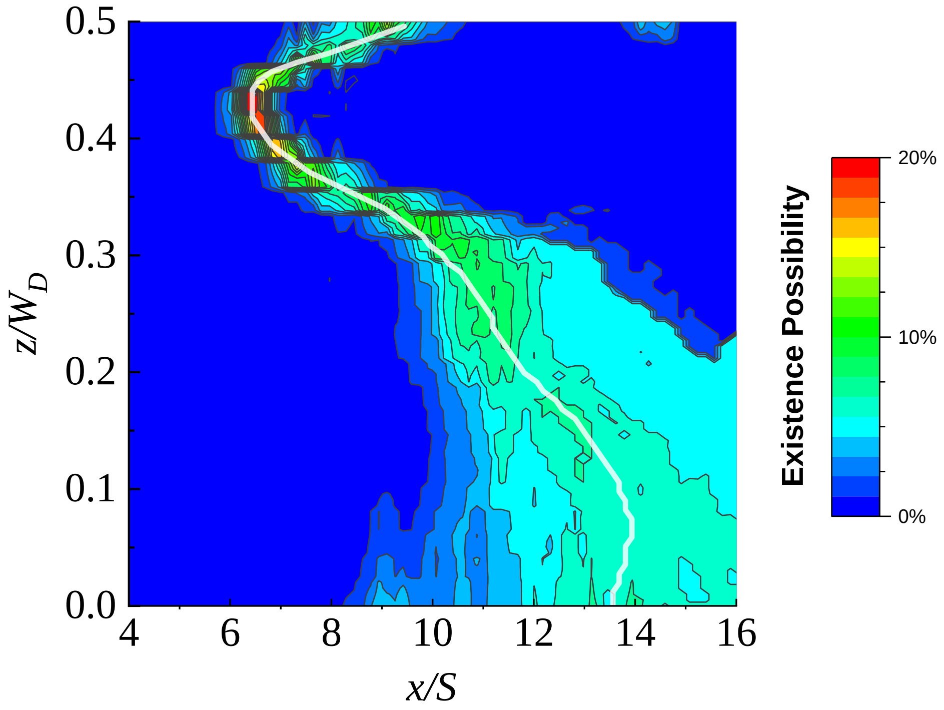

Fig. 4-10. Existence possibility of the flow reattachment; The white translucent line represents the time-averaged reattachment curve.

4.3.7 Time-averaged velocity vector

4.3.7.1 Time-averaged velocity vector in the x-y plane

The mean velocity vectors in *the x-y* plane for z/W_D=0.0, 0.1, 0.2, 0.3 and 0.45 are shown in Fig. 4-11, and the relationship with the heat transfer is considered. In each case, the results of five cross-sections from the vicinity of the side wall (z/W_D=0.45) to the center of the channel (z/W_D=0.0) are displayed side by side. In each figure, the average reattachment position is indicated by ▲ mark and the average separation position is indicated by ▼ mark. A large circulation region spreads after the step at the center position on the flow path, and the flow reattaches to the bottom wall and develops in the downstream flow. When the spanwise direction position is z/W_D=0.1, 0.2, it seems that the flow field is not much different from the center of the flow path, but as the reattachment position advances in the spanwise direction, it moves to the upstream side, the flow towards the bottom wall goes stronger. Furthermore, at z/W_D=0.45 near the side wall, there is also a circulation region near the upper wall. Therefore, it is understood that the flow along the bottom wall becomes strong by meandering the flow affected by the secondary circulation region near the upper wall.

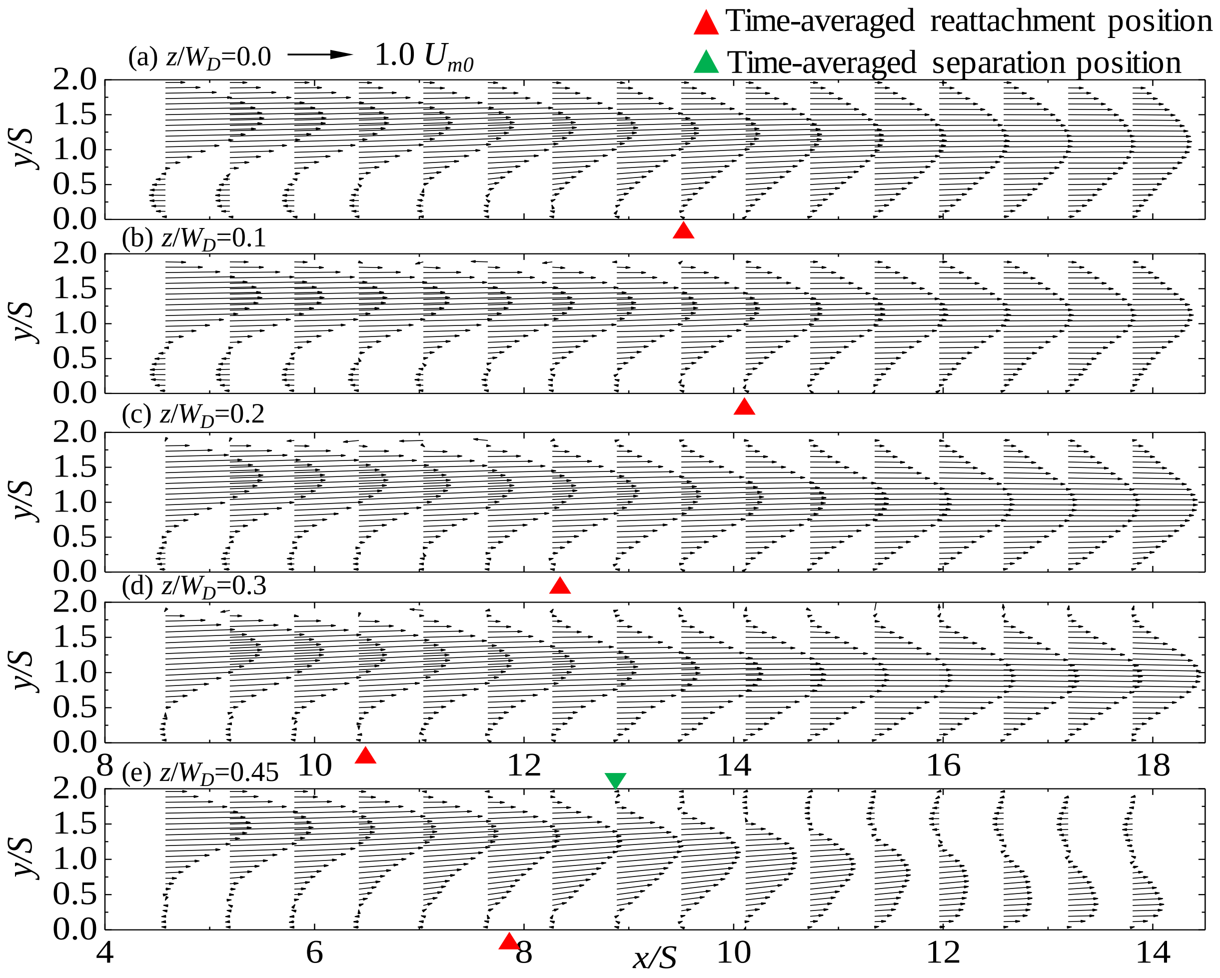

Fig. 4-11. Mean velocity vectors in x-y plane of Re=400 for z/W_D=0.0, 0.1, 0.2, 0.3, and 0.45.

4.3.7.2 Time-averaged velocity vector in the y-z plane

Figures 4-12 (a), (b), (c), and (d) show time-averaged velocity vectors $\bar{u}-\bar{w}$ in y-z plane at flow direction positions x/S=10, 12, 14, and 16 at Re=400. From Fig. 4-12, it is possible to confirm the downwash flow that was reported by Nishii et al. [10] and Suyama et al. [4] at x/S=10 and z/W_D = 0.4 to 0.5. As it goes further downstream (x/S=12 to 14), it flows toward the side wall and then turns to be a flow toward the upper wall. At x/S=14 where the heat transfer is relatively high, a longitudinal vortex like flow is generated near the side wall, as x/S increases downstream to 16, this kind of vortex flow becomes weak. Thus, the generation of longitudinal vortices has a certain promotion effect on heat transfer enhancement.

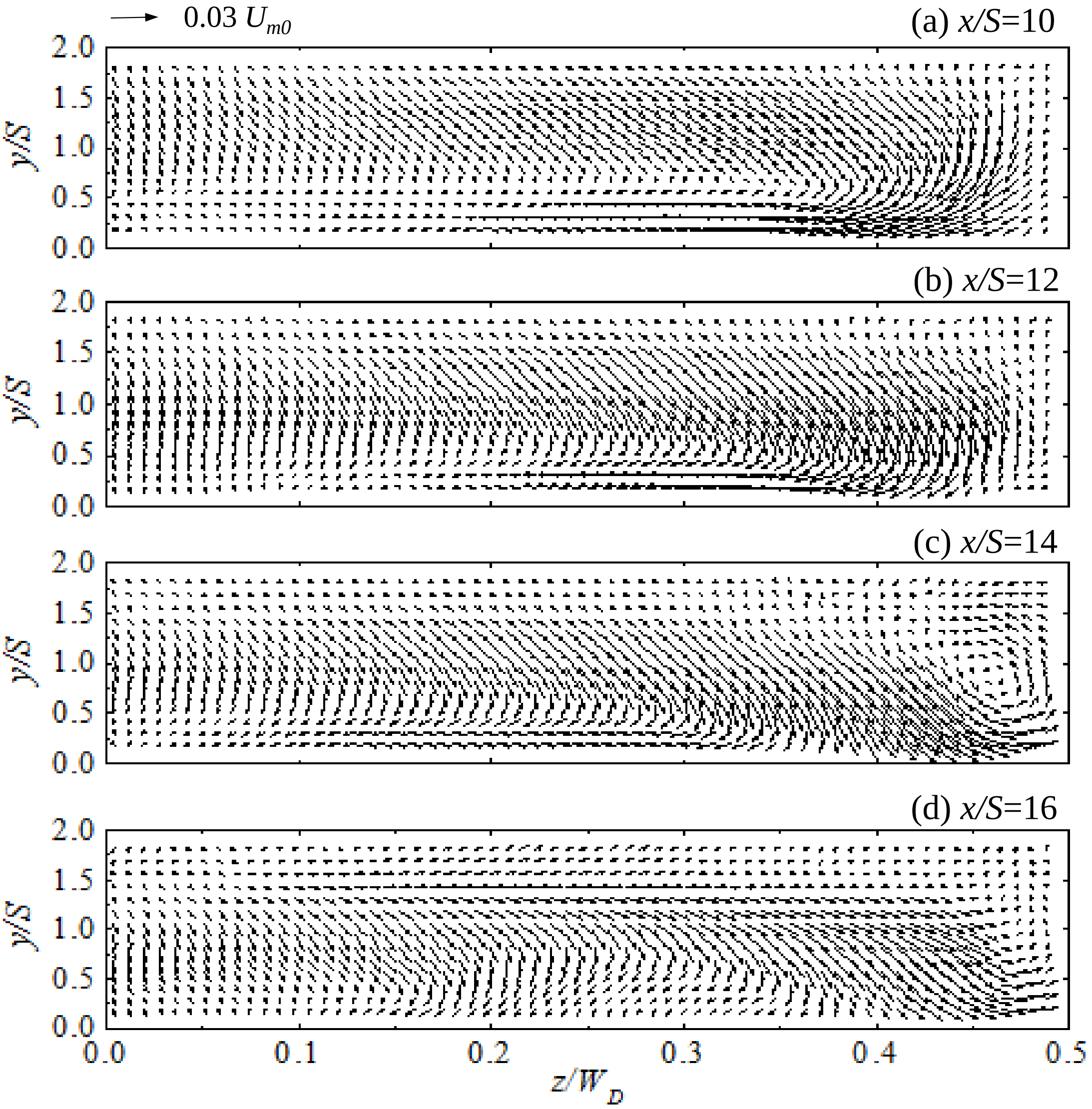

Fig. 4-12. Mean velocity vectors in *y-z* plane of *Re*=400 for *x/S*=10.0, 12.0, 14.0 and 16.0.

4.3.7.3 3D velocity vector in the *y-z* plane at *x*/*S*=14

A Stereo PIV experiment was done and the 3D velocity vector, the *Nu* distribution and the reattachment line were superimposed in one bird-view graph (see Fig. 4-13, 4-14). The velocity vector was taken in the *y-z* plane and *x*/*S* was chosen 10-14 according to the results from Fig. 4-7. The three-dimensional velocity vector information of the three *y-z* planes along the flow direction is represented in Fig 4-13. It could be found that the flow that causes heat transfer enhancement near the side wall has similar three-dimensional flow structures along the streamwise direction. Therefore, the *y-z* plane corresponding to the largest Nusselt number at (*x/S*=14) was selected as the main investigated plane to summarize the general law.

The velocity vector projections of the *y*-*z* plane at *x*/*S*=14 to the bottom wall and the flow entrance section are also shown in Fig. 4-14 so that its components in various directions could be seen more clearly. Near the duct center, the vector in the height direction shows a distorted form. The direction of the vector near the upper wall and bottom wall is from side wall to the center duct, while in the middle height of the water channel, it changes into the opposite direction. In areas where the Nusselt number is small, this spanwise distortion becomes very inconspicuous through the projection view of the velocity vector on the flow entrance cross-section. Pay attention to the side wall, the flow turns to the duct center in the middle height of the channel while it turns to the side wall near the height approaching the upper wall and bottom wall, the downwash flow [1] could be also confirmed near the bottom wall adjacent to the side wall. The velocity vector is also twisted up and down like that near the duct center determined from the streamwise projection view of the velocity vector on the bottom wall. 3D flow structures around this area is quite complicated.

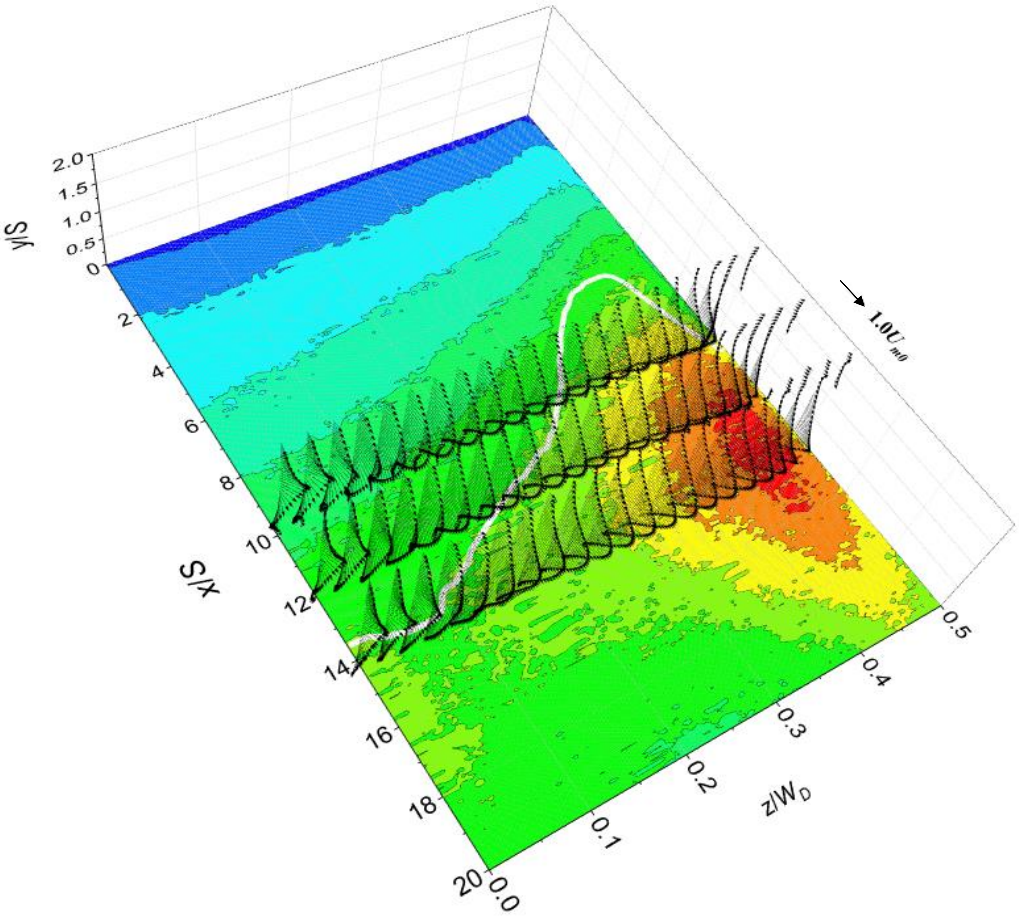

Fig. 4-13. Superimposed diagram of Nusselt Number distribution and 3D velocity vector in the *y*-*z* plane at fixed *x*/*S*=10, 12, 14.

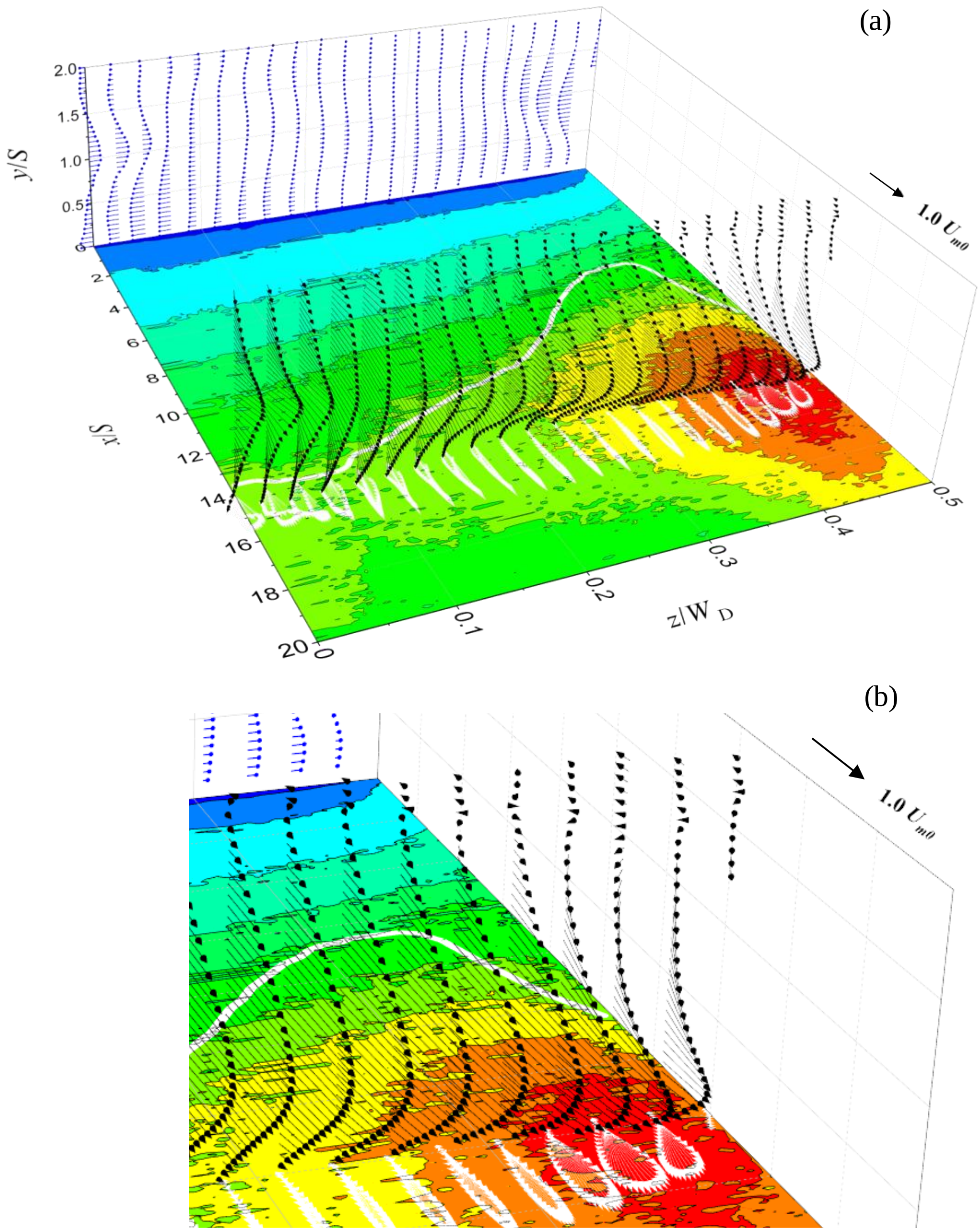

Fig. 4-14. Superimposed diagram of Nusselt Number distribution and 3D velocity vector in the *y*-*z* plane at fixed *x/S*=14.

4.3.7.4 Fluctuation intensity, time-averaged velocity, and vorticity distributions in the *y-z* plane at high heat transfer streamwise position (*x*/*S*=14).

In order to have a clearer understanding of the flow near the higher heat transfer region, dimensionless v/U_{m0}, w/U_{m0}, v_{rms}/U_{m0}, w_{rms}/U_{m0}, and vorticity value colormaps superimposed with velocity vector in the *y-z* plane at x/S=14 were investigated.

As shown in Fig. 4-15, the dimensionless velocity component w/U_{m0} is quite high at z/W_D=0.45 near the bottom wall, the flow was accelerated here to the side wall, moreover, the dimensionless velocity component v/U_{m0} toward the bottom wall is also quite high. This kind of corner flow plays an important role to quickly transfer the heat around there, resulting in enhanced heat transfer on the bottom wall.

To understand the flow instability effects on heat transfer, Fig. 4-15 (c) and (d) were presented. It could be indicated that the turbulent intensity no matter in the spanwise direction or the height direction is pretty high near the upper wall. This is because the fluid from the upper end of the vortex (this vortex could be determined clearly in Fig. 4-15 (e)) impinges the fluid flowing toward the side wall near the upper wall surface, resulting in relatively strong fluctuations. Near the side wall, although the turbulent intensity is lower than that near the upper wall, but higher than that in the other regions near the bottom wall. A high vorticity value area appears above the high Nusselt number region. Thus, the coupling effects of relatively high fluctuation intensity, strong vortex with high-speed velocity component downwashing the bottom wall could make a positive contribution to the heat transfer enhancement. And it’s not just what Nie et al. [16, 18] described: “Jet-like” flow is the main factor that enhances the heat transfer on the lower wall

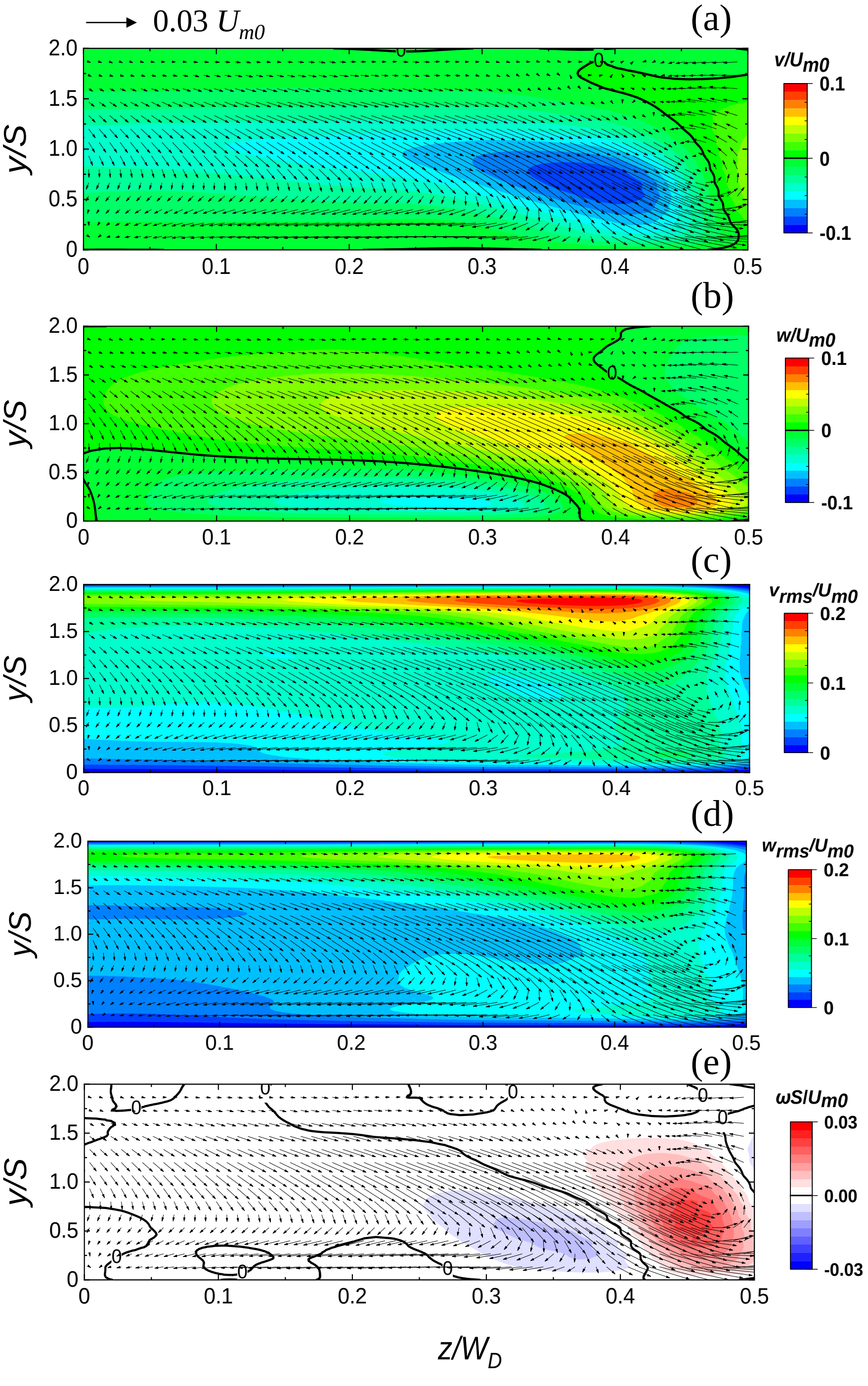

Fig. 4-15. Velocity-related parameters superimposed with velocity vector at x/S=14.

4.3.7.5 Fluctuation intensity, time-averaged velocity and vorticity distribution in the x-y plane at high heat transfer spanwise position (z/W_D=0.45).

Figure 4-16 shows dimensionless time-averaged velocity u/U_{m0}, v/U_{m0}, the fluctuation intensity u_{rms}/U_{m0}, v_{rms}/U_{m0}, and vorticity distribution in y-z plane at z/W_D=0.45. Focusing on the time-averaged velocity vector, it can be seen that there is a reverse-speed region near the upper wall shown in Fig. 4-16 (a). The mainstream flow space is forced to be narrow and the fluid flows meandering toward the bottom wall surface. Therefore, it is considered that the velocity near the bottom wall adjacent to the side wall is higher than that at the center of the flow path where there is no circulation region on the upper wall surface. The dimensionless velocity magnitude u/Um_0 in the streamwise direction shows largest value directly above the high Nusselt number area. Fig. 4-16 (c) and (d) also shows the fluctuation intensity distribution of streamwise component u and height component v. The high value region of u_{rms}/U_{m0} is located at x/S=15-17, wich is a little bit downstream of the maximum heat transfer position. While the high value region of v_{rms}/U_{m0} is located at x/S=13-18, which is near the maximum heat transfer position. From this point of view, it can be concluded that large velocity magnitude in the streamwise direction and strong fluctuation in the height direction occurs near the bottom wall makes a major contribution to heat transfer enhancement.

4.3.7.6 Phase-averaged velocity structures

Figure 4-17 shows the velocity signal v changes over time in the height direction at the maximum position of v_{rms}. A fast Fourier transform (FFT) analysis of the v was carried out as presented in Fig. 4-18. Low-pass filter and rectangular window were used for this FFT analysis, low-pass filter reduces high frequencies of signal according to user desired order and cutoff frequency. Rectangular window is the simplest window, equivalent to replacing all but N values of a data sequence by zeros, making it appear as though the waveform suddenly turns on and off. The dominant frequency was 0.3 Hz, the phase averaging process was performed using this frequency. In order to see how the flow structure in one cycle affects the distribution of the heat transfer in x-y plane. Fig. 4-19 shows the phase averaged velocity in x-y cross section of the region where the maximum heat transfer coefficient values of Reynolds number 400 appears. The vertical axis shows the height direction and the horizontal axis shows the flow direction. The period is divided into four parts. Furthermore, the ↑ mark indicates the position of the peak Nusselt number on the bottom wall surface of the cross-section. It could be seen that the mainstream without large scale vortex passing near the bottom wall surface is traveling to intensively downwash and wind upward the fluid on the bottom wall surface from *x*/*S*=12 to 16. Considering that the region where the maximum heat transfer coefficient appears at *x*/*S*=14, it is considered that the heat transfer was promoted because the periodic downward and upward fluid motion supplies cold fresh fluid of the mainstream to the bottom wall and pushes the hot fluid near the wall toward mainstream, violent heat exchange occurs here.

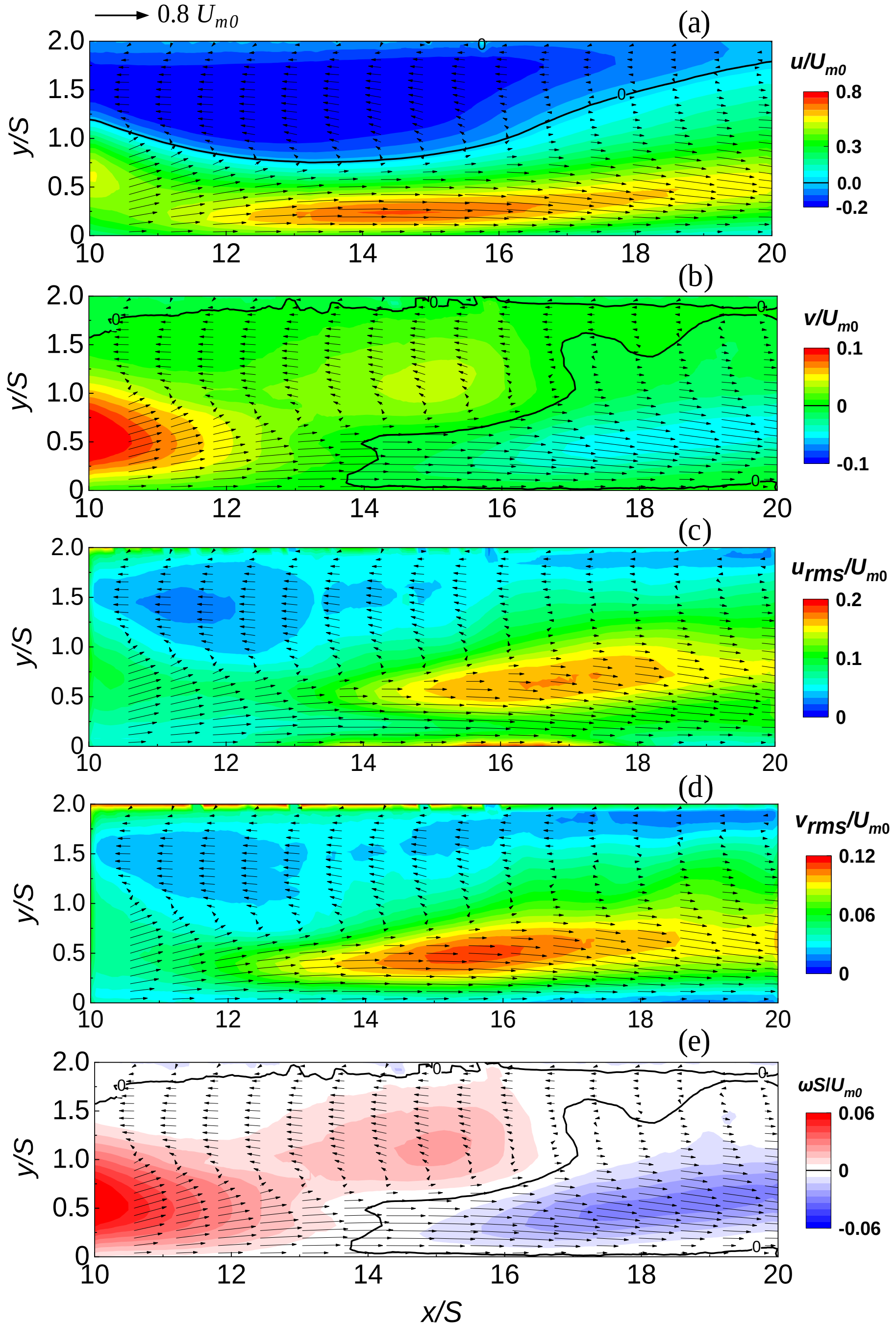

Fig. 4-16. Velocity fluctuation intensity and vorticity contour superimposed with velocity vector.

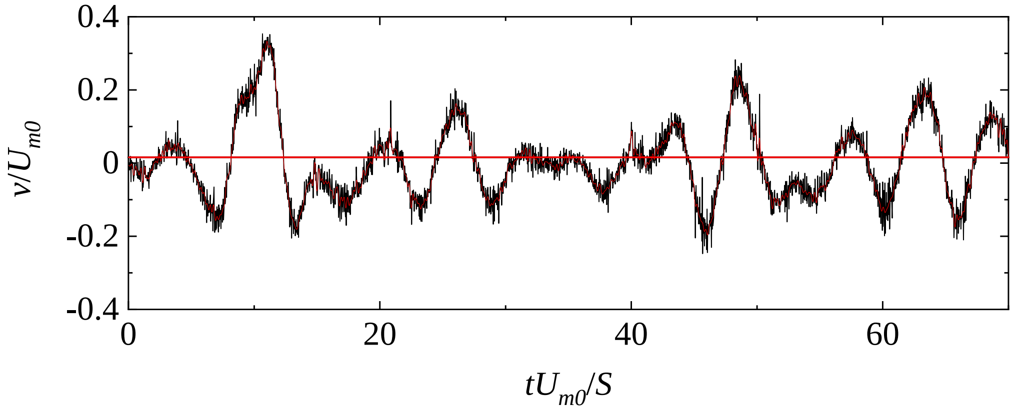

Fig. 4-17. Velocity signal of *v* component at the max position of velocity fluctuation for *Re*=400.

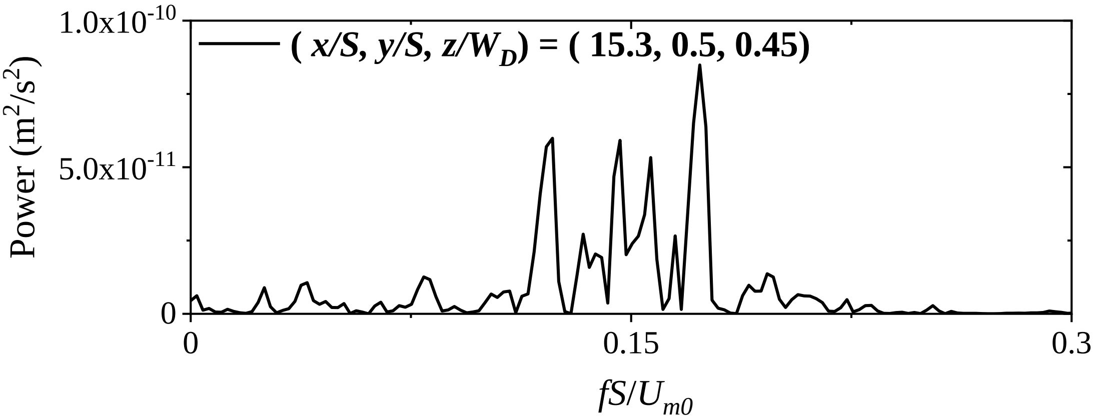

Fig. 4-18. Analysis of velocity component at the max position of velocity fluctuation.

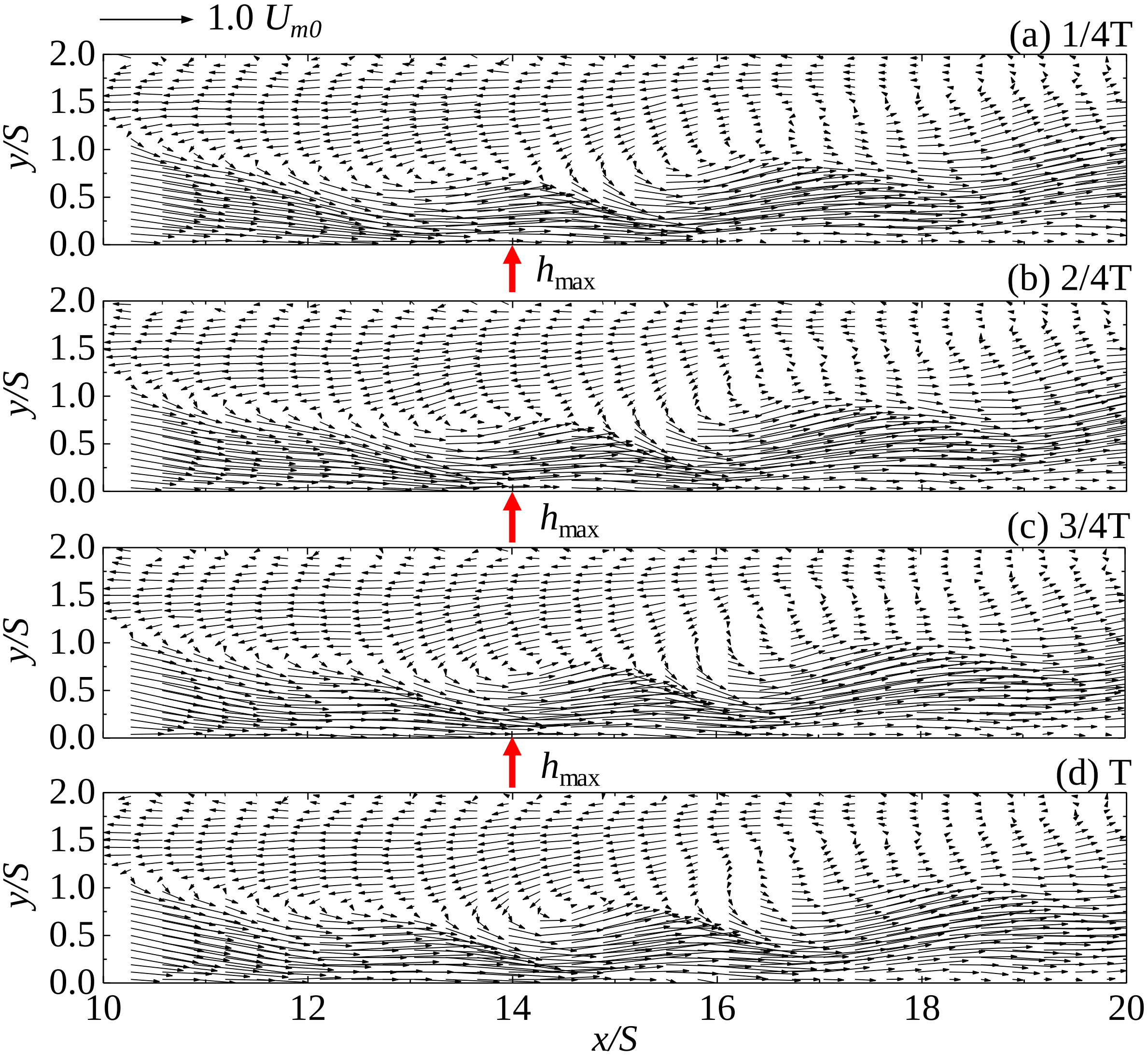

Fig. 4-19. The phase-averaged velocity distribution in x-y plane at z/W_D =0.45 for *Re*=400.

4.4 Conclusion and discussions

Heat transfer experiment using a thermo-sensitive liquid crystal sheet was carried out in a closed stepped water channel with an aspect ratio of 16 and expansion ratio of 2. Spatial distributions of local heat transfer coefficients on the bottom wall were measured under laminar flow conditions. Velocity measurements by 2D PIV and Stereo PIV were also conducted to build the relationship between heat transfer and 3D flow structures. The main results obtained in this study are briefly summarized as follows.

Through careful velocity measurement by PIV, the reattachment locations were extracted under various Reynolds numbers from 200 to 2000. Its three-dimensional characteristics were fully confirmed. The maximum reattachment length near the duct center appears at approximately *Re*=400 in which the largest difference in the reattachment length between the center of the duct and near the sidewall is generated. Thus, the flow and heat transfer investigations were conducted mainly focusing on this characteristic Reynolds number.

The spatial local heat transfer coefficient varies a lot in the spanwise direction in every Reynolds number cases from 400 to 900. It is extremely high near the side wall compared with other areas in each Reynolds number case. The high heat transfer coefficient appears in the immediate vicinity of the reattachment location which is curved upstream. Integrating the velocity-related parameters of different cross-sections, the velocity vector of the Stereo PIV and the phase-averaged velocity vectors, the heat transfer enhancement mechanism near the side wall is clarified. A flow near the side wall from the inlet entrance meanders between the circulation zone adjacent to the step and the secondary recirculation zone near the upper wall, as the flow arrives in the region x/S=10 to 12, it turns into a clockwise flow from the upper wall, passing through the side wall and washes downward the bottom wall. In the downstream side, at x/S=14 where the heat transfer is high, a large counterclockwise flow which is generated from the upper wall, passing through the bottom wall and side wall and then flows back to the upper wall could be observed above the high heat transfer area. Furthermore, this kind of flow has high-speed velocity magnitude and obvious periodicity, making sure that the hot and cold fluid there can be mixed thoroughly and quickly taken away. Thus, other detailed flow factors that affect the heat transfer enhancement besides “jet-like” flow [4, 18] are proposed and clarified.

References

[1] H. Iwai, K. Nakabe, and K. Suzuki, "Flow and heat transfer characteristics of backward-facing step laminar flow in a rectangular duct," *International Journal of Heat and Mass Transfer,* vol. 43, no. 3, pp. 457-471, 2000.

[2] H. Iwai, K. Nakabe, K. Suzuki, and K. Matsubara, "The effects of duct inclination angle on laminar mixed convective flows over a backward-facing step," *International Journal of Heat and Mass Transfer,* vol. 43, no. 3, pp. 473-485, 2000.

[3] J. Nie and B. Armaly, "Reverse flow regions in three-dimensional backward-facing step flow," *International Journal of Heat and Mass Transfer,* vol. 47, no. 22, pp. 4713-4720, 2004.

[4] J. Nie and B. F. Armaly, "Three-dimensional convective flow adjacent to backward-facing step-effects of step height," *International Journal of Heat and Mass Transfer,* vol. 45, no. 12, pp. 2431-2438, 2002.

[5] J. Nie and B. F. Armaly, "Reattachment of three-dimensional flow adjacent to backward-facing step," *J. Heat Transfer,* vol. 125, no. 3, pp. 422-428, 2003.

[6] K. Inaoka and M. Senda, "Heat Transfer and Fluid Flow Characteristics of a Backward-Facing Step Flow in a Duct," *Transactions of the Japan society of mechanical engineers Series B,* vol. 79, no. 804, pp. 1651-1663, 2013, doi: 10.1299/kikaib.79.1651.

[7] K. Inaoka, K. Nakamura, and M. Senda, "Heat transfer control of a backward-facing step flow in a duct by means of miniature electromagnetic actuators," *International Journal of Heat and Fluid Flow,* vol. 25, no. 5, pp. 711-720, 2004.

[8] J. C. Lin, "Review of research on low-profile vortex generators to control boundary-layer separation," *Progress in Aerospace Sciences,* vol. 38, no. 4-5, pp. 389-420, 2002.

[9] L. Chen, K. Asai, T. Nonomura, G. Xi, and T. Liu, "A review of backward-facing step (BFS) flow mechanisms, heat transfer and control," *Thermal Science and Engineering Progress,* vol. 6, pp. 194-216, 2018.

[10] E. Erturk, "Numerical solutions of 2-D steady incompressible flow over a backward-facing step, Part I: High Reynolds number solutions," *Computers and Fluids,* vol. 37, no. 6, pp. 633-655, 2008.

[11] G. Biswas, M. Breuer, and F. Durst, "Backward-facing step flows for various expansion ratios at low and moderate Reynolds numbers," *Journal of Fluids Engineering,* vol. 126, no. 3, pp. 362-374, 2004.

[12] S. Yamada, K. Okamoto, T. Nitta, M. Motosuke, and S. Honmami, "Flow structures by synthetic jets over a backward facing step in low Reynolds number," in *47th AIAA Aerospace Sciences Meeting including The New Horizons Forum and Aerospace Exposition*, 2009, p. 576.

[13] B. F. Armaly, F. Durst, J. C. F. Pereira, and B. Schönung "Experimental and theoretical investigation of backward-facing step flow," *Journal of Fluid Mechanics,* vol. 127, no. -1, pp. 473-496, 1983.

[14] N. Suyama, K. Inaoka, and M. Senda, "Flow Characteristics Over a Backward-Facing Step in a Duct in Low Reynolds Number Range," in *ASME/JSME 2011 8th Thermal Engineering Joint Conference*, 2011, vol. ASME/JSME 2011 8th Thermal Engineering Joint Conference, T10084, doi: 10.1115/ajtec2011-44246. [Online]. Available: https://doi.org/10.1115/AJTEC2011-44246

[15] B. F. Armaly, F. Durst, J. Pereira, and B. Schönung, "Experimental and theoretical investigation of backward-facing step flow," *Journal of Fluid Mechanics,* vol. 127, pp. 473-496, 1983.

[16] J. H. N. F. Armaly, "Three-dimensional convective flow adjacent to backward-facing step - effects of step height," *International Journal of Heat & Mass Transfer,* 2002.

[17] H. Pairleitner, H. Steiner, G. Hasenoehrl, and A. Staudach, "Three‐dimensional power Doppler sonography: imaging and quantifying blood flow and vascularization," *Ultrasound in Obstetrics and Gynecology: The Official Journal of the International Society of Ultrasound in Obstetrics and Gynecology,* vol. 14, no. 2, pp. 139-143, 1999.

[18] B. F. Armaly, A. Li, and J. Nie, "Measurements in three-dimensional laminar separated flow," *International Journal of Heat and Mass Transfer,* vol. 46, no. 19, pp. 3573-3582, 2003.

CHAPTER 5

Transitional Flow and Heat Transfer over a Backward-Facing Step with an Inserted Cylinder

5.1 Introduction

BFS flow is among the most fundamental models to trigger stepwise flow separation and reattachment. The study of such flows has been gaining prominence because of its extensive application in energy system equipment, dump combustors, turbine blades, and heat-exchanging devices [1-3].

Laminar and turbulent flow in a BFS channel has been extensively investigated using experimental [4-7] and numerical methods [8-14]. Additionally, three-dimensional BFS flow has become a popular field of study in fluid dynamics since Armaly et al. proposed the advancement of this method [4]. The importance of three-dimensional characteristics research has been mentioned in the previous chapters.

Few studies have been conducted on the heat transfer characteristics in the unsteady flow regime over a BFS because of instability and complexity issues. Kitoh et al. [15] reported the effects of expansion ratios on the time-averaged reattachment length and improved heat transfer characteristics at an unsteady flow state using the DNS. Xu, Zou et al. [16] numerically investigated the unsteady flow over a three-dimensional BFS. Periodic flow instability influences the heat transfer augmentation at the center of the bottom wall. Tihon et al. [17] experimentally studied the unsteady laminar flow (water) with variable expansion ratios at moderate Reynolds numbers. Their results suggested that the pulsatile inlet flow is essential in the flow structures, reattachment length, and upper wall recirculation zone.

Recently, researchers investigated the influence of obstacles inserted in the BFS on the flow fields and heat transfer. Kumar and Dhiman [18] numerically simulated the flow and thermal fields in a BFS with different cross-stream positions (y_c) of the inserted cylinder in the laminar regime ($1 \leq Re_S \leq 200$). The maximum increase in pressure drop for y_c=1.5 at Re_S=200 was approximately 37%, whereas the maximum Nusselt number increased by approximately 155% when compared with the unobstructed case. Selimefendigil and Öztop [19] applied the system identification method to forecast the thermal property with the effects of pulsating flow over a BFS using a fixed cylinder. A significant enhancement of heat transfer was observed with an increase in Reynolds number, pulsation frequency, and nanoparticle volume fraction. Further, they numerically investigated the effects of the pulsating flow on the heat transfer in a BFS equipped with an adiabatic thin fin. The adiabatic thin fin was not effective for heat transfer. Mohammed et al. [20] simulated a convective nanofluid flow in a BFS with baffles combining laminar and turbulent flows. The locations, distance, and height of the baffles were observed to significantly influence the heat transfer rather than the number and width of the baffles. Selimefendigil and Öztop [21] used a BFS with a corrugated bottom wall in a forced convection nanofluid in their study of heat transfer characteristics. The results showed that the height and length of the corrugation wave-influenced heat transfer enhancement.

The analysis and study of transitional forced convection flow and heat transfer over a backward-facing step by inserting a cylinder is unexplored. In Chapter 4, what kind of flow will improve the heat transfer efficiency of the bottom wall has been studied in detail. Then the focus of this chapter is to set the geometric transformation of the stepped flow model, that is, inserting a cylinder to form an unsteady flow condition near the circulation region. Considering the calculation cost and research purpose, this chapter uses two-dimensional simulation instead of three-dimensional simulation. It is also possible and enough to clarify how the unsteady flow affects the heat transfer of the bottom wall in a stepped duct, and how to improve the heat transfer enhancement. Thus, the primary objective of this study is to transform the laminar flow into a transitional flow in a backward-facing step channel using an inserted cylinder. Furthermore, we investigated the effects of various streamwise and cross-stream positions of the cylinder on the flow fields and heat transfer enhancement using computational fluid dynamics (CFD) simulations. We describe the heat transfer mechanism in a transitional backward-facing step flow in the presence of an inserted cylinder.

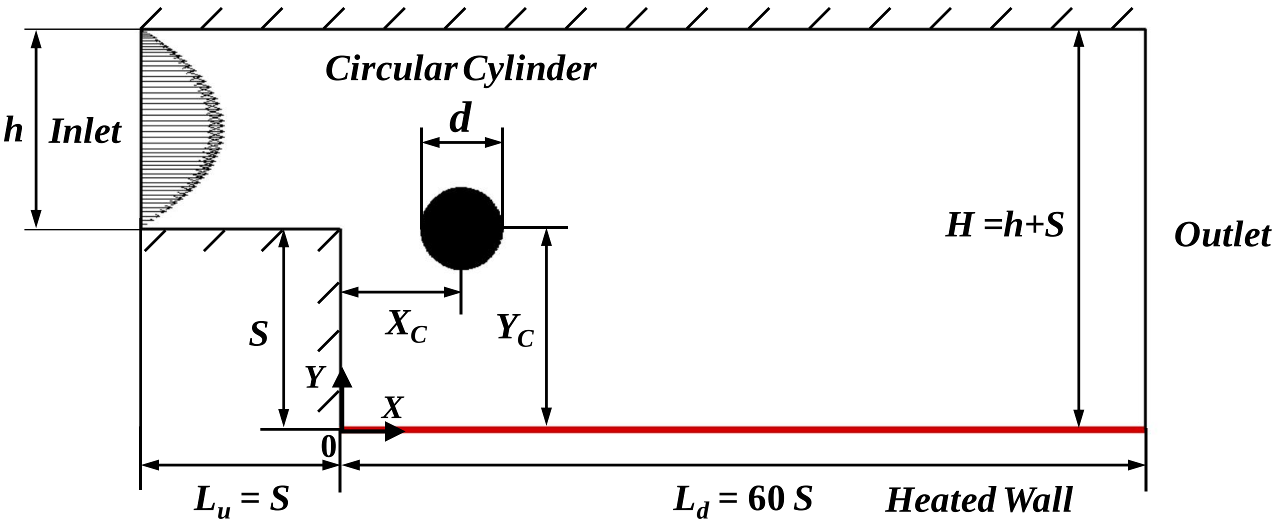

Fig. 5-1. Schematic of the computational domain.

5.2 Numerical methodology

5.2.1 Problem description and mathematical formulation

A schematic of the computational domain is presented in Fig. 5-1. The step height S is the non-dimensional length scale. The upstream of the duct height (h) and channel height downstream from step (H) are maintained constant throughout this study. The duct expansion ratio, $ER=H/h$, was set to 2. The channel lengths, upstream and downstream, of the step are L_u (L_u=1S) and L_d (L_d=60S), respectively. The upstream flow before the step was set at X/S=-1 to avoid the influence caused by the sudden expansion at the step. The length of the calculation region after the step is set sufficient to avoid the influence of outflow. The upstream inlet flow is laminar, fully developed, and isothermal (T_0=293 K). The downstream bottom wall of the BFS is maintained at a uniform temperature (T_W=294 K). The buoyancy effect is negligible because the above inlet flow and bottom wall share similar temperatures. The remaining walls, including the cylinder wall, were treated as adiabatic. A high heat transfer coefficient is attained at the reattachment point, and the primary recirculation zone exhibits an inferior heat transfer property. An adiabatic cylinder is mounted near the top corner in the BFS channel to create disturbances and improve the deteriorated heat transfer in the primary recirculation zone. Various streamwise positions (X_C/S=0.6, 0.9, 1.2, and 1.5) and cross-stream positions (Y_C/S=0.5, 1.0, and 1.5) of the cylinder were investigated with a fixed cylinder size (d/S=0.4).

For the two-dimensional, laminar, incompressible, and unsteady case, the governing equations are: continuity, Eq. (5-1), momentum equations along the *x*- and *y*-axes, Eqs. (5-2) and (5-3), respectively, and energy equations Eq. (5-4).

$$\frac{\partial U}{\partial X}+\frac{\partial V}{\partial Y}=0 \tag{5-1}$$

$$\rho\frac{\partial U}{\partial t}+\rho\frac{\partial U^2}{\partial X}+\rho\frac{\partial VU}{\partial Y}=-\frac{\partial P}{\partial X}+\mu\left(\frac{\partial^2 U}{\partial X^2}+\frac{\partial^2 U}{\partial Y^2}\right) \tag{5-2}$$

$$\rho\frac{\partial V}{\partial t}+\rho\frac{\partial UV}{\partial X}+\rho\frac{\partial V^2}{\partial Y}=-\frac{\partial P}{\partial Y}+\mu\left(\frac{\partial^2 V}{\partial X^2}+\frac{\partial^2 V}{\partial Y^2}\right) \tag{5-3}$$

$$\rho\frac{\partial T}{\partial t}+\rho\frac{\partial UT}{\partial X}+\rho\frac{\partial VT}{\partial Y}=\frac{\mathrm{k}}{\mathrm{C_P}}\left(\frac{\partial^2 T}{\partial X^2}+\frac{\partial^2 T}{\partial Y^2}\right) \tag{5-4}$$

where U and V represent the two instantaneous components of the velocity; T, P, and t represent the temperature, pressure, and time, respectively; and ρ, μ, C_p, and k represent the density, dynamic viscosity, specific heat, and thermal conductivity, respectively. The physical properties of the fluid (air) are assumed to be constants. In the energy equation, the viscous dissipation is assumed to be negligible**.**

The boundary conditions in the non-dimensional form are as follows:

- At the inlet, the streamwise velocity component is assumed according to the velocity approximation which represents a fully developed laminar flow in a rectangular duct [22] and the inlet temperature is uniform, ($U=\frac{3}{2}U_0\left[1-\left(\frac{(Y\text{-}S)\text{-}(H\text{-}S)/2}{(H\text{-}S)/2}\right)^2\right]$, $V=0$ and T_0 = 293 K), for pressure boundary condition, the operation pressure is assumed 101325 Pa.
- At the outlet, the streamwise gradient of flow variables is zero ($\frac{\partial U}{\partial X}=0$, $\frac{\partial V}{\partial X}=0$, and $\frac{\partial \mathrm{T}}{\partial \mathrm{X}}=0$), for pressure boundary condition, the outflow is assumed to be fully developed.
- All walls meet the no-slip condition ($U=0$, and $V=0$). The bottom wall was heated at a uniform temperature (T_W = 294 K). The other walls were considered to be adiabatic.

The local Nusselt number, time-averaged Nusselt number, and time-spatial averaged Nusselt number are respectively defined as Eq. 5-5, 5-6, and 5-7:

$$Nu=\frac{q_w S}{\lambda\ (T_w-T_w)} \tag{5-5}$$

$$\overline{Nu}_t=\frac{1}{\tau}\int_0^{\tau} Nu\ dt \tag{5-6}$$

$$\overline{Nu}=\frac{1}{L}\int_0^{L}\overline{Nu_t}\ dX \tag{5-7}$$

where q_W represents the wall heat flux, and L is the streamwise length of the bottom wall.

The total pressure drop coefficient and Reynolds number are given by Eq. 5-8 and 5-9:

$$dP=\frac{2(\overline{P_0}-\overline{P_{out}})}{\rho U_0^2} \tag{5-8}$$

$$Re=Re_S=\frac{\rho U_0 S}{\mu},\ Re_D=2Re_S \tag{5-9}$$

where is $\overline{P_0}$ the average inlet pressure, $\overline{P_{out}}$ is the average outlet pressure, U_0 is the averaged velocity of the inlet flow, and S is the reference length.

5.2.2 Numerical solution procedure

The numerical study was conducted using the commercial package Ansys Fluent v18.0 (Ansys Inc., PA, USA). The finite volume method is used for the spatial discretization of Eq. (5-1)-(5-4). The convective terms in the Navier–Stokes equations and energy equations are evaluated using the QUICK scheme. The SIMPLE algorithm proposed by Patankar and Spalding [23] is utilized for the coupling of pressure and velocity. The initial conditions of the velocity components and temperature were set as $U=U_0$, $V=0$, and $T_0=293$ K. The grid was generated using the preprocessing tool Ansys ICEM CFD. In Eq. (5-10), the time increment (Δt) between two successive time steps is set to maintain the Courant number (c) to less than 1 and evaluated with the smallest grid spacing (ΔX_{min}) and maximum velocity ($U_{\max}=1.5U_0$).

$$c=\frac{U_{max}}{\Delta X_{\min}}\leqslant 1 \tag{5-10}$$

5.2.3 Grid testing and validation study

Figure. 5-2 (a) shows a magnified view of the non-uniform grid structure for an unobstructed case. Grid refinement was performed in the regions around the walls, where the velocity gradient was high. Similarly, the magnified view of the grid structure with a cylinder is shown in Fig. 5-2 (b). To capture the flow information around the cylinder, a fine grid is established in a square region. The density of the grid is essential in the calculation results. The numerical calculation accuracy is reduced with a coarse grid, resulting in a deviation from the true solution. Contrarily, the very fine grid consumes much more memory and CPU time. Thus, an optimal grid design is essential for balancing calculation accuracy and time consumption.

The grid Reynolds number (Re_g), which defines the minimum grid spacing (ΔX_{min}) as the reference length, can reflect the grid density. It is expressed as Eq. 5-11:

$$Re_g=\frac{\rho U_0 \Delta X_{min}}{\mu} \tag{5-11}$$

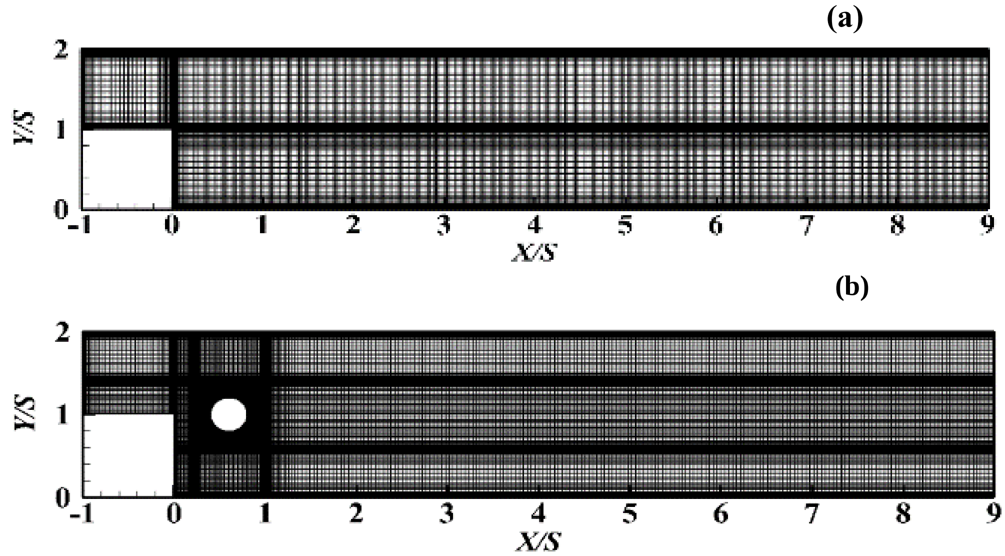

Fig. 5-2. Magnified views of the grid: (a) no cylinder and (b) with a cylinder.

Table 5-1. Grid independence study

Re_g	Total grid number	X_r/S	Deviation (%)	$\overline{Nu_{tmax}}$	Deviation (%)	$\overline{Nu}$	Deviation (%)
16	84,138	0.901	-1.42	13.574	4.73	3.373	-5.57
8	152,898	0.913	-0.11	12.985	0.19	3.505	-1.88
4	209,228	0.914	0.00	12.961	0.00	3.572	0.00

Table 5-1 shows that the grid independence study was conducted with three different types of grid sizes when Y_C=1.0. The deviation was calculated based on the data for Re_g=4. As Re_g decreases, the deviation of these values becomes smaller. When Re_g=8, the minimum deviation is approximately -0.11%, while the maximum deviation is approximately -1.88%, thus meeting the requirement of grid independence. Consequently, Re_g=8 is the value set in these simulations.

The validation of streamwise velocity profiles when *Re*=500 is presented in Fig. 5-3. A flow behavior similar to that observed in the study by Cuerrero and Cotta [24] can be observed and is consistent with our results. For comparison, the result corresponding to the reattachment length at *Re*=700 is shown in Table 5-2 with previously reported 2D research values [4, 5, 25]. The minimum deviation when compared with the experimental results (*ER*=2) of the study by Lee and Mateescu [5] is 1.30%, while the maximum deviation is -6.14% when compared with that (*ER*=1.94) in the study by Armaly et al. [4]. Additionally, the relatively small deviation when compared with the numerical results (*ER*=2) of the study by Sugarawara et al. [25] is -2.32%. However, when compared with present 3D experimental data, the relative error is large and about 22.03%, due to the effects on the side wall.

In the presence of a cylinder, the time-averaged Nusselt number when compared with the numerical results of the study by Kumar and Dhiman [18] when Y_C/S=1.0 and *Re*=200 is presented in Fig. 5-4. The maximum deviation at the peak value was -4.48%. Thus, the reliability and accuracy of our numerical solution procedure can be confirmed.

Table 5-2. Reported values for the time-averaged reattachment length X_r/S at *Re* = 700

Source	X_r/S	Deviation (%)
Present	14.66	0.00
Armaly et al. [4]	13.76	-6.14
Lee and Mateescu [5]	14.85	1.30
Sugarawara et al. [30]	14.32	-2.32
Zou et al. Exp. (*AR*=16, *ER*=2)	11.43	-22.03

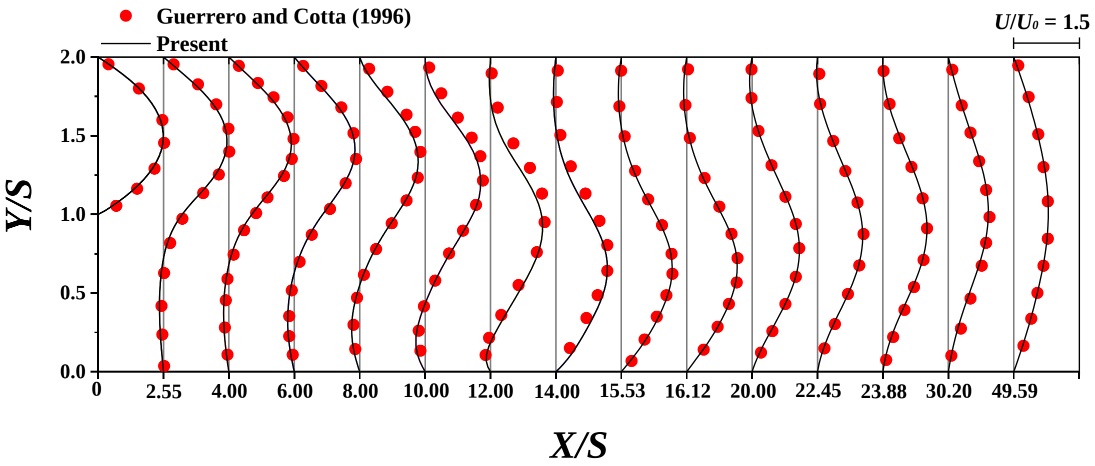

Fig. 5-3. Comparison of streamwise velocity profiles for *Re*=500.

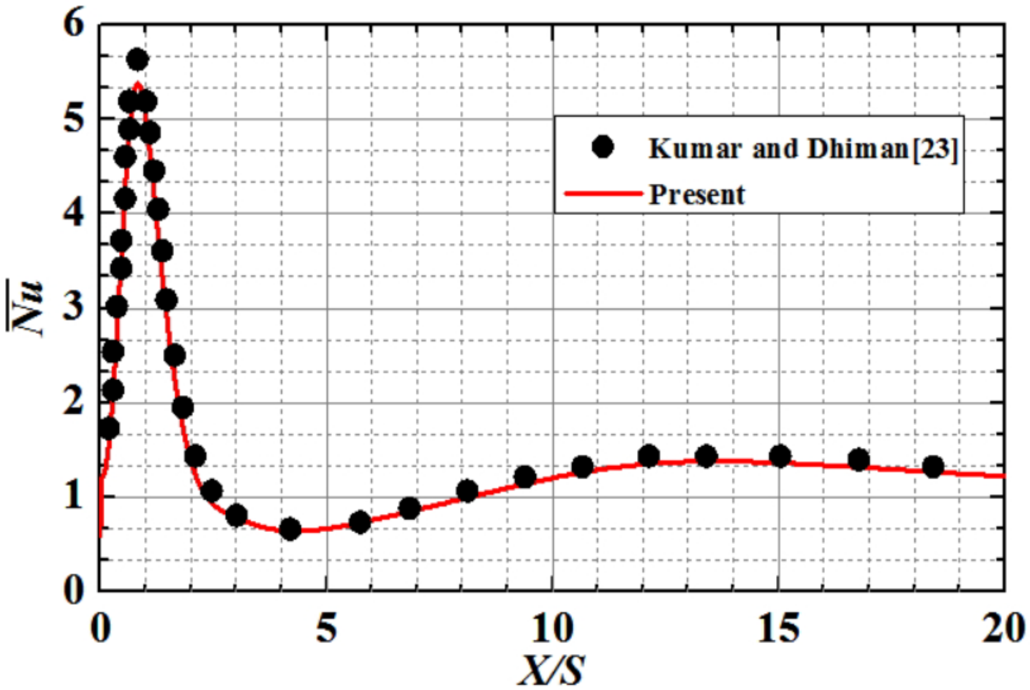

Fig. 5-4. Comparison of the time-averaged Nusselt number distribution.

5.3. Results and discussions

5.3.1 Effect of cross-stream position

Figure. 5-5 presents the flow patterns with the effect of the cross-stream position of the cylinder (Y_C/S=0.5, 1.0, and 1.5) at *Re*=700. Without a cylinder, a steady laminar flow can be observed. The primary recirculation zone appears adjacent to the step with a reattachment length of 14.6. The secondary recirculation zone could be detected downstream near the upper wall. The two recirculation zones after inserting a cylinder at Y_C/S=0.5 share the same structural properties as that of the no cylinder case. Considering the low reverse velocity inside the primary recirculation zone behind the step, the position at Y_C/S=0.5 of the cylinder is not effective for forced convection. The flow state experienced a significant mutation and emerged as a newly formed transitional flow regime at Y_C/S=1.0 and 1.5. Thus, the primary recirculation zone would be broken owing to the divided shear layer, primarily due to the presence of the cylinder. A series of vortices appear near the bottom wall when Y_C/S=1.0. Further, a vortex could be observed near the upper wall. As the position of the cylinder moved to the center of the inlet entrance, the vortex street near the bottom wall disappeared, and the number of vortices near the upper wall increased with reduced sizes.

To investigate the effect of the cross-stream position on the heat transfer characteristics, the time-averaged Nusselt number distributions on the bottom wall for all cases at *Re*=700 are illustrated in Fig. 5-6. Owing to the similar flow structure for the case with no cylinder and Y_C/S=0.5, the curve of the time-averaged Nusselt number on the bottom wall has a similar shape. When the cylinder position Y_C/S=1.0, two peaks are observed, which are much stronger than those in the two aforementioned cases. These strong peaks combined into one in the case where Y_C/S=1.5. Additionally, the positions of their peak values appear at the step for Y_C/S=1.0 and 1.5 when compared with the no-cylinder case and when Y_C/S=0.5. Fig. 5-7 presents the relationship between the time-spatially averaged Nusselt number and total pressure drop coefficient at various cross-stream positions. When compared with the no-cylinder case, a 114% overall heat transfer enhancement on the bottom wall is achieved by inserting a cylinder at Y_C/S=1.0, with a 45% increment in pressure drop. When Y_C/S=1.5, the heat transfer efficiency decreases, accompanied by an increasing pressure drop, when compared with that of Y_C/S=1.0. In conclusion, heat transfer is significantly enhanced when the cylinder position Y_C/S=1.0 along with a slight pressure drop.

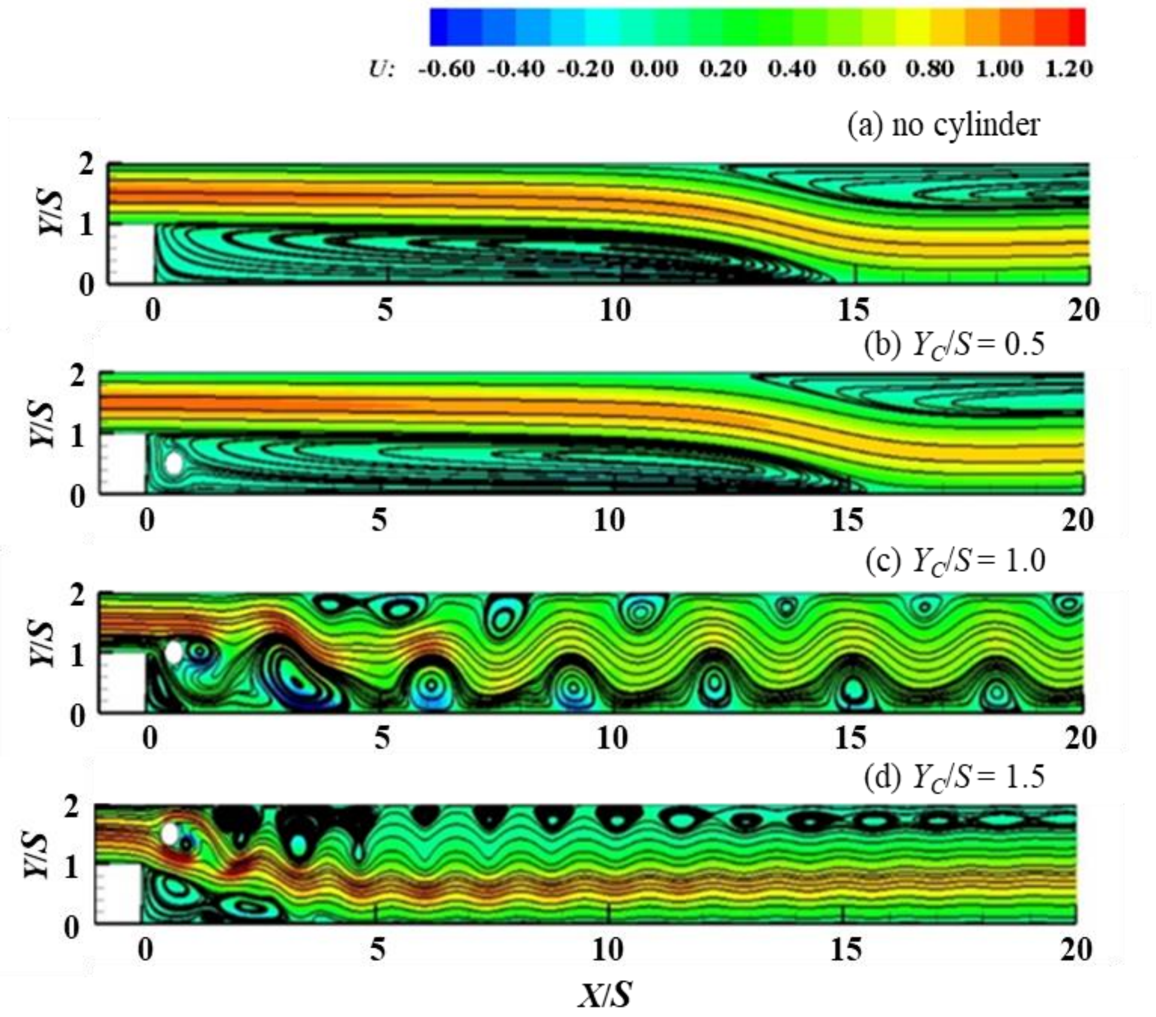

Fig. 5-5. Instantaneous streamlines and streamwise velocity contours with various cross-stream positions of the cylinder for *Re*=700.

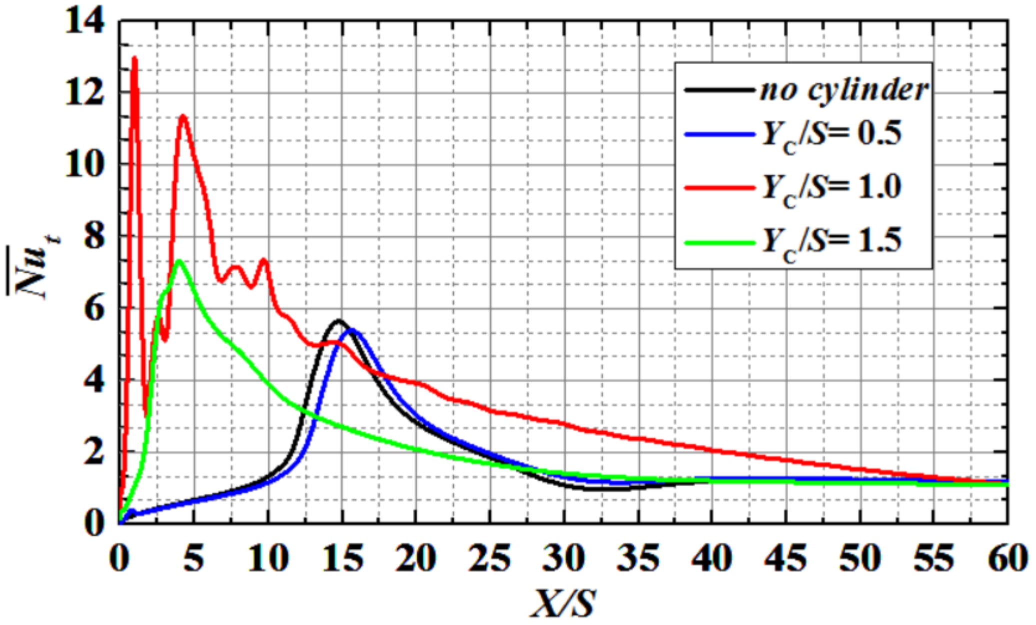

Fig. 5-6. Time-averaged Nusselt number with various cross-stream positions for *Re*=700.

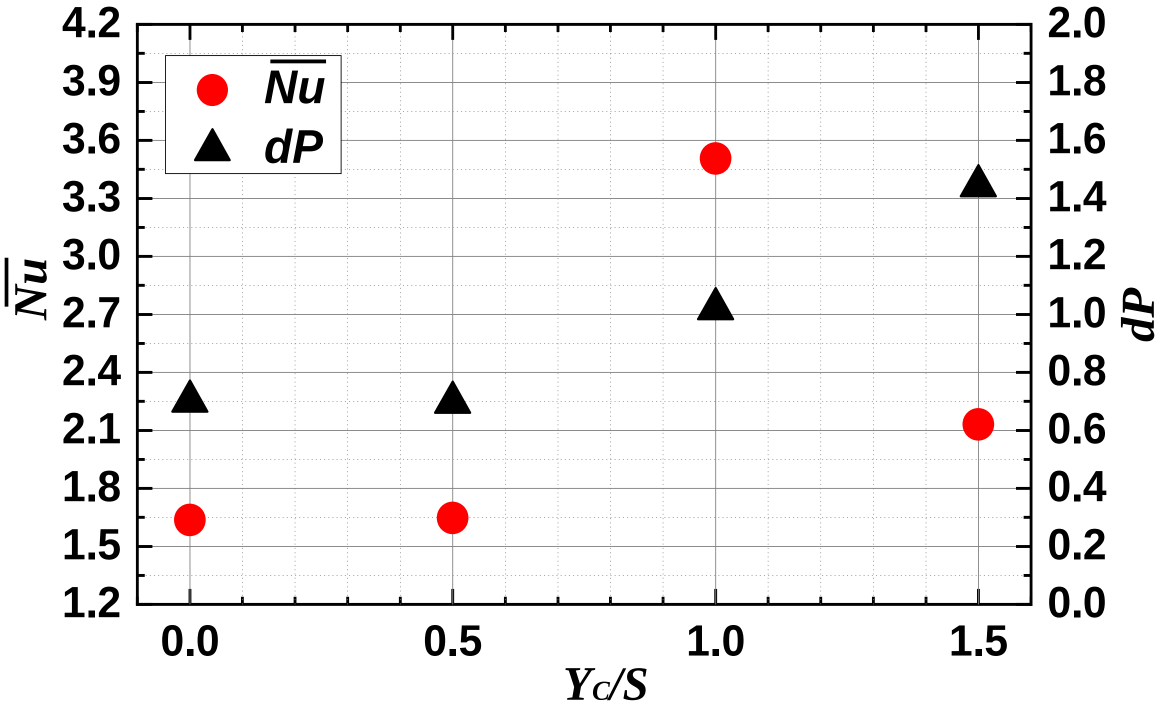

Fig. 5-7. Time-spatially averaged Nusselt number and total pressure drop coefficient with various cross-stream positions for *Re*=700.

5.3.2 Effect of streamwise position

Considering cylinder position $Y_C/S = 1.0$, the flow patterns and heat transfer characteristics were investigated by changing the streamwise positions of the cylinder (X_C/S=0.6, 0.9, 1.2, 1.5). Time-averaged streamlines and streamwise velocity contours with various streamwise positions of a cylinder for Re=700 are shown in Fig. 5-8. The black arrows and red arrows in the figure represent the reattachment points of the primary and third recirculation zones, respectively. As the cylinder moves away from the step, the size of the primary recirculation zone and third recirculation zone increases, and their reattachment point moves downstream from the step. Contrarily, the size of the secondary recirculation zone along the upper wall decreases. When X_C/S=1.5, the secondary recirculation zone disappears while the fourth recirculation zone occurs along the bottom wall.

Figure. 5-9 shows the time-averaged Nusselt number distributions with various streamwise positions for Re=700. The peak positions of the time-averaged Nusselt number approximately correspond to the flow reattachment point of the primary and third recirculation zones. Thus, the peak positions move downstream of the step with the same variation trend of their reattachment points. The two peak values when X_C/S=0.9 are almost consistent with those when X_C/S=0.6. However, the two peak values decrease with an increase in the streamwise position from X_C/S=0.9 to X_C/S=1.5. As shown in Fig. 5-10, from X_C/S=0.6 to X_C/S=1.2, the heat transfer on the bottom wall slightly decreases with a slight increase in pressure drop. When X_C/S=1.5, the heat transfer performance significantly decreases. However, the heat transfer performance is the lowest in the case of no cylinder. Therefore, the cylinder is located at X_C/S=0.6, and when Y_C/S=1.0, the heat transfer performance is relatively optimum.

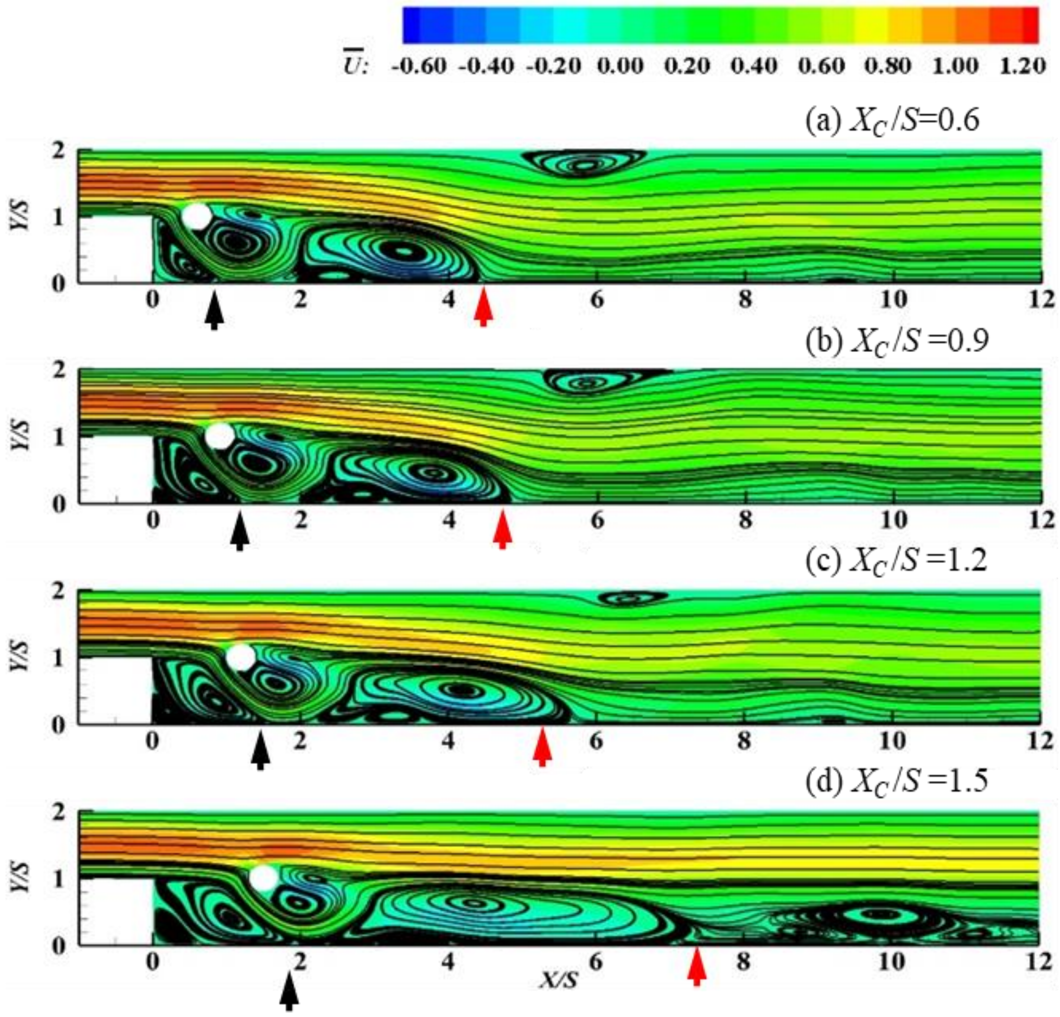

Fig. 5-8. Time-averaged streamlines and streamwise velocity contours with various streamwise positions for *Re*=700.

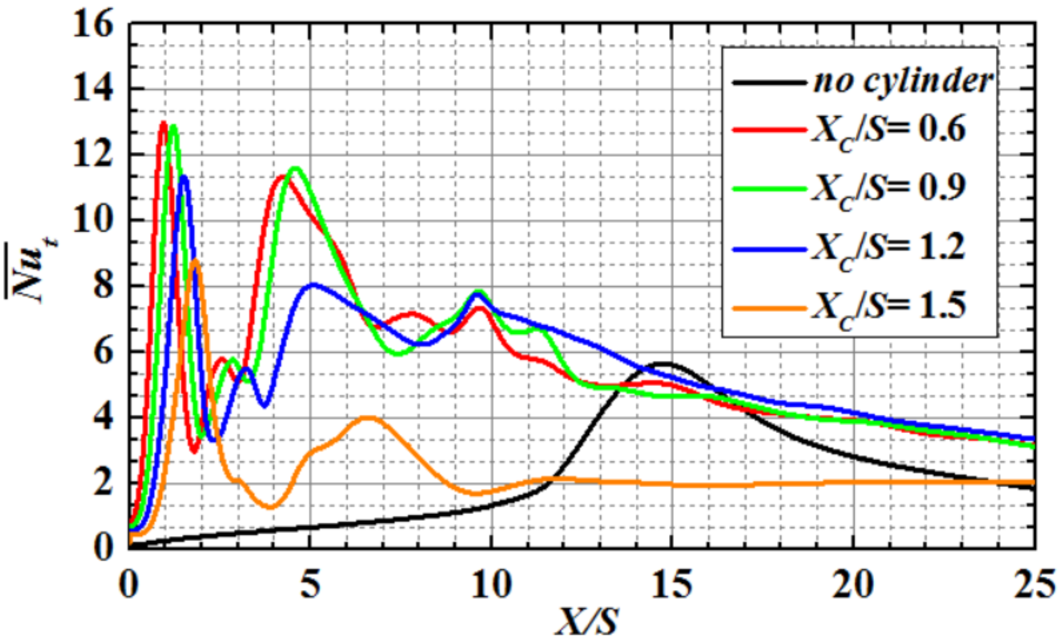

Fig. 5-9. Time-averaged Nusselt number with various streamwise positions for *Re*=700.

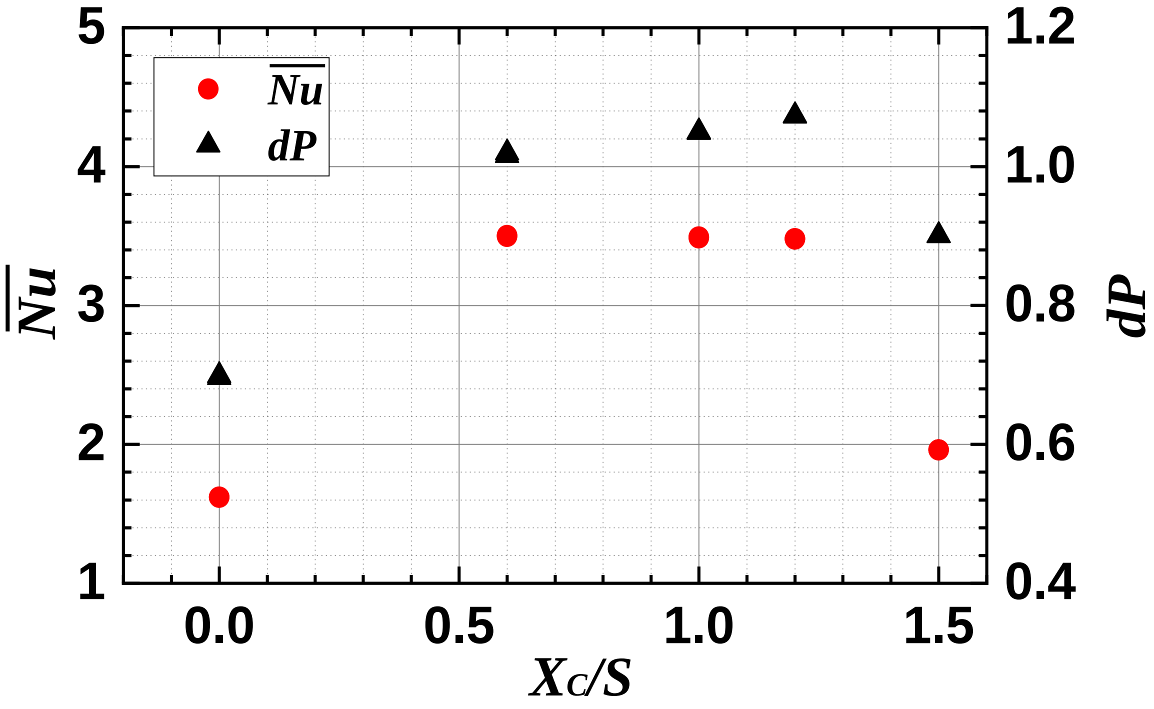

Fig. 5-10. Time-spatially averaged Nusselt number and total pressure drop coefficient with various streamwise positions for *Re*=700.

5.3.3 Heat transfer enhancement mechanism

X_C/S=0.6 and Y_C/S=1.0 at Re=700 were selected to study the periodic flow instability and heat transfer enhancement mechanism in a transitional BFS flow with an inserted cylinder. This selection was based on the results showing higher heat transfer and lower pressure drop described previously.

5.3.3.1 Periodic instability

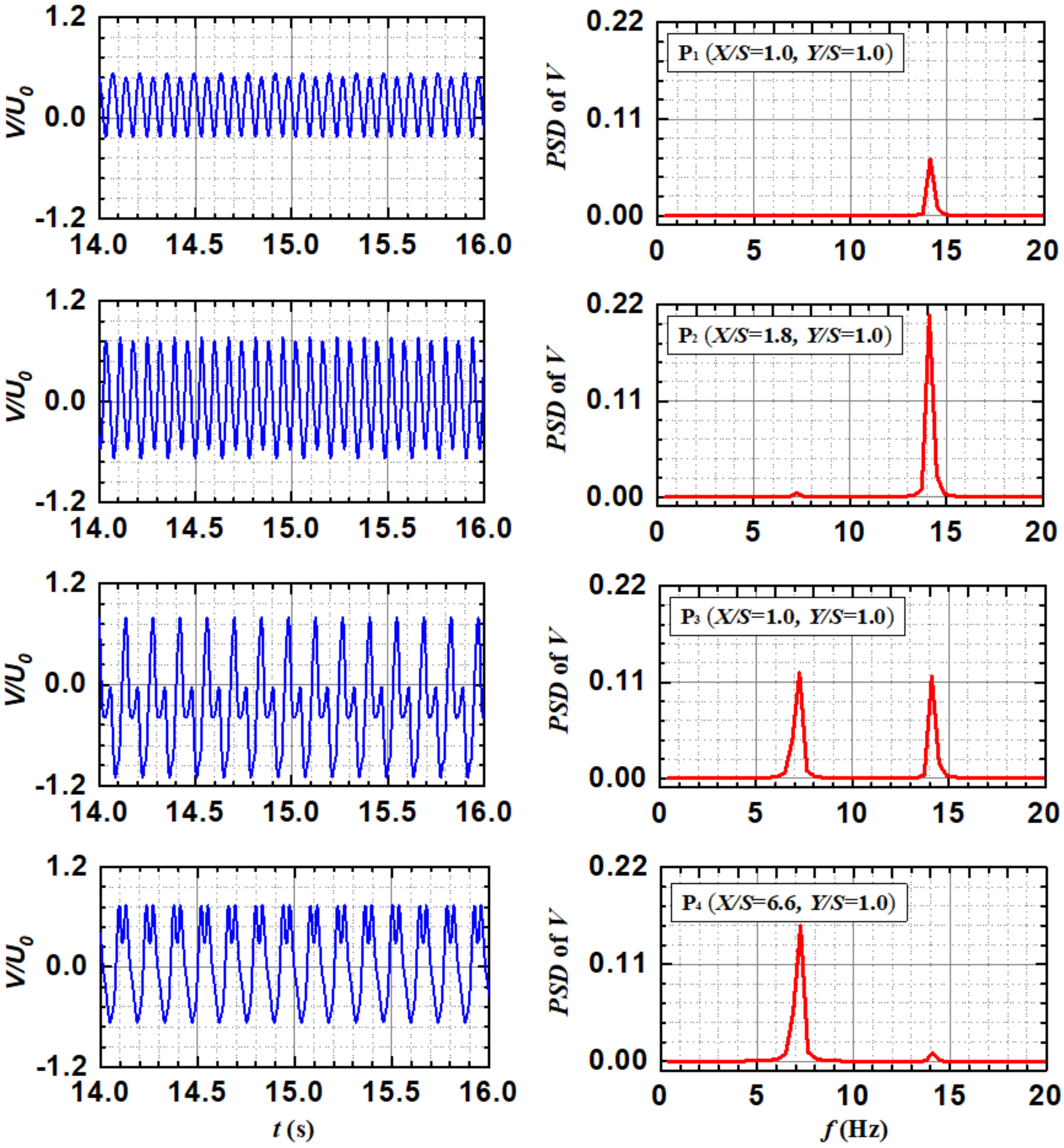

Fig. 5-11. Monitor point results of transverse velocity (V) and power spectral density (PSD) of V at Re =700.

Figure 5-11 presents the monitor point results of the instantaneous transverse velocity (V) and power spectral density (PSD) of V at Re=700. Four monitor points P_1 (X/S=1.0, Y/S=1.0), P_2 (X/S=1.8, Y/S=1.0), P_3 (X/S=4.2, Y/S=1.0), and P_4 (X/S=6.6, Y/S=1.0) were set to monitor the V in the flow field. The fluid velocity fluctuates periodically with the frequency of the basic harmonic. The amplitude of the velocity oscillation increases gradually from point P_1 to P_3, but the amplitude of the velocity oscillation decreases at the downstream point P_4. At the upstream points P_1 and P_2, the power spectrum exhibits a single peak influenced by the inserted cylinder corresponding to the frequency f_C=14.11, while the power spectrum shows a secondary peak with f_S=7.25 at point P_4. The temporal data was taken for 120 s. Thus, as the monitor point moves away from the cylinder, the periodic flow oscillation is primarily influenced by the channel, along with the lesser effect of the cylinder. Furthermore, at point P_3, the periodic velocity oscillation is dominated by two elementary frequencies (f_C and f_S) with the interaction of the cylinder and stepped channel. In Fig. 5-12, the time sequences of the instantaneous streamlines in one cycle are plotted. Vortexes A, B, and C are marked by green, red, and yellow arrows, respectively. Vortex B gradually becomes smaller and moves downstream of the step. In addition, as shown in Figs. 5-12 (a)– (d), vortex A located behind the cylinder gradually sheds and combines with the smaller vortex attached to the bottom wall. As shown in Figs. 5-12 (e)–(h), vortex C dissolves and combines with vortex A and the smaller vortex attaches to the bottom wall. This vortex motion explains the formation of vortex B, as shown in Fig. 5-12 (a).

Figure 5-13 shows the time sequences of the instantaneous vorticity contours combined with the instantaneous temperature contours in one cycle. The red parts correspond to the regions where the vorticity is positive, whereas the blue parts correspond to the regions where the vorticity is negative. Periodic development of the interaction between the positive and negative vorticity regions is essential in the thermal fields. Hence, the thermal boundary layer on the bottom wall deteriorates due to the effect of flow periodic instability.

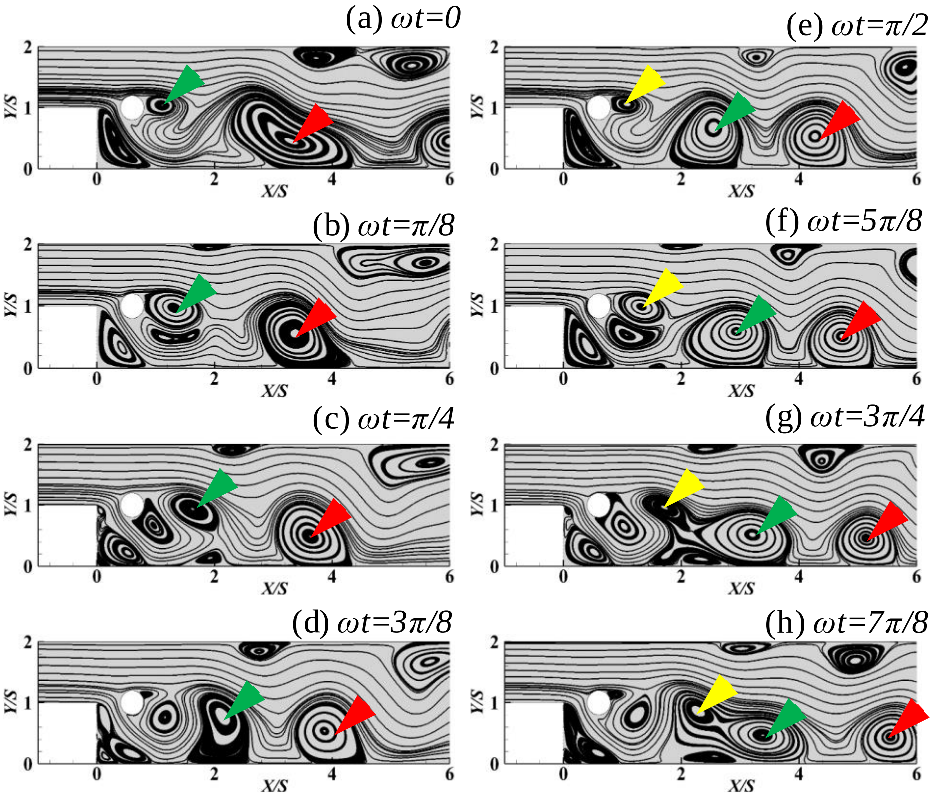
(a) $\omega t=0$
(e) $\omega t=\pi/2$
(b) $\omega t=\pi/8$
(f) $\omega t=5\pi/8$
(c) $\omega t=\pi/4$
(g) $\omega t=3\pi/4$
(d) $\omega t=3\pi/8$
(h) $\omega t=7\pi/8$

Fig. 5-12. Time sequences of instantaneous streamlines in one cycle.

The instantaneous mappings of the fluctuating temperature contours superimposed with the fluctuating velocity vector are plotted in Fig. 5-13. Two fluctuating velocity components, *u* and *v*, and the fluctuating temperature θ are defined as follows:

$$u = U - \overline{U} \tag{5-12}$$

$$v = V - \overline{V} \tag{5-13}$$

$$\theta = T - \overline{T} \tag{5-14}$$

where $\overline{U}$ and $\overline{V}$ correspond to the time-averaged streamwise velocity and normal components velocity, respectively, and $\overline{T}$ is the time-averaged temperature. From the qualitative analysis, Fig. 5-13 presents two types of fluctuating vortex motion corresponding to clockwise and counterclockwise directions of the vortices alternately. The red and blue parts represent the hot fluid ($\theta > 0$) and cold fluid ($\theta < 0$), respectively.

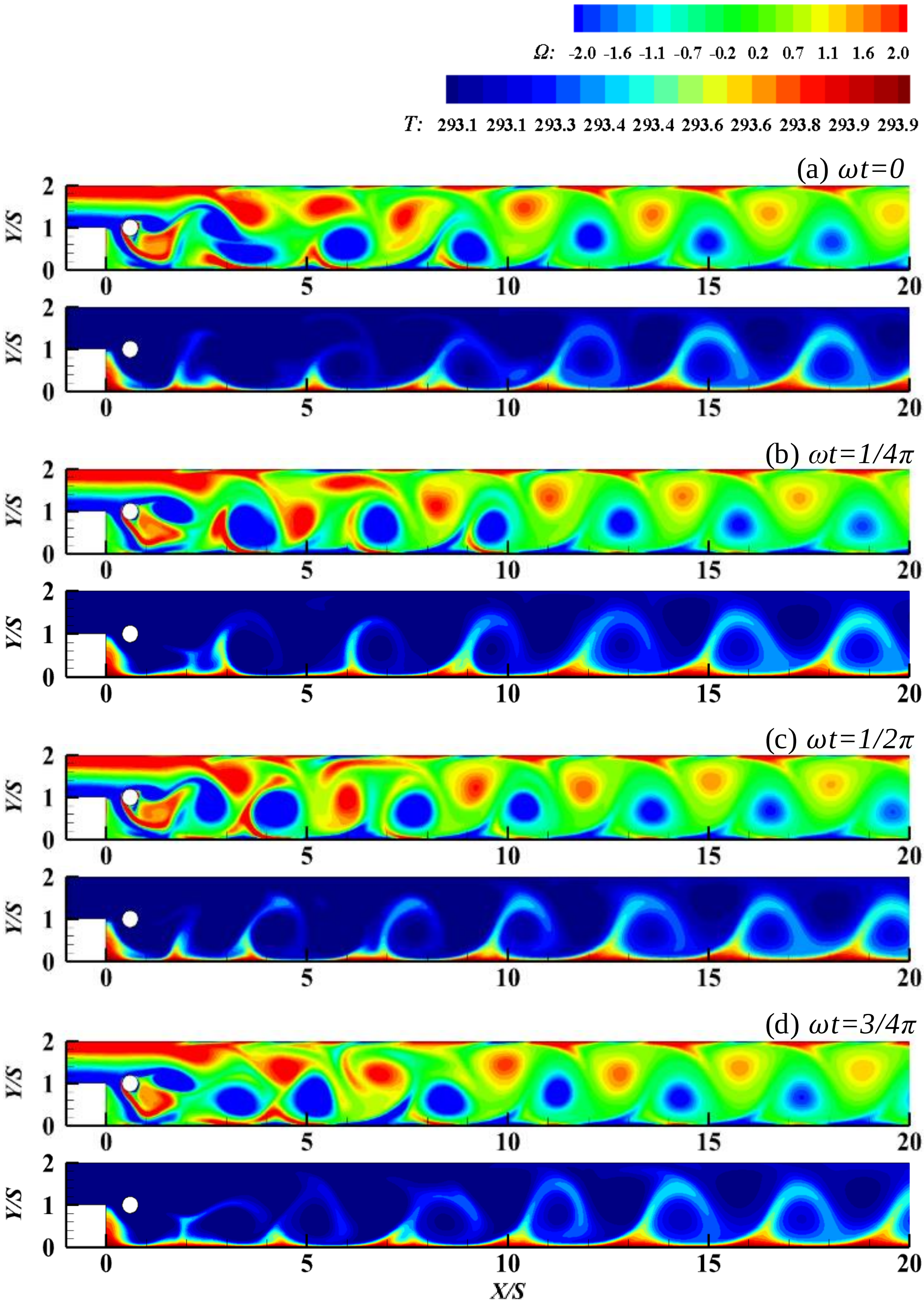

Fig. 5-13. Instantaneous vorticity contours were combined with the instantaneous temperature contours in one cycle.

The black and red arrows in the figure represent the positions of the peak and valley of the local *Nu,* respectively. Most peaks occur at the junction of hot and cold fluids, i.e., the heat transfer effect is better during the interaction. Irrespective of the type, the fluctuating vortex motion has positive effects on the heat transfer to the wall. This is due to the fluctuating vortex that necessitates the flow of the cold fluid from the main flow into the bottom wall. Contrarily, the fluctuating eddies pump away the hot fluid from the bottom wall. Furthermore, the mixing of the hot fluid and cold fluid with the effect of periodic instability of the flow leads to heat transfer enhancement on the bottom wall.

5.3.3.2 Statistical analysis

From the quantitative analysis, the monitor point P_5 (X/S=4.2, Y/S=0.02) near the position of the secondary peak of time-averaged *Nu* plotted in Fig. 5-6 is set to obtain the time sequences of fluctuating velocity (u, v) and fluctuating temperature (θ). Fig. 5-14 illustrates the time variation pattern of the fluctuating velocity field in ten cycles, which is assigned to four quadrants. The calculated fractional contributions to $-\overline{uv}$ and $\overline{v\theta}$ from each quadrant are shown in Table 3. Here, $-\overline{uv}$ represents the fluctuating velocity cross-correlation and $\overline{v\theta}$ represents the cross-correlation of the fluctuating velocity and temperature. As shown in Table 3, the number density of the plotted points is twice as large in the first quadrant ($u>0$, $v>0$) and third quadrant ($u<0$, $v<0$) when compared to those in the remaining two quadrants.

Table 5-3 Frictional contributions to $-\overline{uv}$ and $\overline{v\theta}$ from each quadrant of the u-v plane

Quadrant	Signs of u and v	Signs of θ	Total grid number (n)	$\frac{\sum_{i=1}^{n}(uv)_i}{n\overline{uv}}$	$\frac{\sum_{i=1}^{n}(v\theta)_i}{n\overline{v\theta}}$
1	$u>0$	$\theta>0$	1602	1.076	0.479
	$v>0$	$\theta<0$	0	0	0
2	$u<0$	$\theta>0$	120	-0.056	0.013
	$v>0$	$\theta<0$	702	-0.812	-0.135
3	$u<0$	$\theta>0$	0	0	0
	$v<0$	$\theta<0$	1958	0.977	0.649
4	$u>0$	$\theta>0$	585	-0.178	-0.048
	$v<0$	$\theta<0$	309	-0.007	0.042

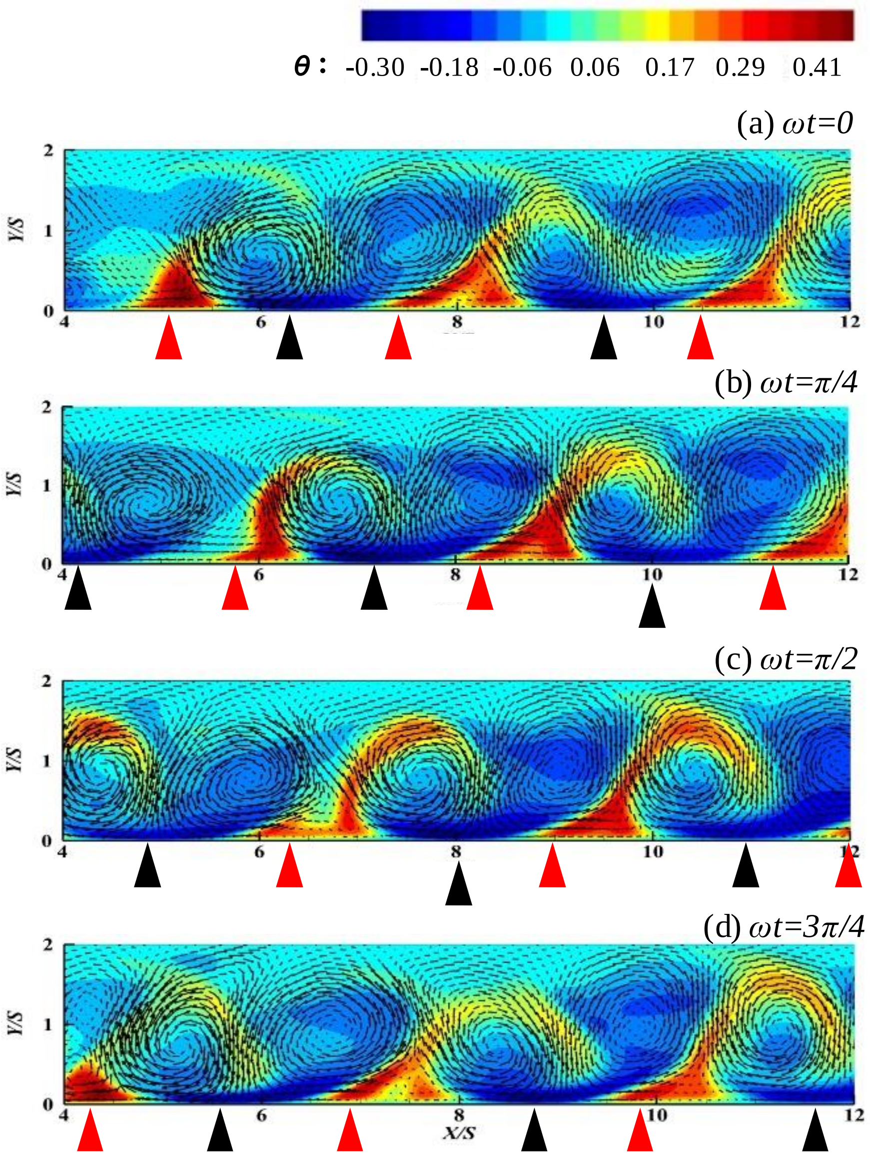

Fig. 5-14. Instantaneous fluctuating velocity vector was combined with the instantaneous fluctuating temperature contours in one cycle.

The fractional contribution to $\overline{v\theta}$ from the hot fluid motion assigned to the first quadrant and from the cold fluid motion assigned to the third quadrant is much greater than that of the other types of fluid motions. Thus, pumping hot fluid from the bottom wall to the main flow region and entraining the cold fluid from the main flow region to the bottom wall region would result in the formation of the secondary peak of time-averaged *Nu*, as plotted in Fig. 5-6. Consequently, the heat transfer on the bottom wall is significantly enhanced when X_C/S=0.6 and Y_C/S=1.0.

5.4 Conclusion and discussions

An incompressible numerical model for the BFS with an inserted cylinder was established to investigate the effects of various streamwise and cross-stream positions of the cylinder on the flow fields and heat transfer. The following are the conclusions of the study:

(1) The simulation results in the case of no cylinder correspond well with the previously reported 2D numerical and experimental results [4, 5, 25].

(2) The heat transfer of the transitional flow on the bottom wall is significantly enhanced when equipped with a cylinder located at X_C/S=0.6 and Y_C/S=1.0. The overall heat transfer enhancement on the bottom wall exhibited a 114% improvement in the presence of a cylinder and a 45% increment in the pressure drop when compared with that of the case with no cylinder.

(3) Considering the effect of the periodic instability of the flow, the secondary peak of the time-averaged Nusselt number was observed when X_C/S=0.6 and Y_C/S=1.0. This occurred when the hot fluid was pumped from the bottom wall to the main flow region and the cold fluid was entrained from the main flow region to the proximal of the bottom wall.

References

[1] A. S. Kherbeet, M. R. Safaei, H. Mohammed, B. Salman, H. E. Ahmed, O. A. Alawi, and M. Al-Asadi, "Heat transfer and fluid flow over microscale backward and forward facing step: a review," *International Communications in Heat and Mass Transfer,* vol. 76, pp. 237-244, 2016.

[2] H. Abu-Mulaweh, "A review of research on laminar mixed convection flow over backward-and forward-facing steps," *International Journal of Thermal Sciences,* vol. 42, no. 9, pp. 897-909, 2003.

[3] H. Togun, "Effect of laminar separation flow and nanofluids on heat transfer augmentation with passive techniques: A review," *International Communications in Heat and Mass Transfer,* vol. 77, pp. 9-14, 2016.

[4] B. F. Armaly, F. Durst, J. Pereira, and B. Schönung, "Experimental and theoretical investigation of backward-facing step flow," *Journal of Fluid Mechanics,* vol. 127, pp. 473-496, 1983.

[5] T. Lee and D. Mateescu, "Experimental and numerical investigation of 2-D backward-facing step flow," *Journal of Fluids and Structures,* vol. 12, no. 6, pp. 703-716, 1998.

[6] P. Kapiris and D. Mathioulakis, "Experimental study of vortical structures in a periodically perturbed flow over a backward-facing step," *International Journal of Heat and Fluid Flow,* vol. 47, pp. 101-112, 2014.

[7] S. Terhaar, A. Velazquez, J. Arias, and M. Sanchez-Sanz, "Experimental study on the unsteady laminar heat transfer downstream of a backwards facing step," *International Communications in Heat and Mass Transfer,* vol. 37, no. 5, pp. 457-462, 2010.

[8] B. Armaly, A. Li, and J. Nie, "Three-dimensional forced convection flow adjacent to backward-facing step," *Journal of Thermophysics and Heat Transfer,* vol. 16, no. 2, pp. 222-227, 2002.

[9] H. Barrios-Pina, S. Viazzo, and C. Rey, "A numerical study of laminar and transitional mixed convection flow over a backward-facing step," *Computers and Fluids,* vol. 56, pp. 77-91, 2012.

[10] G. Biswas, M. Breuer, and F. Durst, "Backward-facing step flows for various expansion ratios at low and moderate Reynolds numbers," *Journal of Fluids Engineering,* vol. 126, no. 3, pp. 362-374, 2004.

[11] Y. Chen, J. Nie, H.-T. Hsieh, and L. Sun, "Three-dimensional convection flow adjacent to

inclined backward-facing step," *International Journal of Heat and Mass Transfer,* vol. 49, no. 25-26, pp. 4795-4803, 2006.

[12] J. Nie and B. F. Armaly, "Three-dimensional convective flow adjacent to backward-facing step-effects of step height," *International Journal of Heat and Mass Transfer,* vol. 45, no. 12, pp. 2431-2438, 2002.

[13] J. H. Nie, Y. Chen, and H.-T. Hsieh, "Effects of a baffle on separated convection flow adjacent to backward-facing step," *International Journal of Thermal Sciences,* vol. 48, no. 3, pp. 618-625, 2009.

[14] J. Nie and B. F. Armaly, "Reattachment of three-dimensional flow adjacent to backward-facing step," *Journal of Heat Transfer,* vol. 125, no. 3, pp. 422-428, 2003.

[15] A. Kitoh, K. Sugawara, H. Yoshikawa, and T. Ota, "Expansion ratio effects on three-dimensional separated flow and heat transfer around backward-facing steps," 2007.

[16] J. Xu, S. Zou, K. Inaoka, and G. Xi, "Effect of Reynolds number on flow and heat transfer in incompressible forced convection over a 3D backward-facing step," *International Journal of Refrigeration,* vol. 79, pp. 164-175, 2017.

[17] J. Tihon, V. Pěnkavová, J. Havlica, and M. Šimčík, "The transitional backward-facing step flow in a water channel with variable expansion geometry," *Experimental Thermal and Fluid Science,* vol. 40, pp. 112-125, 2012.

[18] A. Kumar and A. K. Dhiman, "Effect of a circular cylinder on separated forced convection at a backward-facing step," *International Journal of Thermal Sciences,* vol. 52, pp. 176-185, 2012.

[19] F. Selimefendigil and H. F. Öztop, "Identification of forced convection in pulsating flow at a backward facing step with a stationary cylinder subjected to nanofluid," *International Communications in Heat and Mass Transfer,* vol. 45, pp. 111-121, 2013.

[20] H. Mohammed, O. A. Alawi, and M. Wahid, "Mixed convective nanofluid flow in a channel having backward-facing step with a baffle," *Powder Technology,* vol. 275, pp. 329-343, 2015.

[21] F. Selimefendigil and H. F. Öztop, "Forced convection and thermal predictions of pulsating nanofluid flow over a backward facing step with a corrugated bottom wall," *International Journal of Heat and Mass Transfer,* vol. 110, pp. 231-247, 2017.

[22] R. K. Shah and A. L. London, *Laminar flow forced convection in ducts: a source book for compact heat exchanger analytical data*. New York: Academic press, 2014, p. 3.

[23] S. V. Patankar and D. B. Spalding, "A calculation procedure for heat, mass and momentum transfer in three-dimensional parabolic flows," in *Numerical Prediction of Flow, Heat Transfer, Turbulence and Combustion*: Elsevier, 1983, pp. 54-73.

[24] J. P. Guerrero and R. Cotta, "Benchmark integral transform results for flow over a backward-facing step," *Computers and Fluids,* vol. 25, no. 5, pp. 527-540, 1996.

[25] K. Sugawara, E. Kaihara, H. Yoshikawa, and T. Ota, "DNS of Three-Dimensional Unsteady Separated Flow and Heat Transfer Around a Downward Step," in *ASME 2005 Summer Heat Transfer Conference collocated with the ASME 2005 Pacific Rim Technical Conference and Exhibition on Integration and Packaging of MEMS, NEMS, and Electronic Systems*, 2005: American Society of Mechanical Engineers Digital Collection, pp. 469-477.

CHAPTER 6

General Conclusions and Publication List

6.1 General conclusions

In this thesis, the author focused on investigating details of the three-dimensional flow structures and the related heat transfer characteristics of flows over a backward-facing step in a rectangular duct under relatively low Reynolds numbers. Three-dimensional experiments were performed for backward-facing sep flows and heat transfer. The major findings are summarized below:

In Chapter 2, spatial distributions of flow reattachment position on the bottom wall downstream of a backward-facing step in a duct have been measured by 2D PIV method. Investigations have been done for changing the flow Reynolds number, ranging from steady (*Re*=200) to unsteady (*Re*=1000) flow regimes for the stepped duct having an aspect ratio of 16 and expansion ratio of 2. Non-uniform spanwise distribution of the reattachment length was observed in each case. Within the steady state, the reattachment length shows a unique distribution in the spanwise direction over a channel, that is, having the maximum at the center of the duct but the minimum near the side wall. Generally, the reattachment length increases rapidly as the Reynolds number is increased and has the maximum at the center of the duct at *Re*=400. As the Reynolds number is further increased *Re*>400, the reattachment length conversely decreases due to the flow unsteadiness occurring near the center of the duct. This flow unsteadiness expands to the side wall with the further increase of the Reynolds number, therefore, it makes the spanwise distribution of the flow reattachment position more complicated. The spatial distributions of the reattachment point's existence probability for representative cases (*Re*=200, 400, 600, 800) were studied to further investigate and more clearly clarify the spatial variations of the reattachment phenomena on the bottom wall as time advances. The existence of the side wall restrains the development of the instability from the center of the flow channel to a certain extent, but a high Reyolds number will weaken the influence of the side wall. Time-averaged and instantaneous flow structures were carefully analyzed. The periodicity of the reattachment points, separation points near the side wall and the center of the duct were focused on. Periodic instantaneous reattachment points on the bottom wall appear near the duct center for *Re*=400, the secondary recirculation zone having an obvious periodic movement near the upper wall could be judged by combining the instantaneous separation and reattachment positions near the upper wall.

In Chapter 3, spatial distributions of local heat transfer coefficients on the bottom wall and upper wall downstream of a backward-facing step in a duct flow have been measured by making use of a thermo-sensitive liquid crystal sheet. Heat transfer experiments and three components of the time-averaged velocity measurements by 2D PIV have been done for a wide variety of the flow Reynolds number ranging from *Re*=400 to *Re*=900 flow regimes for the stepped duct having an aspect ratio of 16 and expansion ratio of 2. Obtained local Nusselt number changes not only in the streamwise direction but also spanwise direction, that is, the maximum Nusselt number always appears near the side wall region even if the flow Reynolds number is varied. Two Nusselt number peaks appear near the side wall for *Re*=700, 800, 900, at which the discontinuous reattachment points could be observed near the side wall. Strong downward flow from the step induced along the side wall produces the secondary flow toward the central part of the duct and the area where this secondary flow exists agrees well to the area of the high heat transfer coefficient. High-speed reverse flow from side wall to the duct center can promote the heat transfer on the bottom wall to a certain extent. The flow structure with almost the same velocity magnitude as the reverse flow, but with higher velocity fluctuation downstream the reattachment position near the side wall plays a dominant role in the heat transfer enhancement. When considering the range of 31*S* downstream of the flow channel, the average *Nu* value over the entire bottom wall or upper wall can be estimated by averaging that at its center line in the Reynolds number range from 400 to 900. The ratio of Nu_{max} to Nu_{cmax} in different *Re* on the bottom wall also proves the existence of a three-dimensional feature of this fluid flow model. The three-dimensional flow effect is most obvious at approximately *Re*=400. The three-dimensional characteristics near the upper wall are stronger than that of the bottom wall in the same Reynolds number condition.

In Chapter 4, the reattachment length data near the side wall and the center of the duct have been collected, the distribution of them once again confirmed the obvious three-dimensional characteristics. Reynolds number of 400 was chosen as the main research object because of its largest reattachment length near the duct center and some critical properties described by other researchers. After analyzing the correlation between the velocity-related parameters and the Nusselt number near the bottom wall through the Pearson Correlation method, it could be concluded that the velocity magnitude with high fluctuations in the flow direction can directly affect the heat transfer coefficient in this area. Integrating the velocity-related parameters of different cross-sections, the velocity vector of the Stereo PIV and the phase-averaged velocity vectors, the heat transfer enhancement mechanism near the side wall is clarified: A flow near the side wall from the inlet entrance meanders between the circulation zone adjacent to the step and the secondary recirculation zone near the upper wall, as the flow arrives in the region x/S=10 to 12, it turns into a clockwise flow from the upper wall, passing through the side wall and washes downward the bottom wall. In the downstream side, at x/S=14 where the heat transfer is high, a large counterclockwise flow which is generated from the upper wall, passing through the bottom wall and side wall and then flows back to the upper wall could be observed above the high heat transfer area. Furthermore, this kind of flow has high-speed velocity magnitude and obvious periodicity, making sure that the hot and cold fluid there can be mixed thoroughly and quickly taken away. Thus, other detailed flow factors that affect the heat transfer enhancement besides “jet-like” flow are proposed and clarified.

In Chapter 5, an incompressible numerical model for the backward-facing step with an inserted cylinder was established to investigate the effects of various streamwise and cross-stream positions of the cylinder on the flow fields and heat transfer. The heat transfer of the unsteady laminar flow on the bottom wall is significantly enhanced when equipped with a cylinder located at X_C/S=0.6 and Y_C/S=1.0. The overall heat transfer enhancement on the bottom wall exhibited a 114% improvement in the presence of a cylinder and a 45% increment in the pressure drop when compared with that of the case with no cylinder. Considering the effect of the periodic instability of the flow, the secondary peak of the time-averaged Nusselt number was observed when X_C/S=0.6 and Y_C/S=1.0. This occurred when the hot fluid was pumped from the bottom wall to the main flow region and the cold fluid was entrained from the main flow region to the proximal of the bottom wall.

In this thesis, the effects of 3D flow structure on the heat transfer coefficient on the bottom wall and upper wall in the unsteady laminar flow state were systematically investigated. However, the relationship between the transient fluid flow and the transient heat transfer also needs to be clarified. The common laws of back-ward facing step characteristics (Such as the periodic change of wake flow instability and the Kelvin–Helmholtz instability in the separated shear layer) and the effect of these flow characteristics on heat transfer haven’t been revealed. The flow experiments, heat transfer experiments and velocity-temperature simultaneous measurements need to be carried out. Studying the transient flow and heat transfer problem in unsteady laminar flow, which can not only improve the theory of heat transfer enhancement under BFS condition but also provide a basis and reference for the research and development of high-performance heat exchanger, are desired. In addition, accurate three-dimensional Numerical simulation on transient heat transfer change in the unsteady flow state and the statistics problem of turbulent heat transport is also urgent to be solved.

6.2 Publication list

Chapter 2

“Three-Dimensional Fluid Flow Structure and Reattachment Characteristics of a Backward-Facing Step Flow in a Rectangular Duct”

1: Shuai Zou, Yuji Kohara, Kyoji Inaoka**,** Three-Dimensional Fluid Flow Structure and Reattachment Characteristics of a Backward-Facing Step Flow in a Rectangular Duct, *14th International Conference on Heat Transfer, Fluid Mechanics and Thermodynamics*, Wicklow, Ireland, 1489-1494.

(*Note: Outstanding paper award: Best paper in the session on “Duct and Channel Flow”)

2: Shuai Zou, Kyoji Inaoka, and Mamoru Senda, "Fluid Flow Structure and Periodicity of a Backward-Facing Step Flow in a Duct," in *96th JSME Fluids Engineering Conference*, Hokkaido, Japan, 2018, vol. 1, doi: https://doi.org/10.1299/jsmefed.2018.OS15-12.

3: Shuai Zou, Kyoji Inaoka, and Mamoru Senda, "Experimental Research on 3D Flow Structure over a Backward-Facing Step," in *JSME Kansai Branch 94th Annual General Meeting Lecture*, Kyoto, Japan, 2019, vol. 94, doi: https://doi.org/10.1299/jsmekansai.2019.94.515.

Chapter 3

“Three-dimensional Fluid Flow and Heat Transfer Characteristics of a Backward-Facing Step Flow in a Rectangular Duct”

1: Shuai Zou, Takeshi Murayama, Shogo Motoda, Shumpei Hara, and Kyoji Inaoka, "Heat transfer of three-dimensional backward-facing step flow: local heat transfer coefficients on the bottom wall and upper wall." *The Harris science review of Doshisha University* 61.2 (2020): 125-131.

2: Shuai Zou, Shogo Motoda, and Kyoji Inaoka, "Investigation on Flow Characteristics of Backward-facing Step Flow in a Rectangular Duct using Stereo PIV," *International Research Journal of Advanced Engineering and Science*, vol. 5, no. 4, p. 9, 2020.

3: Shuai Zou, Takeshi Murayama, Shogo Motoda, Wakeda Yoshiki, and K. Inaoka, "Research on the Heat Transfer Characteristics of the Three-Dimensional Backward-facing Step Flow Using Liquid Crystal Sheet Based on SVR Method," in *JSME Kansai Branch 95th Annual General Meeting Lecture*, Japan, 2020, vol. 95, doi: https://doi.org/10.1299/jsmekansai.2020.95.07_714.

4: Shuai Zou, Yuji Kohara, Kyoji Inaoka, and Mamoru Senda, "Three-dimensional Fluid Flow and Heat Transfer Characteristics of a Backward-Facing Step Flow in a Rectangular Duct," in *56th National Heat Transfer Symposium of Japan*, Tokushima, Japan, 2019.

5: Shuai Zou, Takeshi Murayama, Shogo Motoda, Shumpei Hara, and Kyoji Inaoka, "Heat transfer of three-dimensional backward-facing step flow- Local heat transfer coefficients on the bottom wall and upper wall," in *57th National Heat Transfer Symposium of Japan*, Ishikawa, Japan, 2020.

Chapter 4

“Experimental Study on Heat Transfer Mechanism of Periodic Vortex for Unsteady Laminar Flow in a Stepped Duct”

Shuai Zou, Kyoji Inaoka, “Experimental Study on Heat Transfer Mechanism of Periodic Vortex for Unsteady Laminar Flow in a Stepped Duct”, *International Journal of Heat and Fluid Flow* (Submitted 2021)

Chapter 5

“Forced Convection Analysis of Transitional Flow and Heat Transfer over a Backward-Facing Step with active control methods”

Shuai Zou, Jiahui Xu, Kyoji Inaoka, Guannan Xi, Transitional Flow and Heat Transfer over a Backward-Facing Step with an Inserted Cylinder, *International Journal of Science and Engineering Investigations*, Vol. 9, issue 102, July 2020, ISSN: 2251-8843

Publications not included in this thesis

J. H. Xu, S. Zou, K. Inaoka, and G. N. Xi, "Effect of Reynolds number on flow and heat transfer in incompressible forced convection over a 3D backward-facing step," *International Journal of Refrigeration*, vol. 79, pp. 164-175, 2017.

Shuai Zou, Kyoji Inaoka, “Numerical Simulation on Three-dimensional Laminar unsteady Flow and Heat Transfer Characteristics of a Backward-facing step”, *International Journal of Numerical Methods for Heat and Fluid Flow*, (editing 2021)

Nomenclature

1. Chapter 1-4

B	blue light
b	dimensionless blue light
C_f	skin friction coefficient
C_P	specific heat capacity at constant pressure
f	the frequency of the velocity
G	green light
g	dimensionless green light
Gi^*	modified Grashof number
H	duct height
h	the height of the inlet entrance
h_{max}	maximum heat transfer coefficient
L_d	duct length
m	input vector
$\dot{m}$	mass velocity
Nu	Nusselt number
Nu_t	theoretical Nusselt number
Nu_e	experimental Nusselt number
Nu_{bave}	the average *Nu* over the entire bottom wall
Nu_{upave}	the average *Nu* over the entire upper wall
Nu_{bcave}	the average *Nu* at the centerline of bottom wall
Nu_{upcave}	the average *Nu* at the centerline of the upper wall
Nu_{ave}	the average *Nu* over the entire wall
Nu_{cave}	the average *Nu* at the center line of the wall
Nu_{bmax}	the maximum *Nu* over the entire bottom wall
Nu_{upmax}	the maximum *Nu* over the entire upper wall
Nu_{bcmax}	the maximum *Nu* at the centerline of the bottom wall
Nu_{upcmax}	the maximum *Nu* at the centerline of the upper wall
Nu_{cmax}	the maximum *Nu* at the centerline of the wall
Nu_{max}	the maximum *Nu* over the entire wall
P	Pressure
Pr	Prandtl number
$\dot{Q}$	heat transfer rate
qw	heat flux given on the bottom wall or upper wall
R	red light
r	dimensionless red light
Re	Reynolds number
Rea_{bc}	reattachment position near bottom center
Rea_{bs}	reattachment position near bottom side wall
Rea_{uc}	reattachment position near upper center
Rea_{us}	reattachment position near upper side wall
Ri^*	modified Richardson number
S	step height
Sep_{uc}	separation position near upper center
Sep_{us}	separation position near upper side wall
T	temperature
t	time
t^*	$t^*=t*U_{m0}/S$

Greek Symbols

ρ	density
β	volumn expansion coefficient
λ	thermal conductivity of fluid
μ	fluid viscosity
υ	kinematic viscosity
δ	boundary thickness
ξ, $\xi*$	Slack variables

Subscripts

in	inlet value
w	wall value
max	maximum value
min	minimum value
out	outlet
max	maximum
p	predictive value
c	calibration value
e	experimental value
min	minimum
wall	near-wall value

Abbreviations

ANN	artificial neural network
AR	aspect ratio
BFS	backward-facing step
CFD	computational fluid dynamics
CNN	convolutional neural network
CPU	central processing unit
DNS	direct numerical simulation
ER	expansion ratio
FDF	Facade Design Factory
FOV	field of view
LDV	Laser Doppler Velocity
LES	Large Eddy Simulation
MLP	multilayer perceptron
PCC	Pearson’s correlation coefficient
RANS	Reynolds-averaged Navier–Stokes
RMS	root mean square
SVR	support vector regresssion

T_c	calibration temperature
T_{in}	inlet temperature
T_m	bulk temperature
T_p	predictive temperature
T_W	local wall temperature
u	velocity component in the x direction
$\bar{u}$	time-averaged velocity component in the x direction
u_{rms}	fluctuation intensity in the x direction
v	velocity component in the y direction
$\bar{v}$	time-averaged velocity component in the y direction
v_{rms}	fluctuation intensity in the y direction
V	$V = \sqrt{u^2 + w^2}$
w	velocity component in the z direction
$\bar{w}$	time-averaged velocity component in the z direction
W_D	duct width
w_{rms}	fluctuation intensity in the z direction
x	streamwise coordinate
X	$X=R+G+B$
x_r	streamwise location of reattachment point
y	wall-normal coordinate
z	spanwise coordinate

2. Chapter 5

C	Courant number
d	diameter of the cylinder
h	inlet channel height
H	$H=h+S$
k	thermal conductivity
Lu	$Lu=1\ S$
Ld	$Ld=60\ S$
Nu	local Nusselt number
$\overline{Nu_t}$	time-averaged Nusselt number
$\overline{Nu}$	time-spatial averaged Nusselt number
$\overline{P_0}$	the average inlet pressure
$\overline{P_{out}}$	the average outlet pressure
$\bar{T}$	time-averaged temperature
Re_g	grid Reynolds number
Re_S	Reynolds number based on S
U	streamwise velocity in the X direction
U_0	the averaged velocity of the inlet flow
V	transverse velocity in the Y direction
u	streamwise fluctuating velocity
v	transverse fluctuating velocity
$\overline{uv}$	velocity cross-correction
$\overline{v\theta}$	velocity-temperature cross-correction
W	channel width
X	streamwise coordinate
Y	transverse coordinate
X_C	stream-wise position of the circular cylinder
Y_C	cross-stream position of the circular cylinder

Greek Symbols

Ω	instantaneous vorticity
θ	fluctuating temperature
μ	dynamic viscosity
τ	sampling time

Subscripts

max	maximum
min	minimum
out	outlet value
W	wall value

Abbreviations

PSD	power special density

Acknowledgments

First and foremost, I would like to express my sincere gratitude to my supervisor Prof. Kyoji Inaoka for his invaluable guidance and continuous support of my Ph. D. study and related research. Without his valuable advice, I could not achieve the current research results. I would like to say sincerely thankful words to Assistant Professor Shumpei Hara for his patience and assistance in instructing me about my research work. I owe a deep sense of gratitude to Professor Hiroshi Iwai and Professor Masanori Takaoka for their insightful suggestions and comments with kindness.

I would also like to show my appreciation to Professor Guannan Xi for his continuous support and kind care. I am greatly indebted to Mr. Yuji Kohara for his helpful experiment assistant and valuable comments. I own a deep sense of gratitude to Mr. Takeshi Murayama, Mr. Shogo Motoda, and Mr. Daiki Mizuhashi for their help in heat transfer experiments, fluid flow experiments and numerical simulation.

I would also like to thank all the present and former laboratory members in the Heat transfer Laboratory. It is an unforgettable and meaningful thing for my whole life to be a member of you. In particular, I sincerely thank my "translator" Mr. Xiaodan Song, who can make me better communicate with my Japanese lab members. Special thanks are also expressed to Mr. Naoki Higuchi for his various help and heedful care.

I'd like to thank my parents for their unreserved love and support, which are my motivation to move forward, and Dr. Huan Yang for her support and company.

There are still too many thanks needed to be written here. Thank you all who are related to this study.

Shuai Zou

March, 2021